Cranfield University, School of Applied Sciences

Characterisation and Material Removal Properties of the RAP™ Process

William John O'Brien

PhD thesis

2011

Supervisors: Professor John Nicholls and Professor Paul Shore

Acknowledgements

I should like to thank my supervisors, Professor John Nicholls and Professor Paul Shore. I should also like to thank the other members of the RAPT research team, past and present: Mr. Marco Castelli, Dr. Carlo Fanara and Dr. Renaud Jourdain. I am also very grateful to the other research staff and technicians of the Precision Engineering Centre who have given their time to assist me with my work. I wish to thank the staff RAPT Industries for their technical support. Finally, I wish to thank the British Technology Fund and the Innovative Manufacturing Research Centre for their sponsorship of the project.

Abstract

The Reactive Atom Plasma® (RAP) process is a plasma chemical etching process. RAP was developed at RAPT Industries as a process for removing subsurface damage from silicon carbide optics. The process is being investigated at Cranfield University as a novel method for the fine surface correction of large optics, with the aim of shortening the manufacturing period of the next generation of large telescopes. RAP offers material removal rates that are up to 10 times higher than those of ion beam figuring, the current state-of-the-art technique and the convenience in that it can be operated at atmospheric pressure. Much of the work done at Cranfield University has involved applying the process to ULE® (UltraLow Expansion), a titanium silicate glass whose linear coefficient of thermal expansion is $<10^{-8}$ K^{-1}. This material is starting to become a popular material for the fabrication of large telescope mirror substrates and it soon might replace Zerodur (the most popular choice during the 20th century). It has been shown that RAP is very effective at etching ULE without preheating.

In this thesis, an emphasis has been made on the temperature measurements of the plasma torch by atomic emission spectroscopy. These measurements have been performed to estimate the amount of heat delivered to the substrate. Using a combination of absolute line intensity and Boltzmann plots, temperatures between 4000K and 6200K (±500K) were measured in the pure argon plasma plume. In the plumes of the reactive plasmas, the temperatures measured in the reactive plasmas peaked at about 5500K. Although the highest temperatures in the reactive plasmas were lower, the warm gas was spread over a wider volume and the total amount of heat delivered into substrate materials in all cases was roughly the same (200-450W depending on the position of the substrate). Temperatures measured in the coil region of the plasmas peaked at 9000K. Spectroscopic measurements were taken while samples were being etched. It became apparent that when etching ULE, a thin disc of plasma containing titanium formed above the surface, the temperature of which was ~3000K. It was obvious from the Boltzmann plots that local thermal equilibrium did not exist in this plasma.

In simple material removal tests on small ULE samples (<200 mm), removal rates up to 0.2 mm^3/s were measured (using NF_3 as the precursor gas). The material removal rate was dependent upon the torch travel speed, due to greater local temperature rises that occur when the slower travel speeds are used. In similar tests performed upon silicon, comparable volumetric material removal rates were measured but the rate was less dependent on the travel speed due to its high thermal conductivity. When ULE was etched, the roughness on the surface within the etched regions approximately doubled. The Sa values (two-dimensionally mean deviation averaged surface roughness) increased from ~1 nm to >2 nm. This fine roughening on the finest scale is believed to be the due to the redeposition of non-volatile titanium compounds.

Temperatures were also measured upon ULE surfaces being etched using a thermal imaging camera. Temperatures up to 300°C were measured, when a travel speed of 10 mm/s was used. Such temperatures do not greatly exceed those measured by others when performing similar tests using ion beam figuring. The results are encouraging, and as long as things are well managed, it should be possible to apply the process to much larger ULE optics.

TABLE OF CONTENTS

1 Introduction

As our wish to understand the nature of the universe more thoroughly increases, so does the need for larger and more sophisticated telescopes. The demands for being able to fabricate the large area precision optics that need to be installed in these telescopes quickly and efficiently also increases. The mirrors of the world's largest terrestrial telescopes are made up of a large number of segments (usually either hexagonal or 'petal'-shaped). If they were fabricated in a single piece, they would be likely to distort under their own weight and would be extremely difficult to transport. At the time of writing, the world's largest optical telescope is the Keck telescope in Hawaii. It consists of two telescopes, each with primary mirrors that are 10 m in diameter and made up of 36 segments [**1**]. These will, however, be dwarfed by the next 'generation' of telescopes. The European Southern Observatory intends to build the European Extremely Large Telescope (E-ELT). Although it is still in its 'detailed design' phase, it is proposed that it will have a primary mirror that is 42 m in diameter, made up of nearly 1000 segments and covering an area of 1300 m^2 [**2**].

Many projects at the forefront of astrophysics research are envisaged to use telescopes of this size. Some projects involve the search of exosolar planets (planets orbiting nearby stars). Looking further afield, such telescopes will be able to resolve the brightest stars in galaxies as far away as the Virgo cluster (60 million light years away) in order to closely characterise their stellar populations. Larger telescopes will enable astrophysicists to detect "standard candles", such as type 1a supernovae, in more distant galaxies. A 'standard candle' is a stellar object whose luminosity is known precisely and can be used to calculate the distance to the galaxy that contains it. Knowing the distances of those galaxies would in turn help us define the "cosmological constant" and perhaps give us an idea as to the nature of 'dark energy' [**3**]. In essence, larger telescopes will enable us to collect more light from sources that are further away and give us a better understanding of the universe in which we reside.

Commercial applications for large area precision optics also exist. Wafer stepper lithography equipment in the microelectronics industry require large optics; as operational wavelengths become shorter, the optics have to be larger to achieve the requisite resolution. Plans exist for using large reflective and transmissive optics in space-based monitoring systems [**4**]. Fusion reactors, such as the ones at NIF (National Ignition Facility) and HiPER will use large optics for focusing high power lasers [**5, 6**].

Reactive Atom Plasma® (RAP) is an atmospheric plasma etching process. It uses an inductively coupled argon plasma, 18 mm diameter. A chemically reactive gas, typically one containing fluorine atoms, is injected into the centre of the plasma. The heat from the plasma then atomises the gas so that it can react with the substrate material. As long as the reaction products are chiefly gaseous, there is a net removal of material. The plasma torch thus acts as an etching tool and has a Gaussian removal profile. The process was developed by RAPT™ (Reactive Atom Plasma Technologies) Industries, a spin-off company from the Lawrence Livermore National Laboratory in California, which was founded in 2001. RAPT Industries produce advanced silicon carbide optics for defence, aerospace and semiconductor applications [**7**]. RAPT Industries primarily developed the process with the aim of removing residual subsurface damage in silicon carbide optics following mechanical grinding and polishing. Any

form of abrasive polishing imparts a force, which can lead to microscopic cracks in a brittle material under the surface, leading to surface stress. If unchecked, this damage can propagate over time and lead to catastrophic failure [**8**, **9**].

At Cranfield University, the RAP process is being investigated as a novel means of fine figure correcting large optical surfaces. In particular, the research is being steered towards the fabrication of segments that make up the primary mirrors. These segments can be up to 8 m across and their surfaces have to be precise in form to within a few tens of nanometres [**4**]. Steps in the production chain of large telescopic mirrors include machining and grinding the substrate followed by polishing, final figure correction and finally applying a reflective coating if necessary. Ion beam figuring (or IBF) is a technique used for removing material from a surface using ion sputtering. It is used as a non-abrasive technique for fine figure correcting precision optics. Putting it another way, it can be used to remove "high spots" from a surface with the help of time-dwell algorithms (the plasma can be programmed to move more slowly over some regions to remove more material) [**10**]. It has been very successful and can preserve the post-polishing levelled surface roughness (recent work suggests that it could even be used to improve the roughness). However, its material removal rate is slow and the need for it to be operated in a vacuum adds to system complexity and turnaround time. As a result, the IBF phase is a significant bottleneck in the production line. One long term solution would be to construct more IBF facilities, but a better way would be to use an alternative technique that offers a material removal rate that is many times faster.

It has been shown that The RAP process is effective on materials like ULE® (Ultra Low Expansion) glass and silicon carbide, materials from which large mirror substrates are commonly made. Unlike IBF, it can be operated at atmospheric pressure and is more effective at removing subsurface damage. RAP has therefore been envisaged as superseding IBF. Experiments at Cranfield on ULE have demonstrated that removal rates greater than 5 mm^3/minute are possible using RAP. Several microns can be removed over a surface of 1 m^2 in area in a matter of hours, rather than days with ion beam figuring. It is expected that a large optical surface would be processed using RAP after polishing, which would typically be performed using a lap (polishing pad) with a loose abrasive slurry. A ULE surface, after such polishing, might have an Sa (arithmetically averaged surface roughness) of ~1 nm. It is desired that the RAP process could be used to remove the residual damage layer and at least preserve the level of roughness. It has been suggested that if RAP proves to be very successful it might replace the polishing phase altogether.

The Precision Engineering Centre at Cranfield has received funding from two sources to help make this a reality. The first source was the RCUK Basic Technology Program as a part of the Ultra Precision Surfaces (or 'UPS') project which commenced in 2004. The aim of the UPS project was '*to produce surfaces which are ten times as accurate and make them ten times as quickly compared to the current state of the art*' [**4**]. This was a collaborative project with OpTIC Technium, University College London, Zeeko Ltd, Cranfield Precision, UK ATC, Qioptiq and the National Physical Laboratory (NPL). Additional funding has been received from the Innovative Manufacturing Research Centre (IMRC).

In order to do these things successfully with RAP, one must have an accurate idea as to how much material the process is going to remove according to the input

parameters. In other words, the process must be deterministic. If the material removal process is described as being "deterministic", one understands that the operator is able to choose a set of parameters and state, within reasonable error margins, the amount of material that will be removed and from what position on the surface. The process must also be repeatable, which means that the operator must have the ability to set up and carry out the same operation on separate occasions and achieve the same result. There are various parameters that influence the material removal rate: the torch input power, the choice of reactive gas, the flow rates and the position of the surface relative to the torch. Another parameter, which is more difficult to control, is the temperature of at the surface while it is being etched. The plasma torch injects a lot of heat into the substrate material; such heating might have several effects. Most significantly, the rates at which the chemical reactions on the surface take place are temperature dependent and so, correspondingly, is the material removal rate. Large temperature variations might limit the determinism of the process.

Two machines, constructed at RAPT Industries, have been installed at Cranfield University. The first was the RAPT 300 machine, a prototype machine completed in 2005. This has been used to carry out initial material removal tests on small flat samples (mostly samples of ULE). More recently, temperature measurements of both the plasma and the substrate material have been made using this machine. A second machine, "Helios 1200", was installed at Cranfield University in July 2008. This machine's capability is being evaluated and will be used for the fine figure correction of telescopic mirror segments that are up to 1.2 m across.

Generally, the research that has been carried out thus far or is in preparation at Cranfield falls into one of the following categories:

1) Finding out which materials are most amenable to the RAP process, particularly those commonly used in the fabrication of large telescopic optics.

2) Process optimisation; carrying out material removal tests, investigating the evolution of surface form and roughness when various sets of input parameters are used.

3) Finding out how much heat the substrate material is receiving and how is it transferred through the material during the etching process and in turn learn how deterministic the etching process is. Both experimental measurements and computer simulation are being used.

4) To understand the chemical reactions that take place during the process in detail. Few have chemically etched ULE in this way, for example. Understanding the reactions in more detail might make it easier to adjust the removal profile and understand the nature of material that is redeposited on the surface.

5) To investigate the plasma's suitability as an accretion tool, in order to apply coating to a surface.

In this thesis, an emphasis has been made on the work performed on temperature measurements, particularly those made on the plasma plume using atomic emission spectroscopy.

Chapter 2 is a literature review, which includes some of the fundamental concepts related to plasma physics, plasma etching and spectroscopy. A review of the pioneering research into the process is included here. In chapter 3, the RAPT 300 machine and other instrumentation used is discussed. In chapter 4 some of the early material removal experiments that have been performed at Cranfield are discussed. In chapter 5, methodology and results of the spectroscopic measurements are described in detail. In situ temperature measurements, taken using RTD sensors, a pyrometer and a thermal imaging camera are discussed in chapter 6. A summary and recommendations for further research are presented in chapter 7.

2 Literature review

This chapter serves several purposes. It is designed to inform the reader about some of the basic physical and engineering principles that are a prerequisite to understanding the remainder of the thesis. Information about plasmas, atomic emission spectroscopy, thermography, materials used in making telescope mirrors substrates, plasma etching and alternative figure correcting techniques is included. A large part of this chapter also informs the reader about some history regarding the research and development that has taken place into understanding the inductively coupled plasma. There is a significant section about spectroscopic temperature measurement techniques. Finally, early work on RAP is discussed along with a brief review of competing technologies. Emphasis is placed upon research that has had the strongest influence on the experimental work discussed later in this thesis.

Two excellent review papers about research in inductively coupled plasmas, one by Hans Eckert [**11**] and the other by Maher Boulos [**12**] have been of great use in writing this chapter. Although these papers were written in 1974 and 1985 respectively, they provide very good overviews of the research that had been done up until those respective dates and are useful starting points for further reading. Books by Flamm *et al*. [**13**] and Lieberman [**14**] are very useful for gaining a basic understanding of the plasma etching processes and chemistry. Books on plasma spectroscopy by Griem [**15**] and Marr [**16**] have been of use. They both give very detailed overviews of the scientific principles. However, with regards to more practical issues or those more specific to this particular study, scientific journal articles have been used principally. The literature review section of the PhD thesis by Matthew Thornton [**17**], whose work was done at Cranfield University, includes an excellent summary of the various plasma temperature measurement techniques that exist.

2.1 Plasmas

A plasma is often referred to as the fourth state of matter; the first three being solid, liquid and gas. Generally speaking, a plasma can be defined as any state of matter that contains enough free charged particles for its dynamical behaviour to be dominated by electromagnetic forces. That definition includes the free electrons in metals and semiconductors. However, for the most part, plasma physics is concerned with ionised gases. It has been estimated that, by mass, 99% of the baryonic matter in the universe is made up gaseous plasma [**16**] [1].

For a gas to be called a plasma the degree of ionisation need not be very high; indeed a gas with an ionisation ratio of 0.1% has an electrical conductivity that is half that of the same gas fully ionised [**18**]. A gaseous plasma can also been defined as a quasi-neutral gas, one which contains approximately equal numbers of ions and free electrons or possibly electronegative ions, in sufficient density such that the Debye shielding length is much smaller than the macroscopic dimensions of the gas. The Debye length is a characteristic distance in a plasma and is the length over which the Coulomb potential due to a particular ion or electron is effectively screened out by neighbouring oppositely charged particles.

[1] Baryonic matter refers to "normal" matter composed of atoms and nucleons.

The Debye length, λ_D, is equal to

$$\lambda_D = \sqrt{\frac{\varepsilon_0 k T_e}{N_e e^2}} \quad (2.1)$$

where ε_0 is the permittivity of free space (8.854×10^{-12} Fm^{-1}), k is Boltzmann's constant (1.38×10^{-23} JK^{-1}), T_e is the electron temperature, N_e is the electron density and e is the electronic charge (1.602×10^{-19} C). If the electron distribution were to be minutely displaced with respect to the ionic distribution, a restoring force results whose magnitude is approximately proportional to the size of displacement. The result is simple harmonic motion; the fundamental oscillation of frequency is known as the electron plasma frequency. Assuming that the electrons are not degenerate and that their temperature is not so high that they are moving at relativistic speeds, the kinetic energy of the electrons is equal to

$$\tfrac{1}{2} m_e v^2 = \tfrac{3}{2} k T_e \quad (2.2)$$

where m_e is the mass of an electron. The electron plasma frequency, ω_{pe}, is calculated using the formula

$$\omega_{pe} = \frac{v}{\sqrt{3}\lambda_D} = \sqrt{\frac{N_e e^2}{\varepsilon_0 m_e}} \quad (2.3)$$

Although T_e is absent from that equation, N_e is inevitably temperature dependent in a gaseous plasma. Any incident plane wave electromagnetic radiation of frequency higher than the plasma frequency easily penetrates the plasma. On the other hand, radiation of lower frequency is severely attenuated on entering the plasma. The strength of its electric field decays exponentially; the length over which it is reduced by the factor e (= 2.71828) is the called the skin depth. The skin depth, δ, is equal to

$$\delta = \sqrt{\frac{2}{\sigma \mu_r \mu_0 \omega}} \quad (2.4)$$

where σ is the electrical conductivity of the plasma, μ_0 is the permeability of free space, μ_r is the relative permeability (normally close to unity) and ω is the angular frequency of the incident radiation[2]. The energy from the radiation is absorbed and the plasma heats up.

Calculating the skin depth in a plasma requires that the electrical conductivity be known. The electrical conductivity of a plasma is dependent of temperature and pressure. Electrical conductivities in ionised argon have been calculated by Devoto [**19**]. At atmospheric pressure it is approximately $100(\Omega m)^{-1}$ at 6,000K, $1{,}000(\Omega m)^{-1}$ at 8,000K and $10{,}000(\Omega m)^{-1}$ at 20,000K.

Many different types of plasma exist, some are natural and some are man-made. Some of their characteristics are described in figures 2.1 and 2.2.

[2] Whenever ω is used to denote a frequency, rather than f or ν, it invariably refers to an angular frequency in radians per second, i.e. $2\pi \times$ the cyclic frequency.

Plasmas used in materials processing generally fall into two categories: low pressure discharges and high pressure arcs. Low pressure discharges are generally used for etching or coating materials. Methods used to create a low pressure discharge in the laboratory usually involve putting a sufficiently large voltage across a pair of electrodes, such that the intervening gas 'breaks down' and becomes conductive. The breakdown voltage of air at room temperature and atmospheric pressure is around 3000 V/mm, which is huge. This value can be significantly reduced by reducing the pressure of the gas. The pressures used in a direct current glow discharge might be between 0.1 and 10 torr (~10-1000Pa), reducing the required voltage to a few 100V. It is also possible to create a low-pressure discharge by capacitative means, by applying an alternating voltage at radio frequencies, across the electrodes.

High pressure arcs usually refer to processing plasmas that operate at atmospheric pressure or higher. These are generally used to deliver heat to a substrate, such as in cutting, welding or sintering.

Plasmas can also be created using powerful lasers, known as laser induced plasmas [**22**-**26**]. In [**22**], a plasma was created by focusing a pulsed Nd:YAG laser onto a sample that contained copper, iron, nickel and manganese. 4.5 ns long pulses of 100 mJ were used. On a grander scale, a fusion reactor at HiPER is to make use of PETAL **(**PETawatt Aquitaine Laser). To initiate nuclear fusion, a small pellet of deuterium and tritium must be raised to temperatures in excess of 100,000,000°C. This is achieved using lasers of immense power. In the first stage pulses of increasing energy are fired, beginning with femtosecond-long pulses of 3nJ and finishing with nanosecond-long pulses of 100mJ. In the second stage, femtosecond-long pulses of several kilojoules are delivered using a multi-petawatt laser [**6**].

The Sun (from SOHO)

At the centre, the temperature and density is high enough for nuclear fusion, the conversion of hydrogen into helium, to take place. The gas there is fully ionised and completely opaque.

T = 15,000,000°C $N_e = 10^{30}$ m^{-3} $\lambda_D = 10^{-10}$ m

Sun's corona

The Sun's temperature at its surface is just 5500°C. However, gas in the solar atmosphere, the corona, is heated to 2,000,000°C by strong magnetic fields. The gas is very tenuous, and the density is very low as a result.

T = 2,000,000°C $N_e = 10^{12}$ m^{-3} λ_D = 0.1 m

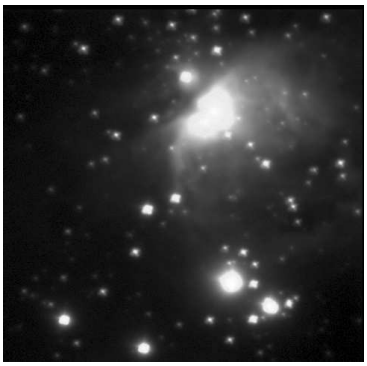

The Great Orion Nebula, photographed by the author.

This is an example of HII region; ultraviolet radiation from very hot, young stars causes surrounding gas to become luminous.

T ~ 10,000°C $N_e = 10^{6}$ m^{-3} λ_D ~ 10 m

Sodium

Metals consist of a gas of free electrons within a solid ionic lattice and could be regarded as being a plasma. The density of free electrons is so high that the free electrons are degenerate, which means that they occupy the lowest energy states that they can occupy. As a result, their electrical conductivity increases with decreasing temperature (the electrical conductivity of insulators and semiconductors generally decreases with decreasing temperature).

T_e ~ 200,000°C $N_e = 2.5 \times 10^{28}$ m^{-3} λ_D ~ 10^{-10} m

Figure 2.1 **Some types of plasma found in nature. Approximate values for the electron temperature (T_e), electron density (N_e) and the Debye length (λ_D) are given [14, 16, 18, 20, 21].**

Fluorescent lighting

Applying a high voltage across electrodes within a tube containing gas at reduced pressure results in fluorescence. Neon lights fluoresce with a characteristic red colour.

Argon glow discharge

In a direct current glow discharge, positively charged ions are drawn towards the cathode and electrons are drawn towards the anode. The plasma becomes luminous close to each electrode; an argon glow discharge has a characteristic blue colour. Such plasmas are often used in analytical chemistry, in which the subject to be analysed is effectively the anode.

T_e ~ 10,000°C $N_e = 10^{14} - 10^{20}$ m^{-3} $\lambda_D \sim 10^{-5} - 10^{-6}$ m

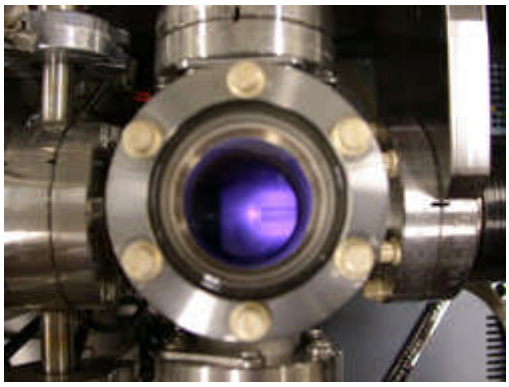

Welding arc

An example of a high pressure plasma. The metal being welded acts as one of the electrodes.

T_e ~ 20,000°C $N_e = 10^{23}$ m^{-3} $\lambda_D \sim 10^{-8}$ m

Ion propulsion

An electrostatic ion thruster was used to propel Deep Space 1, pictured here, launched in 1998. Xenon gas was used. The thruster is similar to a Kaufman drive, which had been developed in the 1960s.

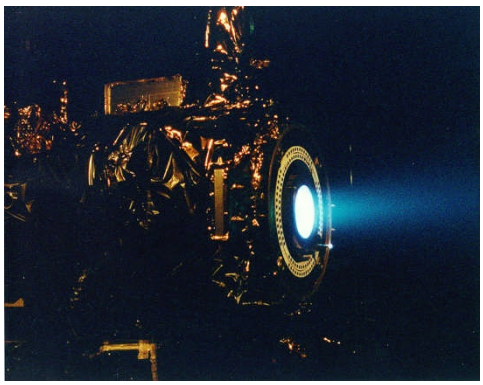

Figure 2.2 **Here are examples of man-made plasmas. Approximate values for the electron temperature (T_e), electron density (N_e) and the Debye length (λ_D) are given where available. [14, 16, 18, 21]**

2.1.1 Thermal equilibrium in plasmas

A plasma usually consists of populations of atoms, positively charged ions in various ionisation states and free electrons. If the energy states of a given population can be characterised by Boltzmann statistics[3], that population has a definable temperature. If the temperatures of all constituent populations in a plasma are equal to each other at a particular point in space, the plasma is said to be in complete local thermal equilibrium (CLTE) at that point. That is to say

$$T_{\mathrm{e}} = T_{\mathrm{atoms}} = T_{\mathrm{ions+}} = T_{\mathrm{ions2+}}$$

Singly charged ions are generally regarded to be separate entities from highly excited atoms. It is not absolutely correct as, for example, the differences between a singly charged ion and a highly excited atom are not so distinct, but is generally an acceptable simplification.

One common characteristic of low pressure discharges is that it is very rare that local thermal equilibrium exists anywhere. This is because the free electrons respond very much more quickly to changes in electromagnetic fields than do the positively charged ions, because of their lower mass, and the neutral particles do not respond at all. The electrons therefore heat up very quickly. They can then either lose energy by radiating or by colliding with the neutral atoms or ions, and thus transfer energy to them by conduction. The existence of thermal equilibrium can only exist if the energy loss by conduction greatly exceeds that by radiation. Collisions are infrequent in low density plasmas, so radiative losses usually win.

In high-density (thermal) plasmas, the populations are usually much closer to being in thermal equilibrium. Strictly speaking, a plasma could only be in complete local thermal equilibrium if it were contained in a blackbody cavity. However, it is generally considered reasonable to state that it is in local thermal equilibrium (LTE) if the Griem criterion is satisfied, which states that the amount of energy that the electrons lose by collisions must exceed the amount that they lose by radiation by at least an order of magnitude.

For a particular excitation state in a hydrogen atom or hydrogenic ion (one that contains only one electron), LTE is satisfied if

$$N_e > 7 \times 10^{24} \frac{Z^6}{n^{17/12}} \sqrt{\frac{kT_e}{E_H}} \quad [m^{-3}] \qquad (2.5)\ [\mathbf{27}]$$

where Z the spectroscopic ion charge, n is the excitation state, T_e is the plasma electron temperature and E_H the ionisation energy of hydrogen, 1310 kJ/mol. If CLTE exists in such a plasma, the condition is satisfied for all values of n.

In regions where a plasma is not in local thermal equilibrium, it might still be regarded as being in partial local thermal equilibrium (PLTE), in which the above condition is only valid for higher values of n.

[3] The temperature of a substance is a measurement of the kinetic energy of the particles. In reality, whenever a large number of particles are concerned, the particles can have a wide range of different energies as defined by the Maxwell-Boltzmann distribution. The temperature is just a representation of the ensemble average particle kinetic energy.

If at least PLTE is satisfied, the relative population densities of ions in successive ionisation states can be calculated using the Saha equation. The ratio of the particle density of ions in state $S+1$ divided by that in state S is given by

$$\frac{N_{S+1}}{N_S} N_e = \left(\frac{2\pi m_e kT}{h^2} \right)^{\frac{3}{2}} \frac{2Z_i(T)}{Z_i(T)} e^{-\frac{E_i}{kT}} \qquad (2.6)$$

where E_i is the ionisation energy concerned and h is Planck's constant (= 6.626×10^{-34} Js). For this reason, PLTE is sometimes referred to as Local Saha equilibrium (LSE).

2.1.2 Demixing processes in plasma gas mixtures

Gas mixtures are frequently incorporated into plasmas for industrial applications. Even if the gas mixture is completely homogeneous and the relative concentrations of the gases are known prior to insertion into the plasma it is not always correct to assume that the relative concentrations remain the same at all positions within the plasma. Temperature and pressure gradients within the plasma can lead to local changes in the homogeneity; a plasma can become demixed within certain regions. External electric fields can also lead to demixing.

The theory behind demixing phenomena is explained very well by Anthony Murphy [**28**]. Several gas compositions that are frequently used in welding arcs were investigated in this article. Results from numerical models were included and compared to experimental results deduced from spectroscopic measurements. One of the mixtures considered was an argon and helium mixture (10% helium by mass, 47.4% helium by atoms at low temperatures). Figure 2.3, taken from [**28**], shows how the mole fraction of each gaseous species (the number of free particles representative of that species per unit volume divided by the total number of particles per unit volume) changes with temperature for that argon-helium gas mixture. As the temperature is increased above 8,000 K, argon starts to become ionised; an argon atom becomes an Ar^+ ion and an electron. As one gas particle has effectively become two particles, the total mole fraction of argon starts to increase with increasing temperature and the mole fraction of helium decreases. The total argon mole fraction reaches a maximum at about 17,000 K, but starts to decrease as the helium starts to become ionised. The lower graph in figure 2.4 shows a temperature profile that might exist in a radially symmetric argon-helium arc plasma. The gradients in temperature lead to gradients in the total mole fractions of the two gases in the regions where the temperature is between 8,000 K and 17,000 K for reasons just described. The mole fraction gradient incurs diffusion between the two gases, which tries to equalise this gradient. The diffusion leads to an increase in the total mass fraction of helium and a decrease in the total mass fraction of argon within the higher temperature region. The upper graph in figure 2.4 shows how the mass fractions of the two gases vary when demixing is taken into account. In the absence of demixing processes, the mass fraction of helium and argon would remain at 0.1 and 0.9 respectively throughout. This process is known as demixing due to mole fraction gradients. Generally speaking, in a mixture of two atomic gases, demixing due to mole fraction gradients leads to an increase in the mass fraction of the chemical element that has the higher ionisation energy when the plasma temperature is within the range in which one element is ionised and the other is not.

Demixing can also be caused by collisions between the species. In the case of the argon-helium mixture, between around 8000 K and 17,000 K, collisions between the argon atoms and helium atoms cause the helium atoms to be pushed towards regions of higher temperature. Collisions between the helium atoms and both argon ions and the free electrons cause the helium atoms to be pushed in the opposite direction. Overall, the mass fraction of helium (the lighter element) increases in the regions of high temperature.

Thermal diffusion, also leads to demixing whenever a temperature gradient is present. Usually, but not always, in a mixture of two atomic gases this causes a net flow of the lighter chemical element awards regions of higher temperature. The three demixing processes so far described all drive diffusion in the same direction in the argon-helium plasma described here. This is not the case for all gas mixtures. The graph in figure 2.5a shows a simulated temperature map for a typical 10% helium in argon arc plasma; the graph in figure 2.5b shows computed values of the total helium mass fraction within this plasma. The total helium mass fraction peaks at > 0.2.

If at least one of the gases involved is molecular, additional demixing effects can result from the dissociation of these molecules. If a homonuclear diatomic molecule, such as H_2, N_2 or O_2 dissociates, one molecule becomes two atoms and the mole fraction of that gas increases. The resulting mole fraction gradient induces diffusion from regions of higher temperature to regions of lower temperature. This leads to a decrease in the mass fraction of the element in the region in which it is being dissociated. Figure 2.6 shows simulated temperature and nitrogen mass fraction maps in an argon-nitrogen mixture (20% nitrogen by mass) in a 200 A, 5 mm diameter welding arc. As the temperature of such an arc is increased, nitrogen molecules start to become dissociated at ~6000 K and become fully dissociated at ~7000 K. Demixing due to molecular dissociation becomes significant between those two temperatures. As can be seen in figure 2.6, there is a trough in the mass fraction of nitrogen in the region where the temperature is between 6000 K and 7000 K. Close to the plasma axis, the mass fraction of nitrogen increases to over 0.25, the result of demixing due to frictional forces.

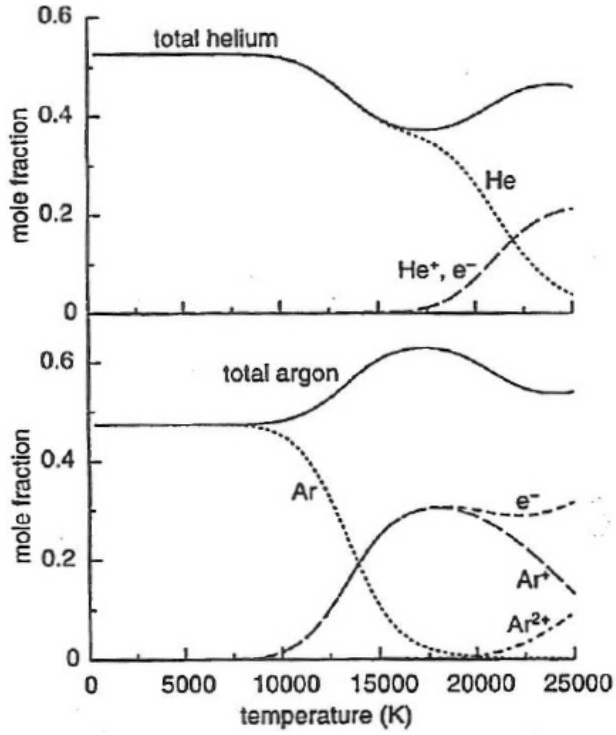

Figure 2.3 **The mole fractions of the various species that would exist in a argon-helium plasma (10% helium by mass and 47.4% helium by atoms at low temperature) as a function of temperature [28].**

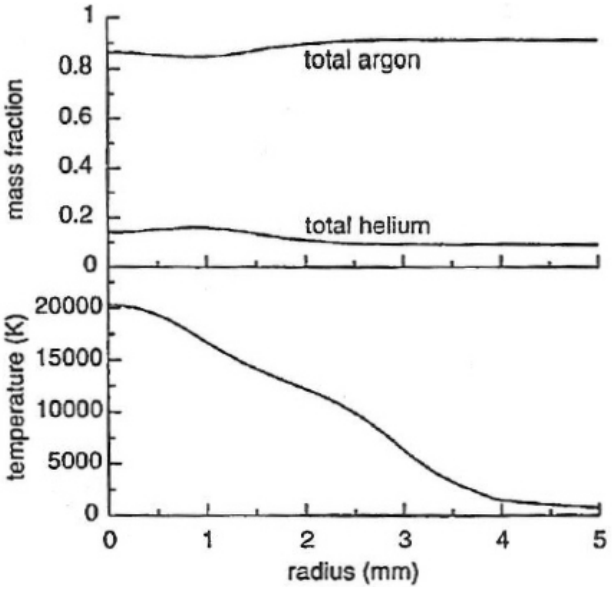

Figure 2.4 **The upper graph shows how the total argon and helium mass fractions would vary within an argon-helium arc if it had the temperature profile displayed at the lower graph. The changes in the mass fractions of the gases at small radii are the result of demixing [28].**

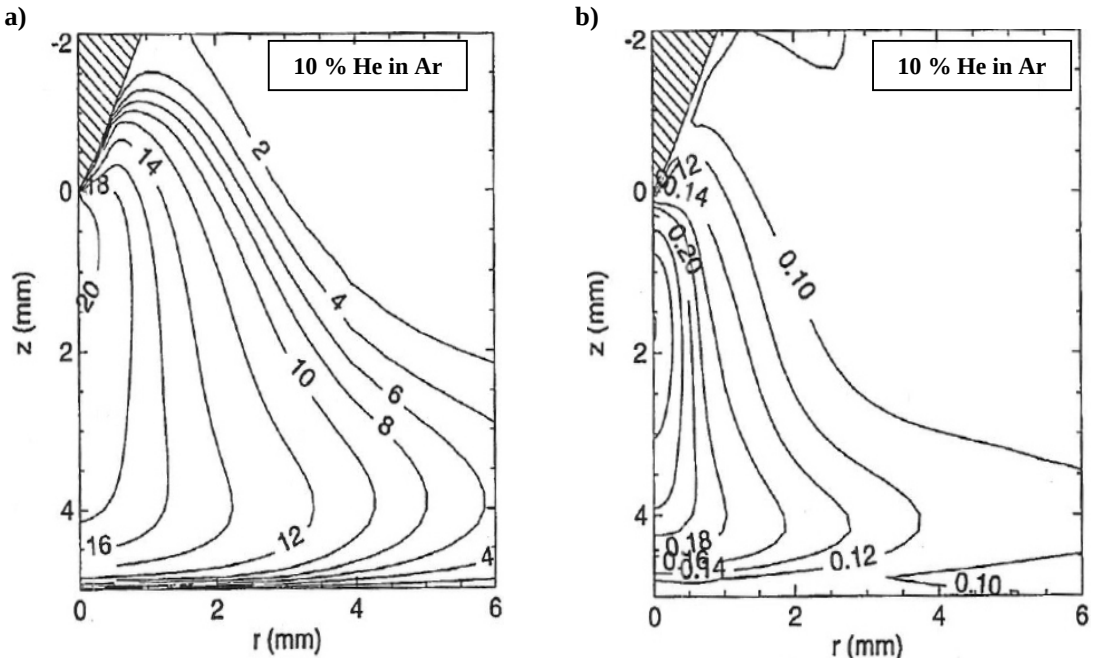

Figure 2.5 **a) Computed temperature map for a 200 A, 5 mm radially symmetric argon-helium arc plasma (10% helium by mass) with an input flow of 10 L/min. Temperatures are in kK. b) Computed total helium mass fraction map for the same arc [28].**

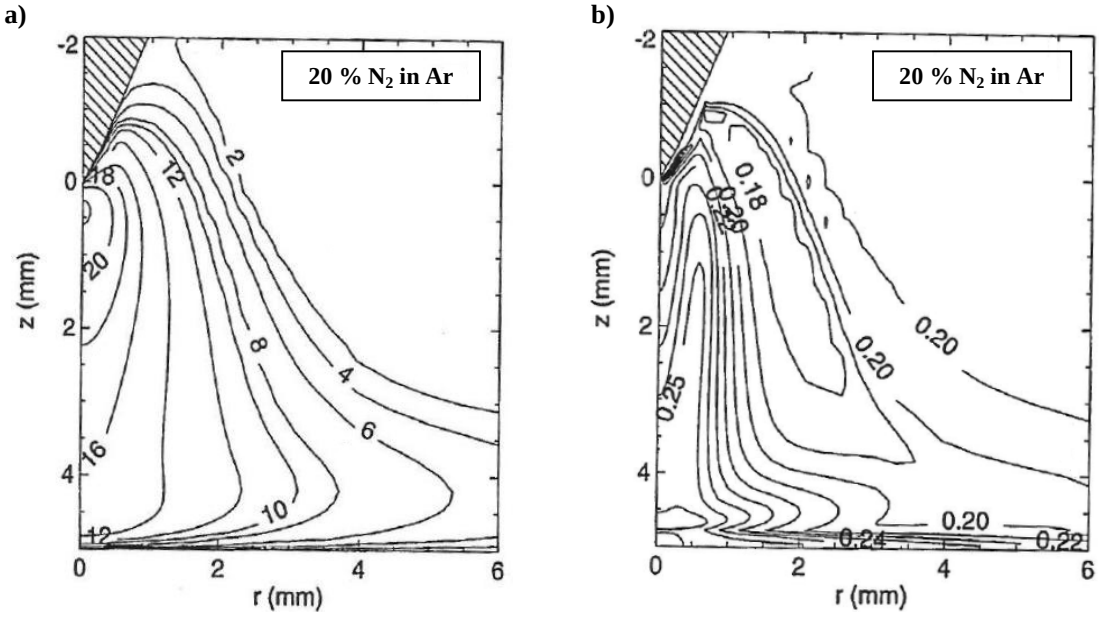

Figure 2.6 **a) Computed temperature map for a 200 A, 5 mm radially symmetric argon-nitrogen arc plasma (20% nitrogen by mass) with an input flow of 10 L/min. Temperatures are in kK. b) Computed total helium mass fraction map for the same arc [28].**

2.1.3 Inductively coupled plasma

In an inductively coupled plasma, or ICP, an RF current is passed through a coil, typically several turns of copper tube. Gases are pushed though the coil's axis and become ionised and heated by the rapidly varying magnetic field induced by the coil. The plasma forms a closed conducting loop, known as the plasma core, which acts like a single turn secondary coil in a transformer. An ICP is also known as an electrodeless plasma; the lack of electrodes is a significant advantage as it alleviates problems that might result from contamination. Typically, gases are pumped through a quartz tube, a barrier that prevents the plasma from shorting out the copper coil. The coil is normally water-cooled to prevent it from melting; sometimes the quartz tube is water-cooled as well.

Low pressure induction arcs have existed since the end of the 19th century. Use of the first induction arcs operated at atmospheric pressure was reported by George Babat in 1942 [**29**]. Such ring discharges had to be ignited at low pressure before being brought up to atmospheric pressure. The first induction torch was invented by Thomas Reed in 1961 [**30**]; a diagram and photograph of it are shown in figure 2.7. At a pressure of ~1 torr the gas broke down when the voltage inside the outer tube exceeded about 100V. He inserted a graphite rod to help initiate breakdown; induced currents in the rod caused it to warm and lower the density of the surrounding gas, promoting its breakdown.

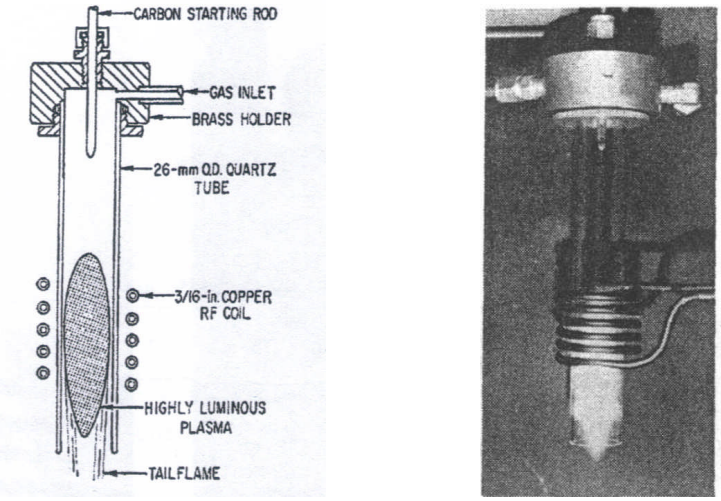

Figure 2.7 **The plasma torch developed by Reed in 1961. It was a 1.5 kW, 26 mm diameter torch, operated at 4 MHz [30].**

Atmospheric ICP torch designs have changed little since Reed's invention. Nowadays it is more common to use a tesla coil to aid ignition, particularly in plasmas of smaller diameter. In these smaller ICPs it is usually possible to ignite the plasma at atmospheric pressure, rather than igniting it at lower pressure and then raising the pressure. It is also possible for ICPs to operate above atmospheric pressure, up to ~40 atm, although the energy losses due to radiation increase dramatically at elevated pressure. Although the coils of most torches are helical in shape, spiral-shaped coils are not uncommon.

The most common uses of ICPs are in spectrochemical analysis. In such a torch, an aerosol (which contains the material to be analysed) is injected into the plasma through the central tube. The particles in the aerosol are subsequently broken up by the

heat of the plasma, and the atoms or molecular fragments can subsequently be analysed using mass spectroscopy or atomic emission spectroscopy. Spectrochemical ICPs are often used for sample analysis in ecological and biological sciences [**31**].

A typical spectrochemical ICP torch is depicted in figure 2.8. The outer flow, F1, is usually the largest, typically between 10 and 20 slm[4]. The outer flow is usually introduced in a swirl motion to help cool the outer tube and facilitate the creation of a closed conducting loop. The intermediate flow, F2, is usually called the plasma gas flow and is usually around 1 slm. The central flow, F3, or carrier gas flow, contains the analyte and is usually ≤1 slm. The central flow must be large enough to fully penetrate the plasma but not so large that the particles pass through too quickly and do not have time to become fully broken up. The three tubes are usually made of quartz, although sometimes the intermediate tube is made of aluminium. The intermediate tube is often widened at its base to help the outer gas flow cool the outer tube. The outer and intermediate flows almost invariably consist of pure argon.

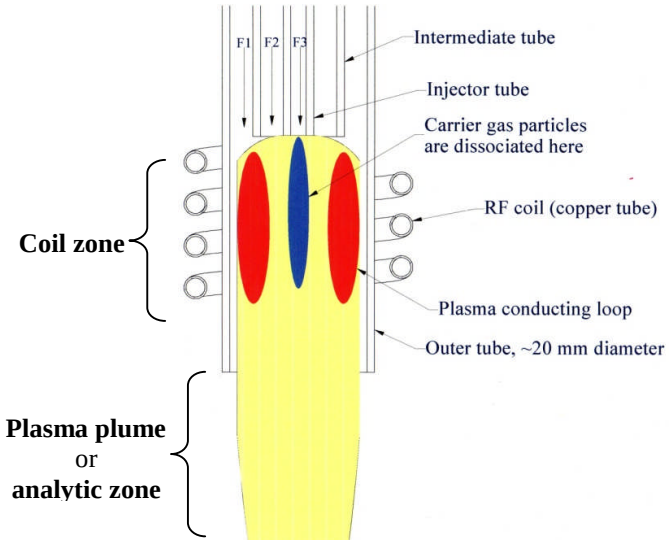

Figure 2.8 **A spectrochemical ICP torch usually has three concentric tubes. The three flows are F1: cooling gas (10-20 slm), F2 plasma gas (1-2 slm), F3 carrier gas ≤1 slm.**

In any ICP torch, a plasma region within the coil is known as the coil zone. The plume, the luminous region below the confinement tube, is often known as the analytic zone in a spectrochemical ICP.

ICPs are also used in the production of optical fibres [**32**], in the spray coating of metals and ceramics [**33**] and in the nucleation and growth of sub-micron powders [**34**, **35**].

Argon is not always the chosen gas; air, nitrogen, oxygen, hydrogen, helium, neon, krypton and xenon have all been used in atmospheric ICPs [**36-39**]. The minimum sustaining power when using argon is much less than when using molecular gases. Argon is more abundant, and hence cheaper, than the other inert gases, making it usually the most attractive option. Sometimes a second gas is used in combination with argon.

[4] 1 slm = 1 Standard litre per minute. A volumetric flow rate stated in standard litres per minute is not the actual volumetric flow rate but is the equivalent flow rate in terms of particles if it were an ideal gas at 0°C and at 1 atmosphere pressure.

The first attempts at modelling an ICP were conducted by Freeman and Chase in the 1960s [**40**]. In their model, the channel model, the plasma was considered to be a cylinder of uniform conductivity of radius (r_n) subject to a spatially uniform magnetic field, whose magnitude varies sinusoidally with time (see figure 2.9). The confinement tube is assumed to be kept at room temperature and a thin layer exists between it and the plasma. They applied the simplified Elenbass-Heller equation and Maxwell's equations. The model assumes that the energy dissipation in the core was balanced by radial heat conduction to the wall of the plasma confinement tube. Although the model is simplistic, it has been used to show that eddy currents are induced in the plasma. The magnitude of the current is greatest at larger radii (within the skin depth).

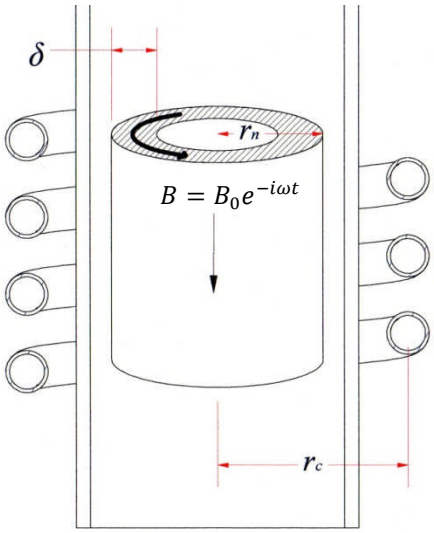

Figure 2.9 **In the earliest and simplest models on atmospheric ICP, the plasma was represented as a cylinder of uniform conductivity of radius r_n (a few millimetres smaller than the inner radius of the confinement tube). The rapidly changing magnetic field leads to eddy currents within the outer portion of the plasma (within the skin depth, δ). The effect is analogous to the induction heating of metals.**

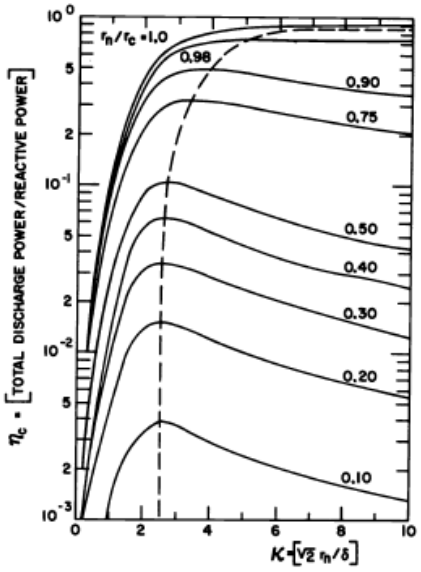

Figure 2.10 **The coupling efficiency plotted against coupling parameter for various values of r_n/r_c (plasma diameter to coil diameter ratio) [41].**

Figure 2.10 is based on calculations performed by Mensing and Bödeker [**41**], based on the channel model. It shows how the coupling efficiency (the fraction of the RF power absorbed by the plasma) varies with the "coupling parameter" (= $\sqrt{2}r_n/\delta$) and with the plasma to coil radius, r_n/r_c.

It is best to have a plasma diameter as close to the coil diameter as is possible to achieve maximum efficiency. Therefore the torch's outer tube should be as close to the inner diameter of the coil as is reasonably possible. The plasma to coil radius ratio can be improved by scaling things up but that results in an increase in the minimum power needed to sustain the plasma. An ICP is usually designed so that a plasma radius divided by the skin depth, r_n/δ, is between 1.5 and 4 to achieve optimum coupling. As the skin depth is dependent on the operating frequency, it is important that the driving frequency is set to an appropriate value to satisfy that condition. The driving frequencies typically used range from 0.2 MHz for larger outer tubes (~20 cm in diameter) up to 50 MHz for smaller tubes (~1 cm in diameter) [**11**,**12**].

RF generated plasmas usually come equipped with a matching load network, which can automatically adjust the impedance of the coil to help achieve optimum coupling. Such a network includes two tuneable capacitors, one in series with the coil one in parallel, as shown in the circuit diagram in figure 2.11.

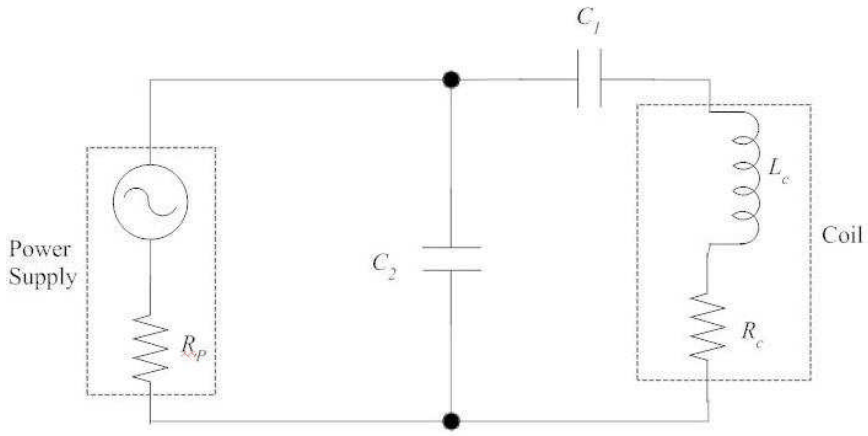

Figure 2.11 Matching load network

If the coil has a resistance, R_C, and an inductance L_C, its overall complex impedance is $R_C + j\omega L_C$, where $j = \sqrt{-1}$. If the complex impedance of the capacitor is $-j/(\omega C)$, the overall impedance of the coil and matching load network is equal to [**14**]

$$\left(j\omega C_2 + \frac{1}{R_C + j\left(\omega L - 1/\omega C_1\right)} \right)^{-1} \qquad (2.7)$$

Maximum coupling is achieved when the real part of this is equal to the internal resistance of the power supply, i.e.

$$R_C + \frac{1}{R_C}\left(\omega L_C - 1/\omega C_1\right)^2 = R_P . \qquad (2.8)$$

C_2 is adjusted so as to cancel out the imaginary part, thus

$$\omega C_2 = \frac{{R_C}^2}{\left(\omega L_C - 1/\omega C_1\right)} + \left(\omega L_C - 1/\omega C_1\right) \quad (2.9)$$

In modern systems the capacitors are usually tuned automatically, which is very advantageous as the coil's inductance increases on ignition.

2.1.4 ICP diagnostics

Because of the enclosed nature of the ICP torch, doing intrusive measurements can be difficult. For that reason, the most commonly used technique used for measuring temperature in an ICP is atomic emission spectroscopy. Some of the techniques for doing this are discussed in section 2.2.

Most early spectroscopic measurements on ICP torches involved taking measurements in the coil region. Temperatures deduced from spectroscopic measurements performed by Reed are discussed in his groundbreaking paper [**29**], although the values he reported, between 14,000 and 19,000°C, were subsequently found to be erroneously high. Initially, all temperature calculations assume the existence of local thermal equilibrium. However, in the early 1970s it became clear that this is not always a valid assumption. Dale Henderson [**42**] deduced the gas temperatures by firing nylon spheres through an ICP torch, one very similar to Reed's, at supersonic speeds. The stand-off distances of the bow shocks were measured using high-speed photographs. From this data he was able to calculate the frozen sound speed of the gas, and thus deduce its temperature. He compared his measurements with those produced by spectroscopy. He was able to show that the electron temperature exceeds the atomic temperature by about 900°C within the skin depth region (~6 mm deep) and approaches equilibrium towards the centre. Stanley Leonard [**43**] investigated the extent of local thermal equilibrium in an ICP that was 14cm in diameter. By comparing temperatures measured using relative line intensities and using absolute line and continuum intensities he found, to his surprise, that local thermal equilibrium did not exist anywhere inside the coil zone. The electron temperatures were generally ~2000°C higher than the atomic temperatures.

In larger ICPs, measurements have been made using magnetic or electro-static probes. For this type of measurement the probe diameter must be much smaller than a plasma diameter to retain good resolution, hence the task is rather more difficult in narrower plasmas. Hans Eckert performed many magnetic field measurements in an atmospheric ICP, in [**44**] for example, using a water-cooled probe. His measurements showed that the magnetic field strength is depleted close to the plasma axis. Eckert has shown that it is possible to deduce temperatures in an ICP from the magnetic field measurements provided that radiation losses can be neglected. Figure 2.12 compares temperature calculated by Eckert from his magnetic field measurements to temperatures determined by spectroscopy, by Leonard [**43**] in a very similar plasma torch.

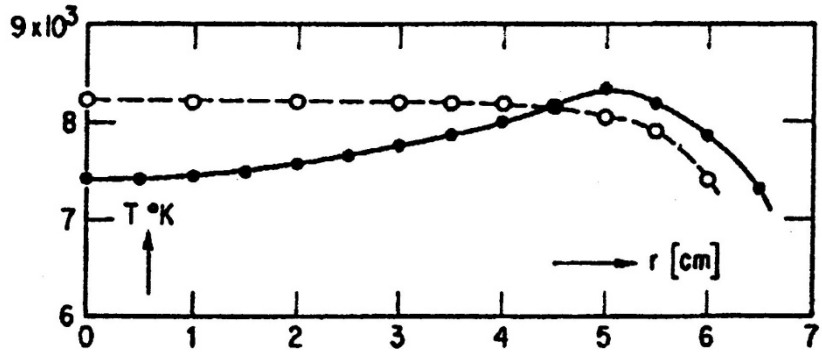

Figure 2.12 **Temperature measurements in the core of an ICP (filled circles) compared to temperatures determined from magnetic field measurements (open circles). This graph was taken from [11].**

Some authors have performed diagnostic measurements using Langmuir probes, usually a double Langmuir probe, which uses two electrodes which are usually made of tungsten wire [**45**-**47**]. By inserting these into the plasma and applying a potential, a current can be measured and electron temperature and density can be deduced from the current to voltage (I-V) relationship, the current being approximately $\propto \exp(-eV/kT)$. Measurements in an ICP plume have been carried out by Lu *et al.* [**45**]. Considerable measures were required to overcome the noise. Noise was too big a problem when a gas flow through the central tube was used so they only took measurements without any central flow. The accuracy of the measurements is also somewhat sensitive to the level of precision of the I-V relationship used.

Another important set of parameters is the gas particle densities. Atomic densities can be calculated by means of Rayleigh scattering. Farmer *et al.* [**48**] calculated neutral argon particle densities by measuring the angle of deflection of plane polarised light of an argon-ion laser. This technique generally gives good results at temperatures below 10,000K. At higher temperatures the Rayleigh scattered signals become overwhelmed by free electron emission.

Measuring the free electron density can be very useful as it helps determine whether local thermal equilibrium exists within a plasma at a given position. This can be calculated from the Stark broadening profile of atomic emission lines (this effect is described in section 2.2.4.6). An alternative method is to use Thompson scattering. Provided that the electrons in the plasma are moving at non-relativistic speeds, they can be made to oscillate using electromagnetic radiation, and then emit dipole radiation at the same frequency but in a different direction. Thus the radiation is scattered. Huang *et al.* [**49**] were able to determine electron densities, electron temperatures and gas temperatures with one set of measurements in an argon ICP. A Nd:YAG laser was used to induce both Rayleigh scattering by the neutral particles and Thompson scattering by the electrons. Considerable complexity is added to the experimental setup to carry out these measurements. However, the resulting accuracy can be rather better than what can be deduced from Stark broadening measurements, particularly in the plasma central region.

Measuring flow patterns and velocities within an ICP can be challenging, particularly within the coil zone. One of the first to report such investigations was Chase, who measured flow patterns using tracer techniques and high-speed photography [**50**]. He showed that recirculatory vortices exist in the coil zone due to electromagnetic

pumping. An illustration of such vortices is shown in figure 2.13. Others have come to similar conclusions using water-cooled pitot tubes [**51**]. More recently, velocity measurements have been performed using laser Doppler anenometry (LDA). In LDA, micron-sized particles are added to the fluid in question. Two beams of laser light, usually split beams from the same laser to ensure coherence, are combined to make a pattern of interference fringes at a point on the fluid. Some of the light is scattered off the particles and measured with a photodetector. The fringe pattern measured oscillates at a frequency related to the speed of the particles perpendicularly to the laser beams and the viewing line of the detector, thus the speed can be determined.

Lesinski *et al.* measured velocities inside the coil zone of a 50 mm diameter torch using LDA [**52**]. Their results are summarised in figure 2.14. Measurements of the plasma gas velocities were made by seeding the gas with a fine carbon powder. Measurements of the central velocities were made using silicon particles, 33 μm in size. Three sets of tests were made using different central flows and different powers. Just upstream of the coil, velocity distributions were roughly parabolic in shape; on the downstream side they were much flatter. The distributions were rather more sensitive to flow rate than to torch power. In figure 2.14b, measurements of the plasma gas and central particle flow velocities along the central axis of the torch are shown, along with that of cold gas measurements (that of the gas before ignition). The RF coil clearly has a big influence on the gas velocity.

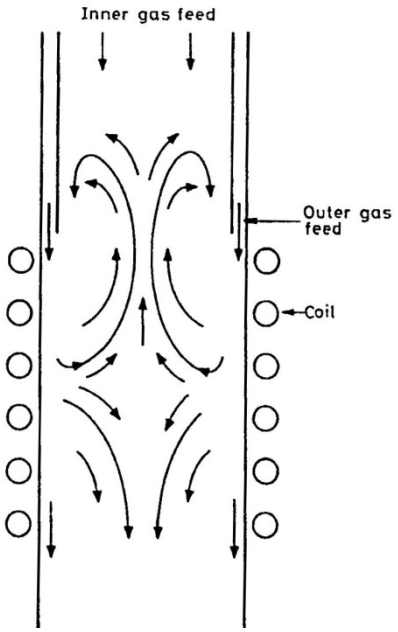

Figure 2.13 **An illustration of the recirculatory vortices that might be observed in an ICP due to electromagnetic pumping in the absence of a central feed.**

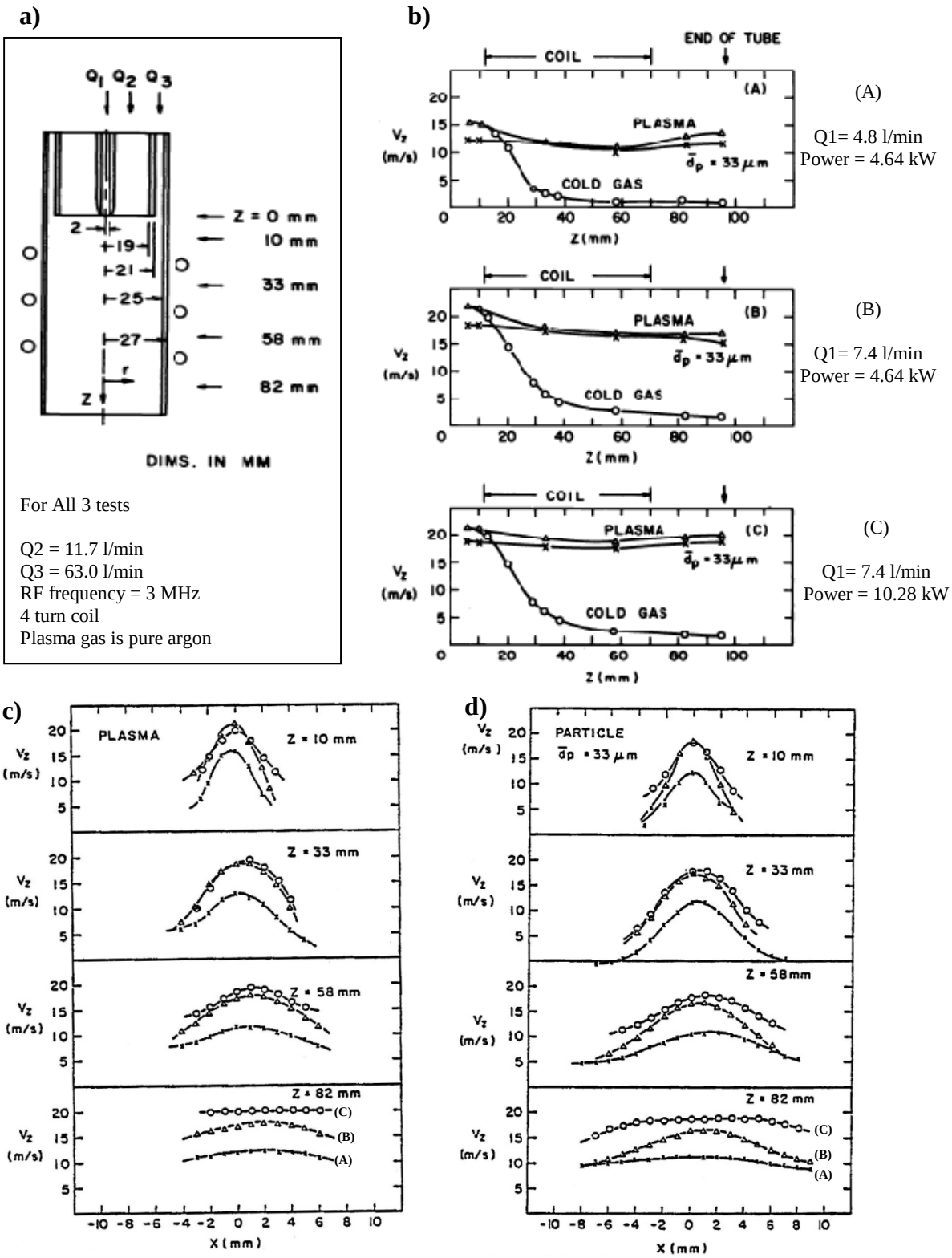

Figure 2.14 **Velocity measurements taken by Lesinski *et al.* using laser Doppler anenometry. a) dimensions of plasma torch and parameters common to all tests. b) Velocity measurements along torch centre line; the central flow and torch powers used in the three separate experiments are given. c) Plasma gas velocity profiles over the central region of the torch at various heights. d) Central gas particle velocity profiles over the central region of the torch at various heights [52].**

2.1.5 ICP modelling techniques

Much has been learned about ICPs from diagnostic measurements. However, carrying out these measurements is not always straightforward, particularly when taking intrusive measurements in narrower ICPs, and are often time-consuming and expensive. In some instances, one might be concerned that the taking of these measurements alters the nature of the plasma. For these reasons, numerical modelling techniques have been extensively used to characterise ICPs.

As was mentioned in 2.1.3, the first model of an atmospheric ICP was the channel model devised by Freeman and Chase. This model, and its immediate successors, were one-dimensional models used for calculating radially symmetric profiles of the plasma properties at the centre of the coil zone. Some initial refinements to the channel model were made by Eckert. In [**53**] he allowed for spatial variations in the electrical and thermal conductivities of the plasma and was able to calculate a radial temperature profile. In [**54**], Eckert took things further by allowing for power losses by radiation. The latter model predicted that there should be an off-axis maximum in the temperature, whereas the radiationless case predicts a maximum along the axis. It was also found that as much as 50% of input power can be converted into radiation as long as the plasma ring remains attached to the confinement tube wall.

Miller and Ayen were the first to propose a two-dimensional model and so could calculate radial and axial temperature distributions [**55**]. Ramon Barnes and his associates [**56**-**58**] extended this model, so as to calculate temperature, velocity and energy-balance distributions in spectrochemical argon and nitrogen ICPs. Javad Mostaghimi *et al.* used a computer model to calculate two-dimensional emission patterns on a spectrochemical ICP [**59**]. For a number of elemental analyte candidates, regional variations in the atomic emission intensity were calculated in an 18 mm diameter plasma. Maher Boulos was able to explain the formation of recirculatory vortices under particular operating conditions. The result was based on the solution of the corresponding momentum, continuity and energy equation simultaneously with the one-dimensional electromagnetic field equations [**60**]. Up until the late 1980s only the axial component of the magnetic field was considered in models. It was found that for small ICPs with operating frequencies above 40 MHz, the radial field components could not be neglected and it was also not possible to calculate temperature fields in spectrochemical ICP that include internal tubing. For these reasons, vector potential models were developed for calculating the two-dimensional field effects [**61**]. Radiative losses were treated rigorously in models produced by Proulx *et al.* [**62**], for example. They showed that radiative losses can increase significantly if the plasma becomes contaminated by metallic vapours.

Most models to date have assumed local thermal equilibrium. Some models have allowed for deviations in local thermal equilibrium, known as “two temperature models.” The first to propose such a model were Mostaghimi *et al.* [**63**]. For an ICP 2 cm in diameter, the model yielded significant deviations from LTE throughout the coil zone when operated with argon at 0.3 atm. At 1 atm, most of the modelled plasma was in LTE except close to the confinement tube. The two temperature model predicts that the electron temperature close to the confinement tube is ~1000 K greater than that predicted by the LTE models. It has been shown that deviations from thermal equilibrium increase with increasing drive frequency [**64**].

In the 21st century, three-dimensional models of ICPs have been devised. In these models the helical shape of the coil is taken into account; previously the coil had always been approximated to a series of flat rings. A mathematical model has been described in some detail by Xue *et al.* [**65**]. In their model, Lorentz forces due to the coil were taken into account. The model was implemented using FLUENT, a commercial finite volume analysis software package, a powerful tool for solving problems involving fluid dynamics.

In 2005, Bernardi *et al.* [**66**] discussed results from a very similar model, again using FLUENT. The paper mostly focuses upon temperature, power dissipation, and axial velocity fields. Maps displaying these quantities have been shown for a variety of torch configurations, some of which involve spiral coils or elliptical tubes. However, no allowance for deviations in local thermal equilibrium has been accounted for in these models.

Colombo *et al.* [**67**] briefly describe a model produced using FLUENT of an 18 mm diameter ICP. Figure 2.15a shows a temperature map; temperatures have been calculated in regions of the plume where it would be too cold to measure the temperature by spectroscopy. Figure 2.15b displays gas flow patterns; flows through each tube are colour-coded. The cooling gas in the outer tube moves in the swirl motion upstream of the discharge but then the axial component dominates as it approaches the plasma. The plasma gas flow through the middle tube is not sufficient to create a swirl motion at any point. The central flow creates a recirculation vortex as the gas exits the injector tube; the central flow has to be strong enough to oppose the backward motion of the vortex. The vortex pattern increases the mixing of the plasma and injected gases, making a more homogenous mixture.

Much of this had been described using the earlier models. However, the value of being able to produce three-dimensional models that are flexible and to easily produce aesthetically appealing diagrams should not be underestimated.

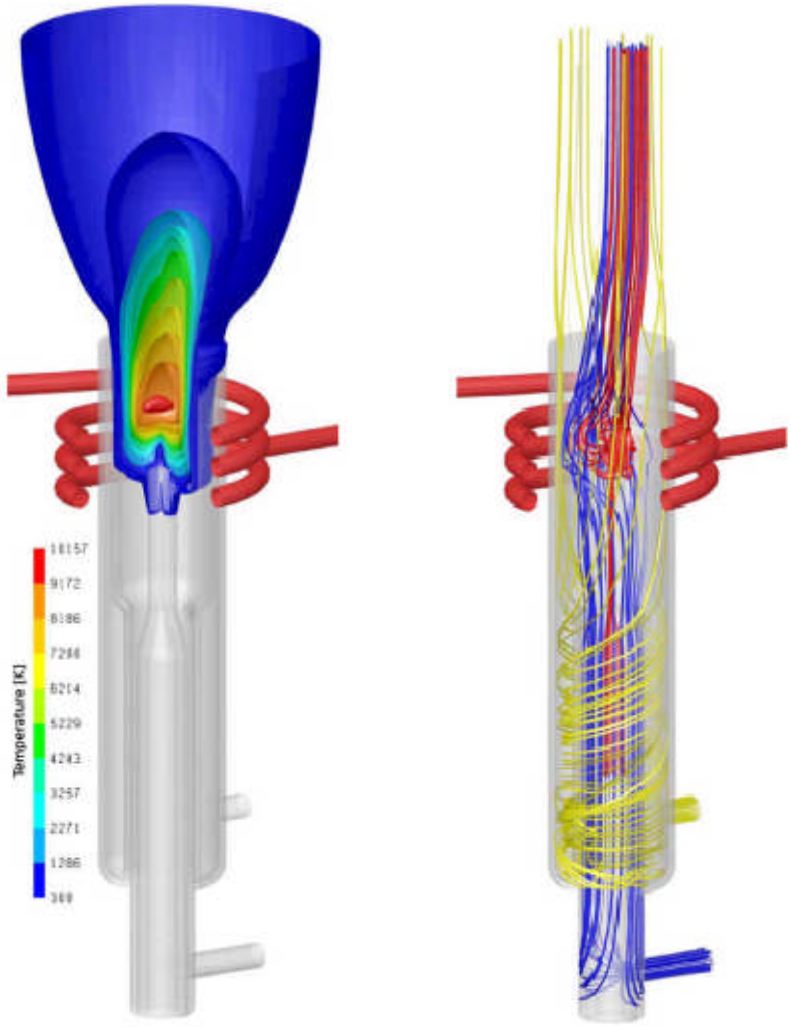

Figure 2.15 **a) Temperature map of an 18 mm diameter argon ICP, created by Colombo *et al.* [67], using FLUENT. b) Gas flow patterns of the same plasma. The flows used were cooling gas (yellow) 7.6 slm, plasma gas (blue) 1 slm and central gas (red) 1 slm.**

2.2 Plasma Spectroscopy

A plasma's emission spectrum can cover a very wide range of wavelengths. In plasmas below 10^6K, the continuum emission is emitted most intensely between the ultra-violet and far infra-red. Cyclotron and synchrotron sources, where electrons are accelerated by strong magnetic fields, are usually very strong emitters of radio waves. X-ray and gamma rays are emitted only by the hottest plasmas. The gamma rays produced by fusion reactors are a significant health and safety hazard, and have to be contained using thick lead shielding. In molecular plasmas emission lines due to changes in their vibrational or rotational energies states[5] are generally found in the microwave and infrared regions of the spectrum. Atomic emission lines exist over a wide portion of the spectrum, but are usually studied between roughly 200 nm and 1000 nm, which includes the visible region of the spectrum.

[5] All molecules have modes of vibration and rotation. Each mode can occupy only discrete (quantised) energy levels.

2.2.1 Stimulated emission

Atomic line emission is the result of changes in the electron configuration within atoms. At absolute zero, all the electrons within an atom spend all their time occupying the lowest energy states that they can possibly occupy (i.e. they are degenerate). If the atom is heated, or excited by other means, there is a chance that an electron might be elevated into a higher energy state. That electron will probably spend a very short period of time before dropping back to a lower state, emitting a single photon of light in the process. This process is known as spontaneous emission. The frequency of the emission, f, is related to the energy change, ΔE, by the simple formula

$$\Delta E = hf. \qquad (2.10)$$

The duration that it is likely to spend in higher energy state is $\sim \Delta E/h$, a result of Heisenberg's uncertainty principle. Its value usually turns out to be $\sim 10^{-8}$ s, but can be significantly longer for the so-called forbidden transitions.

Every element has a unique set of emission lines that correspond to all of the permitted energy changes that can occur. Hydrogen's spectrum is as the simplest and the frequencies can all be calculated exactly. It is rather more difficult for other elements as each electron's energy state is perturbed by the influence of the other electrons. However, so much experimental and theoretical work has been done that one can easily determine what element exists in a sample by matching the central wavelengths of emission lines with values that have already been tabulated. The element helium was actually discovered spectroscopically in 1868 by astronomer Norman Lockyer while studying the Sun's corona during a total eclipse.

Before taking spectroscopy measurements, one must first construct a suitable measurement system. If the task is to produce temperature or particle density maps of the plasma, one must take a series of measurements, looking along different lines of sight, and perhaps looking at a series of wavelength bands. A means of source reconstruction must then be used to convert the line of sight intensity values into local emission coefficient (or emissivity) values (light energy emitted per unit volume per unit wavelength per unit solid angle). The final step is to determine temperature from the local emissivity values. Each of these tasks is discussed in the subsequent sections.

2.2.2 Spectroscopic equipment

A device which separates broadband light into separate frequency bands for spectroscopic measurements is called a monochromator. The first monochromators used were triangular glass prisms. The refractive index of glass varies with the wavelength of the light passing through it such that light of shorter wavelength is refracted through a greater angle. Most of today's monochromators use blazed reflective diffraction gratings. The simplest kind of monochromator is shown schematically in figure 2.17a. The grating has a surface with a series of identical grooves (reflective 'zig-zags'). The angle at which a ray of light is reflected off the grating, β, depends on the incident angle α, the groove separation d, and its wavelength λ, by the grating equation [**68**],

$$n\lambda = d(\sin\alpha \pm \sin\beta) \qquad (2.11)$$

where n is an integer (the order). The light of a given wavelength is reflected through many different angles (corresponding to different values of n) but predominantly

through the angle corresponding to $n = 1$. Figure 2.16 illustrates how light of different wavelength is reflected through different angles.

The grating in a monochromator is rotatable so that only a narrow frequency band reaches the detector. The groove spacing, *d*, is crucial in determining the monochromator's resolution. Reducing the groove spacing results in an increase in the difference between the angles of reflectance of light of different wavelengths. It also makes the intensity peaks for each order finer. The groove densities vary between ~50 per mm to 3000 per mm. The resolution can be improved by increasing the path length. It can be increased further by using two gratings, hence the double monochromator shown in figure 2.17b [**68**].

Intensities of the light of different wavelengths are then detected usually using either a charge-coupled device (CCD) or a photomultiplier tube (or PMT). CCDs are usually cooled to reduce the noise level. In less expensive units, this is done using fans and heatsinks. This can be done much more effectively by cooling them cryogenically using liquid nitrogen or even liquid helium. PMTs are extremely sensitive and some are able to detect individual photons. However, PMTs are rather bulkier than CCDs and only one frequency band can be examined at a time. In recent decades it has become possible to purchase small spectrometers which include a monochromator and CCD in a single compact unit. These cannot compete with the larger monochromators in terms of resolution but are very much less expensive and more convenient. The angle of the grating in such a unit is normally fixed when assembled and the CCD can measure intensities over a large frequency range at once.

A diagram of a typical spectroscopic acquisition set-up is shown in figure 2.18. Photographs of a 1 m-long SPEX® monochromator with CCD acquisition equipment and a small Ocean Optics compact spectrometer are shown in figure 2.19.

In many spectroscopic measuring systems, an image of the source is projected onto the entrance slit of a monochromator. Alternatively, light can be collected and delivered to the monochromator using optical fibres. A computer-controlled scanner would normally be used to move the image with respect to the collecting optics in order to examine different regions of the plasma. A Fabry–Pérot interferometer is often used to help filter out unwanted light.

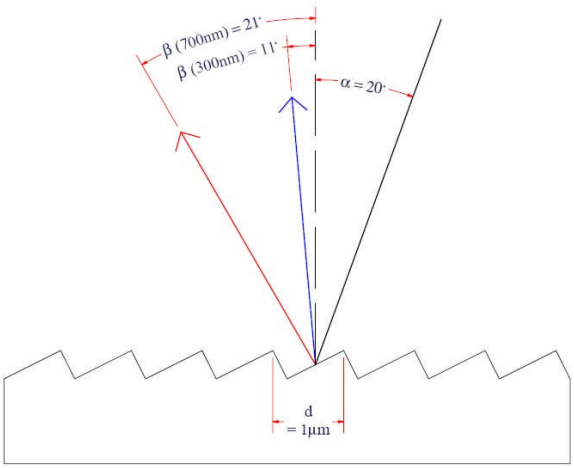

Figure 2.16 **Incident light is reflected off a blazed grating at an angle dependent on its wavelength.**

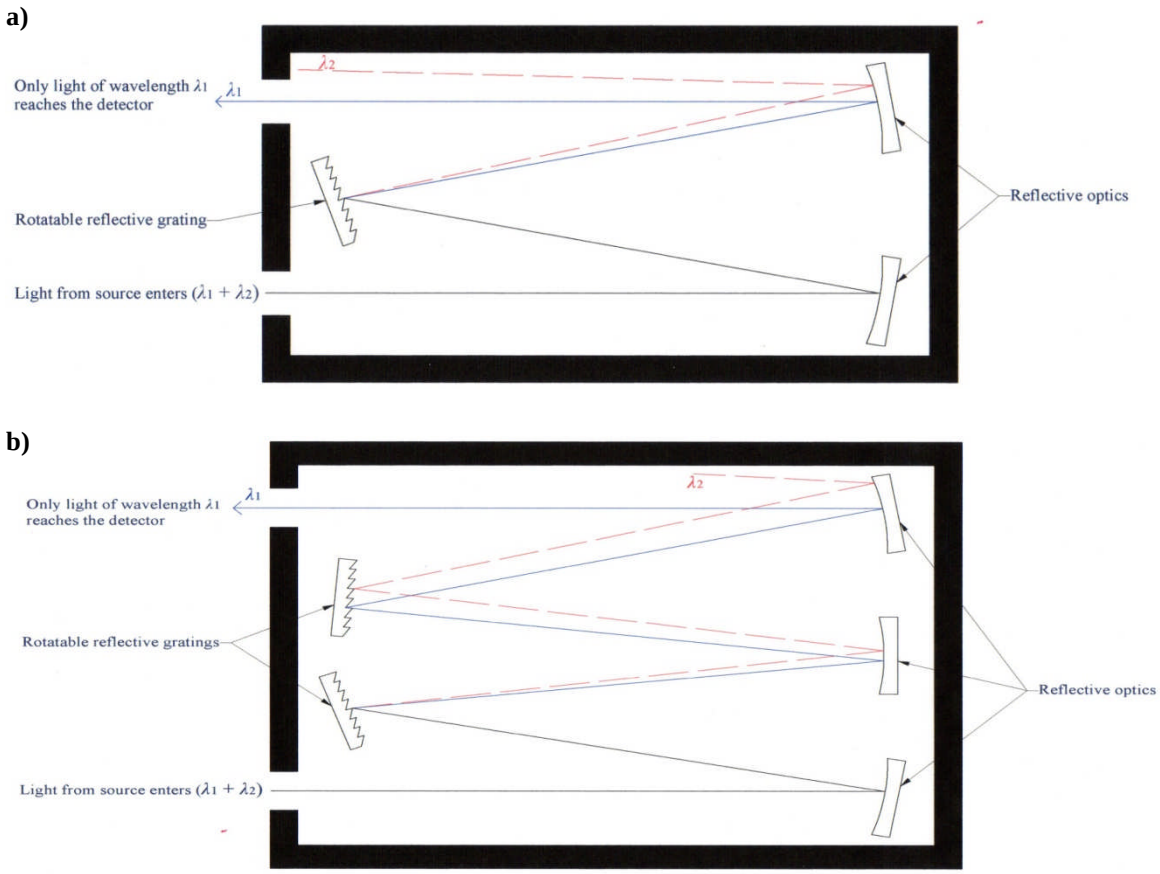

Figure 2.17 **Schematic diagrams of a) A single monochromator and b) A double monochromator. The gratings can be rotated so that only light in this discrete wavelength band passes through the exit slit. In the diagrams, light of wavelength λ_1 passes through but light of wavelength λ_2 does not.**

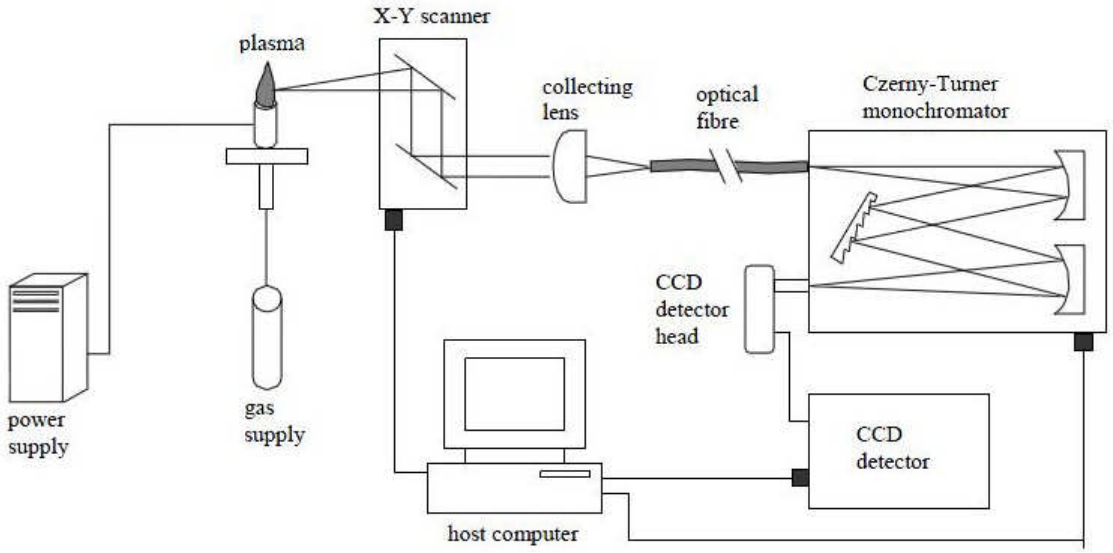

Figure 2.18 **A diagram of a typical set-up used for a plasma diagnostic measurements. The X-Y scanner is used to collect light from different regions of the source. Light from an ICP is focused into the core of on optical fibre using the collecting lens. Light is transported via the optical fibre to the monochromator. With the help of a blazed reflective grating, only light within a very small bandwidth is directed to the CCD detector head [69].**

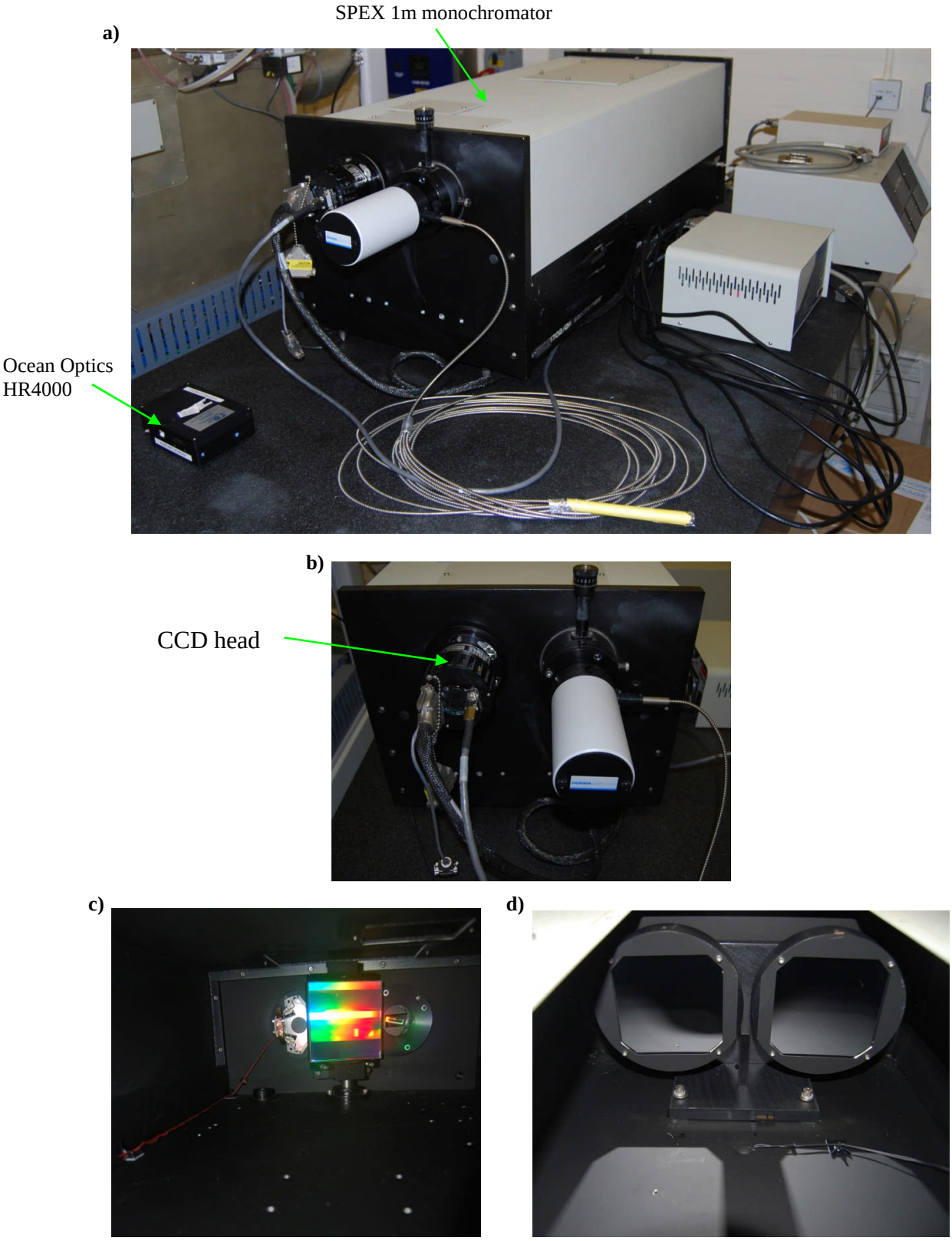

Figure 2.19 **a) 1 m-long SPEX monochromator with a Jobin Yvon CCD measuring kit, plus an Ocean Optics HR4000, a compact spectrometer which contains a linear CCD detector.**
b) CCD head entrance slit.
c) Blazed reflective grating inside the1m SPEX monochromator.
d) mirrors at the opposite end.

2.2.3 Source reconstruction

2.2.3.1 Radon inversion

Figure 2.20 shows a section through an optically thin emissive medium of arbitrary shape. Let us suppose that the emission coefficient (light emitted per unit volume per unit solid angle) along this plane has the two dimensional distribution $\varepsilon(x,y)$. Our endeavour is to determine the form of this distribution. One might start by taking spectroscopic measurements. The difficulty is that it is only possible take measurements along a given line of sight; that line of sight passes through regions of varying emission coefficient.

If the intensity were measured along the line of sight, L, which is inclined at an angle θ and an offset, b, relative to the origin (see figure 2.15), the total emission, I, integrated at all points along the, can be expressed

$$I(b,\theta) = \int_L \varepsilon(x,y)\mathrm{d}l \qquad (2.12)$$

where dl represents an incremental distance along line L. This quantity can be referred to as the Radon transform of the emission coefficient distribution at coordinates d and θ (Radon transform coordinates). A Radon transform is commonly denoted by $R[\ ]$. This can be rewritten in vector coordinate form whereby the emission coefficient is denoted by $\varepsilon(\boldsymbol{r})$, where $\boldsymbol{r}$ is the position vector relative to the origin of a point on the line L (see figure 2.21). Alternatively, $I(b,\theta)$ can be expressed

$$I(b,\theta) = R[\varepsilon(\boldsymbol{r})](b,\theta) = \int_{\mathrm{R}^2} \varepsilon(\boldsymbol{r})\,\delta(b-\boldsymbol{r}.\boldsymbol{i})\mathrm{d}\boldsymbol{r} \quad (2.13) \quad [\mathbf{70}]$$

where δ represents the Dirac delta function[6]. The vector $\boldsymbol{i}$ represents the unit vector parallel the line L; it has the Cartesian coordinates ($\cos\theta$, $\sin\theta$) and the polar coordinates (1, θ). The R^2 symbol next to the integrand represents all points on a two-dimensional Euclidean plane. The Dirac delta function ensures that only position vectors corresponding to points on the line L contribute to the integral.

$\varepsilon(\boldsymbol{r})$ can be recovered using the inverse Radon transform, or Radon inversion

$$\varepsilon(\boldsymbol{r}) = R^{-1}[I(b,\theta)](\boldsymbol{r}) = \int_{-\infty}^{\infty} \varepsilon(\boldsymbol{w})e^{2\pi\mathrm{j}k\boldsymbol{r}.\boldsymbol{i}}\,\mathrm{d}\boldsymbol{w} \quad (2.14).$$

where $\varepsilon(\boldsymbol{w})$ is the Fourier transform of $\varepsilon(\boldsymbol{r})$ and $\mathrm{j} = \sqrt{-1}$. $\boldsymbol{w}$ is the wave vector, which has the polar coordinates (w, θ). Equation 2.14 can be rewritten

$$\varepsilon(r,\phi) = \int_0^{\pi}\int_{-\infty}^{\infty} w\,\varepsilon(w,\theta)e^{2\pi\mathrm{j}kr\cos(\theta-\phi)}\,\mathrm{d}w\,\mathrm{d}\theta \qquad (2.15).$$

Using the Fourier slice theorem, which states that the one-dimensional Fourier transform of the Radon transform at an angle θ is a slice of the two-dimensional Fourier transform of the inverted Radon transform of the same angle, it can be shown that

$$\varepsilon(r,\phi) = R^{-1}[I(b,\theta)] = \frac{1}{4\pi^2}\int_0^{\pi} PV\int_{-\infty}^{\infty}\frac{\partial I(b,\theta)}{\partial b}\frac{1}{r\cos(\theta-\phi)-l}\,\mathrm{d}b\,\mathrm{d}\theta \quad (2.16)$$

The 'PV' before the integrand denotes the Cauchy principal value, and is the integral is the Hilbert transform of $\frac{\partial}{\partial b}I(b,\theta)$ [**71**].

[6] The Dirac delta function, $\delta(x) = 1$ if $x = 0$ or $\delta(x) = 1$ if $x \neq 0$.

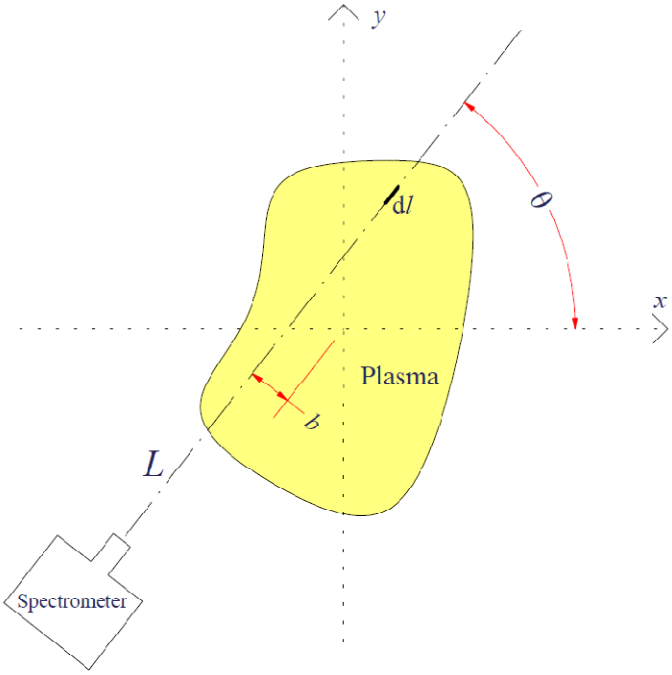

Figure 2.20 **An intensity measurement is taken of plasma, whose emission coefficient distribution is unknown, along a line of sight *L*, which lies on the *x*-*y* plane. *L* has the coordinates *b* (closest distance to the origin) and *θ* (azimuthal angle counter-clockwise relative to *x*-axis) which are known as Radon transform coordinates.**

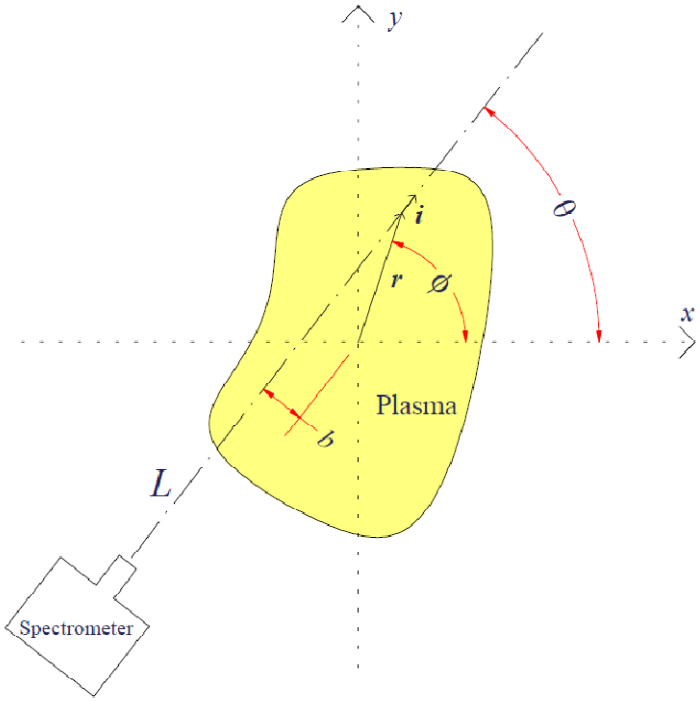

Figure 2.21 **A position along the line *L* can be defined using the vector *r* which has the polar coordinates (*r*,*ϕ*). The vector *i* represents the unit vector parallel the line *L*. For all *r* vectors that represent a point along the line *L*, the value of *r.i* (the inner product of the two vectors) is equal to *b*.**

Equation 2.16 represents a Radon inversion. If we were able to take line of sight intensity measurements of this hypothetical two-dimensional plasma from a sufficiently large number of angles between 0 and π radians and from a sufficiently large number of offset values (b) at each angle to make it possible to express $I(b, \theta)$ as an exact function, $\varepsilon(\underline{r})$ can be deduced. In practice, this is never completely possible and some approximations and assumptions have to be made to solve the inversion.

Although the emission coefficient distribution in a plasma is being discussed, the same logic can be applied to any two-dimensional scalar distribution that has to be determined from a series of straight line integrated measurements in any application. Radon inversions are used in a wide variety of image reconstruction applications, such as computer axial tomography and in the electron microscopy of macromolecular assemblies.

For this formulism to be exact, it is assumed that the measured quantity is integrated along a straight line that is infinitesimally thin. This can never be truly realised. When spectroscopic measurements are taken, the spatial resolution depends on the collecting optics used. If very precise measurements are expected, the measured intensity distribution should be separated from the aperture function (which would be a delta function for a wide rectangular slit[7], for example) by deconvolution.

2.2.3.2 Abel Inversion

The Abel inversion is a convenient method of calculating a two-dimensional emission coefficient distributions from line of sight intensity data in instances where the distribution is known to be axially symmetric along a particular plane. Figure 2.21 shows a section through an axially symmetric plasma of radius, R. As the radial emission coefficient distribution is independent of the azimuthal angle, it can be written as $\varepsilon(r)$. The Radon transform along line L is now only a function of b and is independent of the angle θ. For the simplicity we can set $\theta = 90°$ so that the line L is parallel to the y-axis (see figure 2.22). If $\varepsilon(r)$ is believed to be equal to zero outside of the radius R, $I(b)$ is the result of the integral

$$I(b) = \int_{-\sqrt{R^2-b^2}}^{\sqrt{R^2-b^2}} \varepsilon(r)\mathrm{d}y \qquad (2.17).$$

As $\varepsilon(r)$ is symmetric about the x-axis

$$I(b) = 2\int_{0}^{\sqrt{R^2-b^2}} \varepsilon(r)\mathrm{d}y \qquad (2.18)$$

This can be rewritten using polar coordinates

$$I(b) = 2\int_{b}^{R} \varepsilon(r)\frac{\mathrm{r}}{\sqrt{r^2-b^2}}\mathrm{d}r \qquad (2.19)$$

This special instance of the Radon transform is known as Abel transform. $\varepsilon(r)$ can be recovered using the Abel inversion

$$\varepsilon(r) = \frac{1}{\pi}\int_{r}^{R} \frac{1}{\sqrt{b^2-r^2}}\frac{\partial I(b)}{\partial b}\mathrm{d}b \qquad (2.20)$$

[7] A wide rectangular slit, in this context, means a slit that is sufficiently wide such that diffraction effects are not significant. At optical wavelengths, this is the case for apertures > 0.1mm.

If $I(b)$ is known for a sufficiently large number of values of b between 0 and R, $\varepsilon(r)$ can be recovered. Taking measurements from a greater number of b-values generally improves the accuracy of the reconstruction. Equation 2.20 can be rewritten

$$\varepsilon(v) = \frac{1}{\pi}\int_v^{R^2} \frac{1}{\sqrt{u-v}}\frac{\partial I(u)}{\partial u}\mathrm{d}u \quad \text{where } u = b^2 \text{ and } v = r^2. \qquad (2.21)$$

In a real situation it is likely that an experimentalist would intuitively choose to take measurements of $I(b)$ at equally spaced values of b. Nestor has devised a straightforward scheme for performing an Abel inversion when a set of parallel measurements has been taken equally spaced intervals across a plane, which is widely used [**72**]. Let us suppose that the source is divided into a set of concentric rings of thickness a (equal to the lateral separation of the measurements) along the lines shown in figure 2.23a. Let us now consider the specific measurement taken at the position shown in figure 2.23b. If $\varepsilon(u)$ is assumed to be a linear function of u within each zone,

$$\varepsilon(ak) = -\frac{1}{\pi}\sum_{n=k}^{N-1} \frac{I(u+(n+1)^2a^2) - I(u+n^2a^2)}{(n+1)^2a^2 - n^2a^2} \int_v^{R^2} \frac{1}{\sqrt{u-(ak)^2}}\mathrm{d}u \quad (2.22)$$

where $k = r/a + 0.5$ and $N = R/a + 0.5$.

It can be shown that

$$\varepsilon(ak) = -\frac{2}{\pi}\sum_{n=k}^{N-1}\left[\big(I(a(n+1)) - I(an)\big) \times \frac{\sqrt{(n+1)^2-k^2} - \sqrt{n^2-k^2}}{a(2n+1)}\right]. \quad (2.23)$$

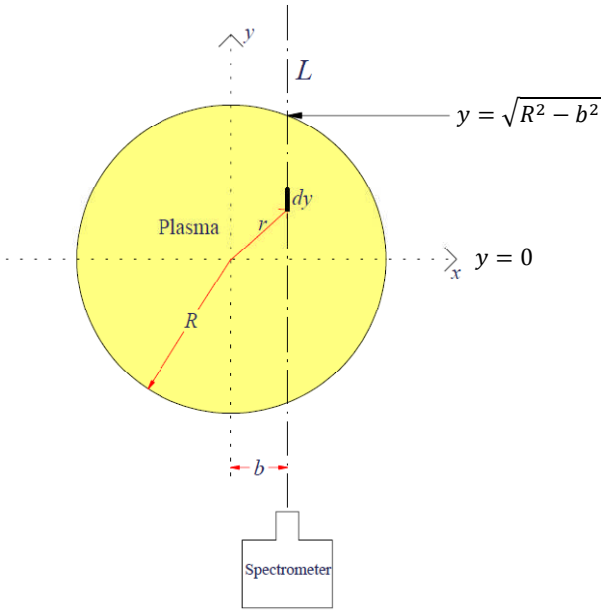

Figure 2.22 **If the emission coefficient distribution of a source is believed to be radially symmetric, it can be recovered by taking a set of measurements along the plane from just one angle and performing an Abel inversion. Because of the symmetry, it is only necessary to take measurements are positive offsets (*b*-values). However, experimentalists investigating a real plasma would normally take measurements at positive and negative offsets to assist in defining the central axis and verifying the symmetry.**

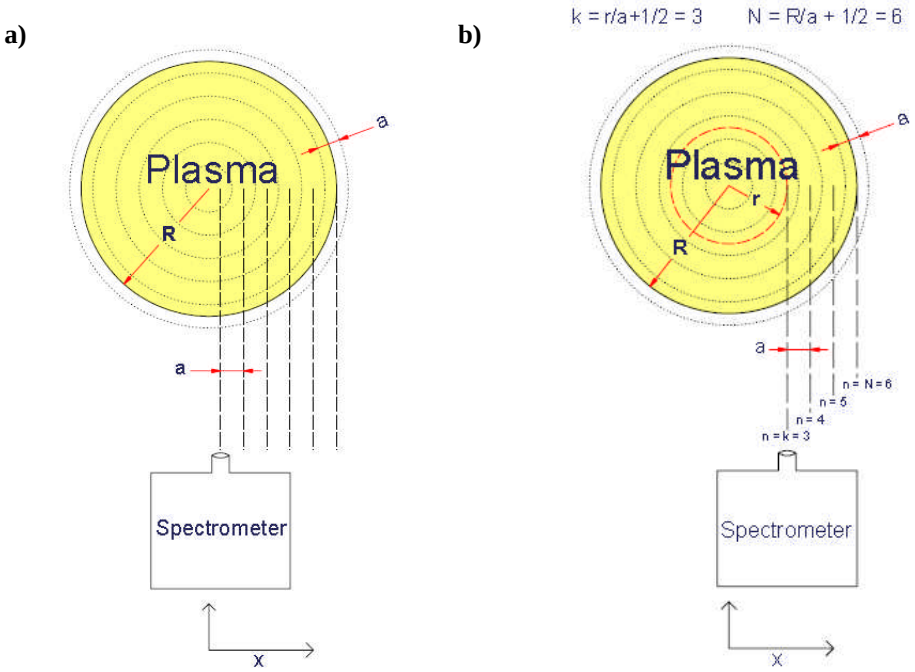

Figure 2.23 **To use Nestor's method for performing an Abel inversion, measurements have to be taken at equally spaced positions, as suggested in a). The values for *k* and *N* are given in b) for the determination of the $\varepsilon(r)$ for one particular measurement; the solution is dependent on all measurements taken at larger radii.**

Aguilera *et al*. have devised an intuitively straightforward method of solving the Abel inversion that can be used in situations where the lateral resolution of the measurement system is relatively large compared to the radius of the plasma, as is often the case when optical fibres are used for taking samples, for example [**73**]. In this method, the source is divided into shells of equal thickness. The thickness should be equal to the spatial resolution of the measurements and the emission coefficient is assumed to be equal at all points within a given shell. The emission coefficient within the *i*th shell out from the centre can be calculated using the formula

$$\varepsilon(k=i)=\frac{1}{V_{ii}}\left(I(i)-\sum_{k=i+1}^{N}[\varepsilon(k)V_{ik}]\right) \quad (2.24)^{8}$$

where V_{ik} represents the volume of material within the shell k that intersects the viewing line strip i (see figure 2.24). To perform this calculation, it is necessary to begin taking measurements at the edge (where $i = N$) and work inwards. V_{ik} can be calculated using the formula

$$V_{ik}=\Delta z\Delta y^2\left\{(i-1)\left(\sqrt{(k-i)(i+k-2)}-\sqrt{(k-i+1)(i+k-1)}\right)+i\left(\sqrt{(k-i)(i+k)}-\right.\right.$$

$$\left.-\sqrt{(k-i-1)(i+k-1)}\right)+(k-1)^2\left[\tan^{-1}\left(\frac{i-1}{\sqrt{(k-i)(i+k-2)}}\right)-\tan^{-1}\left(\frac{i}{\sqrt{(k-i-1)(i+k-1)}}\right)\right]+$$

$$\left.k^2\left[\tan^{-1}\left(\frac{i}{\sqrt{(k-i)(i+k)}}\right)-\tan^{-1}\left(\frac{i-1}{\sqrt{(k-i+1)(i+k-1)}}\right)\right]\right\} \quad (2.25).$$

The formula V_{ii} can created substituting k with i in equation 2.25 (omitting terms which involve taking the square root of a negative number)

$$V_{ii}=\Delta z\Delta y^2\left\{(i-1)(\sqrt{2i-1})+i^2\left[\pi/2-\tan^{-1}\left(\frac{i-1}{\sqrt{2i-1}}\right)\right]\right\} \quad (2.26).$$

[8] Slightly different notation is used in [**73**]. The author has adjusted the notation to make it easier to explain diagrammatically and so that the equations can be easily compared to the equations describing Nestor's solution to the Abel inversion.

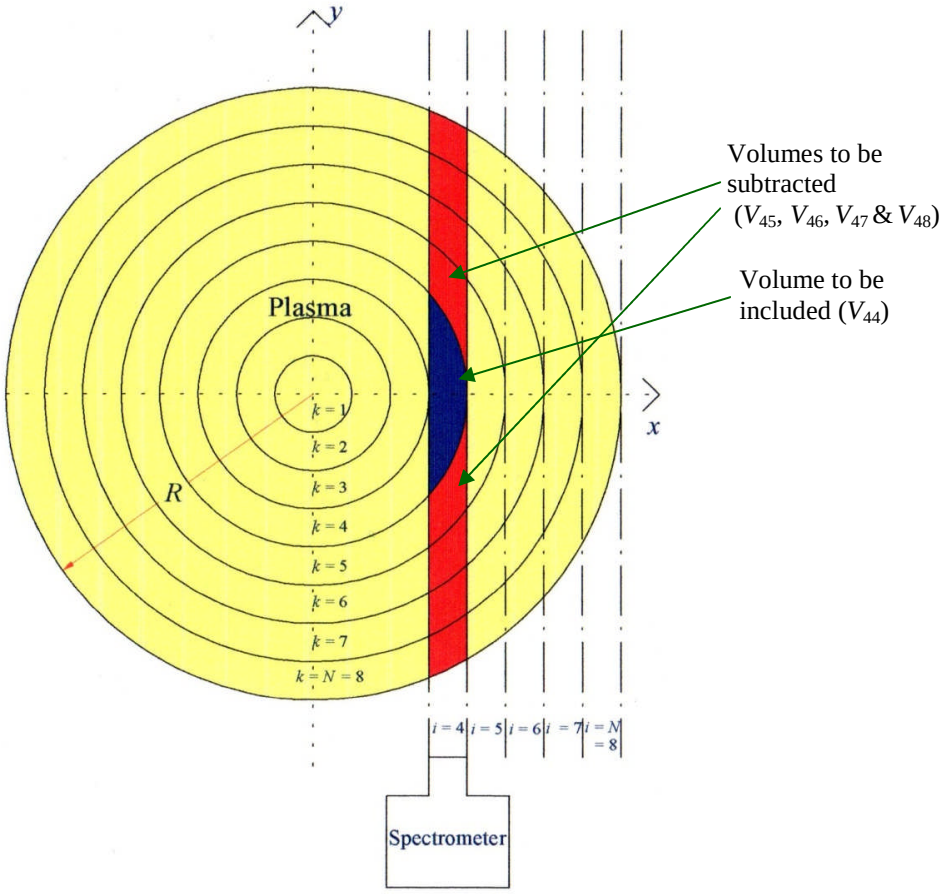

Figure 2.24 **Aguilera *et al.* have devised a simple method of solving an Abel inversion in situations where the spatial resolution is equal to the spacing of measurements. The plasma is divided into N cylindrical shells of equal thickness (equal to the measurement separation), and the emission coefficient is considered to be constant within a given shell. If we wish to the find the emission coefficient of the fourth shell out from the centre (k = 4), for example, one would take an integrated measurement along the strip marked i = 4 and then subtract the contributions from the outer shells (k = 5, 6, 7 & 8). In order to achieve that it is necessary to have taken measurements along the strips i = 5, 6, 7 & 8 to calculate the emission coefficient in the outer regions and then calculating volumes using equation 2.25.**

2.2.3.3 Source reconstruction in plasmas that are not axially symmetric

The Abel inversion is only an exact means of determining the emission coefficient distribution within a plasma (or other emissive media) if it is optically thin and axially symmetric. Maldonado and Olsen [**74**] have devised a source reconstruction scheme for plasmas in which deviations from axial symmetry exist. This has become known as Maldano-Olsen inversion. Its inversion formula is

$$\varepsilon(x,y) = \frac{\alpha}{\pi^3}\sum_{k=0}^{\infty}\sum_{m=0}^{\infty} g_m \frac{\sqrt{k!\,(m-k)!}}{(m+2k)!} \times Re\left\{\left(\int_{-\pi}^{\pi} e^{-im\phi}\,\mathrm{d}\phi \times \int_{-R/2}^{R/2} I(l,\phi)H_{m+2k}(\alpha l)\mathrm{d}l\right)\times (-1)^k \frac{\alpha}{\sqrt{\pi}}\sqrt{\frac{k!}{(m+k)!}}\left(\alpha^2(x^2+y^2)\right)^{m/2} e^{im\phi} L_k{}^m\left(\alpha^2(x^2+y^2)\right)\right\} e^{-\alpha^2(x^2-y^2)} \quad (2.27)$$

where g_m = ½ for m = 0 and g_m = 1 for m > 1, α is a Gaussian length scale factor, $H_{m+k}(\alpha l)$ represents Hermite polynomial[9] of order $m+2k$ and argument αl, $L_m{}^k(d)$ represents the associated Laguerre polynomial[10] and Re{ } denotes the real part. This formulism assumes that the distribution can be approximated to a radial Gaussian distribution.

In practical circumstances, this can never be solved analytically; it has to be solved numerically. This is difficult because it requires that measurements be taken at a large number of angles between 0 and π radians. The Maldonado-Olsen formulism is still only valid for emissive media that are optically thin. Ghosh Roy has demonstrated how the Maldano-Olsen inversion is related to the Radon inversion [**71**]. In the same article he showed how the Radon inversion can be applied to the source reconstruction of plasma sources in which a significant amount of absorption exists.

In practical situations, the reconstruction of sources that are close to being axisymmetric are often carried out by first performing an Abel inversion, based upon a set of measurements taken from one viewing angle, and then adjusting the two-dimensional distribution so that is consistent with measurements taken from other angles. Gao *et al.* [**69**] took measurements of an argon ICP in both the coil zone of the plasma and in the plume. They took measurements from orthogonal angles at a series of heights and measured across the full width of the plasma. Far away from the coil they observed a high level of symmetry and were able to use an Abel inversion without any difficulty. The measurement profiles inside the coil zone were rather less symmetric. To account for this they took measurements from additional angles and made the necessary adjustments to the inferred emission coefficient distribution so that it would fit all the measurements as closely as possible. They also took end-on measurements (i.e. looking towards the plume along the plasma axis) which helped to verify the extent of the asymmetry.

---

[9] Hermite polynomial definition: $H_n(x) = (-1)^n e^{x^2/2}\frac{d^n}{dx^n} r^2 e^{-x^2/2}$

[10] Associated Laguerre polynomial: $L_n{}^k(x) = \frac{e^x x^{-k}}{n!}\frac{d^n}{dx^n}(e^{-x}x^{n+k}) = \sum_{m=0}^{n}(-1)^n \frac{(n+k)!}{(n-m)!(k+m)!m!}x^m$ [**75**]

Yasutomo *et al*. [**76**] described a method for handling asymmetry in a situation where measurements have been taken across the full width of the source from a single angle; the viewing line must be perpendicular to the axis of asymmetry. In this method, the intensity profile as measured, $I_M(y)$, is divided into symmetric and asymmetric components, $I_s(y)$ and $I_A(y)$ respectively and

$$I_M(y) = I_S(y) + I_A(y) \quad (2.28).$$

At a given *y*-position, $I_S(y)$ is equal to the average of the measured value at that position, $I_M(y)$, and the measured intensity at the opposite side of the origin $I_M(-y)$. $I_A(y)$ is half of the difference between $I_M(y)$ and $I_M(-y)$:

$$I_S(y) = \frac{1}{2}\big(I_M(y) + I_M(-y)\big) \quad (2.29)$$

$$I_A(y) = \frac{1}{2}\big(I_M(y) - I_M(-y)\big) \quad (2.30).$$

Equation 2.28 can be rewritten

$$I_M(y) = g(y)I_S(y) \quad (2.31)$$

where $g(y)$ is a weight function (= 1 + $I_A(y)/I_s(y)$). Figure 2.25 shows graphs taken from [**76**] which display the usefulness of this method. Figure 2.25a shows a profile of hypothetical emission coefficient distribution along the *y*-axis. The two-dimensional distribution is symmetric about the *x*-axis but asymmetric about the *y*-axis and has the equation

$$\varepsilon(r,y) = \big(1 + 0.5\sin(\pi y)\,(1 + 10r^2 - 23r^4 + 12r^6)\big) \quad (2.32).$$

The distribution that would be measured by spectroscopy is shown in figure 2.25b and has the equation

$$I_M(y) = \frac{16}{105}\big(1 + 0.5\sin(\pi y)\,(19 + 34y^2 - 125y^4 + 72y^6)\big)\sqrt{1 - y^2} \quad (2.33).$$

Because the distribution is only asymmetric about the *y*-axis, the emission coefficient distribution can be written as

$$\varepsilon(r,y) = g(y)\varepsilon_S(r,y) \quad (2.34)$$

where $\varepsilon_s(r,y)$ which is the symmetric component of the emission coefficient distribution which can be recovered by applying an Abel inversion to $I_s(y)$, the average of the $+y$ and $-y$ distributions. Numerical methods can then be employed to find an appropriate form for the weight function, $g(y)$, in order to provide a match for the observed data as closely as possible.

Figure 2.25c shows the result when a simple Abel inversion is applied to each half of the measured intensity distribution. The result is not close to the real distribution and includes a discontinuity which cannot be physically realised. Figure 2.25d shows the result of Yamasuto's method; an Abel inversion was applied to $I_S(y)$ and an appropriate 5^{th} order polynomial was found to represent $g(y)$.

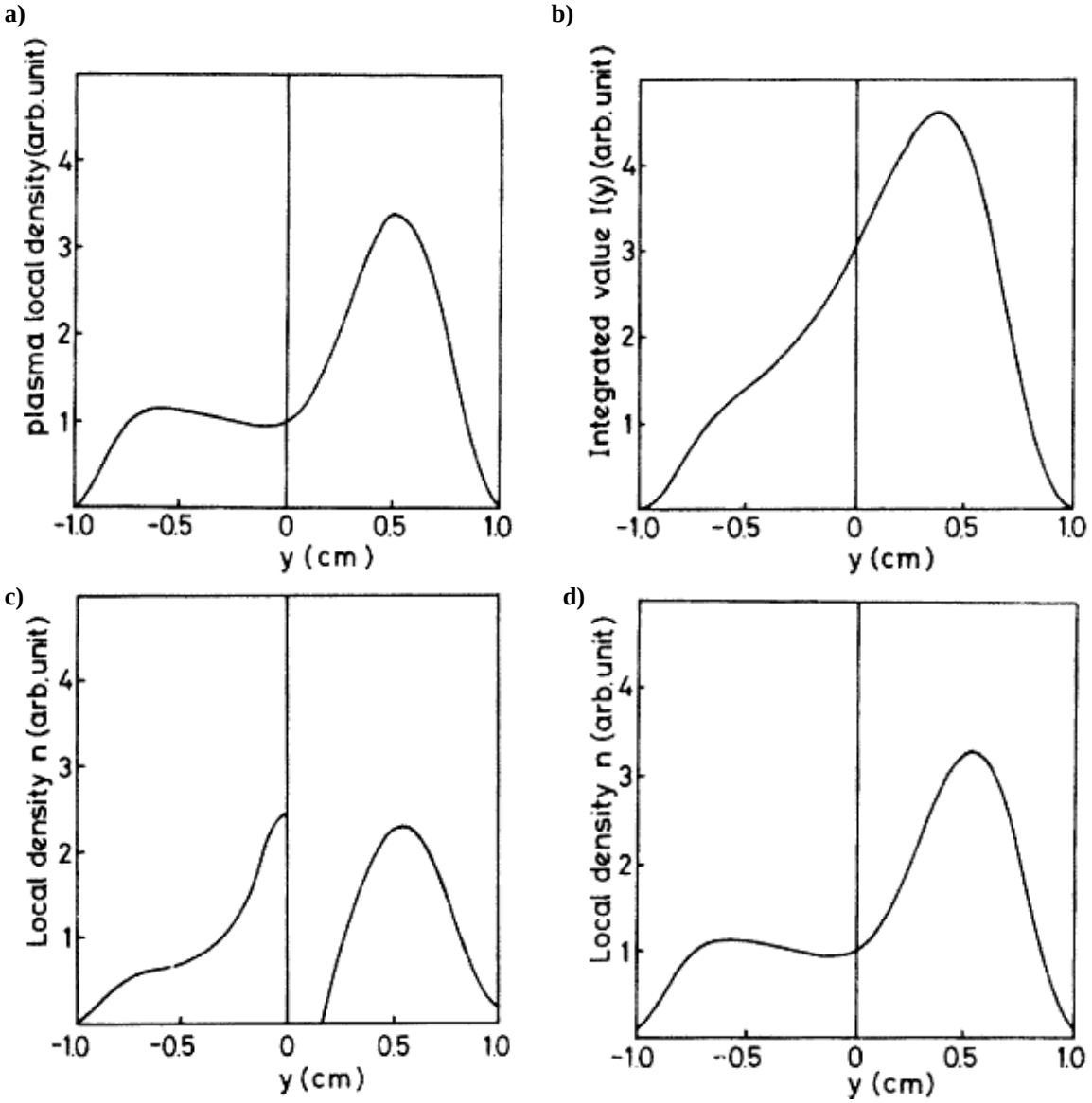

Figure 2.25 **These graphs are taken from Yasutomo *et al.* [76] and show the results for a test for their method of adapting the Abel inversion to deal with an asymmetric profile. a) A test emission coefficient distribution. b) The intensity distribution that would be measured if a plasma had the test emission coefficient distribution shown in a). c) The result following a simple Abel inversion. d) The result from the adapted method. Clearly, the result from the adapted method is much closer to the original distribution.**

The benefits of Yasutomo's are obvious. However, it is only appropriate in circumstances where measurements have been taken from one angle on the viewing line that is perpendicular to the axis of asymmetry.

Tomassini and Giulietti introduced a method of mapping the electron density from interferometric measurements in a laser induced plasma in which deviations from axial symmetry are known to exist [**24**]. As with Yasutomo's method, the distribution of the measured values from one angle (phase difference in this instance) is divided into symmetric and asymmetric components. Slight deviations from axial symmetry are handled by applying a truncated Legendre Polynomial expansion (up to order 1), accounting for variations in electron density with varying azimuthal angle.

Cristoforetti *et al.* [**77**] discussed how an equivalent method can be applied to determining the emission coefficient distribution in a similar laser-induced plasma from spectroscopic measurements. The emission coefficient distribution along a plane at height *z* was approximated using this expansion

$$\varepsilon(r,z,\phi) = \sum_{n=0}^{\infty} \varepsilon_n(r,z) P_n(cos\phi) \approx \varepsilon_0(r,z) + \varepsilon_1(r,z) cos\phi \quad (2.35)$$

where $P_n(\cos\phi)$ denotes the Legendre polynomial of $\cos\phi$ of order *n*. The symmetric component, $\varepsilon_0(r,z)$, can be solved by applying an Abel inversion to the symmetric data

$$\varepsilon_0(r,z) = \frac{1}{\pi}\int_r^R \frac{1}{\sqrt{y^2-r^2}} \frac{\partial I_S(y,z)}{\partial y} \mathrm{d}y \quad (2.36).$$

The magnitude of the asymmetric component, $\varepsilon_1(r,z)$, can be solved by applying the following inversion

$$\varepsilon_1(r,z) = \frac{r}{\pi}\int_r^R \frac{1}{\sqrt{y^2-r^2}} \frac{\partial}{\partial y}\left(\frac{I_A(y,z)}{y}\right) \mathrm{d}y \quad (2.37).$$

Aguilera's method for solving the Abel inversion was used to find $\varepsilon_0(r,z)$.

This method, the Tomassini-Aguilera method, was tested on various simulated asymmetric distributions of the form

$$\varepsilon(r,\phi) = E_0\sqrt{1-\frac{r^2}{R^2}} + E_1\sqrt{1-\frac{r^2}{R^2}} cos\phi \quad \text{for } r \le R \quad (2.38)$$

where E_0 and E_1 are constant emission coefficient values. Figure 2.26 displays how successfully the emission coefficient distribution can be reconstructed using the Tomassini-Aguilera method for varying values of the ratio E_1/E_0 (a large E_1/E_0 ratio corresponds to a greater level of asymmetry). The agreement was considered acceptable for E_1/E_0 values of 0.3.

Figure 2.27 shows results when this method was applied to experimental data, the measured intensity distribution of an atomic zinc emission line in laser-induced plasma on a brass target. The emission coefficient values calculated using both the Tomassini-Aguilera algorithm and the axisymmetric Aguilera algorithm applied to $I_s(y)$, the average measured intensities of the two halves, are displayed. Simple inspection of the results shown in figure 2.27 suggests that the Tomassini-Aguilera reconstruction method can compensate for the slight asymmetry in this particular type of plasma. However, these results do not in themselves prove that the emission coefficient values computed using the Tomassini-Aguilera are significantly closer to the real values than those computed using just the Abel inversion. It also does not prove that the particular polynomial expansion used (a Legendre expansion of $\cos\phi$) is the most appropriate one.

Elder *et al.* [**78**] described a technique whereby an Abel inversion can be applied to a plasma that is not optically thin. An iterative procedure was discussed in which it is possible to find convergence even with a transmission ratio as low as 10%. The technique was applied to a low temperature sodium-seeded nitrogen plasma. Temperatures were deduced from measured intensities of the sodium D-line (the emission line responsible for the familiar yellow colour of sodium lamps). The plasma's opacity was determined by taking three sets of intensity measurements across the D-line frequency band, one set with just the plasma, one with a plasma and with a

G. E. ribbon lamp positioned behind the plasma and a third set with just the G. E. ribbon lamp. From these measurements, it was possible to determine how much light was absorbed from the ribbon lamp by the plasma.

Franceries *et al.* [**79**] carried out a feasibility study of a three-dimensional tomographic reconstruction technique known as MART (multiplicative algebraic reconstruction technique). As with other reconstruction techniques, the process involves making an estimate of the two-dimensional emission coefficient function and making a series of adjustments, based on the measured data, until convergence is found. To test the procedure, measurements were taken of the same arc plasma from seven different angles along the same plane. Their results were compared to those produced by numerical simulations. Artificial noise (5%) was added to the measurements to test the method's robustness. Excellent agreement was achieved, even with the artificial noise and when just four of the seven projections were used.

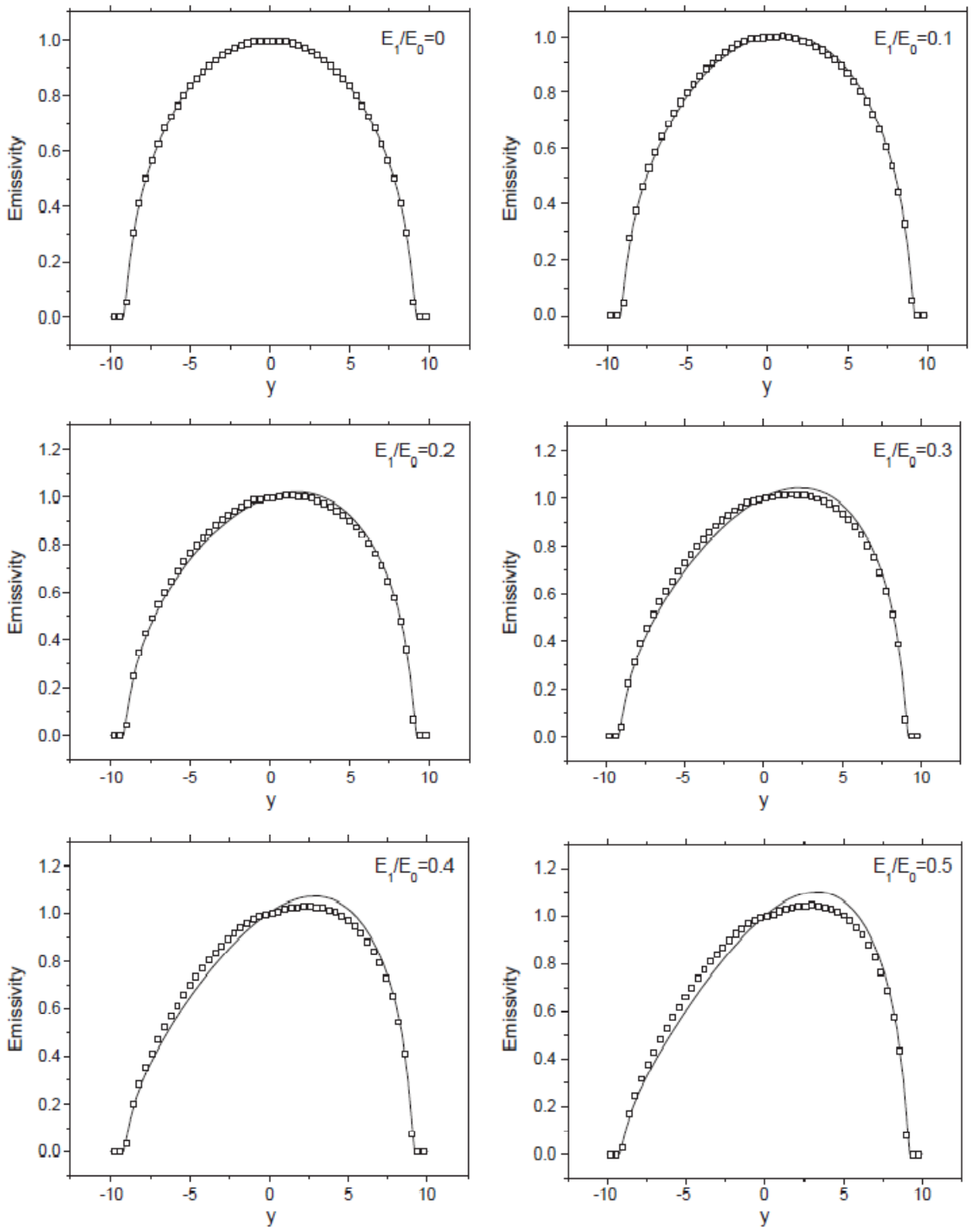

Figure 2.26 **These graphs are taken from [77] and show the results of a test of the Tomassni-Aguilera algorithm. A 2-dimensional, asymmetric emissivity (emission coefficient) distribution was simulated of the form shown in equation 2.38. Various values of the ratio E_1/E_0 were tried. In each graph, the solid line shows the simulated distribution and the hollow squares show the results from the reconstruction technique. The agreement was considered acceptable for E_1/E_0 ratios up to 0.3.**

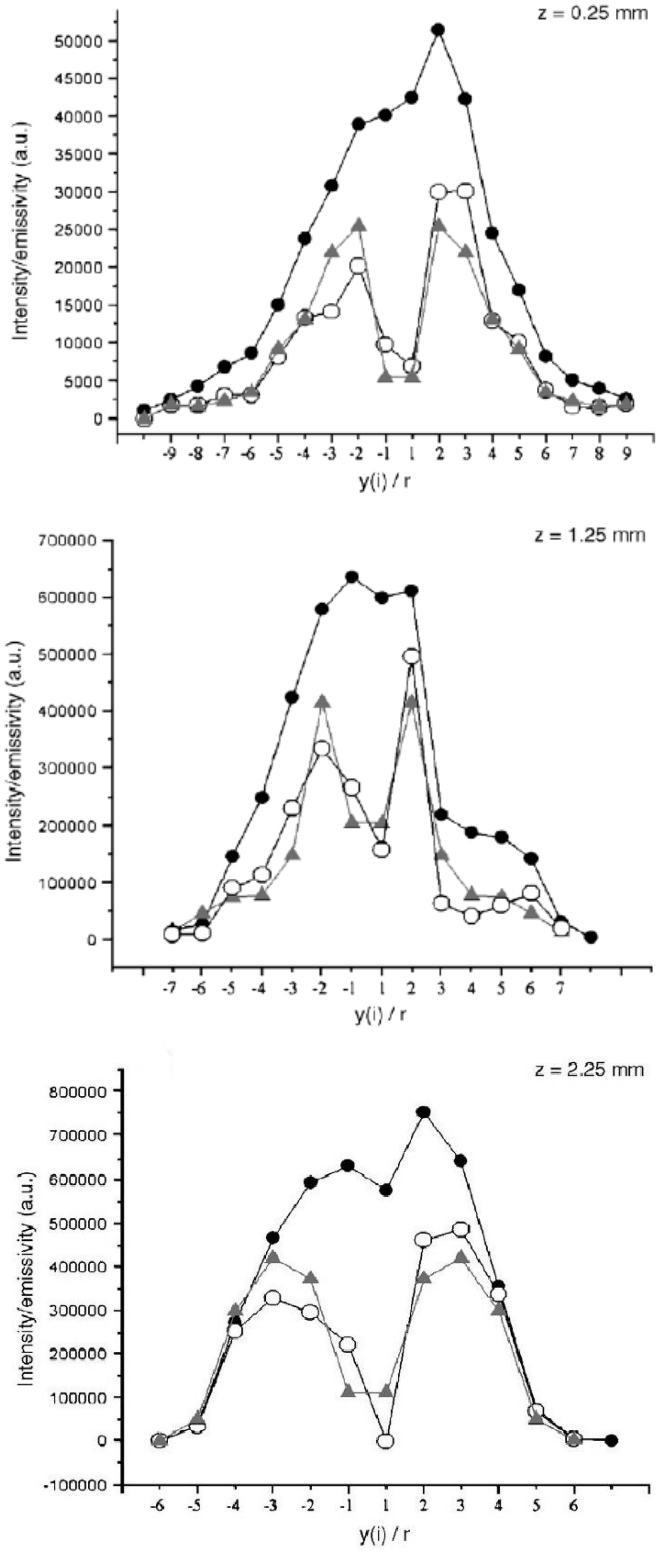

Figure 2.27 **These graphs are taken from [77]. The black circles display the measured intensity distribution of an atomic zinc emission line at 472.2 nm in a laser-induced plasma on a brass target. The grey triangles show the emissivity distribution when reconstructed using the axisymmetric Aguilera algorithm. The white circles show the emissivity distribution when reconstructed using the Tomassini-Aguilera algorithm.**

2.2.4 Measurement of temperature

Many techniques for measuring temperature in plasmas exist; some of which are discussed in this section. Each has its advantages and disadvantages. A method that is very useful for calculating temperatures in one type of plasma might be hopeless in another. Indeed the most appropriate method in one region of a plasma might be different to that in another region of the same plasma. It might take several attempts to find the right method.

2.2.4.1 Doppler broadening

Because of Heisenberg's uncertainty principle, one cannot define the energy of an atomic or ionic state, and hence the emission wavelength resulting from a transition, with absolute precision. As a result, an atomic emission line has a 'natural' line profile covering a narrow spread in wavelength. This profile in the wavelength domain is Lorentzian in shape and known as a Breit-Wigner distribution [**15**, **16**]. In practice, visualising this profile is only possible under very special circumstances. When observing atomic transitions at optical wavelengths, the extent of natural broadening is usually exceeded by that of Doppler broadening by about an order of magnitude.

Doppler broadening is the result of the Brownian motion of particles within the source. The perceived wavelength of transmission from a given atom or ion is either red-shifted or blue-shifted, depending on its motion relative to the observer. As long as there is a large number[11] of particles involved and their energies follow a Maxwellian distribution, the result is that spectral lines become Gaussian in shape in the wavelength domain [**15**, **16**]. The degree of broadening depends on the temperature. The width of the peak at the half-height (FWHM) in terms of wavelength ($\Delta\lambda$) can be calculated using the formula

$$\Delta\lambda = \frac{2}{c}\sqrt{2\ln 2\frac{kT}{M}}\lambda_0 \qquad (2.39)$$

where M is the mass of the atom or ion, λ_0 is the central wavelength of the line, k is Boltzmann's constant and c is the speed of light. Let us consider the argon transition at 696.54 nm. The FWHM of the Doppler-broadened profile that would be expected at various temperatures are given in table 2.1.

Examples of experiments in which temperatures have been determined from the Doppler broadened line profiles include work by Turgeon and Shepherd [**80**], where temperatures of aurorae were determined from atomic oxygen lines and by Kleinmann and Cajko [**81**], where temperatures of an atmospheric argon discharge were measured from argon emission lines. Very fine resolution spectroscopic equipment is usually required for this type of measurement and the measured profile might have to be deconvolved from the profile that results from dispersion within the spectrometer (which is often known as the instrumental profile).

[11] A 'large number of particles' implies a macroscopic system. If the number of emitting particles involved within the spatial and temporal resolution of the measurements is $>10^6$, the number may be regarded as large.

Table 2.1 **Expected FWHM of the Doppler-broadened profile of the 696.54 nm line a range of temperatures.**

Temperature / K	FWHM of 696.54nm line /nm
5000	0.00558
10000	0.00789
15000	0.00966
20000	0.01115
25000	0.01247
30000	0.01366
35000	0.01476
40000	0.01578
45000	0.01673

2.2.4.2 Absolute line method

The emission coefficient for a given transition, the energy emitted per unit volume per unit solid angle by an atom or ion in ionisation state S as a result of that transition, can be calculated using the formula

$$\varepsilon_{UL} = \frac{1}{4\pi} A_{UL} h f_{UL} \frac{N_S(T)}{Z_S(T)} g_U \exp\left(-\frac{E_u}{kT}\right) \qquad (2.40)$$

where A_{UL} is the Einstein transition probability, f_{UL} is the frequency of the radiation, Z_S and N_S are the internal partition function and particle density of the emitting species respectively and g_U is the degeneracy of the upper energy state of the transition[12]. The letters U and L denote the upper and lower energy levels. If one is able to determine the emission coefficient, this formula can be used to calculate the temperature. This requires knowledge of all of the other terms in the equation. That can be difficult as the partition function and particle density are both temperature dependent.

The partition function for a given species is a dimensionless quantity given by

$$Z = \sum_{i=0}^{\infty} \left(\exp\left(-\frac{E_i}{kT}\right) \right) .^{13} \qquad (2.41)$$

This quantity derives from the theory of equilibrium statistical mechanics and is encountered whenever the macroscopic behaviour of a system is governed by a large ensemble of particles which, on a microscopic scale, can only occupy one of a series of discrete energy states. To calculate this exactly, one would have to add an infinite number of terms. Inevitably, some of the energy states are very much larger than others. As the temperature is increased, so does the number of significant terms of the summation. In argon, up to about 14,000K, it is generally sufficient to only include the largest five terms. Much work has gone into calculating partition functions for most

[12] The degeneracy on an atomic state is the number of energy states which, at least in the absence of a magnetic field, are of the same energy and is equal to $2J+1$, where J is the total angular momentum quantum number (always either zero or an integer). The degeneracy is therefore always an odd-numbered integer. This definition should not be confused with that of the degenerate electron gases mentioned at the start of this chapter.

[13] Any text book on statistical mechanics provides a derivation of internal partition function in the canonical ensemble, such as [**82**].

common elements. For atmospheric argon plasmas, values are tabulated in, for example, articles by Olsen [**83**] up to 30,000 K for a plasma in LTE and Chowdury [**84**] up to 45,000 K, for a plasma in local Saha equilibrium. Values of the partition functions and particle densities are plotted in figure 2.28, using values tabulated by Olsen [**83**]. The particle densities were calculated with the help of the Saha equation (equation 2.6). It was also assumed that the plasma particles behave as an ideal gas, which states that

$$P = NkT \qquad (2.42)$$

where P is the pressure of a gas.[14] For a noble gas such as argon, the ideal gas law is a very close approximation.

Accurate temperature determination from an absolute line intensity measurement requires that the geometry of the measuring system and the effects of absorption and dispersion in the optical set up are taken into account. Using a calibration source of known luminosity can help to solve this problem.

[14] The ideal gas equation is the result of combining Boyle's law (pV = constant) with Charles' law ($V \propto T$).

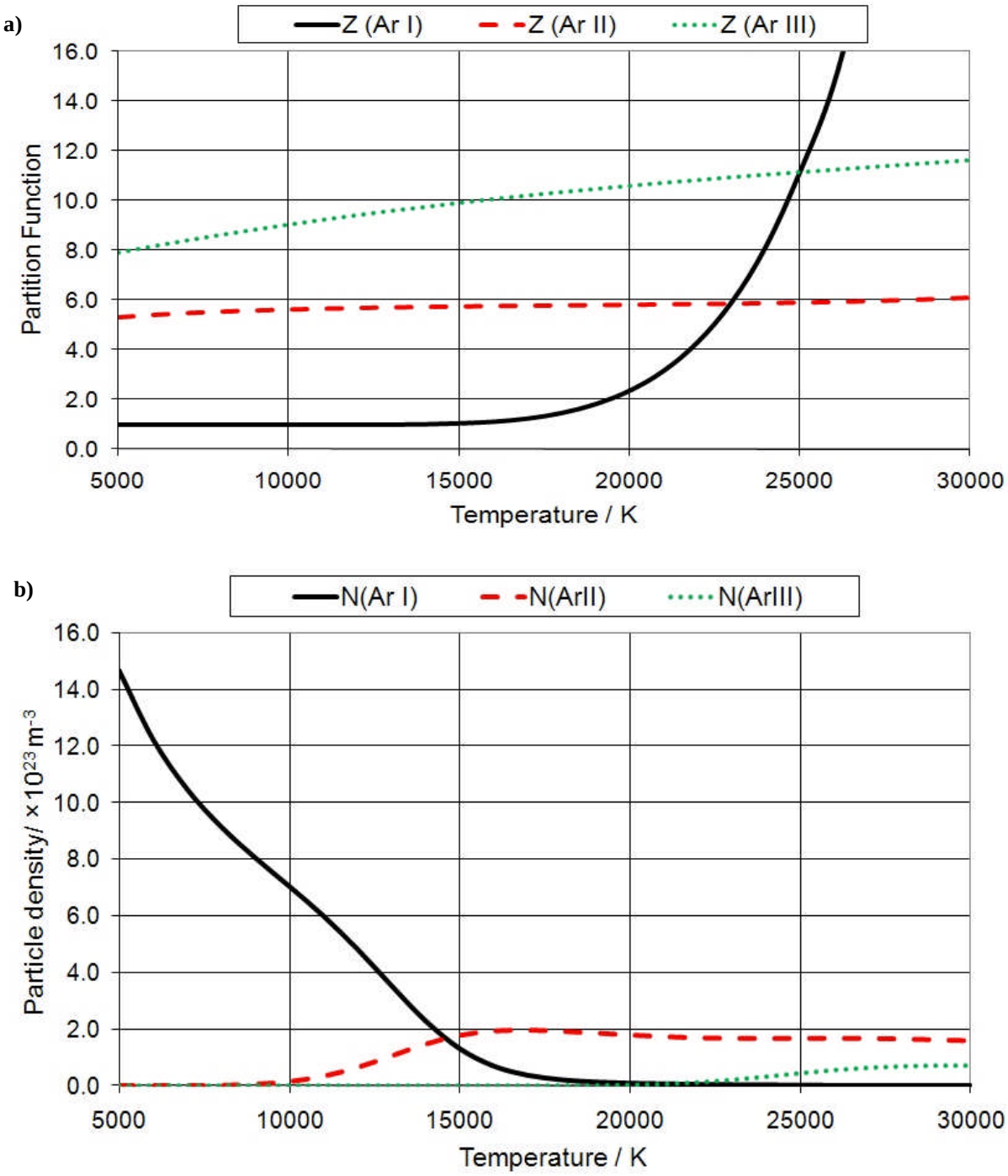

Figure 2.28 **a) The partition functions and b) the particle densities of neutral argon (Ar I) and ionic species (Ar II and Ar III) [15] in an atmospheric argon plasma, from values tabulated by Olsen [83].**

[15] Roman numerals written after an element symbol are used to denote the ionisation state of the element concerned. The number, as written, is equal to ionic charge plus one, i.e. neutral argon is denoted by Ar I, a singly charged ion by Ar II, etc.

2.2.4.3 Relative line methods

Relative line methods of temperature determination involve measuring the intensity of at least two lines in the plasma. If the emission coefficients of two emission lines of the same species (lines '1' and '2') at a particular point are given by ε_1 and ε_2, their ratio is given by

$$\frac{\varepsilon_1}{\varepsilon_2} = \frac{A_1 f_1 g_1}{A_2 f_2 g_2} \exp\left(-\frac{E_{U1} - E_{U2}}{kT}\right) \qquad (2.43)$$

provided that the upper energy states of the transitions are in local thermal equilibrium with each other. The ratio is thus just dependent on known variables and temperature. However, normally quite a large temperature increase is required to induce a significant change in the ratio. Unless the intensities of the lines are measured very accurately it might be difficult to deduce the temperature at all accurately.

The accuracy can be improved by measuring the intensity of more than two lines and creating a Boltzmann plot. Equation 2.40 can be rewritten

$$\ln\left(\frac{\varepsilon_{UL}}{f_{UL} A_{UL} g_U}\right) = -\frac{E_U}{kT} + \ln\left(\frac{hN_S}{4\pi Z_S}\right) \qquad (2.44).$$

If, for a series of transitions of the same species, the left-hand term is plotted against the upper energy level, the result should be close to a straight line. The gradient of that line is equal to $-1/kT$. It is therefore possible to calculate the temperature even if the number densities and partition functions of the species are not known. It might also be possible to calculate an accurate temperature even if systematic errors have been made when taking measurements or calculating the line intensities, should it turn out that all the measurements are incorrect by the same ratio.

This method offers significant advantages over the absolute line method. However, producing a Boltzmann plot means measuring the intensity of a series of emission lines, which can be time-consuming. Also, the quality of the straight line fit depends on the extent to which LTE exists. If there are significant departures from LTE, atoms responsible for different transitions are effectively at different temperatures. This can result in points on a Boltzmann plot not falling on a straight line, but on a curve with the emission lines of higher upper energy radiating more intensely than might be expected. Kaga *et al.* [**85**] used temporally resolved Boltzmann plots to measure temperatures of iron atoms, which were excited using a helium RF plasma. In some of the plots, those taken immediately after plasma ignition, results were not close to falling on a straight line.

Gao *et al.* [**69**] took measurements of an 18 mm diameter argon ICP torch. A compromise was made. Boltzmann plots were taken at a handful of positions, using the intensities of about 30 atomic emission lines. The plots taken were of high quality, such as the one in figure 2.29, indicating that at least partial local thermal equilibrium existed almost everywhere. At all other positions, the temperature was calculated only using the relative intensities of the emission lines at 518.77 nm and 696.54 nm, a worthwhile time-saving tactic as measurements were taken from a large number of positions. In most regions, the temperatures they measured were in very good agreement with those predicted computationally using a two temperature model (see figure 2.30b). The

disagreements on the coolest regions of the plume are expected to be because the plasma is cooled when it mixes with cold air more effectively than was predicted by the model.

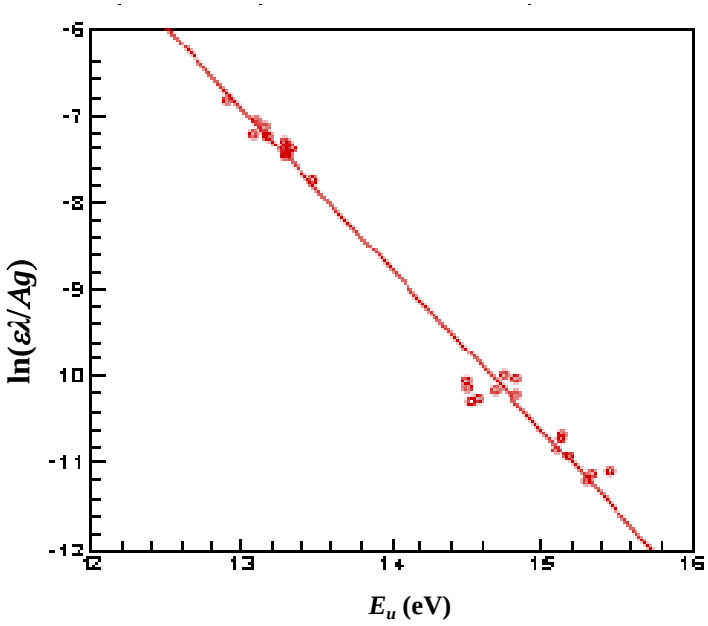

Figure 2.29 **An example Boltzmann plot from emissivity measurements taken of an argon ICP [69].**

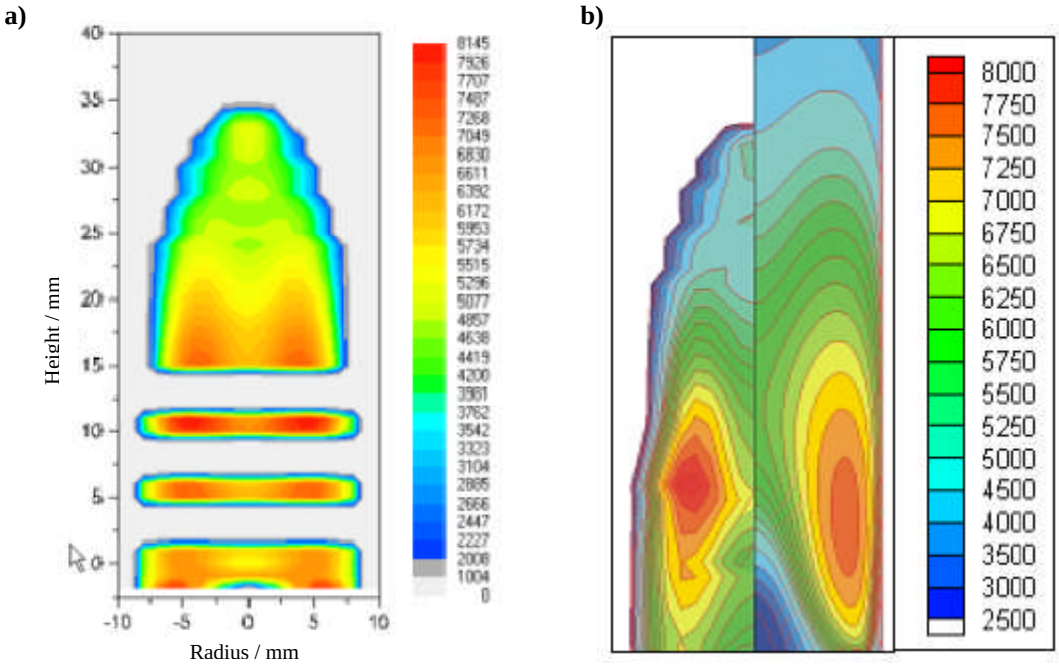

Figure 2.30 **a) Temperature measurements in an argon ICP produced by Gao *et al.* [69]. b) A set of temperature measurements from the same work are compared to those calculated using a two-temperature model.**

Things can be taken further by using Saha-Boltzmann plots whereby intensity measurements are taken of the same element at different ionisation stages. Combining equations 2.6 with equation 2.44 gives

$$\ln\left(\frac{\varepsilon_{UL}}{f_{UL}A_{UL}g_U}\right) - S\ln\left(\frac{2}{N_e}\left(\frac{2\pi mkT}{h}\right)^{3/2}\right) = -\frac{E_U}{kT} + \ln\left(\frac{hN_S}{4\pi Z_S}\right) \qquad (2.45)$$

where S is the ionisation state (0 for neutral particles, 1 for singly charged ions etc). If the terms on left-hand side are plotted against E_U, the result should be a close straight line. Although T appears on the left-hand side, its influence is small and one only need insert an approximate value. This has an advantage over the regular Boltzmann plot in that a greater spread of upper energy levels is covered, making the straight line fit more accurate. However, this benefit is only apparent if there is a significant ionisation fraction.

Saha-Boltzmann plots were used successfully in [**22**] on a laser induced plasma that included ions of iron, nickel and manganese. Noriyasu Ohno *et al.* successfully used Saha-Boltzmann plots in an RF inductive argon plasma (known as a RIP or RF Inverter Plasma torch) at pressures between 70 kPa and 90 kPa [**86**]. They tried to determine temperatures using ordinary Boltzmann plots, but believed them to be inaccurate due to the low electron density and hence lack of LTE.

2.2.4.4 Fowler-Milne method

The Fowler-Milne method can be used in circumstances where it is known that the hottest part of the plasma is along the central axis. Equation 2.40 can be expressed

$$\varepsilon_{UL}(T) = C\frac{N_S(T)}{Z(T)}\exp\left(-\frac{E_U}{kT}\right) \qquad (2.46)$$

where $C = A_{UL}hf_{UL}g_U / 4\pi$. All of the terms in C are independent of temperature.

At lower temperatures, $\varepsilon(T)$ for argon increases with temperature due to the exponential factor. However, increasing the temperature causes the gas to expand and increases the amount of ionisation, therefore $N_S(T)$ decreases. As a result, $\varepsilon(T)$ rises to a maximum with increasing temperature before it starts to fall. The temperature that corresponds to the maximum emission coefficient is called the normal temperature. Provided that the temperature along the central axis of the source is greater than the normal temperature, there will be an off-axis maximum in the emission coefficient. This maximum can be used as a means of calibrating all of the measurements and all of the temperatures can be deduced from the emission coefficients of one emission line. For Ar I (neutral argon) the normal temperature is ≈15,000 K. For Ar II (singly charged ion) it is ≈26,000K. Although ingenious, this method could only be used in very special circumstances. This method was used successfully by Thornton [**17**] for studying a TIG (tungsten inert gas) arc.

2.2.4.5 Continuum emission

Many methods have been devised for measuring plasma temperature from the continuum emission. The most significant source of continuum emission in laboratory plasmas is usually free-bound emission, resulting from the recombination of electrons with positively charged ions. The emission coefficient per unit wavelength for free-bound emission that converts an ion in the ionisation stage *S* to one in ionisation state *S-1*, as a function of wavelength and temperature can be calculated using the formula

$$\varepsilon_{fb}(\lambda,T) = \frac{e^6}{12\pi^2(\epsilon_0 c)^3\sqrt{6\pi m^3 kT}} \times \frac{S^2 g_S N_e N_S}{\lambda^2 Z_S(T)}\left(1-\exp\left(-\frac{hc}{\lambda kT}\right)\right)\xi(\lambda,T)_S$$

or $$\varepsilon_{fb}(\lambda,T) = 1.632 \text{ x } 10^{-43}\text{Wm}^4\ \text{K}^{0.5}\text{sr}^{-1} \times \frac{S^2 g_S N_e N_S}{\sqrt{T}\lambda^2 Z_S(T)}\left(1-\exp\left(-\frac{hc}{\lambda kT}\right)\right)\xi(\lambda,T)_S \quad (2.47).$$

The function $\xi(\lambda,T)$ is known as the Biberman–Schlüter factor, a dimensionless constant which compensates for deviations in energy levels in multi-electron (non-hydrogenic) ions.[16]

The other significant source of continuum emission in thermal plasmas arises from free-free radiation. This is emitted by free electrons that are decelerated by nearby atoms or ions but do not become bound. This is also known as bremsstrahlung (braking) radiation. The emission coefficient function that results from free electrons interacting with neutral atoms is equal to

$$\varepsilon_{ffa}(\lambda,T) = \frac{8e^2}{3\pi\epsilon_0 c^3}\left(\frac{kT}{2\pi m}\right)^{3/2} \times \frac{N_e N_0}{\lambda^2} exp\left(-\frac{hc}{\lambda kT}\right) G(\lambda,T)_0$$

or $$\varepsilon_{ffa}(\lambda,T) = 1.026 \text{ x } 10^{-34}\text{Jm}^2\ \text{K}^{1.5}\text{s}^{-1}\text{sr}^{-1} \times \frac{N_e N_0}{T^{3/2}\lambda^2} exp\left(-\frac{hc}{\lambda kT}\right) G(\lambda,T)_0 \quad (2.48).$$

where $G(\lambda,T)$ is the Gaunt factor, again a correction factors for atoms heavier than hydrogen[17]. The emission coefficient function that results from free electrons interacting with positively charged ions is equal to

$$\varepsilon_{ffi}(\lambda,T) = \frac{e^6}{12\pi^2(\epsilon_0 c)^3\sqrt{6\pi m^3 kT}} \times \frac{S^2 N_e N_S}{\lambda^2}\left(exp\left(-\frac{hc}{\lambda kT}\right)\right) G(\lambda,T)_S$$

or $$\varepsilon_{ffi}(\lambda,T) = 1.632 \text{ x } 10^{-43}\text{Jm}^4\ \text{K}^{0.5}\text{s}^{-1}\text{sr}^{-1} \times \frac{S^2 N_e N_S}{\sqrt{T}\lambda^2}\left(exp\left(-\frac{hc}{\lambda kT}\right)\right) G(\lambda,T)_S \quad (2.49).$$

Measuring temperature from continuum emission has been most successful in hydrogen or helium plasmas where the theory can be applied exactly. Values of the Biberman–Schlüter and Gaunt factors have been calculated for other elements; figure 2.31 is taken from [**87**] showing how these values vary with wavelength for argon at 12,000K.

Separating the measured continuum emission into its constituent parts can be a challenge, particularly if there is a significant population of multiply charged ions. Figure 2.32, taken from [**88**], shows how the normalised continuum emission coefficients (the relative proportions of the total continuum emission from each component) in an atmospheric argon plasma at 13,500K varies with wavelength.

[16] Atoms from which all but one electron is removed are known as hydrogenic ions. Energy levels in such ions can be calculated exactly (using the Rydberg energy) as can be done for the hydrogen atom.

[17] In some literature the Gaunt factors are still referred to as Biberman–Schlüter factors, or all are just known as Biberman factors.

Clearly free-bound emission dominates; in such circumstances, it is often reasonable to only use equation 2.47. As long as $kT >> hc/\lambda$, as is frequently the case, the continuum emission coefficient is then $\propto T^{-0.5}$.

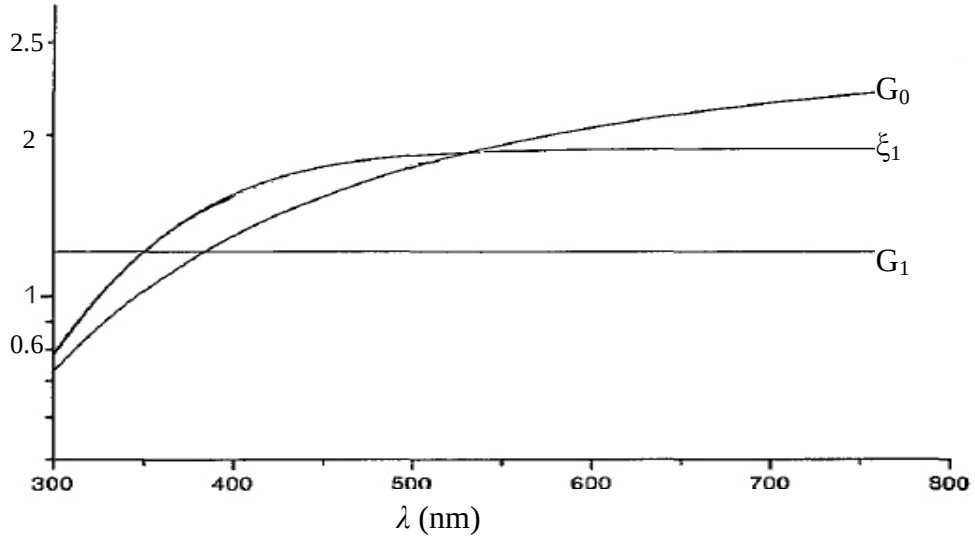

Figure 2.31 **The Biberman–Schlüter and Gaunt factors plotted against wavelength for argon at 12,000 K and a 25% of ionisation fraction [87].**

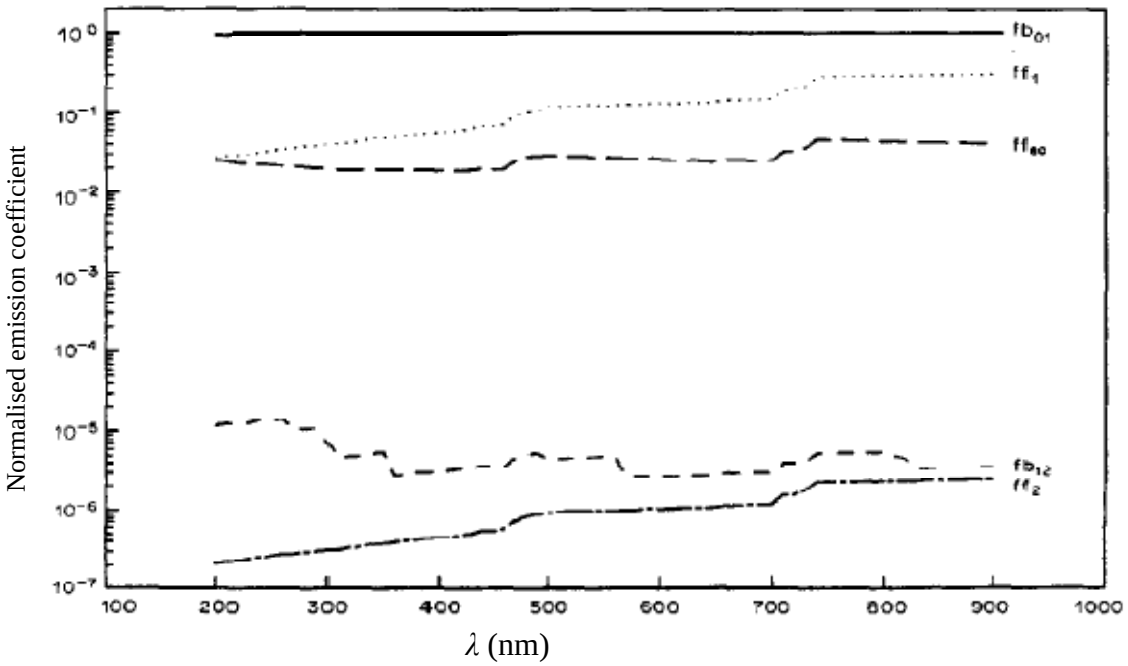

Figure 2.32 **The normalised continuum emission coefficients (relative proportions of each contribution) in an atmospheric argon plasma at 13,500 K as a function of wavelength. The contributions displayed are: fb_{01} = the free-bound emission by electrons recombining with singly ionized ions, ff_1 = free-free emission by electrons interacting with singly ionized atoms, ff_{ea} = the free-free emission by electrons interacting with neutral atoms, fb_{12} = the free-bound emission by electrons recombining with doubly ionized ions and ff_2 = free-free emission by electrons interacting with doubly ionized atoms [88].**

Some have used a combination of line emission and continuum emission for calculating temperature. The theory of using line-continuum ratios is well explained in [**88**] and its usefulness in temperature measurements of laser induced plasmas of silicon is discussed in [**23**]. If equation 2.40 is combined with the Saha equation (equation 2.6)

$$\varepsilon_{UL} = \frac{hfA_{UL}g_U N_e N_{S+1}}{4\pi Z_{S+1}(T)}\left(\frac{h^2}{2\pi mkT}\right)^{3/2}\exp\left(\frac{E_L - E_U}{kT}\right) \quad (2.50).$$

As long as at least PLTE is satisfied in the plasma and the densities of the atoms and singly charged ions are very much larger than those of multiply charged ions, it is reasonable to state that the ratio of the emission coefficient of a line transition divided by the continuum emission coefficient, integrated over the bandwidth $\Delta\lambda$, is equal to

$$\frac{\varepsilon_{UL}}{\varepsilon_c} = \frac{h^4(\sqrt{3}\epsilon_0 c)^3}{\Delta\lambda 4e^6 kT}\frac{A_{UL}g_U Z_{atom}(T)}{Z_{ion}(T)} \times \frac{{\lambda_c}^2 \exp\left(\frac{E_i - E_U}{kT}\right)}{\xi\left(1 - exp\left(-\frac{hc}{\lambda_c kT}\right)\right) + G_{ion}\exp\left(-\frac{hc}{\lambda_c kT}\right)}. \quad (2.51)$$

where λ_c is the central wavelength within the waveband chosen. Figure 2.33 shows how this ratio should vary with temperature. The calculations were done using three different bandwidths.

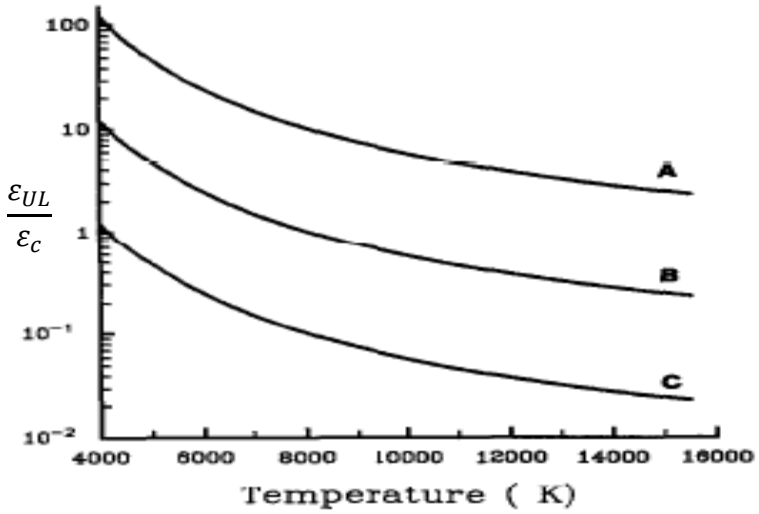

Figure 2.33 **Calculated values of the ratio of line to continuum emission coefficient as a function of temperature for three bandwidths (A 0.1 nm, B 1 nm and C 10 nm). The 430 nm atomic argon emission line was used for these calculations. ξ was set to 1.8 and G_{ion} set to 1.1 [89].**

Rouffet *et al.* [**90**], in 2008 devised an interesting set of methods for temperature measurement in an atmospheric argon plasma, primarily for use in large plasmas (several cm or more) in which the self-absorption of line emission can be significant. They divided the spectrum into three sections. Three different techniques were used to calculate temperature based on these measurements, two of which were based on the ratio of the continuum emission between two of the three spectral regions. All of the measurements were taken using either a low resolution spectrometer or with a three colour camera. They were able to cover temperatures between 5000 K and 20,000 K with only a few percent error compared to the theoretical values. They proved that it is possible to obtain high-quality temperature measurements across that range using relatively inexpensive spectroscopic equipment.

2.2.4.6 Stark effect

Doppler shifts are not the only source of emission line broadening in plasmas. Many lines are divided into a series of peaks due to effects such as spin-orbit coupling or, in the presence of a strong magnetic field, the Zeeman effect. There are also various forms of pressure broadening which result from interactions between neighbouring particles. Interactions between the electric fields of nearby charged particles leads to Stark broadening. Interaction between neutral atoms of the same kind can lead to resonance broadening. Interactions between atoms of different type can lead to Van de Waals' broadening [**15**, **16**].

The Stark effect is usually the most pronounced of the pressure broadening effects in regions of high electron density. It results in emission lines having a Lorentzian profile whose width at the half height is approximately equal to [**91**-**93**]

$$2 \times 10^{-22} N_e \omega \left(1 + 5.5 \times 10^{-6} {N_e}^{0.25} \alpha \left(1 - \frac{0.0068 {N_e}^{1/6}}{\sqrt{T_e}} \right) \right) \quad (2.52).$$

Stark broadening parameters are listed in [**91**], for example. However, for all elements other than hydrogen, there are significant uncertainties. For this reason, a small amount of hydrogen is sometimes added to a plasma, as was done by Degout and Catherinot in a tungsten inert gas arc [**94**]. The amount of broadening is relatively temperature insensitive. However, as described in section 2.1.4, it can be used to calculate the electron density, which can be used in calculating temperature.

De Regt *et al.* measured absorption profiles in a 22 mm diameter argon ICP [**92**]. They were able to separate the Gaussian Doppler shift profile from the Lorentzian profile. It had been assumed initially that the pressure broadening was solely due to Stark effect but it was found that, at larger radii, there was a significant contribution from Van de Waals broadening. Another significant disadvantage of using Stark broadened profiles to calculate electron density is highlighted in this paper, which is that it can be difficult to obtain accurate line profiles of the central region following an Abel inversion.

2.2.4.7 Absorption Spectroscopy

The vast majority of spectroscopic studies of induction arcs are based on atomic emission spectroscopy. However in cooler plasmas, <10,000°C, it is not uncommon to use absorption spectroscopy. Instead of determining temperature from the height of peaks in the emission spectrum, it is determined from the depth of inverted peaks by relatively cold gas as it absorbs light at particular frequencies from another light source of known luminosity behind. The surface temperature of stars is measured in this way, as the surface (photosphere) absorbs light from the warmer interior.

In [**95**], temperatures were measured by absorption spectroscopy in a sodium seeded nitrogen discharge. Measurements were taken of emission lines known to be self-absorbed within the plasma with a 'Garton-type' flash tube tungsten ribbon lamp behind the plasma. Provided that LTE existed between the states involved in the transition, it was possible to calculate temperatures from the absorption coefficient using the Planck distribution.

While it makes sense to use a broadband source for measuring absorption profiles, it can be done using a tuneable narrowband source; in [**92**], for example, an infrared diode laser was used.

2.3 Thermography

Infrared radiation has been associated with heat ever since it was discovered by William Herschel in 1800. While performing spectroscopy work on sunlight, using a glass prism he noticed that the reading given by a thermometer on the wall rose and deduced that 'invisible' light was warming it. It is now commonly known that everything around us emits infrared radiation. This radiation is known as blackbody or cavity radiation. A perfect blackbody is something which absorbs all of the electromagnetic radiation incident upon it. An external observer sees some of that radiation re-emitted by the blackbody and the spectrum of the re-emitted radiation is a function of temperature. This function is the Planck distribution [**82**, **96**], the power emitted per unit surface area of the source per unit wavelength is equal to

$$I(\lambda, T) = \frac{2hc^2}{\lambda^5\left(1-\exp\left(\frac{hc}{\lambda kT}\right)\right)} \qquad (2.53)$$

The intensity peaks at a particular wavelength, which can be calculated using the Wien Displacement Law

$$T\lambda_{\text{peak}} = B \qquad (2.54)$$

where B is the Wien Displacement constant, = 0.002897 m.K. It so happens that at temperatures between 9 K and 4000 K, the peak is in the infrared part of the spectrum, hence the link between heat and infrared light. The overall (bolometric) intensity of a blackbody source (energy emitted per unit surface area) is equal to

$$I = \sigma T^4 \qquad (2.55)$$

where σ is the Stefan-Boltzmann constant, = 5.670×10^{-8} $\text{Wm}^{-2}\text{K}^{-4}$. The temperature of a perfect blackbody can be deduced very easily. However, few objects are close to being a perfect blackbody (the cosmic microwave background radiation is a notable exception). For a 'greybody', i.e. anything which is not a perfect blackbody, equation 2.55 becomes

$$I = \varepsilon\sigma T^4 \qquad (2.56)$$

where ε is the emissivity of the material, a dimensionless quantity equal to the amount of radiation emitted divided by the amount that a perfect blackbody at the same temperature would emit[18]. The expression is only completely correct if ε is independent of wavelength. In practice, there is always some variation.

By using a pyrometer or infrared camera, we can deduce the temperature of an object that is opaque to infrared radiation if we know the emissivity. Figure 2.34 shows a typical atmospheric transmittance spectrum. Infrared cameras are usually tuned to measure radiation in a wavelength band somewhere between 8 μm and 12 μm, where

[18] It is unfortunate that both thermographers and plasma spectroscopists use the word 'emissivity' to mean different things and use the same symbol. The term is often used in place of the 'emission coefficient' described in section 2.2.

the transmittance is high. Thermography has been used very successfully in very many industrial and domestic applications.

The emissivity of non-metallic materials between 8μm and 12μm is usually above 0.9. The emissivity of metals and semiconductors is usually much lower, but can be larger than expected if there is a significant oxide layer on the surface.

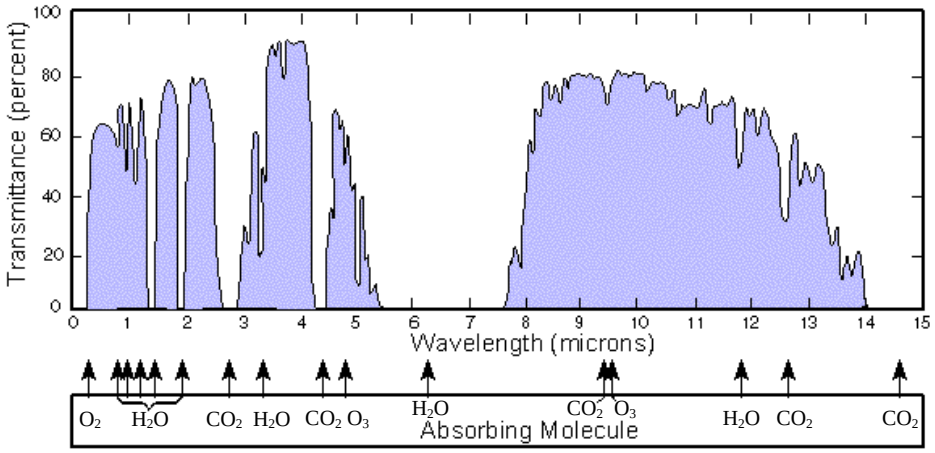

Figure 2.34 **Atmospheric infrared transmittance spectrum. The molecular species responsible for the most significant emission lines are indicated [96].**

2.4 Telescopic Mirror Substrate Materials

As was mentioned in chapter 1, the primary mirrors of today's largest optical telescopes are made up a number of segments. These segments are usually either hexagonal in shape or 'petal-shaped' which fit together to make a large, concave reflective surface that is either parabolic, hyperbolic or occasionally spherical in shape. A honeycomb structure is usually machined into the reverse side of the substrate to reduce the weight of the segments without reducing their rigidity.

Zerodur is manufactured by Schott Optik and is a mixture of vitreous and ceramic components. It is chiefly composed of SiO_2 (50-80%) and Al_2O_3 (20-50%) with traces of oxides of titanium, zirconium, lithium, magnesium and phosphorus. It has been the most popular choice of material for large terrestrial optical telescope mirror substrates since the 1980s. The primary mirrors of the Keck Telescope are made of Zerodur. Zerodur has a very low coefficient of thermal expansion (CTE). This is important because temperature gradients across the part can lead to surface stress and a change in form. The low CTE helps to limits this. It is relatively easy to grind and polish and is easily coated. Its high optical homogeneity makes it a useful material for transmissive optics too. However, Zerodur is expensive and time-consuming to produce as the heat treatment process can take as long as a year to complete [**97**, **98**].

ULE is a clear titanium-silicate glass manufactured by Corning, also known as Corning 7972. It is composed of SiO_2 (92.5%) and TiO_2 (7.5%) and is made by reacting silicon tetrachloride with titanium tetrachloride in a furnace. The linear CTE is quoted as being '*0 ± 30 ppb/°C between 5°C and 35°C with a 95% confidence level*'. For comparison, the linear coefficient of thermal expansion of fused silica is 600 ppb/°C at 20°C. ULE has a low density, a big advantage for use in airborne and space systems and is more homogeneous than Zerodur. However, ULE is harder and more brittle and it is more difficult to grind and polish than Zerodur [**99**, **100**]. The 8 m diameter primary mirrors of the Gemini Observatory telescopes are made of ULE [**101**].

Silicon carbide is a nonoxide ceramic material. There are several ways of manufacturing silicon carbide. The type most usually used for making of mirror substrates is sintered silicon carbide (SSiC), which is manufactured by Boostec. SSiC has a crystalline structure and very isotropic properties. Although silicon carbide is denser than Zerodur and ULE and has a higher CTE, it can withstand temperatures up to ~1600°C without loss of strength. Unfortunately, silicon carbide is very porous and the surface must have a coating applied to it by chemical vapour deposition (CVD) if it is to be of any use. This coating has to be at least 100 μm thick prior to grinding; this vastly increasing the production cost of fabricating SSiC optics. It is a popular choice for space telescope mirrors [**102**-**104**]. The Herschel Space Observatory, which was launched in May 2009, largest space telescope ever built at the time of writing, detects emission between the far infrared and sub-millimetre wavelengths, enabling astronomers to image some of the coolest and most distant objects in the Universe. Its primary mirror is parabolic, 3.5 m in diameter and was made from 12 segments of silicon carbide brazed together [**105**].

Examples of optics made of Zerodur, ULE and silicon carbide are shown in figure 2.35. Transmission spectra of Zerodur and ULE are shown in figure 2.36. Graphs showing the coefficient of thermal expansion of Zerodur and ULE are shown in figure 2.37.

Other materials have been used for making primary mirrors. Beryllium is a common choice for cryogenically cooled space telescopes, the James Webb Space Telescope mirrors will be made of beryllium [**106**]. Beryllium has a very high specific stiffness but it is not usually considered for very large optics due to its cost. Other materials that have at least been considered include Astrosital®, a glass-ceramic similar to Zerodur, nickel-plated aluminium alloys [**107**] and fibre-reinforced resins such as Cesic® [**108**, **109**].

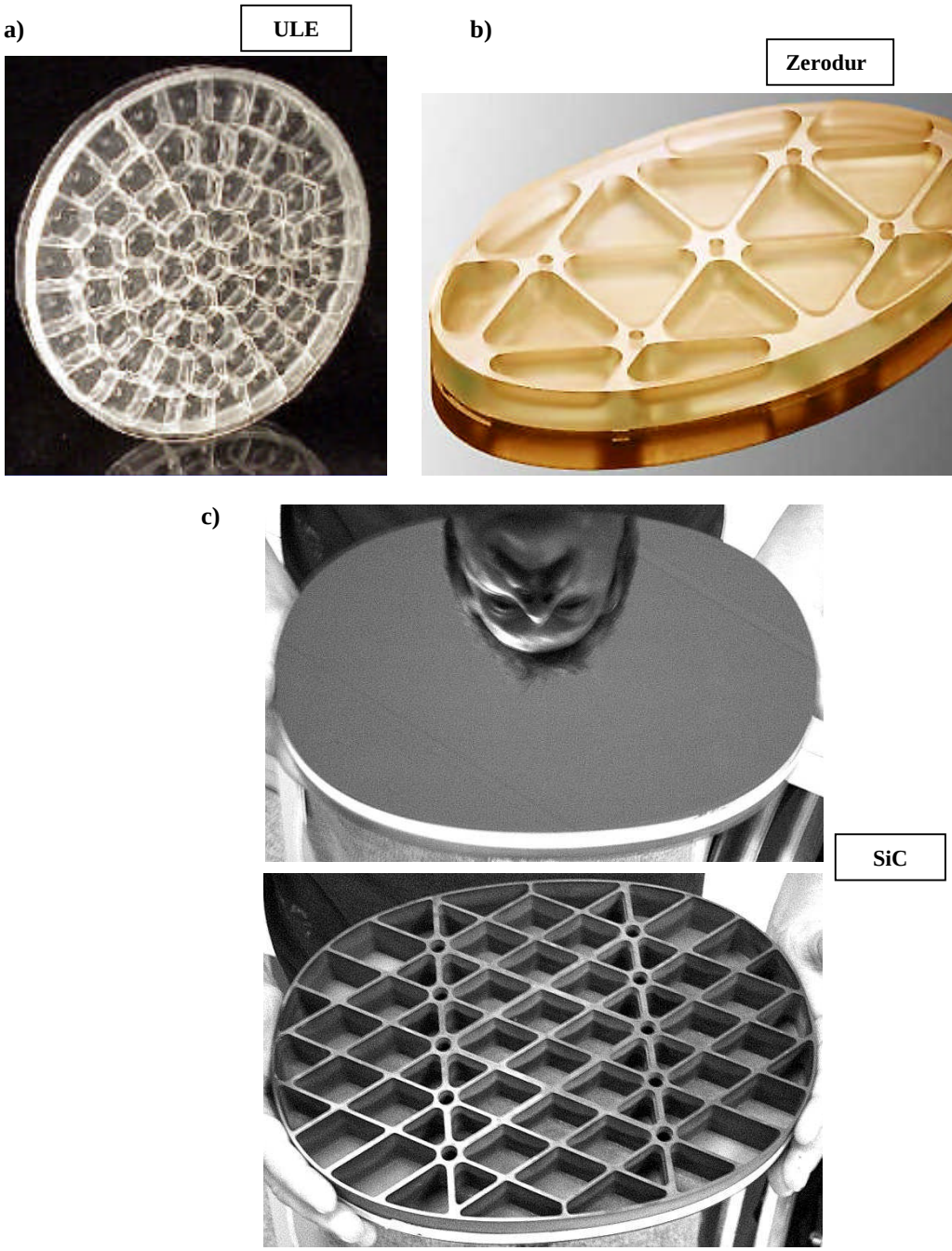

Figure 2.35 **Mirror substrates made from a) ULE, b) Zerodur (for a satellite mirror mount) [98] and c) a CVD coated silicon carbide mirror [104].**

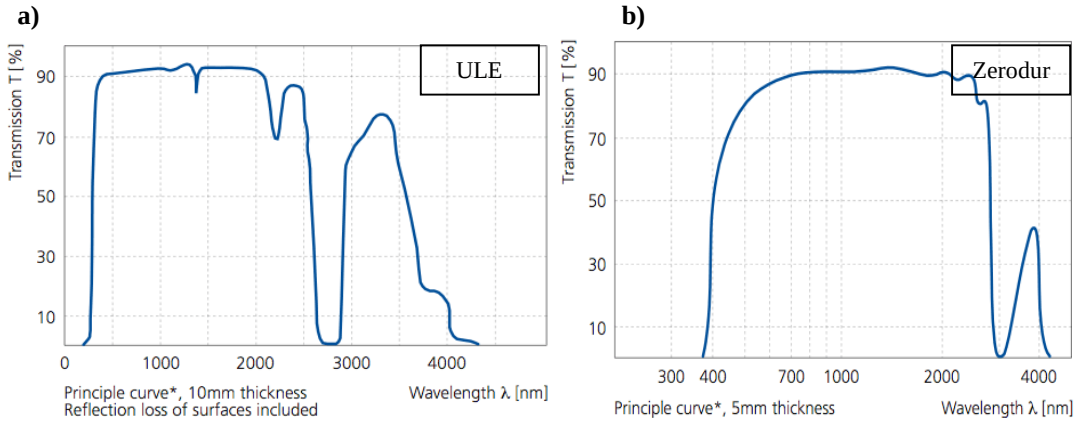

Figure 2.36 **The transmission spectrum of a) a 5 mm thick piece of ULE and b) a 5 mm thick piece of Zerodur. Zerodur's yellow tint results from the higher transmission at the red end of the visible spectrum [98].**

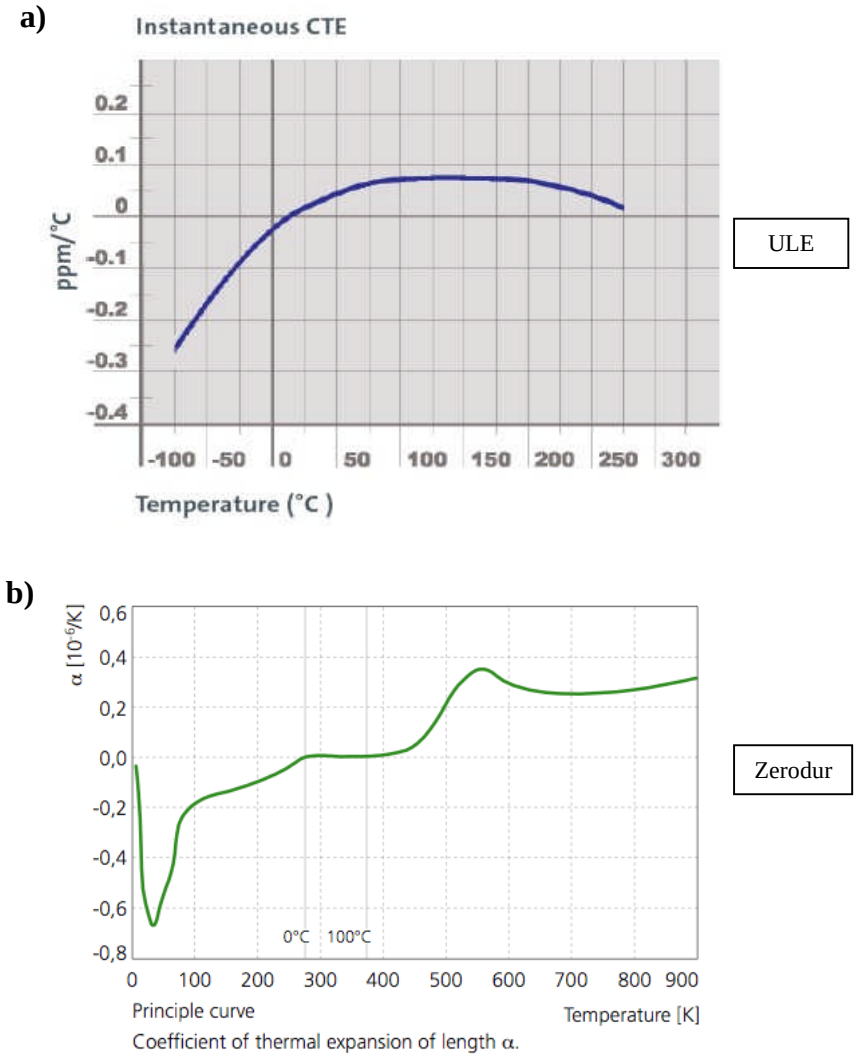

Figure 2.37 **The linear coefficient of thermal expansion of a) ULE (Corning 7972) [99] and b) Zerodur [98].**

2.5 Plasma etching

Many the most significant applications of plasma technologies in industry involve either the removal of material from a surface (plasma etching) or the deposition of a coating onto a surface (plasma coating). Plasma etching first became popular during the early 1970s for use in the manufacturing of microelectronic devices and today a wide variety of plasma processes are used in the production of integrated circuits. To name but a few, the deposition of aluminium and high-temperature superconducting films, the use of oxygen discharges to grow SiO_2 films on silicon, the doping of silicon with boron atoms using boron trifluoride and the use of oxygen discharges to remove photoresist or polymer films [**14**].

Plasma etching has an advantage over wet chemical etching in that the plasma can be made to etch more favourably in one direction, the direction in which the gas particles are moving (anisotropic etching) whereas a liquid etchant usually etches evenly in all directions (isotropic etching). Anisotropic etching can offer a significant advantage over isotropic etching, which is illustrated in figure 2.38. When fabricating microelectronic devices it is usual to place a stencil, which made from a material that is unaffected by the etchant, on top of a thin film of a material which is susceptible to the etchant (most commonly doped silicon). It is desirable for the width of the etched track produced in the film (the separation between two electrically conducting regions) to be as close to that of the gap in the stencil as possible. This can best be achieved if the etchant acts in the vertical direction, i.e. anisotropically. Isotropic etching leads to undercuts in the film, and thus increases the effective width of the gap. If the film has a thickness, *T*, and the stencil width is *D*, the width of the gap at the top becomes $D + 2T$ by the time the etchant has cut through the film at the centre. As an example of what is achievable using plasma etching, figure 2.39 shows a trench etched in single crystal silicon, which is 0.2 μm wide and 4 μm deep [**13**, **14**, **21**, **110**, **111**].

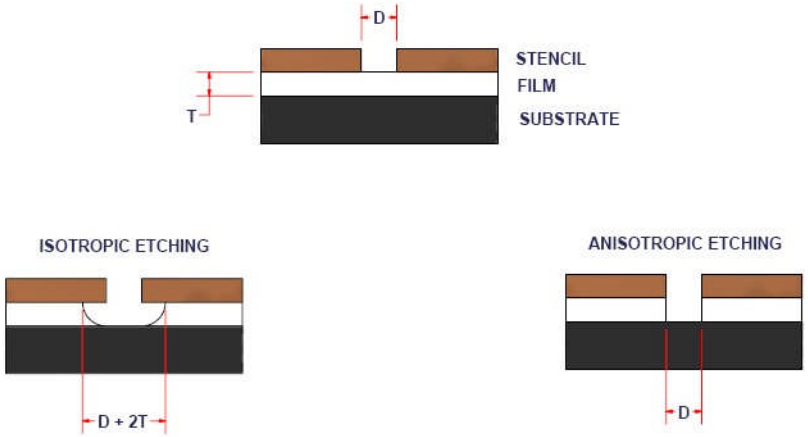

Figure 2.38 **Isotropic and anisotropic etching. Isotropic etching leads to an effective increase in gap width equal to twice the thickness of the film.**

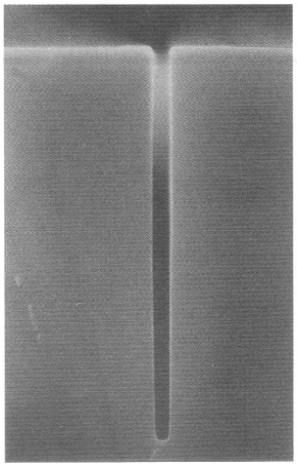

Figure 2.39 A trench etched in single crystal silicon, 0.2 μm wide and 4 μm deep [14].

A plasma can be used to remove material from the surface by two distinct mechanisms: ion bombardment or chemical attack. Sometimes both mechanisms act simultaneously. Each is described separately first.

2.5.1 Sputtering

Sputtering is a mechanical means of etching whereby the surface is bombarded with positively charged ions and the impact energy is sufficient to break bonds in the target material. Sputtering is a highly unselective way to etch. This can be advantageous in that it can be used to etch a wide range of materials. However, it has the disadvantage in that it can be difficult to mask parts of the substrate with a stencil as the stencil might be etched as well [**13**].

In 1961 H.R. Kaufman invented the multi-aperture electron bombardment ion source. This generates a well-collimated beam of ions. It was originally designed not as a device for etching, but for spacecraft propulsion. A diagram of a Kaufman ion drive is shown in figure 2.40. The plasma gas is bombarded with electrons by thermionic emission from the cathode and becomes ionised. An electric field then accelerates the resulting ions through an extraction grid. Ion energies of several keV can be attained. Beam diameters can be as large as 30 cm, resulting in currents greater than 1 amp. A low energy electron beam is usually fired at the target material as well to neutralise positive charge build-up on the surface [**14**, **21**].

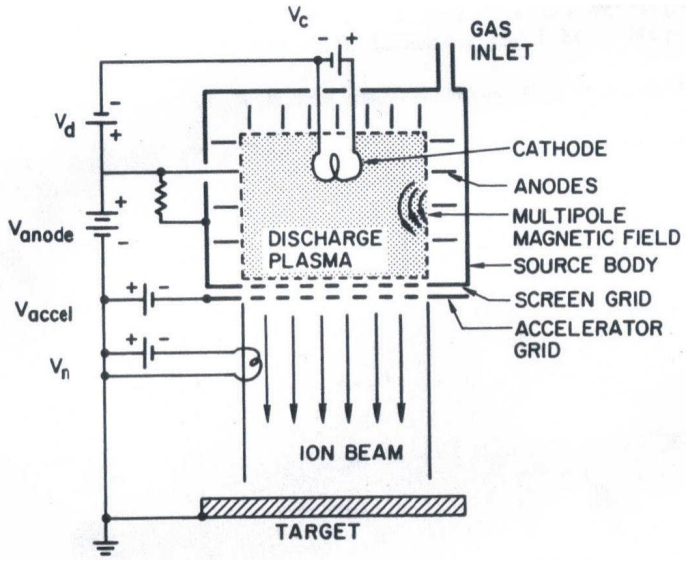

Figure 2.40 The Kaufman ion drive [14].

For an ion propulsion drive it is usual to use a heavy inert gas, such as xenon. For ion etching device, argon is by far the most common choice. An alternative means of generating high energy ions is the microwave ion drive, also known as the Electron Cyclotron Resonance (ECR) drive, in which microwave power is used to ionise the gas. A schematic diagram is shown into figure 2.41.

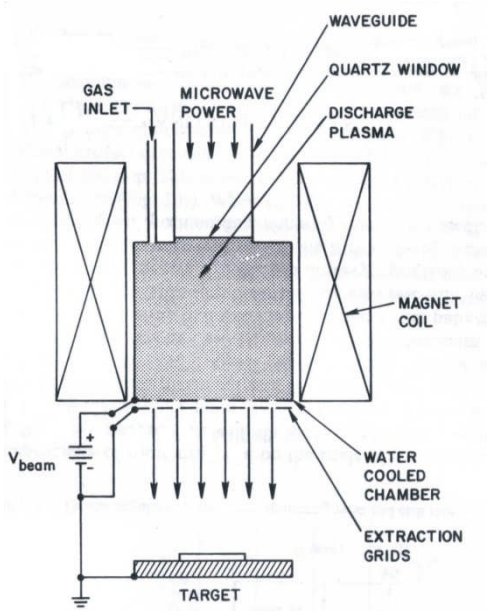

Figure 2.41 Microwave Ion Drive [14].

2.5.2 Plasma chemical etching

An alternative plasma etching mechanism is chemical etching, by which neutral atoms or molecules react chemically with the surface material to form volatile products. Some materials are very much more susceptible than others to different reactive species, thus alleviating the lack of selectivity problem encountered when sputtering. It is usually easier to achieve a higher material removal rate (MRR) using chemical etching techniques without damaging the surface. However, plasma chemical etching is slightly less anisotropic than sputtering, although significantly more so than is wet chemical etching.

Materials that are susceptible to plasma chemical etching include silicon, silica glasses, silicon carbide, Si_3N_4, germanium, GaAs, GaN and metals such as aluminium, titanium and nickel.

In a low pressure plasma chemical etching systems a molecular gas, typically one containing atoms of either fluorine, chlorine or oxygen is introduced into a plasma and atomised by high energy electrons. Commonly used fluorine-containing gases include F_2, CF_4, SF_6, NF_3, ClF_3, XeF_2, XeF_6 and CHF_3. CF_4 and SF_6 are usually preferred over F_2 because of their lower toxicity. However, when etching with CF_4 or SF_6, unsaturated species can form in the discharge which can react with the fluorine radicals and leave polymeric residues on the target material's surface.

The chemical reaction mechanisms between fluorine radicals and silicon are well understood. When a clean silicon surface is exposed to atomic fluorine, a fluorinated crust forms very quickly, which can be up to 5 atomic layers deep. Subsequent fluorine atoms attack the bonds beneath the surface. If they attack silicon bonds very close to the surface, this can result in the release of gaseous radicals of SiF_2,

$$F + F + Si(s)\text{--}Si(s) \rightarrow SiF_2(g).$$

The SiF_2 then quickly combines with other fluorine radicals or molecules to produce molecular radicals of SiF_3 an excited state,

$$SiF_2(g) + F \text{ (or } F_2) \rightarrow SiF_3^*(g) \ (+ F).$$

The excited radical quickly becomes unexcited and chemilumineses in doing so with a broad peak at around 500 nm [**13, 110**].

$$SiF_3^*(g) \rightarrow SiF_3(g) + \text{photon}$$

$$SiF_3(g) + F \rightarrow SiF_4(g).$$

Alternatively, if the fluorine atoms attack silicon bonds further down, it might not be possible to release gaseous radicals of SiF_2 and instead two further fluorine radicals are required so as to release stable molecules of SiF_4.

$$F + F + Si\text{---}Si\text{---}Si(s) \rightarrow Si\text{---}SiF_2\text{---}Si(s)$$
$$\qquad\qquad\quad |$$
$$\qquad\qquad\quad Si$$

$$F + Si\text{---}SiF_2\text{---}Si(s) \rightarrow Si\text{---}SiF_3(s).$$

$$F + Si\text{---}SiF_3(s) \rightarrow SiF_4(g).$$

To promote anisotropic etching, hydrogen is frequently added to the discharge. For example, $CF_4 + H_2$ is sometimes used for making deep narrow trenches. The hydrogen reacts with the fluorine to produce fluorocarbon polymers which coat the sides of a trench so that it can only be etched at the base. This process is known as deep reactive ion etching (DRIE).

Sometimes oxygen is added to increase the etch rate. The reaction of CF_4 with silicon and O_2 is

$$Si + CF_4 + O_2 \rightarrow SiF_4 + CO_2.$$

Figure 2.42 shows how the rate of etching silicon using CF_4 varies with differing concentrations of O_2. The highest etch rate occurs with 16.3% oxygen; at higher concentrations, oxygen chemisorbs into the silicon and inhibits the etching. When etching silica, the optimum oxygen concentration was found to be 22%. Adding oxygen also helps to suppress the formation of polymeric residues.

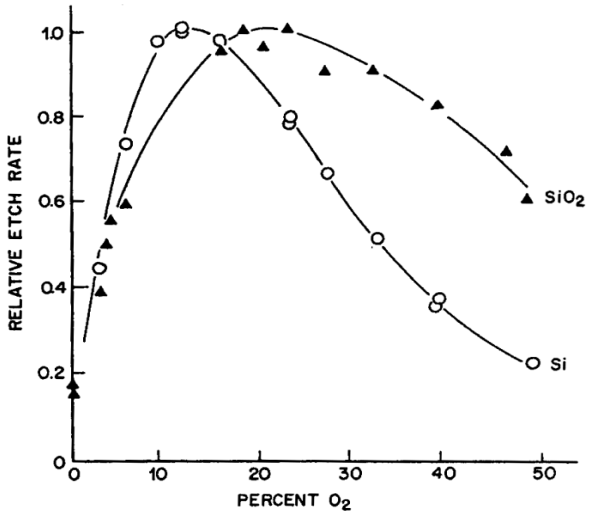

Figure 2.42 **The normalised etch rate of CF_4/O_2 mixtures on silicon and silica wafers in a parallel plate reactor plotted against the proportion of oxygen in the mixture. The pressure was 0.35 torr, the power density was 0.16 W/cm^2 [13, 110].**

The dependence of etch rate, and hence material removal rate, on temperature, T, has been found to be of the form

$$\text{—} \qquad \text{—} \qquad (2.57)$$

where C and E_A are constants given in table 2.2 for silicon and silica, N_F is a concentration of fluorine radicals and R is the molar gas constant (= 8.31 J/mol/K). Figure 2.43, shows how the etch rate varies between 250 K and 400 K when the fluorine radical density set to 3×10^{21} m^{-3}. The gradient of the line is primarily due to the Arrhenius factor; the $\sqrt{T}$ factor only has a weak influence [**13**].

Table 2.2 **Constants for silicon and silica that can be used in equation 2.57.**

	Si	SiO_2
C (m^{4}s^{-1}K$^{-1/2}$)	4.77×10^{-30}	1.02×10^{-30}
E_A (activation energy in kJ/mol)	10.4	15.7

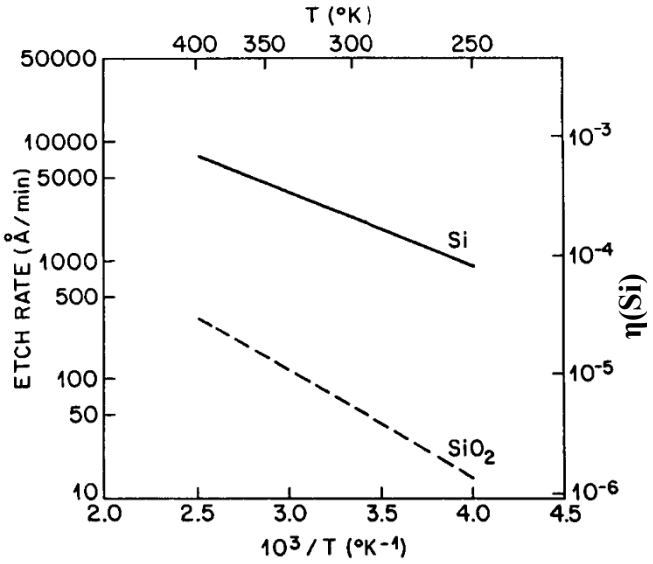

Figure 2.43 **The etch rate that would be achieved on silicon and silica resulting from equation 2.57 using the data in table 2.2 and setting the fluorine radical density to 3×10^{21} m^{-3}. η(Si) is the probability that an impinging silicon atom leaves the surface as part of a gaseous silicon fluoride molecule [13].**

2.5.3 Ion-enhanced energetic etching

Ion-enhanced energetic etching uses both sputtering and chemical etching. High energy ions are used to disrupt the target surface, making it more susceptible to chemical attack. Figure 2.44 shows how using argon ions with XeF_2 can yield an etch rate on silicon that is many times faster than the sum of what each species would achieve on its own; the two mechanisms are described as synergistic.

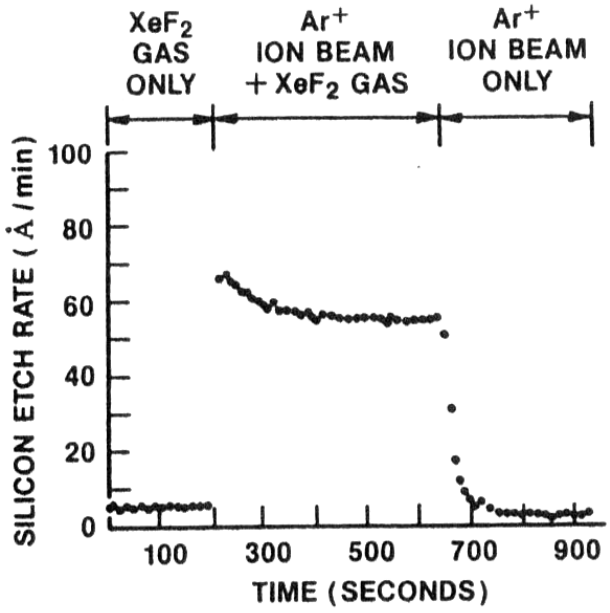

Figure 2.44 **The combination of sputtering with argon ions and chemical attack using XeF_2 can result in an etch rate on silicon that is many times larger than the sum of what each method is capable of achieving on its own [13, 110].**

2.6 Techniques used for the fine figuring of large optics

In the 1980s, plasma etching techniques were applied to the problems of the fine figure correction of precision optics. In order to achieve accurate figure correction, it is crucial that the material removal process be deterministic; one has to know, for a given set of input parameters, how much material is going to be removed at a particular position within a given period of time. It is desirable to be able to adjust the removal function in order to be able to suppress features of different spatial size.

The demands for using plasma etching techniques for the fine figuring of optics are different to those required for etching integrated circuits on silicon. The materials used to make large precision optics are more difficult to etch so material removal rates are generally lower. However, the need for an etching process to be anisotropic is not so great.

Any mechanical grinding and polishing action on a brittle material can induce microcracks under the surface, known as subsurface damage. The extent of damage depends on the size of the grit on the grinding wheel or polishing pad. Optics are often polished in several stages using successively finer grits, removing most of the subsurface damage induced from the previous step. The polishing of large optics is usually done nowadays using a loose abrasive slurry (containing grains of cerium oxide, for example) sprayed onto a rubber membrane (a rotating polishing pad). Loose abrasives induce rather less subsurface damage than fixed abrasives. As a rule of thumb, one tries to remove material to a depth three times that of the damage layer. It is important to remove as much subsurface damage as possible. Microcracks and defects well below the surface can lower the strength of optical substrates by providing an abundance of nucleation sites that can propagate catastrophically if the part is under transient stress. Macroscopic cracks have appeared in many large telescope optics during installation and have needed emergency repair as a result [**9**].

It is never possible to remove all the damage if the act of removing it induces further damage. Plasma etching offers alternative, nonabrasive, ways of removing the damage layer.

2.6.1 Ion Beam Figuring

Ion beam figuring (IBF) has been widely used as a final figuring technique in the production of large telescopic optics. Its use has been proposed for projects such as the E-ELT, mentioned in chapter 1. It removes material from a surface by sputtering with high-energy argon ions. By controlling the shape of the ion beam and the dwell time it has been used to correct surface errors of millimetre spatial size range to within a few nanometres in the vertical direction. Such precision is very difficult to achieve using only mechanical polishing.

The use of ion sputtering for the figuring of optics was instigated in the late 1980s. In 1987, Wilson and McNeill demonstrated the potential of IBF by correcting the figure of 300 mm diameter flat samples of fused silica, Zerodur and copper using a prototype machine [**112**]. In the case of the fused silica optic, the peak-to-valley was reduced from 1.1 μm to 0.7 μm. A 1" diameter beam was used, operating at an ion energy of 1.5 keV and a beam current of 40 mA. The etching process lasted five hours (the time in which the beam was switched on). IBF was subsequently adopted by the Eastman Kodak Company and they set up the Ion Figuring System (IFS), a dual chamber system

capable of operating upon parts of maximum size 2.5 m × 2.5 m × 0.6 m. Trial experiments on a 0.5 m diameter ULE optic were reported by Allen and Romig [**113**]. In the same article, tests were discussed in which the ion beam was rastered over a lightweight fused silica optic to achieve 'neutral removal' (this is discussed in section 2.7). Temperatures were measured under the front surface, at the centres of square-shaped pits that had been machined into the underside, using thermocouples to identify any impact on the optic's structural integrity due to the ion beam. Temperatures up to 125°C were measured. Sharp temperature fluctuations of 30°C were measured whenever a plasma passed overhead. These fluctuations were larger than expected and might have been damaging to the small optic used in this test. However, no evidence of damage was seen in the ∅0.5 m mirror. In 1991, Allen *et al.* at Kodak reported surface error correction on one of the Keck Telescope's 1.8 m Zerodur sections [**114**]. In 1992, Allen *et al.* reported the etching of a ULE mirror 'petal' of 0.65 m^2 area using IBF [**115**]. The surface was rastered[19] four times using 3 different beam diameters (Ø15 cm, Ø8 cm and Ø5 cm). Between each iteration the surface height was measured using a Fizeau interferometer and the ion beam was programmed to move more slowly (dwell) over the higher regions. The peak to valley (P-V) error was reduced from 5.040λ to 0.171λ. The rms (root mean square) error was reduced from 0.620λ to 0.015λ. The four iterations took 95 hours to complete in total.

C. Egert [**116**] in 1999 discussed how the surface roughnesses of various materials evolved as a result of ion beam figuring. It was found that the surface roughnesses of fused silica, single crystal silicon, germanium, electroless nickel, sapphire and polycrystalline CVD silicon carbide did not increase significantly when depths shallower than <5 μm were removed. Fused silica showed no increase in roughness when depths up to 23 μm were removed. The roughnesses of aluminium and copper surfaces did increase significantly, by several tens of nanometres per micron removed.

Kurushima *et al.* [**117**] in 2008 described measurements they made of the surface roughness of substrates while being etched using an argon ion beam with the aim of developing the "next generation" of extreme ultraviolet lithography (EUVL) systems. Mechanically polished surfaces of ULE with an rms roughness ~0.1 nm were machined to a depth of 50 nm using a focused ion beam ~0.5 mm in diameter. Measurements of the mid-spatial frequency roughness (MSFR, spatial features of periods between 1 mm and 1 μm[20]) were made using a white light interferometer and the high spatial frequency roughness (HSFR, spatial features of periods between 1 nm and 1 μm) using an atomic force microscope. Figure 2.45, shows how these roughnesses changed when being etched with ion beams of different ion energy. The MSFR remained more or less unchanged at all ion energies. However, the HSFR did increase, and increasingly so at higher ion energies.

[19] By rastering, one understands that the tool (ion beam) is moved in a zigzag fashion so as to remove material over a wide area.

[20] Mechanical grinding and polishing tend to imprint very fine periodic peaks and valleys on a surface profile, resulting from the manner in which the grits remove material. Such repeated features can have a characteristic distance, a "period", the reciprocal being known as the "frequency". A surface profile might contain a superposition of many repeated features that can be separated by Fourier analysis.

The same group carried out similar work on Zerodur surfaces a year earlier [**118**] and found that those surfaces roughened due to the difference in MRR between silica and the grains of β-quartz solid solution of size ~100 nm. Their target was to keep the HSFR below 0.15 nm, which was achievable using a 3 keV beam on ULE. When a 3 keV beam was applied to Zerodur, the achieved HSFR was 0.44 nm.

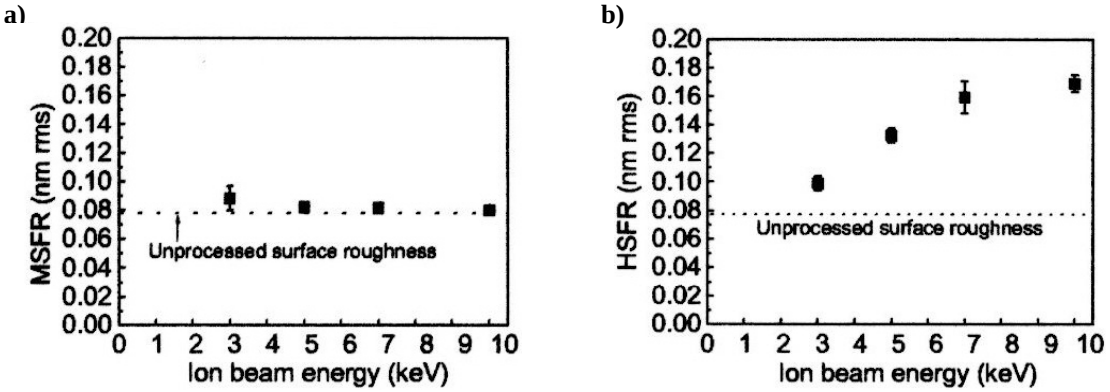

Figure 2.45 **a) The mid-spatial frequency roughness (MSFR) and b) the high spatial frequency roughness (HSFR) measured on a ULE surface following ion beam etching with different beam energies. The dotted line on both graphs represents the surface roughness of the unprocessed ULE surface [117].**

Gailly *et al.* [**119**] in 1999 described investigations they had performed regarding thermal effects in small BK7[21] and Zerodur optics as a result of ion beam figuring. The surface profiles of circular samples (∅105 mm × 12 mm) were measured using an interferometer before and after etching the surfaces with a static ion beam. As expected, Gaussian removal profiles were measured at the centre of the discs. However, in the case of BK7, thermal distortion around the sample edge caused the shape to change from concave to convex. Temperature measurements of the surface being etched were made using an infrared camera. The highest temperature measured on the Zerodur surface was about 150°C (work by other authors showed that thermal distortion in Zerodur becomes apparent at temperatures above 180°C). Measurements were also made using thermocouples positioned a few millimetres under the surface. Using a thermal imaging camera, temperature profiles were measured and gradients as high as 40°C/cm were recorded. The importance of being able to tune the ion beam parameters in order to achieve a suitable compromise of maximising the etching rate without overheating the sample was highlighted.

One way to remove material more quickly over a large area but to keep the ion energy low and minimise surface heating is to use a broader beam. At the Leibniz-Institute for Surface Modification in Leipzig, a 200 mm diameter argon ion beam from a Kaufmann drive has been used with the aim of figuring large optics with areas ~1 m^2. In 2004, Frost *et al.* demonstrated that it is possible to actually lower roughness of surfaces of quartz glass and silicon using a technique known as ion beam direct smoothing [**120, 121**]. In ion beam direct smoothing, relaxation mechanisms in the development of surface topology during ion beam erosion are exploited. On silicon they were able to reduce the Rq (rms roughness) from 2.1 nm to <0.2 nm with an ion

[21] BK7 is a highly homogenous and transmissive borosilicate crown glass, very commonly used in precision optics.

beam energy of 500 eV, inclined at 45° from normal incidence after an hour of etching. On quartz, the Rq was reduced from 0.45 nm to 0.11 nm over a scanned area, 1 μm × 1 μm in size, with an ion beam energy of 600 eV, at normal incidence, after removing material to a depth of approximately 300 nm.

IBF has proved to be a very useful tool for the fine figure correction of large telescopic optics and the possibility of using sputtering to actually improve surface roughness after polishing is a tantalising prospect. However, the slow material removal rate and the need to operate in a vacuum (<0.001 atm) make it currently the slowest phase in the production line when fabricating very large optics. It is also not completely effective at removing residual subsurface damage that remains after polishing as high-energy ions can themselves induce additional damage.

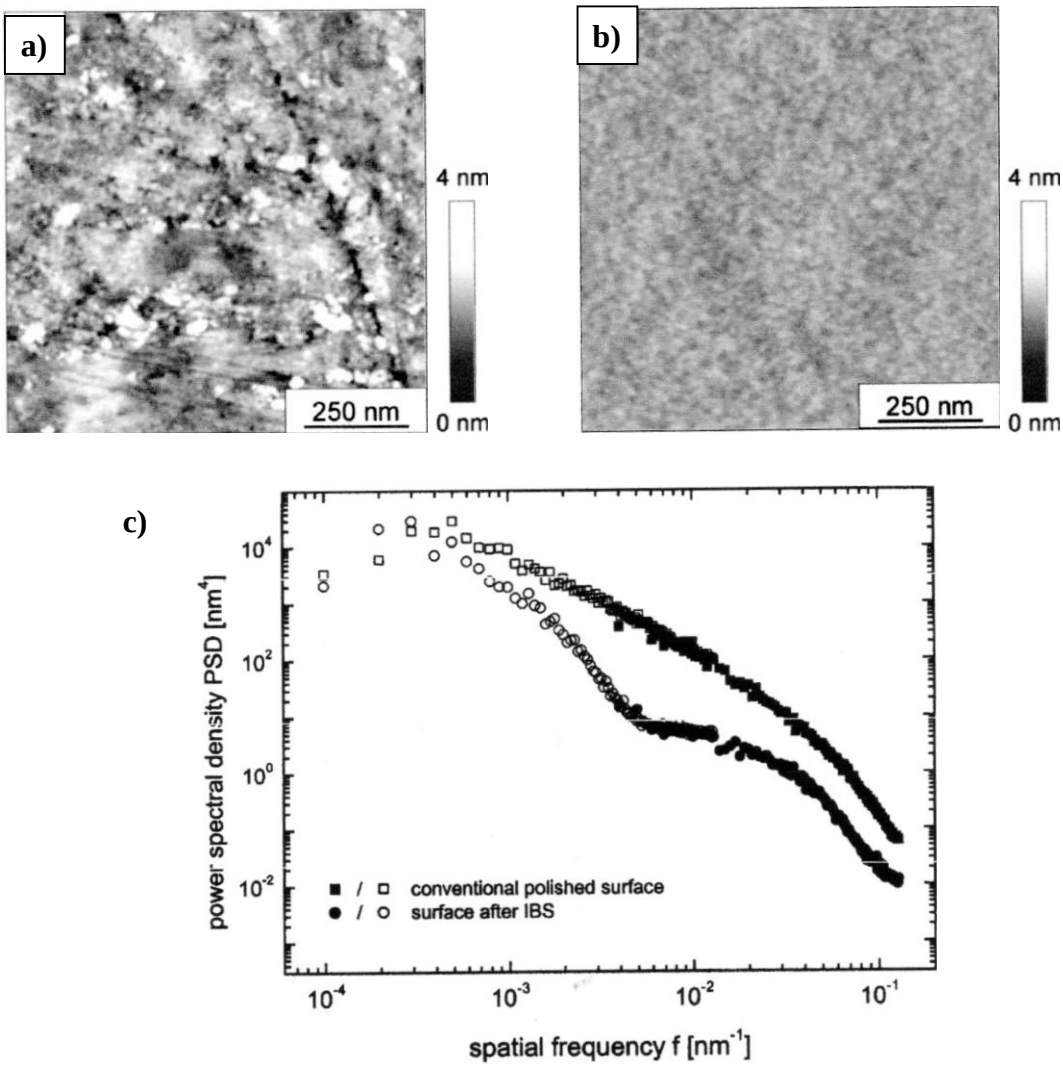

Figure 2.46 **AFM images of quartz glass surface a) before and b) after ion beam direct smoothing (ion energy 600 eV, normal incidence, ~300 nm etch depth). c) Angular averaged power spectrum density (PSD) functions before and after smoothing. The PSDs are calculated from the height images by taking a Fourier transform. These images and graphs were taken from [120].**

2.6.2 Reactive Ion Beam Etching

In the case of reactive ion beam etching (RIBE), chemically reactive gases are added to the ion beam to instigate ion-enhanced energetic etching. This increases the selectivity of the etching and can lead to much higher etch rates. As mentioned in section 2.5.3, RIBE has been used successfully in the semiconductor industry. Frost *et al.* reported experiments in which semiconductors indium arsenide (InAs) and indium antimonide (InSb) were etched using argon-nitrogen mixtures [**122**]. Using pure nitrogen they managed to reduce the Rq of surfaces of these materials from 0.4 nm ± 0.1 nm to 0.2 nm ± 0.1 nm, even over extended etch periods.

Significantly higher material removal rates can be achieved using RIBE than using IBF. However, the general opinion is that this benefit is outweighed by the increase in system complexity [**4**].

2.6.3 Magnetorheological finishing

A magnetorheological fluid consists of spheres of magnetic material that are <1 μm in diameter, suspended in a carrier liquid whose viscosity greatly increases in the presence of a magnetic field and becomes quasi-solid. Magnetorheological fluids were first used as a polishing tool in Minsk in the late 1980s. The fundamentals of the process were adopted by The Centre for Optics Manufacturing (COM) in 1994, and subsequently magnetorheological finishing (MRF) was developed. MRF is a novel method of optics figure correction in which a magnetorheological fluid is sprayed onto a spinning wheel to create a "ribbon". A dc magnetic field is used to stiffen the fluid in the contact region so that it can abrade material away. The first commercial MRF machine was developed by QED Technologies in 1998. The magnetorheological fluids used in this process most commonly contain carbonyl iron spheres and non-magnetic abrasives, such as cerium oxide, suspended in water [**123**].

MRF has proved to be very successful for figure correcting precision optics and material removal rates up to 10 μm/minute have been claimed on optical glasses with a spot area 10 mm × 15 mm (~1 mm^3/minute). A fivefold increase in material removal rate has been predicted. MRF is able to maintain rms surface roughness down to ~1 nm. MRF's advantages as a tool for removing material from large optics and lightweight optics were reported by Shorey *et al.* [**124**]. The material removal rate is relatively insensitive to errors in the vertical positioning of the optic, so it is highly deterministic. Details of experiments in which quilting errors (features introduced by previous polishing steps or by gravity/cryogenic effects) in lightweight optics were removed using MRF are included. QED currently supply machines for figuring optics up to 400 mm across; larger machines are under development [**4**, **123**, **124**].

As the material removal method is abrasive, it is possible that MRF might incur additional subsurface damage.

2.6.4 Atmospheric plasma etching methods

Ion beam figuring and reactive ion beam etching have to be operated in a vacuum. In the mid-1990s, the development of alternative plasma figuring techniques started that use atmospheric pressure (thermal) plasmas. Such techniques include Plasma Jet Machining (PJM), developed at the Leibniz-Institute for Surface Modification [**125**], Plasma Chemical Vaporization Machining (PCVM), developed at Nikon [**126, 127**], and Atmospheric Pressure Plasma Polishing (APPP) [**128**], developed at the Harbin Institute of Technology in China. In all instances, a fluorinated gas is atomised by the plasma such that fluorine radicals can chemically attack the surface, as described in section 2.5.2. Their ability to remove subsurface damage is greater than that of IBF. These techniques have yet to be applied to large optics (> 0.25 m^2).

A pencil-shaped argon plasma with carbon tetrafluoride (CF_4) used for plasma jet machining is shown in figure 2.47. Such a plasma has been shown to produce removal profiles which are close to Gaussian in shape (see figure 2.47c). Arnold *et al.* [**125**] expressed the importance of minimising the heat flux when etching thermally insulating materials, such as fused silica or ULE. It has been made possible to reduce the gas temperature to below 50°C using pulsed microwave excitation. For situations where it is not practical to reduce the gas temperature, a comprehensive model has been developed to account for the time-evolving temperature distribution.

In 2008, Yamamura *et al.* reported experiments aimed at improving the flatness of quartz crystal wafers, made to be used in quartz resonators, by means of NC-PCVM (Numerical Control Plasma Chemical Vaporization Machining) [**127**]. In this process, a wafer was moved underneath a stationary electrode using a numerically controlled motion stage. A helium plasma was used with CF_4 and oxygen. The photograph in figure 2.49 shows the plasma over a quartz crystal wafer. Its effectiveness at improving surface form is shown in figure 2.50. As was mentioned in section 2.5.2, oxygen can be very useful in improving the etch rate of fluorinating precursors. They found that the optimum O_2/CF_4 ratio was about 0.2 by volume. In a spectroscopic experiment, the intensity of the atomic fluorine emission line at 739.8 nm was greatest when the ratio was 0.2. In the same article, the depths of trenches created in quartz crystal resulting from a single pass at a constant speed through the plasma were reported. They found that the trench depth was proportional to the inverse of the scanning speed (the speed at which the motion table was moved underneath the plasma). This is what one would intuitively expect, because if the scanning speed were halved, a given point on the surface would be exposed to the plasma for twice the period. In earlier work, the same authors did similar work on quartz glass [**128**]. In that instance, they found that the relationship was non-linear (see figure 2.51b). They attributed this to the fact that the thermal conductivity of quartz crystal is 10.4 $Wm^{-1}K^{-1}$, which is much greater than that of quartz glass (1.47 $Wm^{-1}K^{-1}$). Therefore, when etching trenches on quartz glass, the surface temperature rises to a higher value than when etching quartz crystal; this increased local heating increases the etch rate at that position.

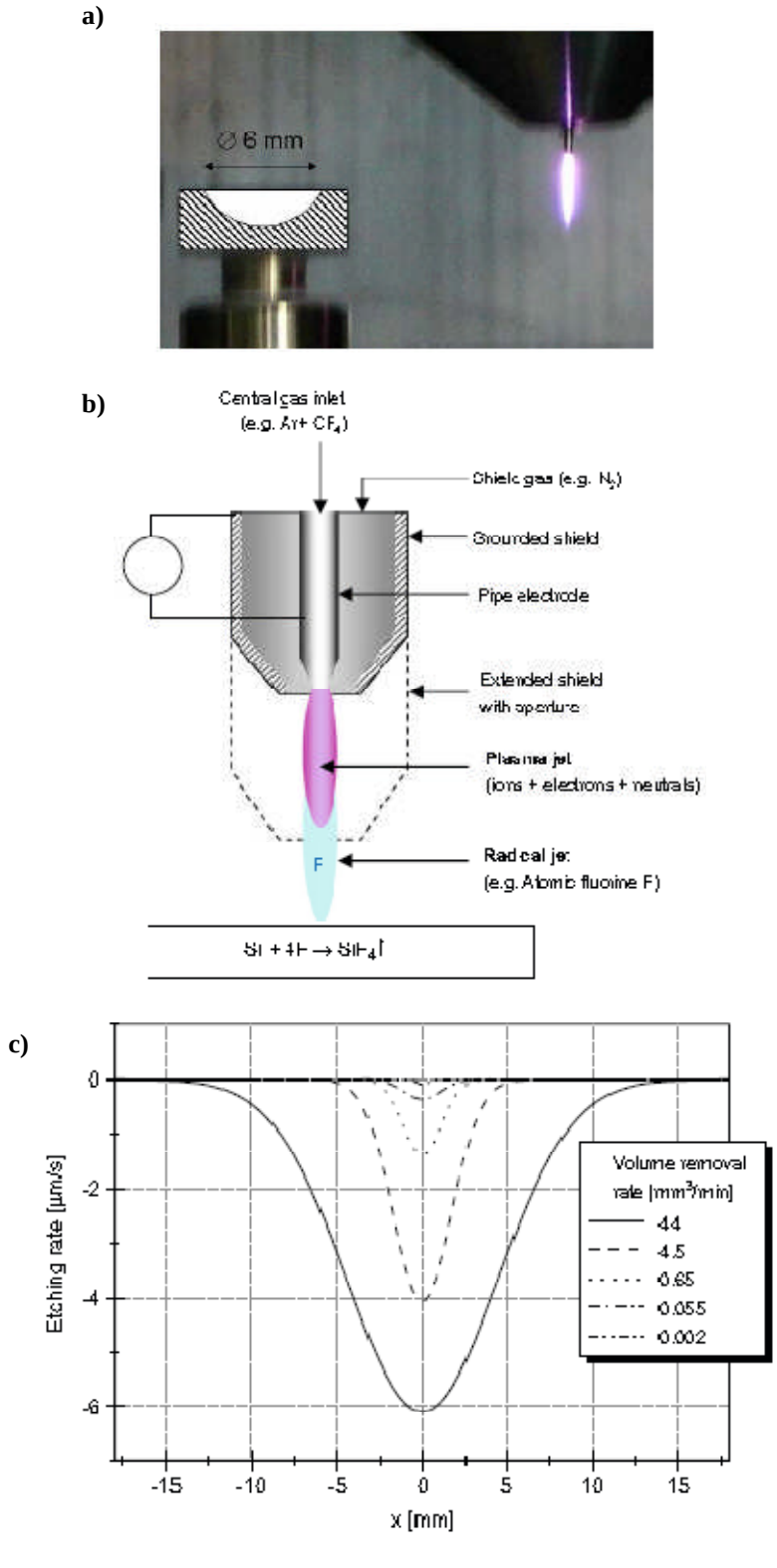

Figure 2.47 **Plasma jet machining (PJM), developed at the Leibniz-Institute for Surface Modification, has been used for the fine figuring of small optics with surfaces bearing exotic aspheric forms. a) The plasma, b) schematic diagram, c) A variety of Gaussian removal functions can be achieved with full width at half maxima as fine as 370 µm [125].**

Figure 2.48 **A lens being etched using PCVM; a plasma is created at the tip of an electrode within a chamber containing SF_6 and helium at atmospheric pressure. According to Nikon, this process has achieved a form accuracy better than 0.1 µm, and an Ra (arithmetically averaged surface roughness) better than 0.5 nm [126].**

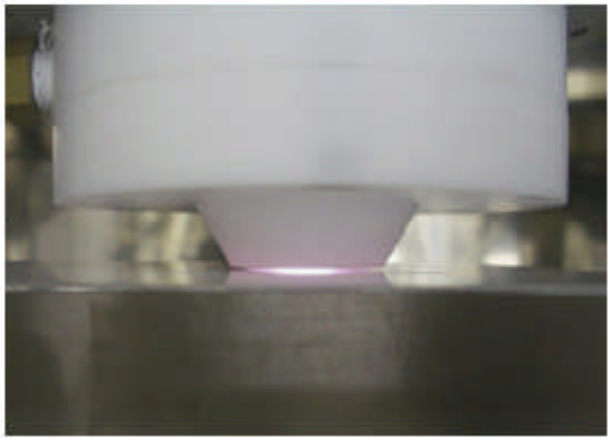

Figure 2.49 **A quartz crystal wafer being etched using NC-PCVM. The electrode is held between 0.1 mm and 0.5 mm away from the wafer surface, behind an insulating shield of Teflon [127].**

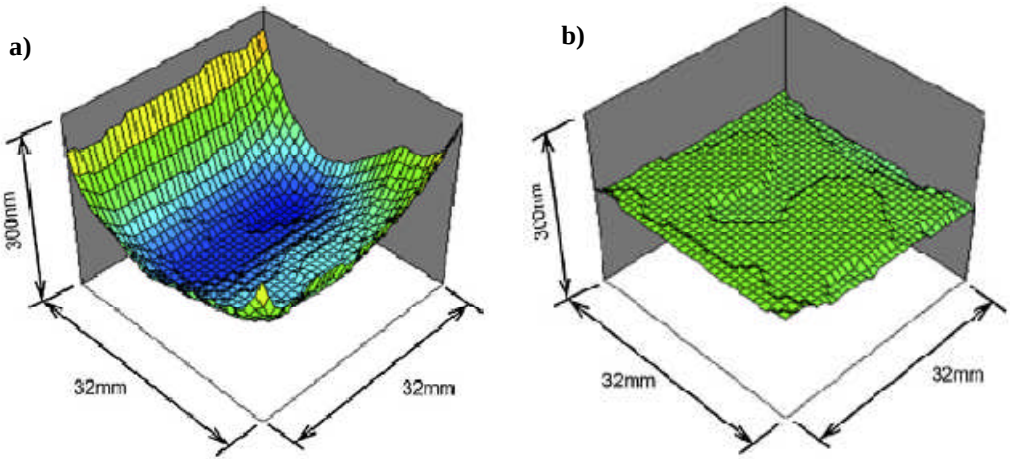

Figure 2.50 **The surface height maps of an AT quartz crystal wafer a) prior to NC-PCVM and b) after NC-PCVM [127]. The peak-to-valley was improved from 245 nm to in 49 nm.**

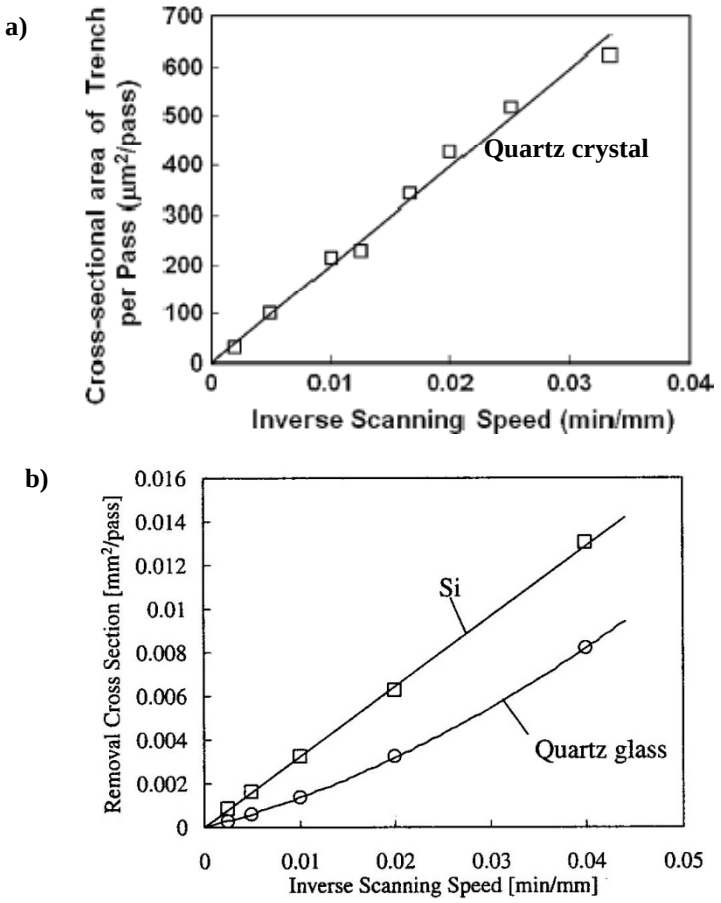

Figure 2.51 **a) The cross-sectional area of trenches etched upon quartz crystal using NC-PVCM as a function of the inverse scanning speed, taken from [127]. b) The cross-sectional area of trenches etched upon silicon and upon quartz glass using NC-PVCM as a function of the inverse scanning speed, taken from [128]. The non-linear relationship in the case of quartz glass is believed to be due to its low thermal conductivity.**

APPP is the newest of the three aforementioned atmospheric plasma processes. The principles of the process and the results of early experiments were reported by Zhang *et al.* in 2007 [**129**], although specific details about the plasma torch and exact experimental details are limited. They developed a capacitively-coupled atmospheric plasma torch in house. A capacitively-coupled plasma is a similar to an ICP, but it has an electrode along its central axis. They used helium as the plasma gas and carbon tetrachloride as the precursor. It was designed to remove material over a broad area (50 mm in diameter). In [**129**] the plasma is described as being "cold", and therefore does not overly heat the sample. On single crystal silicon, they achieved a removal rate of 32 mm^3/minute. The maximum temperature measured on the wafer was 90°C. They managed to improve the surface's roughness; the Ra was reduced from 1.76 nm to 0.63 nm. The plasma was analysed spectroscopically and the existence of fluorine radicals in the plasma was confirmed (see figure 2.52).

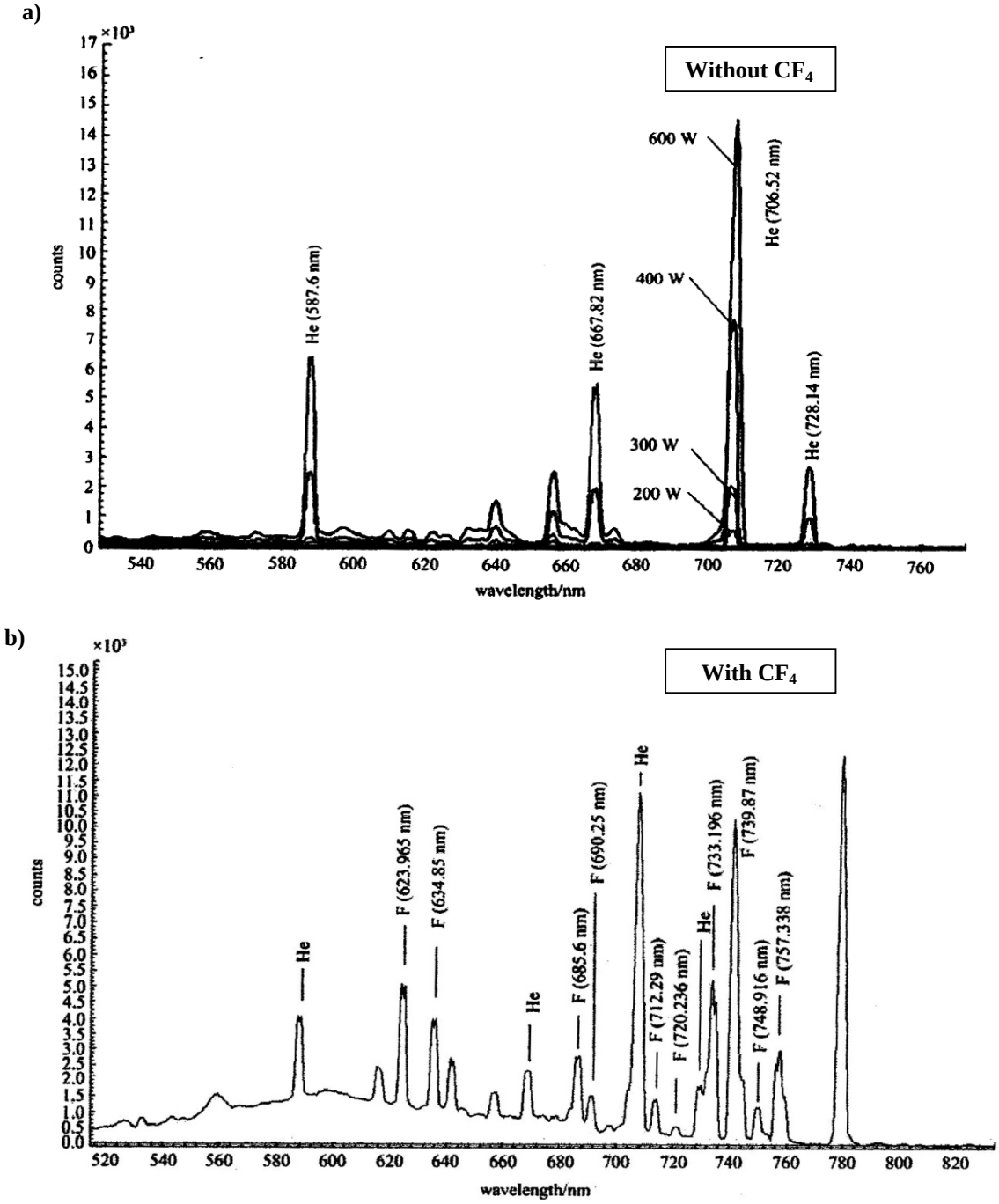

Figure 2.52 **A helium atmospheric capacitively coupled plasma was analysed spectroscopically a) without CF_4 using 4 different plasma powers and b) with CF_4. The existence of fluorine emission lines in the spectrum with CF_4 indicates the existence of fluorine radicals, which can react with the substrate material from [129].**

The plasma chemical etching process to which the remainder of this thesis is devoted is the Reactive Atom Plasma® process. The RAP process was developed by RAPT^{TM} Industries, a spin-off company from the Lawrence Livermore National Laboratory in California, founded in 2001. RAPT Industries have developed the process principally for removing subsurface damage from silicon carbide optics used in defence, aerospace and semiconductor applications.

The RAP process uses an inductively coupled argon plasma. The reactive gas becomes atomised within the coil zone of the ICP in the same way that the analyte would be in a spectrochemical ICP. In the first instance carbon tetrafluoride (CF_4) was the chemical etchant of choice. However, higher removal rates can be obtained when using nitrogen trifluoride (NF_3) and sulphur hexafluoride (SF_6) as their enthalpies of atomisation are lower (bond energies are listed in table 2.3). It has been shown experimentally that the "apparent" activation energy for the dissociation of NF_3 into NF_2 + F is a mere 125.9 kJ/mol [**130**]. As a result, NF_3 should be >80% dissociated into NF_2 + F, as it passes through the coil zone, where the temperature is expected to be in excess of 8000°C.

SF_6 can be synthesised very easily using sulphur vapour and fluorine gas. NF_3, on the other hand, cannot be synthesised using nitrogen and fluorine gases and, as a result, is very much more expensive. Commercially it is usually synthesised by the reaction of ammonia and fluorine in the presence of molten ammonium fluoride [**131**].

As with IBF, the removal profile is Gaussian. It readily etches quartz, silica and silicon. It can be used to etch silicon carbide but the material has to be preheated to at least 200ºC for it to work.

Table 2.3 Properties of CF_4, NF_3 and SF_6 (*at 293K and 1 atm pressure) [131 - 133].

	CF_4	NF_3	SF_6
Bond energy (kJ/mol)	485	277.8	285
Boiling point (°C)	-126	-129.1	-50.8
Density* (kg/m^3)	3.63	2.97	6.15
Viscosity* (μPs)	17.0		26.6

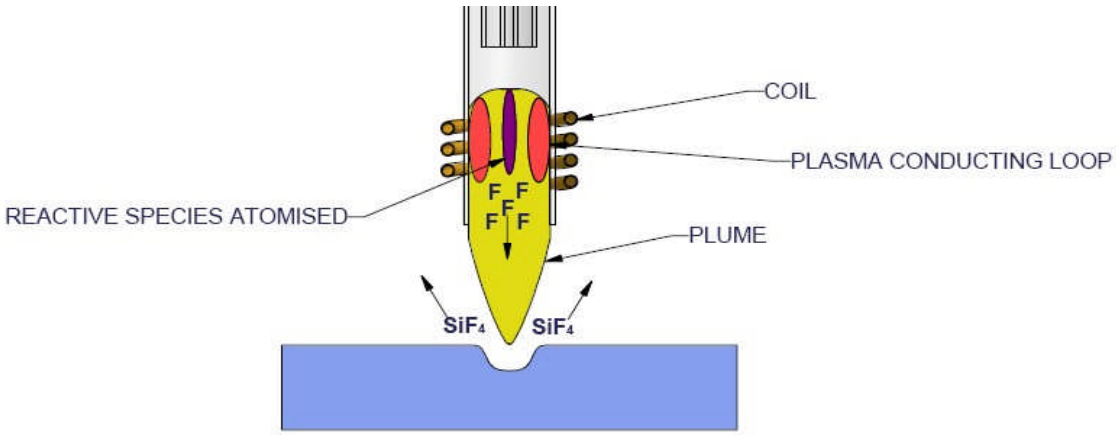

Figure 2.53 The RAP process uses an atmospheric argon ICP, into which a fluorine-containing gas is added. Gases are atomised so that fluorine radicals and chemically attack the target material. The removal profile has a Gaussian shape.

2.7 Early research on RAP

At the time of writing, only a modest number of publications exist regarding RAP. In 2006, Verma *et al.* of RAPT industries reported the ability of the process to remove subsurface damage in fused silica and silicon carbide [**9**]. Thin discs of those materials (∅75 mm × 2 mm) were ground on one face, some with a 3 micron fixed diamond abrasive lap and others with a 9 micron fixed diamond abrasive lap. This resulted in the shape of the opposite face becoming more convex, an effect known as the Twyman effect[22]. The amount of surface stress is proportional to the size of the deflection. Material was subsequently removed from the ground side using RAP, in layers 2 μm thick at a time. After each removal, the shape of the unground faces were measured and, after a few iterations, their shape returned to what they were originally, indicating a reduction in stress. CF_4 was the etchant used in these tests. The results are displayed graphically in figure 2.54. Although it is evident that the process is able to alleviate subsurface damage in silicon carbide that results from previous grinding, these tests do not prove beyond any doubt that no additional damages is added. It nonetheless demonstrated that RAP, still an embryonic process, had considerable potential.

The first article describing research at Cranfield University on RAP was published in 2005 and discussed the first trials on ULE [**135**]. Large material removal rates were obtained without preheating the samples. NF_3 was the etchant gas. These were also the first tests performed using the 300 mm prototype machine (described in section 3.1). Removal profiles were determined by passing samples through the plasma at a constant speed so as to etch a trench (on this machine the plasma is stationary). The sample travel speeds used ranged between 600 and 2400 mm/minute. Material removal rates up 0.55 mm^3/s were demonstrated. The removal profiles were found to be Gaussian. There was little variation in the widths of the trenches; the mean FWHM of the trenches was 17.5 mm and standard deviation was 1.4 mm. In the article it is stated that the relationship between trench depth along the centre line and travel speed "*appears to be exponential*", although no analysis is shown in the article to support this claim. It would be more logical to expect that the trench depths would be proportional to the reciprocal of the travel speed, as was reported for PCVM on quartz crystal in [**127**] (see figure 2.51a). However, as the thermal conductivity of ULE is very low (1.31 $Wm^{-1}K^{-1}$), there might be deviations from the expected linear relationship.

Tests were performed with the NF_3 concentration set to either '10%' or '20%', corresponding to NF_3 flow rates of 40 sccm and 80 sccm respectively[23]. Additionally, tests were carried out with two different torch powers, 1250 W and 1500 W. The material removal rates were significantly higher when using the higher concentration, as can be seen in figure 2.55, though it did not quite double the MRR. Even so, the increased NF_3 concentration proved to be more effective at increasing the removal rate than the increased power.

---

[22] Twyman describe the effect in these words, "*If a very thin piece of glass, grey on both sides, be polished so that it can be examined through its thickness and polarised light be applied, stress can distinctly be seen near each surface; if now one side be polished strain disappears from that surface, and the glass bows up on polishing the remaining grey side, the glass becomes parallel again, and strain entirely disappears.*" [**134**]

[23] NF_3 is normally supplied in gas bottles, heavily diluted in argon. The percentage refers to the relative proportion of NF_3 in argon by volume.

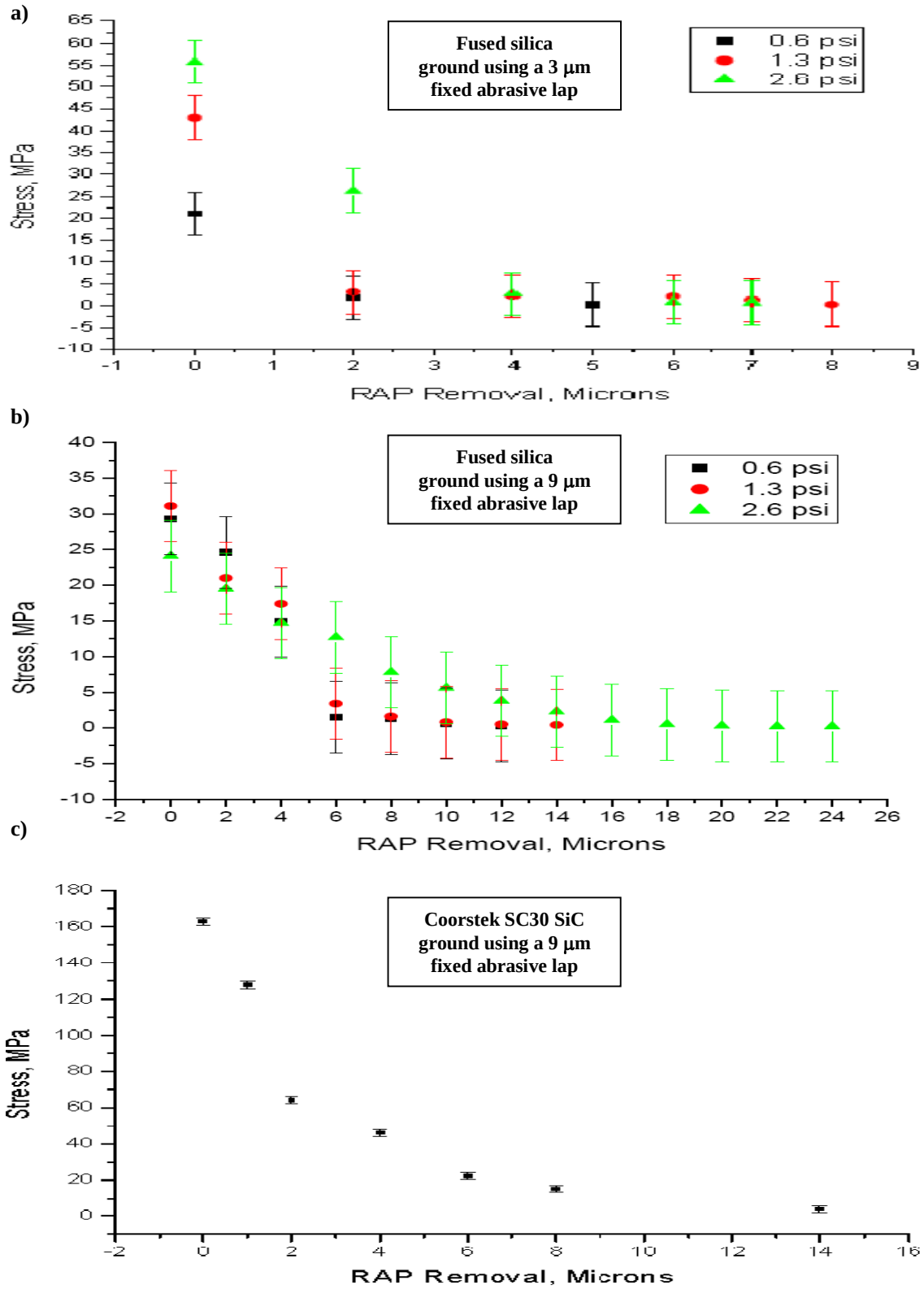

Figure 2.54 **Results published by Verma *et al.* [9]. a) Residual stress in fused silica glass ground using a 3 µm fixed abrasive lap under various pressures versus the material removal depth by RAP processing. b) as a) but ground using a 9 µm fixed abrasive lap. c) Residual stress in Coorstek SC30 SiC ground using a 9 µm fixed abrasive lap vs. RAP removal depth.**

Fanara *et al.* also carried out simple temperature measurements using a pyrometer while ULE samples were moved through the plasma [**135**]. Figure 2.56 shows how the measured temperature on a ULE surface at the position where the plasma happened to be located varied as the sample was moved through the plasma. The two peaks in each graph display the results at two different speeds. Both temperature profiles peak at the same temperature, implying that the level of heating is insensitive to the NF_3 concentration. It was deduced that the amount of heating resulting from the chemical reactions are negligible compared to that resulting from plasma.

The fact that high material removal rates can be achieved on ULE without any preheating is particularly advantageous when manufacturing large optics. To uniformly warm an object of area >1 m^2 that is made of a material of low thermal diffusivity ($7.9 \times 10^{-7} m^2/s$) would be extremely difficult.

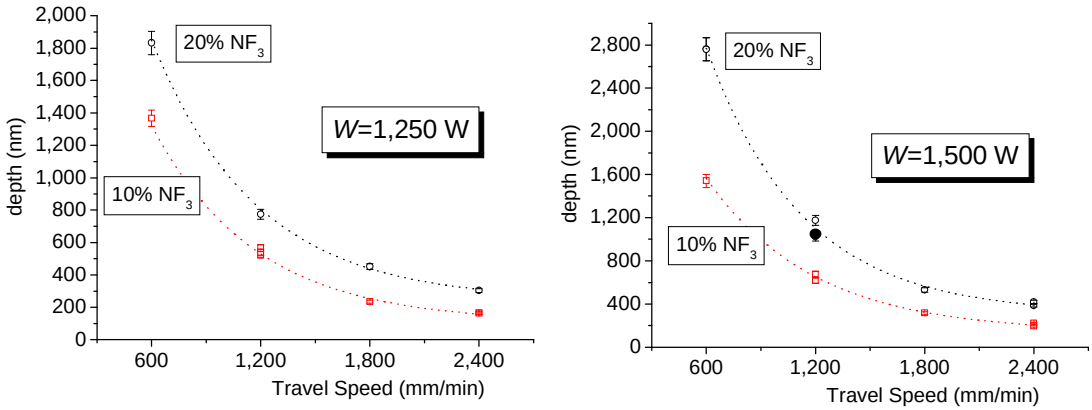

Figure 2.55 **The depths of single trenches are plotted against the travel speed for tests in which two different NF_3 concentrations and two different torch powers were used [135].**

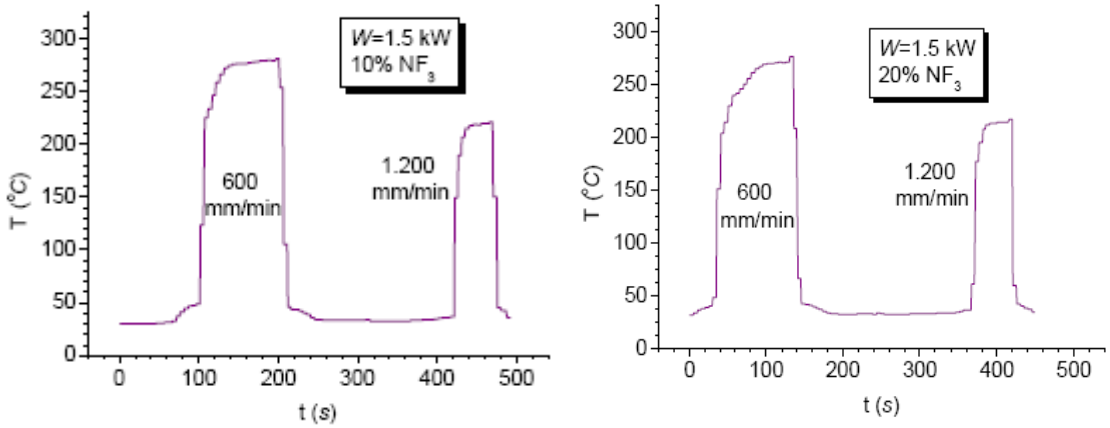

Figure 2.56 **Two graphs showing how the sample temperature increased as it was moved through the torch. In both instances, two passes were made at different speeds, producing the two peaks [135].**

2.7.1 Neutral removal

As any etching plasma has a diameter that is invariably smaller than the optics being etched, merely etching a pit or a trench with a Gaussian cross-section onto a substrate material is of little use in itself. To remove a layer of material from a surface over a wide area of equal depth everywhere (neutral removal) it is normal to raster the surface at a constant speed, so that the plasma remains over every point on the surface for the same period of time. The simplest rastering scheme is to move the plasma over the surface in a simple zig-zag or serpentine path as illustrated in figure 2.57a. It is fairly easy to show that if the removal function is a perfect Gaussian, even with a rather coarse 'pitch', a very flat surface can be attained as illustrated in figure 2.58. It goes without saying, perhaps, that it is never possible to achieve such perfection in practice.

Alternative rastering schemes exist to reduce the amount of heat imparted to any one area of the surface at any one time. One scheme is staggered rastering, illustrated in figure 2.57b. A staggered path is made up by a series of zig-zags with a larger pitch (known as the 'stagger') and successive zig-zags are displaced from each other by a smaller distance (known as the 'step'). For the passes to be equally spaced, the stagger must be an exact multiple of the step. In both examples shown in figure 2.57, 36 passes are made separated by 2 mm over an extent of 70 mm. The passes are just made at different times. Other schemes have also been devised, such as crosshatched rastering, in which passes are made across the sample in orthogonal directions.

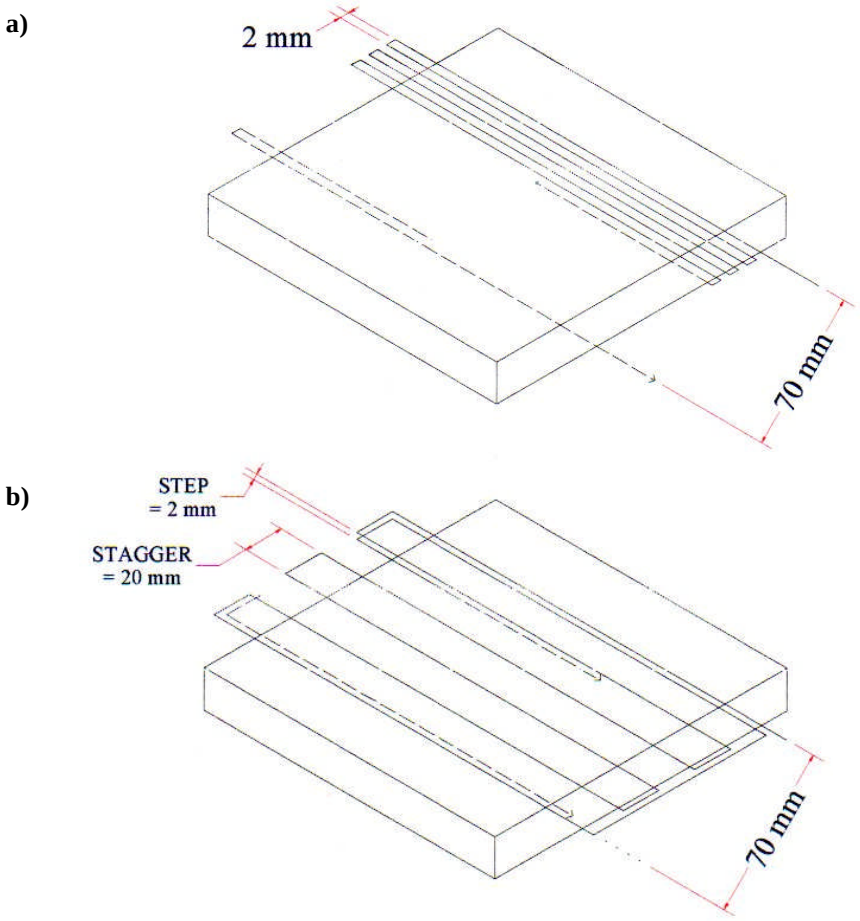

Figure 2.57 **The path that the plasma makes over the sample in a) a serpentine rastering path and b) a staggered rastering path.**

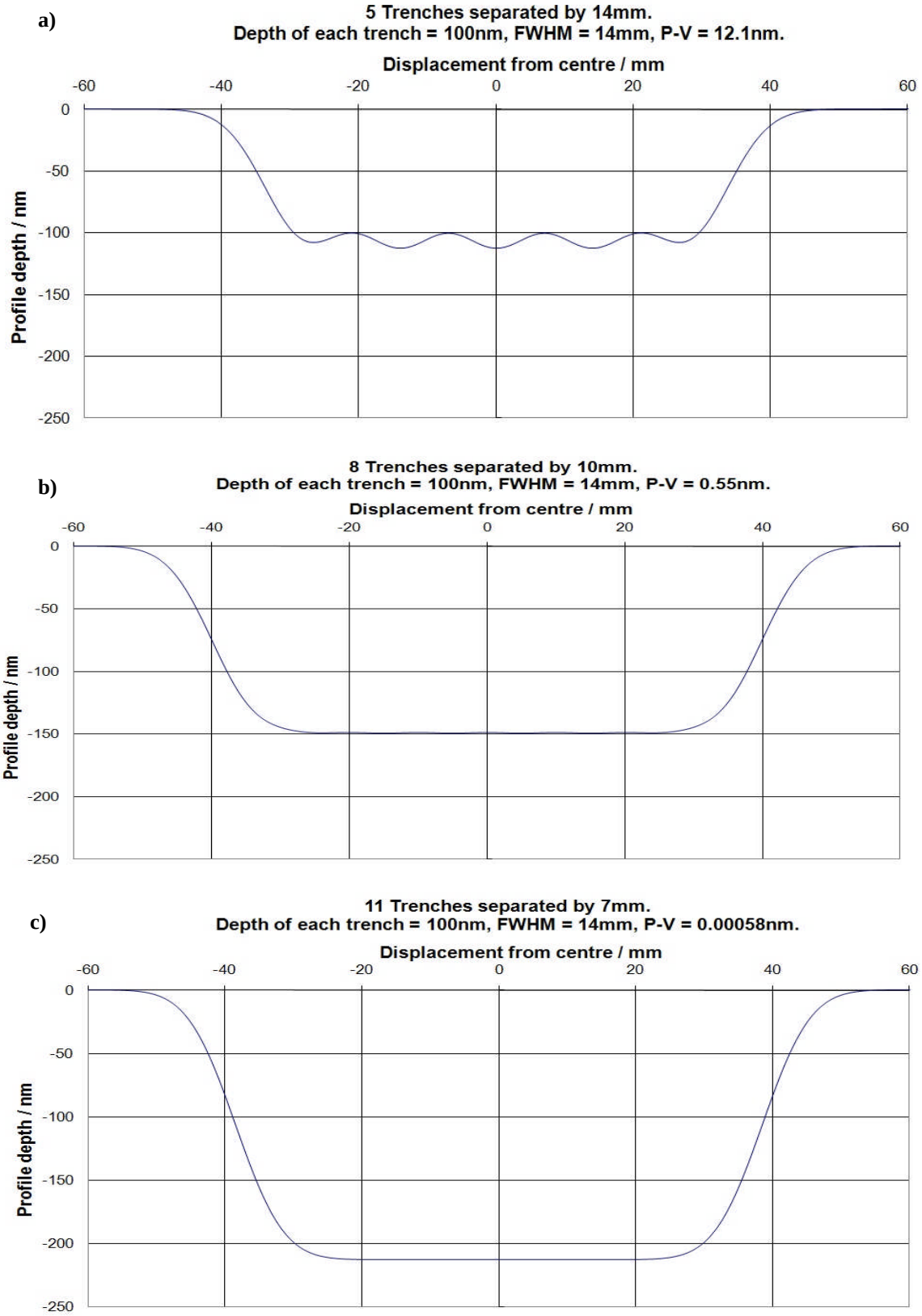

Figure 2.58 Computed profiles showing the results that one might expect to see from rastering tests if the removal profile were a perfect Gaussian of identical shape each time. Even with a pitch of 7 mm, which is fairly coarse, the peak to valley (P-V) along the base of the trench is negligible.

Neutral removal tests have been performed at RAPT Industries on silicon carbide using both serpentine and staggered rastering schemes. The base of an extended trench created by serpentine rastering bowed up, whereas that produced by staggered rastering was much flatter, as indicated by the graphs in figure 2.59.

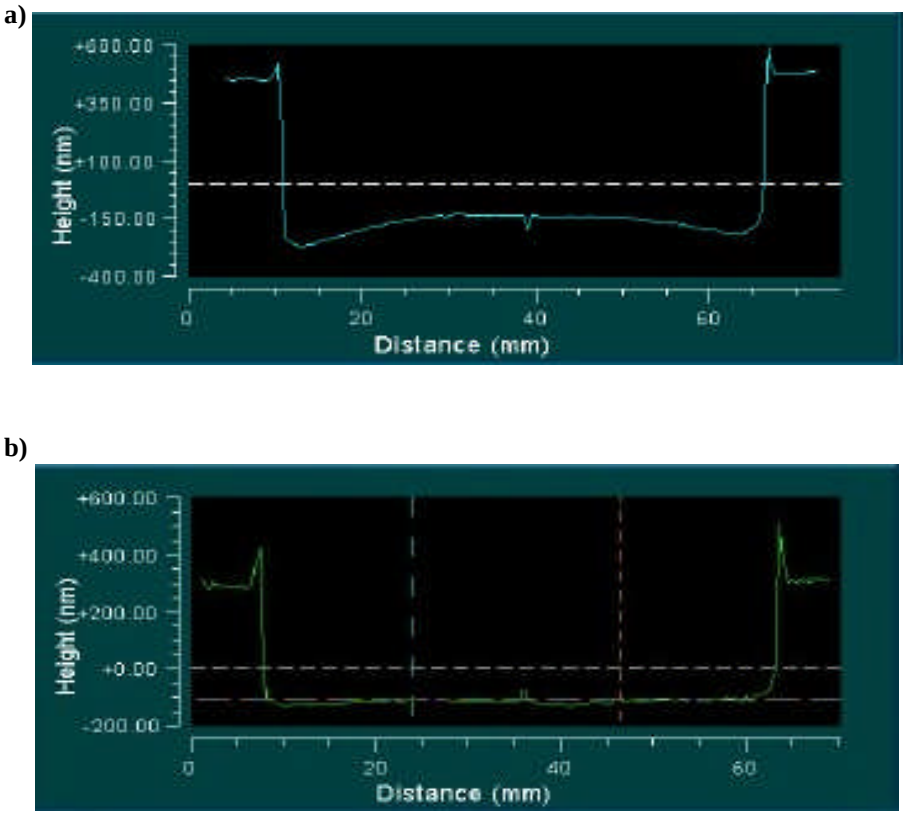

Figure 2.59 **Cross-sections through trenches on silicon carbide produced through a) a serpentine rastering algorithm and b) staggered rastering [136].**

Since the inception of the RAP process, RAPT Industries have refined the plasma torch. On the most recent version an aperture exists at the exit of the torch. The FWHM of the removal function depends on the size of aperture used. Reducing the diameter of the aperture gives the operator more control when suppressing surface features of smaller spatial size. Currently, the available FWHMs of the removal or profile are 12 mm, 50 mm and 25 mm. It is intended that for some future systems that the aperture be brought down to just 25 μm [**137**]. The aperture is made of copper and is designed to absorb some of the heat from the plasma gas. Subrahmanyan and Gardopee also reported on the ability of the process to figure the edges of large mirrors [**137**]. Grinding and polishing the edges of the substrate is often problematic as part of the tool frequently overhangs the edge. On a silicon carbide paraboloid mirror 150 mm across, they were able to perform figure correction right out to the edges and correct for edge roll from previous material removal processes.

3 Instrumentation

3.1 RAPT300 machine

The RAPT300 prototype machine was installed at Cranfield University in 2005. All of the research discussed hereafter is based on work done using this machine. The RAPT300 has been used for process characterisation and for diagnostic purposes and is able to accommodate flat workpieces that are 300mm wide and/or long or smaller. The plasma torch is stationary near the centre of the chamber. The sample workpieces are mounted on a precision motion stage and are moved through the plasma plume. Although the plasma torch stays still and the sample moves, in discussion it is often more convenient to talk about the torch moving relative to a stationary part. The term "torch travel speed" is used to describe this motion.

Figure 3.1 shows schematic views of the machine and various photographs are displayed in figure 3.2 on subsequent pages. The flow of the argon and the reactive gases into the system are controlled using mass flow controllers. A mass flow controller contains a mass flow sensor and a proportional control valve, which is used to set the desired output flow. An Allen Bradley PLC (programmable logic controller) controls the power supply, tesla ignition coil, sample stage heater and mass flow controllers. Although this has a user interface, it is more convenient to use the NView software program on the integrated computer. The motion stage is controlled separately. The user can write programs in G-code and run them on the computer and control motion stage. The vertical position of the stage can only be controlled manually, using a micrometer screw adjuster.

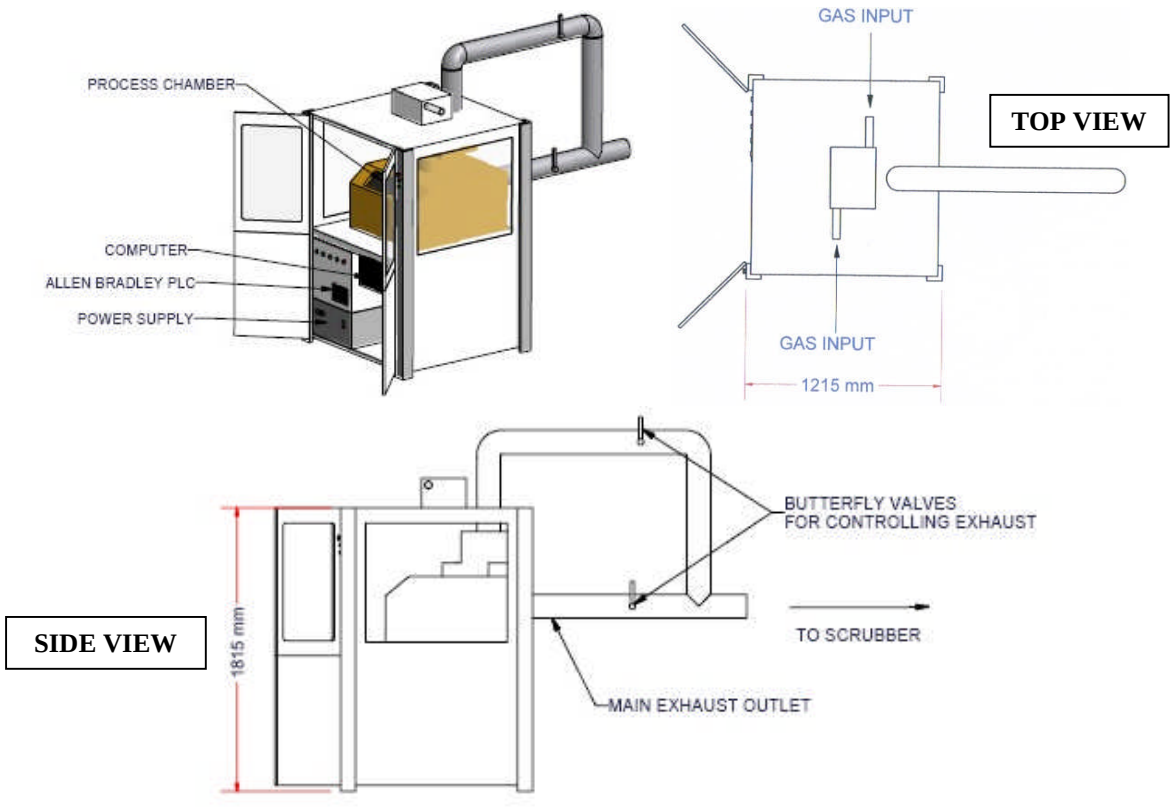

Figure 3.1 Schematic views of the RAPT300 machine

Figure 3.2 a) The RAPT300 machine with spectrometer installed

b) Above the chamber

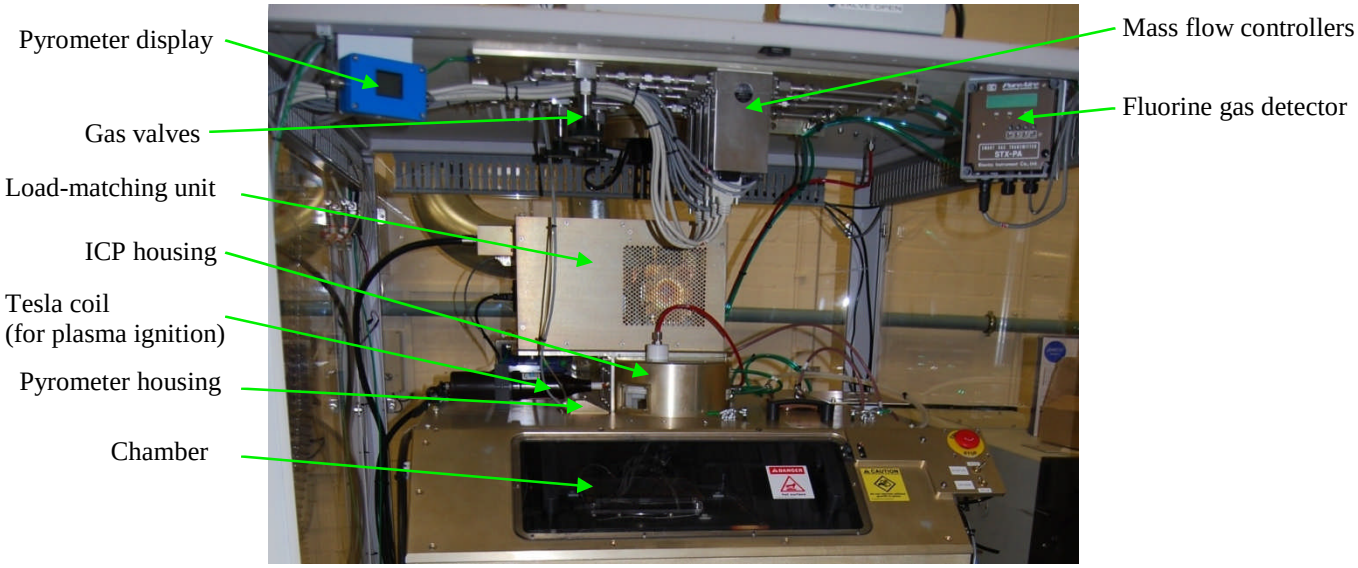

c) Below the chamber

d) Right-hand side view

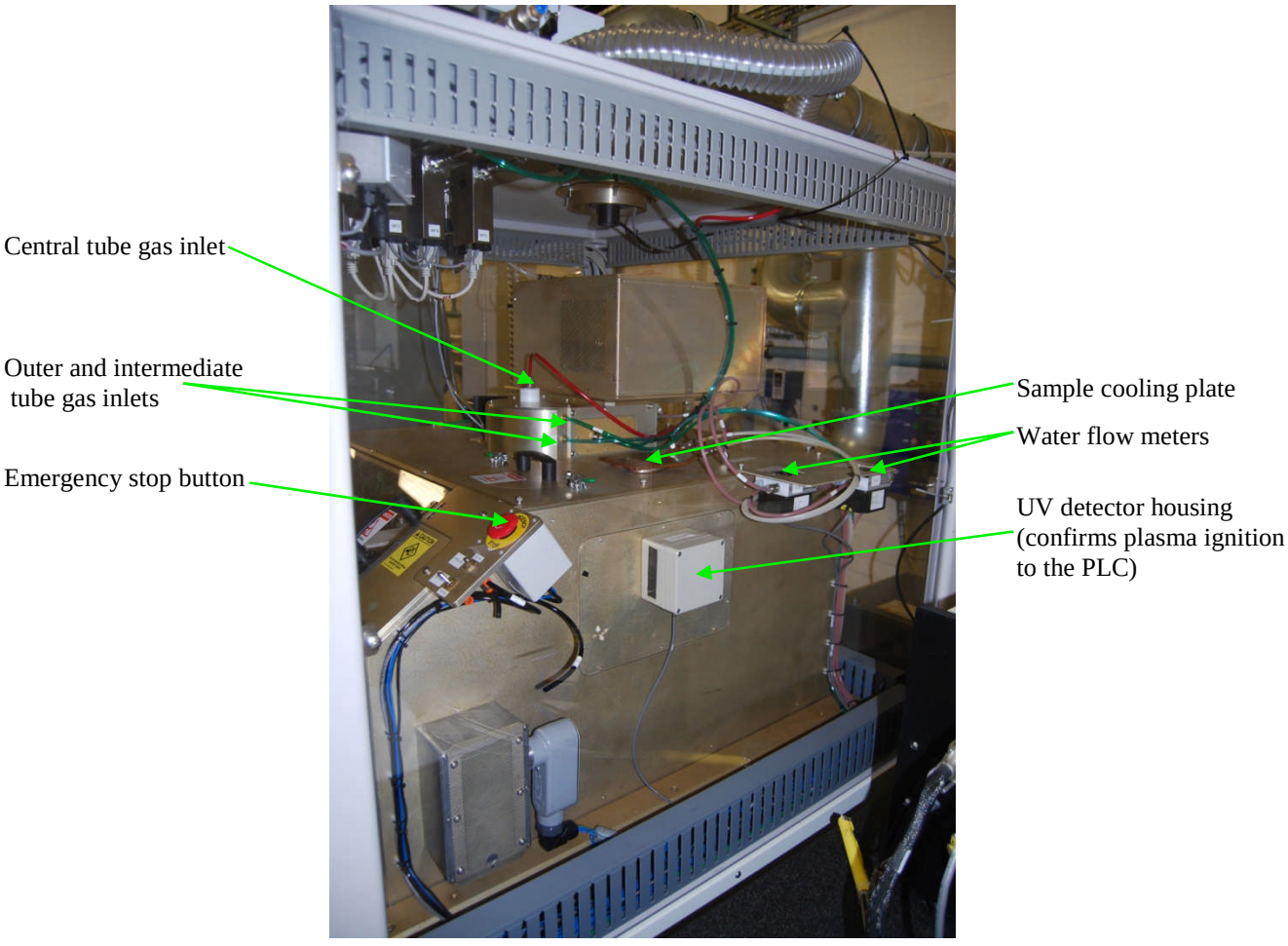

e) Separate mass flow controller and pneumatic valve for the reactive gas on top of the machine

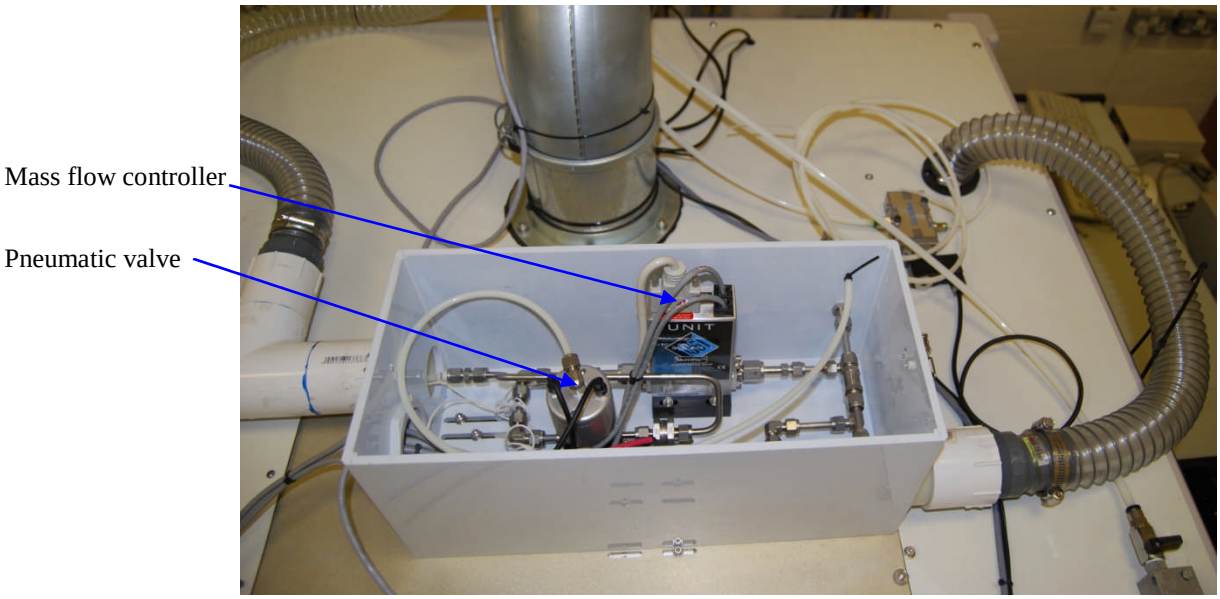

f) Inside the chamber left-hand side view

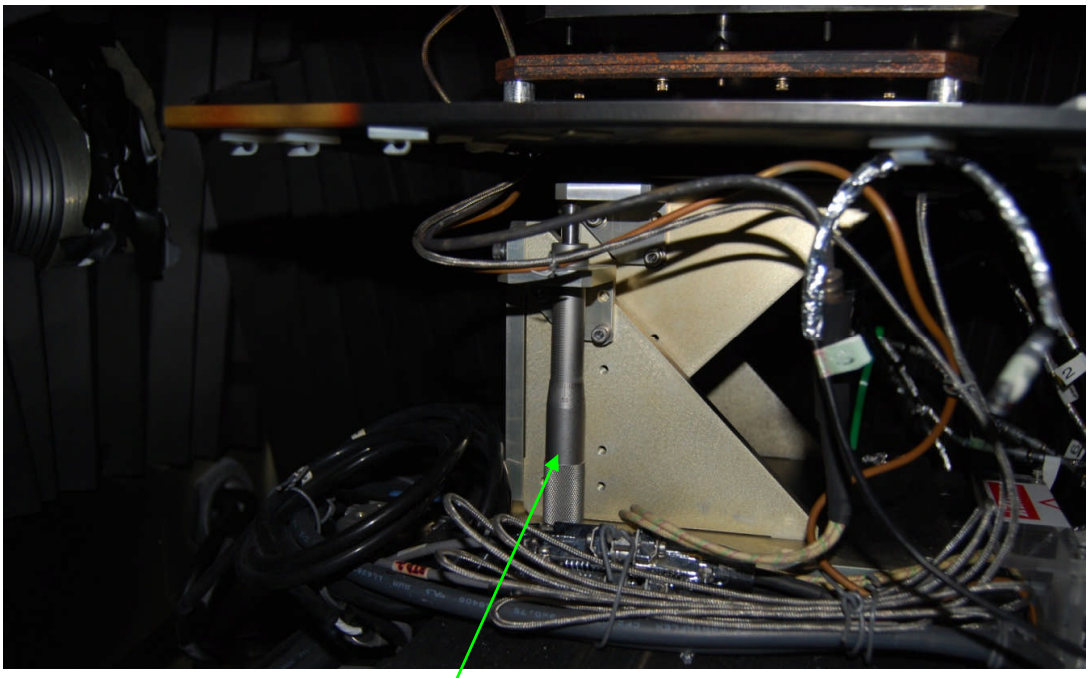

g) Inside the chamber, front view

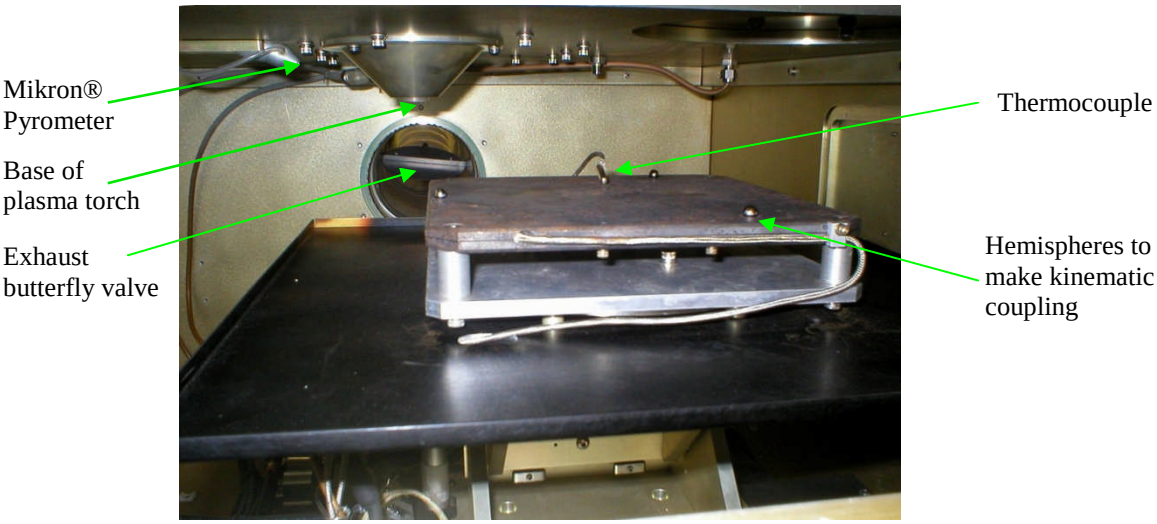

h) View under the torch housing, following the painting of the walls and ceiling inside the chamber.

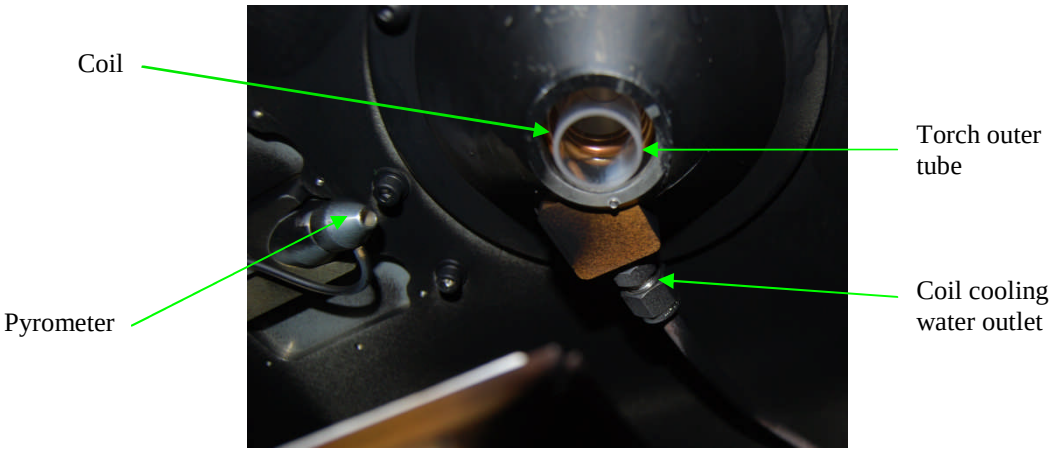

i) RF copper coil, following the machining of a window in the housing.

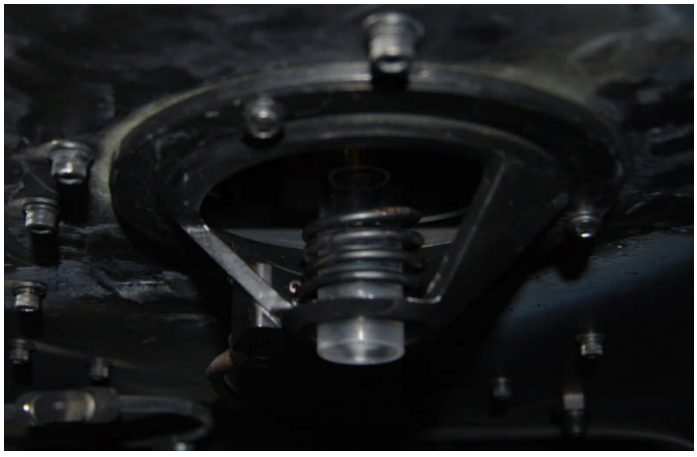

Figure 3.3a shows the plasma torch used in the RAPT300 machine. It is very similar to one that might be used in spectrochemical analysis. The RF generator operates at a frequency of 27.12 MHz. The input power to the coil can be varied; the useful range is roughly between 600 W and 1.5 kW. The copper coil and generator are cooled using chilled water. The flow rates that have been most commonly used in experiments are given in figure 3.3b.

a)

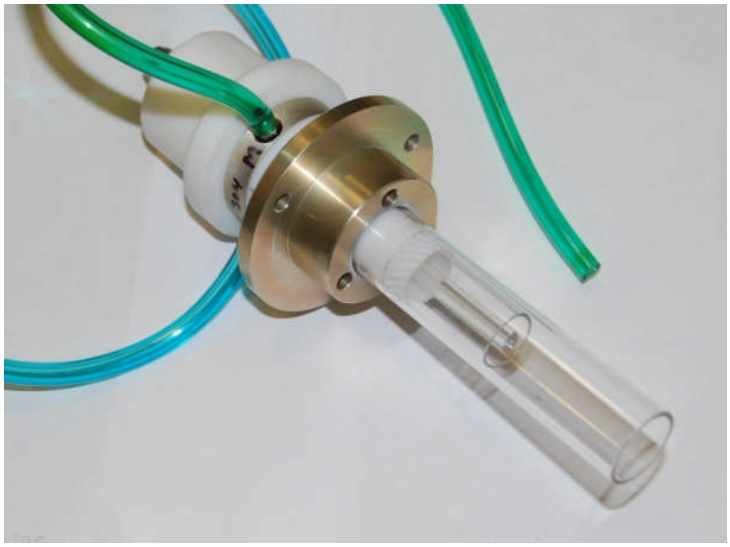

b)

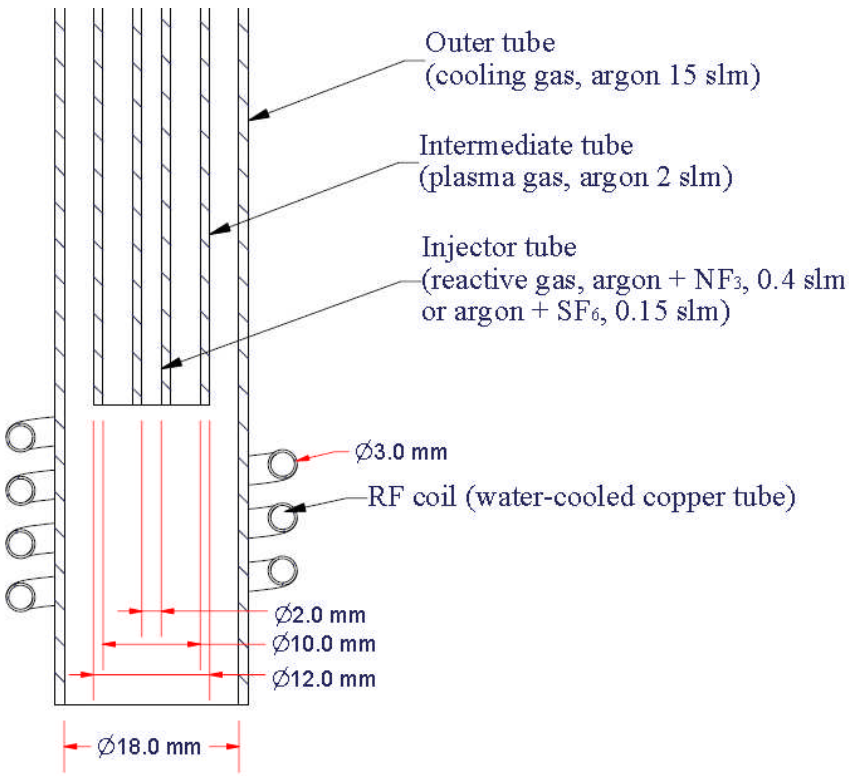

Figure 3.3 **a) The RAPT machine plasma torch. b) Dimensions and typically used gas flow rates.**

3.2 Surface Metrology

The RAP torch is being investigated as a tool for removing microscopic amounts of material from surfaces. A means of measuring the topology of the surface is necessary so that the material removal rate can be quantified. There are three classes of technique for achieving this: contact techniques, optical techniques and scanning probe microscopy. Contacting systems normally use a conical stylus to measure surface form. On some surfaces the stylus can inflict an unacceptable amount of damage, hence the need for non-contact methods. Optical techniques include focus detection, interferometry and light scattering. All of these techniques require surfaces to have some reflectivity for them to work (> 15%). The lateral resolution of optical metrology instruments is limited by the wavelength of the light used, due to diffraction effects. In situations where a lateral resolution of ~1 Å or better is required, scanning probe microscopy should be used. There are several classes of scanning probe microscopy, including scanning tunnelling microscopy and atomic force microscopy [**138**, **139**].

Most of the surface metrology discussed in chapter 4 involved the use of the Zygo PTI™, a homodyne phase shift interferometer, and the Talysurf Coherence Correlation Interferometer 6000 (CCI), a white light interferometer. Some measurements have been taken using the Fisba FST10, which is very similar to the Zygo PTI. These devices are discussed in the next two sections.

3.2.1 Phase shift interferometer

Both the Zygo PTI and the Fisba FST10 use a helium-neon laser (632.8 nm). Their principle of operation is equivalent to that of a simple Michelson interferometer. A schematic of such an interferometer is shown in figure 3.4a and photographs are shown in figure 3.5. Light from the laser is split at a beamsplitter. Half of the light is then reflected straight back off a reference mirror, the other half is delivered to the surface. The two reflected beams then recombine at the beamsplitter and interfere as they are delivered to the detector. Lenses are used to expand the size of the beam so that large areas (up to 105 mm × 105 mm) can be examined simultaneously. Phase–shift interferometers like this are quick to use as fringes can be seen irrespective of the distance between the sample and lenses.

The measured intensity, I, varies with the optical path difference, Δz, according to the formula

$$I(\Delta z) = A\left(1+\cos\left(4\pi\frac{\Delta z}{\lambda}\right)\right) \qquad (3.1)$$

where A is the average intensity of the source and λ is the laser wavelength. It follows that if there is a deviation greater than $\lambda/4$ between sampling points there is an ambiguity in the measurement [**140**]. As a result, it might not be possible to measure the form over parts of the surface that have a steep gradient, although it might still be possible for the software to calculate the surface heights on opposite sides of a discontinuity. When measuring a transparent sample material, there is likely to be a problem with multiple reflections as some light is reflected internally at the base of the sample. Such secondary reflections can be suppressed by, for example, coating the underside with petroleum jelly.

These instruments have been used for measuring surface form and determining material removal rates. To do this, the surfaces were measured before and after processing; the pre-process data was subtracted from the post-process data. The intereferometer set-ups include a translational stage with tilt adjusters for positioning a sample.

3.2.2 Coherence Correlation Interferometer

Some interferometers use a heterodyne laser that has strong emission in two separate frequency bands. If the laser used emits light at two frequencies, λ_1 and λ_2, with the same intensity, A, equation 3.1 becomes

$$I(\Delta z) = A\left(1+\cos\left(2\pi\Delta z\frac{\lambda_1+\lambda_2}{\lambda_1\lambda_2}\right)\left(2\pi\Delta z\frac{\lambda_1-\lambda_2}{\lambda_1\lambda_2}\right)\right) \quad (3.2).$$

Figure 3.7b shows I as function Δz for this distribution. As the optical path difference is increased the fringes disappear and reappear again. The change in Δz between consecutive fringe maxima is approximately equal to

$$\frac{\lambda_1\lambda_2}{2|\lambda_1-\lambda_2|} \quad (3.3).$$

The modulation in fringe height allows the use of vertical scanning interferometry to improve the dynamic range of the instrument whereby the degree of modulation or coherence is measured rather than just the phase information.

The Talysurf 6000, supplied by Taylor-Hobson, advances on this principle by using a white light source. Figure 3.4b shows a schematic diagram of how white light interfermometer usually works. Figure 3.7c shows how the measured intensity depends on the optical path distance when a white light source (i.e. 400 nm to 700 nm) is used. Fringes are only bright when the two path lengths are close to matching [**138**, **140**]. This means that the separation between the objective lens and the sample has to be adjusted to match the pathlengths, which can be time-consuming. A microscope objective lens is used to focus light onto a small area. White light interferometers usually include a Mirau interferometer. A Mirau interferometer contains a reference mirror. Some of the light from the source is reflected onto the mirror using a semi-reflective surface. Light reflected off the reference mirror in the Mirau interferometer interferes with light reflected off the sample surface and the superposition of the two is received by the photodetector. The vertical position of the reference mirror is controlled using a piezoelectric transducer. The user sets the vertical height scanning range and the reference mirror is moved through that range accordingly.

When using the CCI, point-to-point deviations of up to 600 nm can be measured, alleviating the problem of steep gradients. Internal reflections off the lower face of a thick sample are never a problem when using a white light interferometer as they do not produce fringes.

Unfortunately, it is only possible to view a small area at any one time using the CCI. The interferometer was supplied with the objective lens of magnification 20 × and 50 ×. The viewable area and the maximum measurable gradients with each objective are shown in table 3.1.

This instrument has been used, almost exclusively, for measuring surface roughnesses.

a)

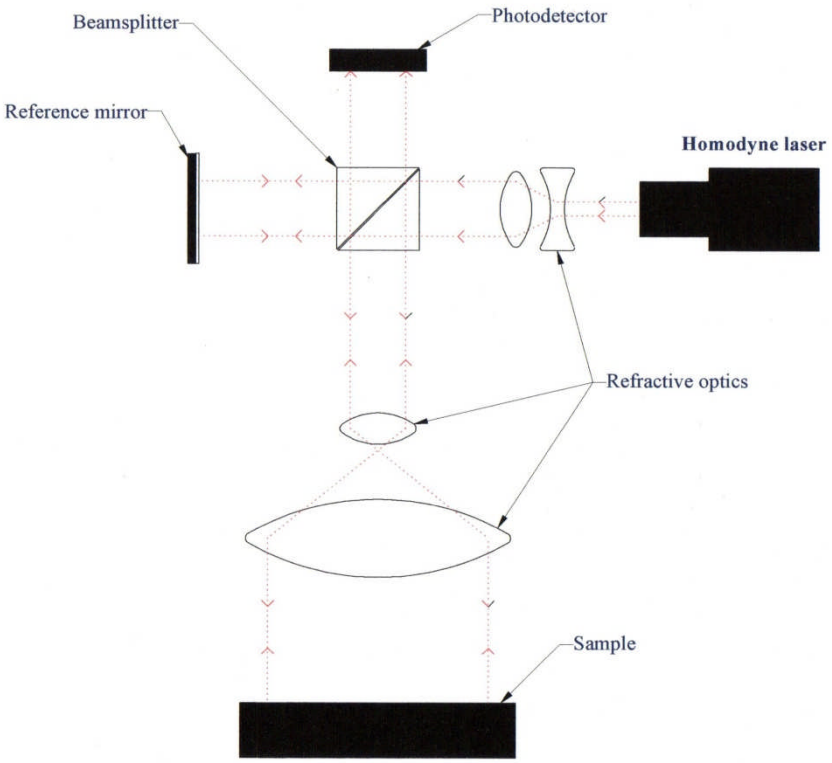

b)

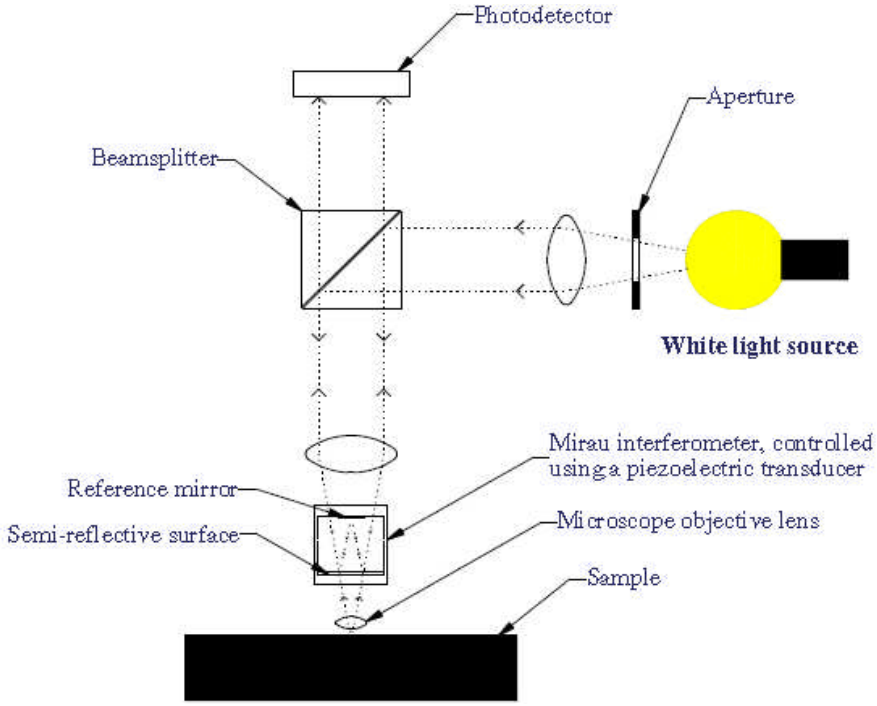

Figure 3.4 **Schematic diagrams of a) a phase-shift interferometer and b) a white light interferometer. Although split cubic beamsplitters are depicted here, it is common to use semi-silvered mirrors instead.**

a)

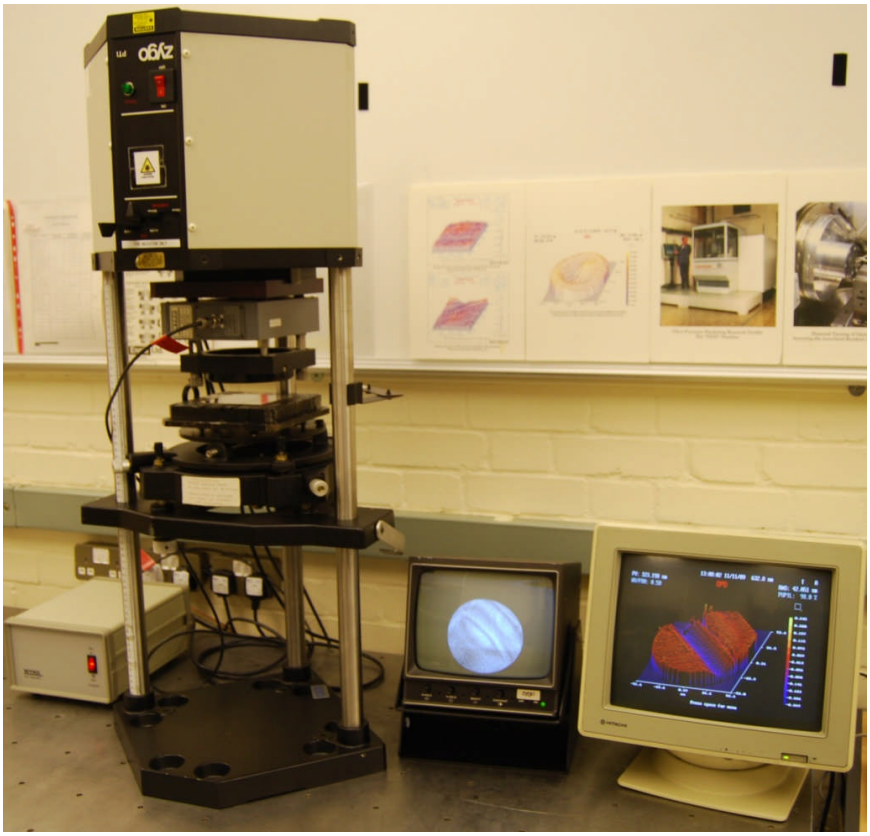

b)

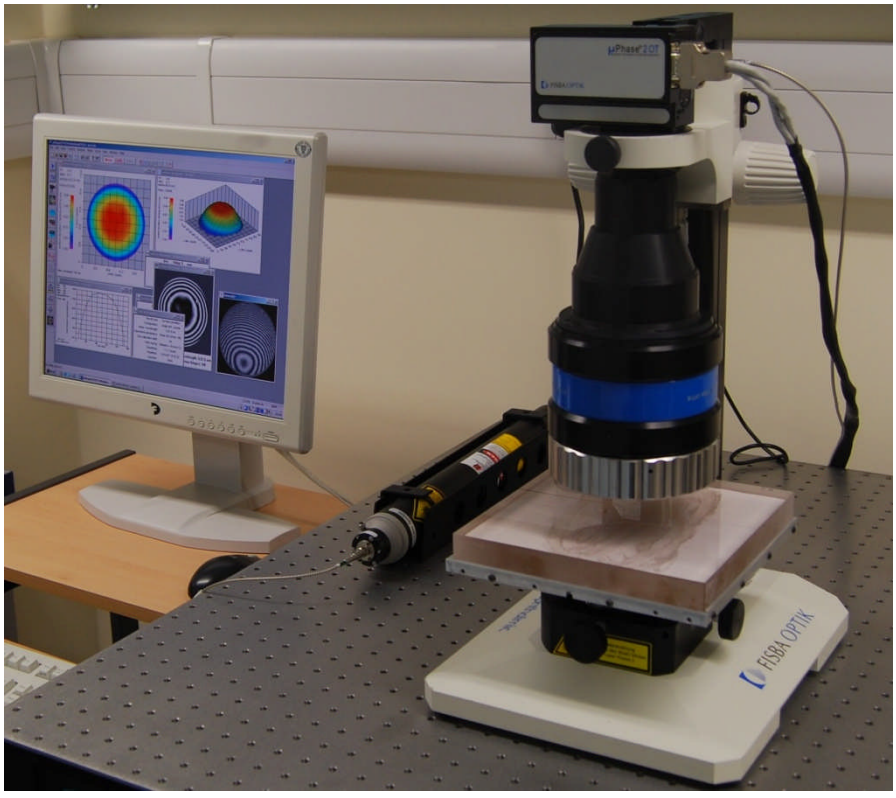

Figure 3.5 **Two homodyne phase shift interferometers that are used for measuring surface form: a) the Zygo PTI and b) the Fisba FST10.**

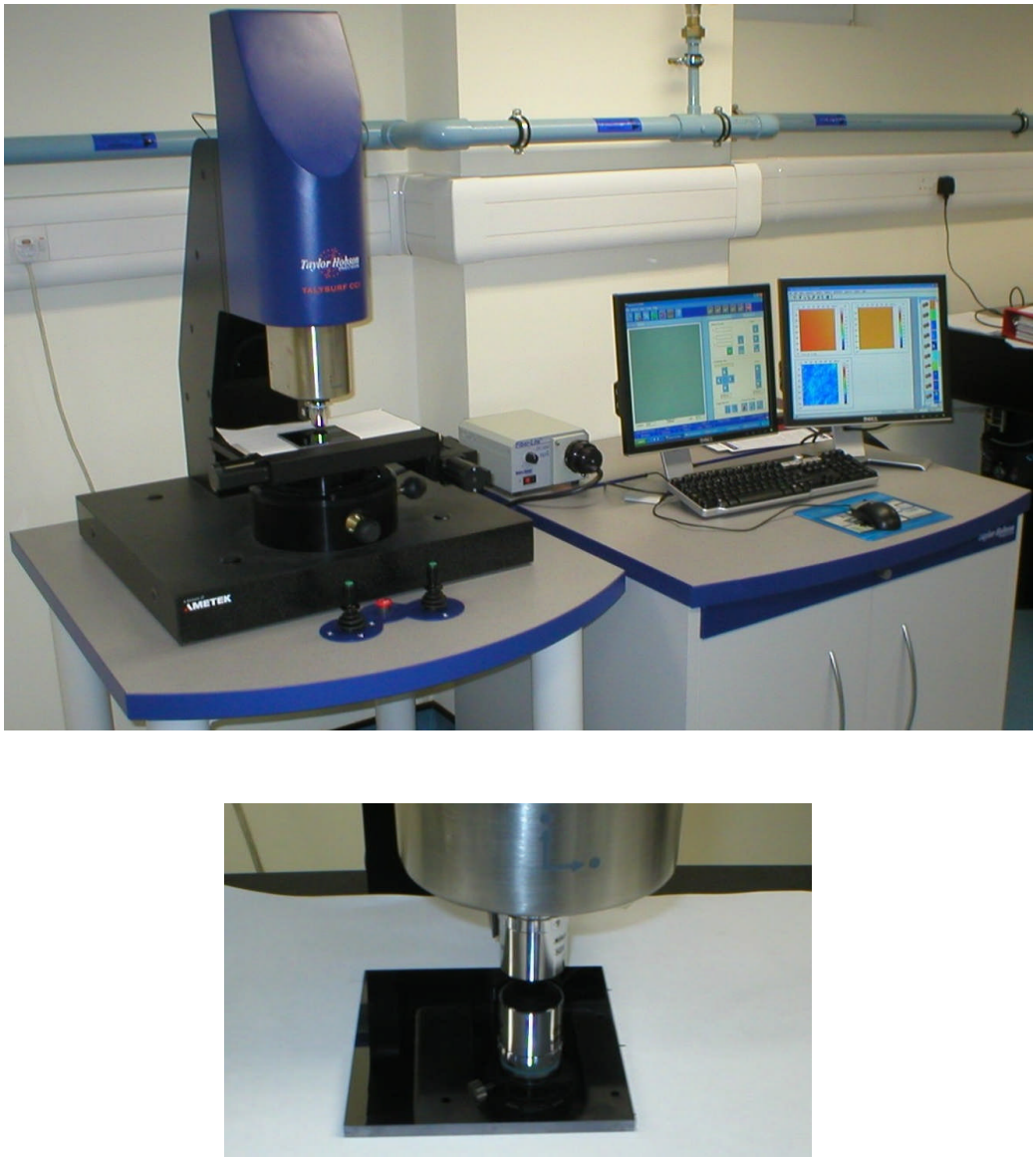

Figure 3.6 **The CCI being used to measure the roughness of a surface of a plate of silicon.**

Table 3.1 **The capabilities of the CCI with the supplied objective lenses**

Objective lens magnification	20 ×	50 ×
Viewable area	900 μm × 900 μm	380 μm × 380 μm
Lateral sampling resolution	0.62 μm	0.25 μm
Maximum measurable gradient	14.5°	22°

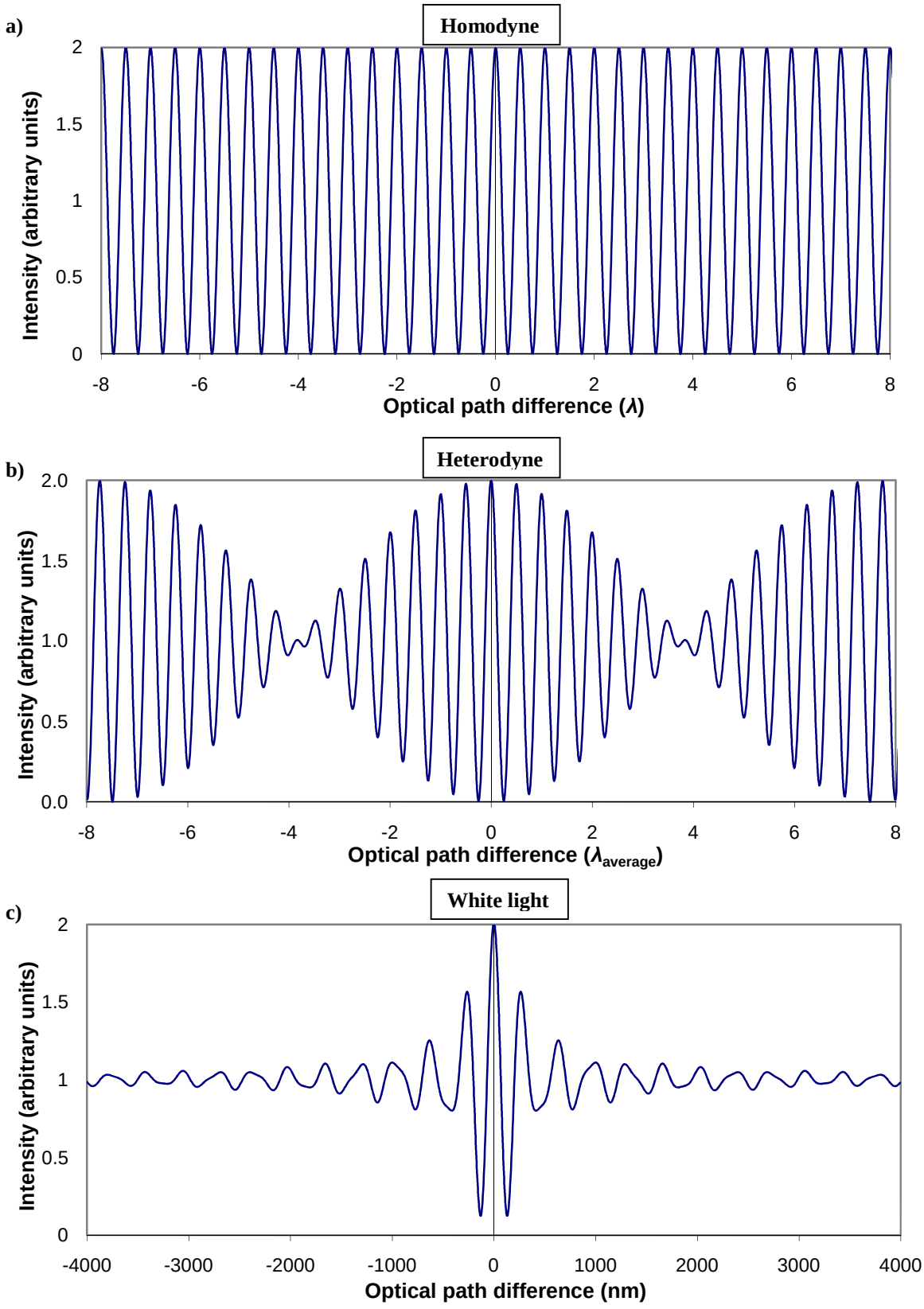

Figure 3.7 **Variation of the measured intensity at a single measuring point with the optical path difference when using a) a homodyne laser source, b) a heterodyne laser source (plotted against the average wavelength of the two tones) and c) a white light source. In the case of a white light source, sharp fringes are only seen when the optical path difference is close to zero.**

3.3 Spectroscopic sampling equipment

An Ocean Optics HR4000 spectrometer containing a Toshiba 3648 pixel linear CCD array detector was used for all spectroscopic measurements. It had been tuned to simultaneously measure intensities of wavelength between 400 nm and 850 nm (giving an average channel separation of 123 pm[24]). The spectrometer was purchased with an 'H3' grating and 5 µm wide slit. As a result, the spectrometer has a resolution of 240 pm. This means that it would be impossible to distinguish pairs of emission lines whose central wavelengths are separated by less than 240 pm. A diagram of the spectrometer is shown in figure 3.8.

Two techniques were used for collecting the light. The first method involved using a collimating lens, with an aperture of about 3 mm and focal length of 20 mm, to focus light into the core of a multi-mode optical fibre with a core diameter of 400 µm (as shown in figure 3.10). The fibre was supplied with the jackets and female SMA connectors at each end, onto which the lens can be mounted (see figure 3.9). The lens was mounted upon the RAPT 300's precision motion stage, as shown in figure 3.11. Moving the motion stage enables the operator to sample different regions of the plasma.

The second technique involved using, as named by Ocean Optics, a Gershun tube. This consists of two 1" diameter barrels, which can be screwed onto the SMA (SubMiniature version A) connector on the optical fibre. A disc, which has a chamfered hole at the centre, is fitted onto the front of the tube whose diameter determines the viewing angle. Its assembly is shown in figure 3.12. Several discs are supplied, each with a different sized hole. The possible viewing angles (depending on the disc chosen and whether just one or both of the 1" tubes are used) are: 1º, 2 º, 3 º, 6 º, 8 º, 10 º, 14 º, 16 º, 20º & 28°. Both the tubes and disc are made of black anodised aluminium. Figure 3.13 shows a diagram of the set-up with the 3° aperture in place. Figure 3.14 shows a photograph of the Gershun tube mounted on the RAPT 300's motion stage.

1) SMA male connector
2) Rectangular entrance slit (5 µm wide in the spectrometer used).
3) Filter
4) Collinating mirror.
5) H3 blazed reflective grating.
6) Mirror focusing light onto the CCD.
7) Toshiba 3648 pixel linear CCD detector.

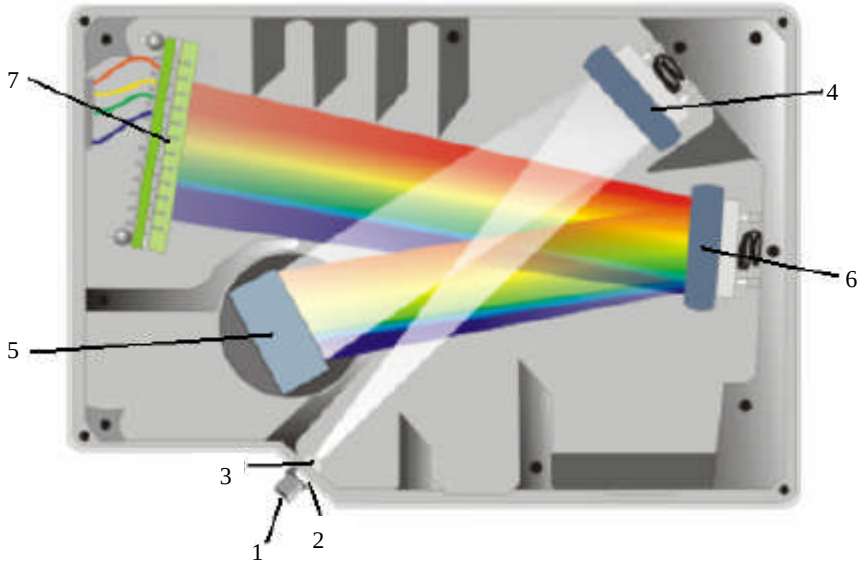

Figure 3.8 **A schematic diagram showing the contents of the Ocean optics HR 4000 spectrometer.**

[24] 1 pm = 10^{-12} m.

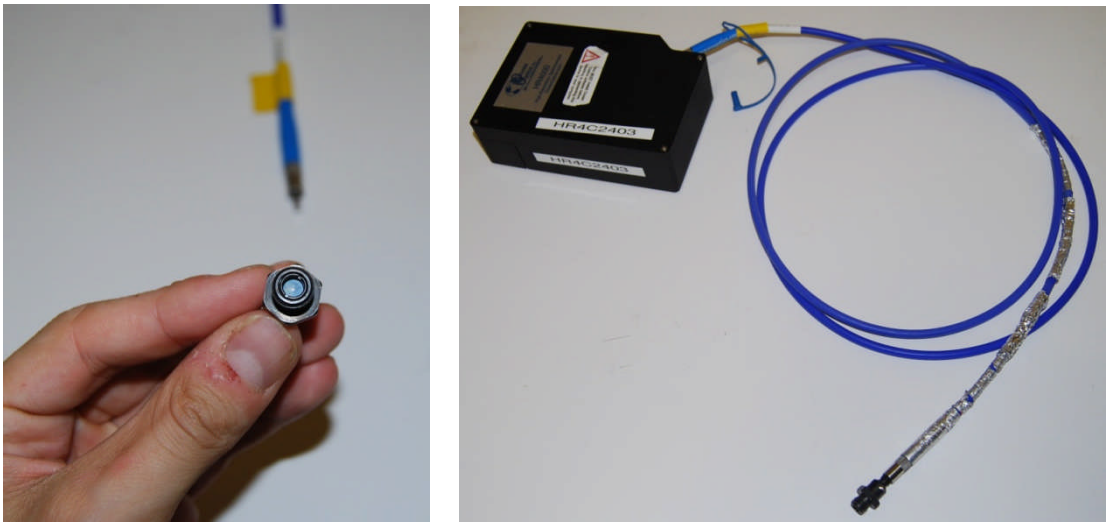

Figure 3.9 **An Ocean Optics UV-74 collimating lens mounted onto a UV-VIS high OH content optical fibre assembly (aluminium tape was applied to help prevent the jacket from thermal damage).**

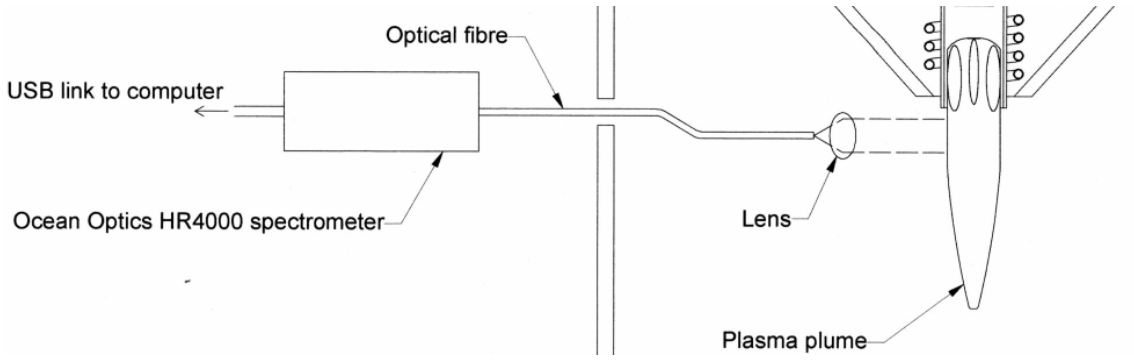

Figure 3.10 **Light is collected using a collimating lens, which can be repositioned by mounting it onto the precision motion stage within the chamber. An optical fibre was used to transmit the light to spectrometer outside the chamber.**

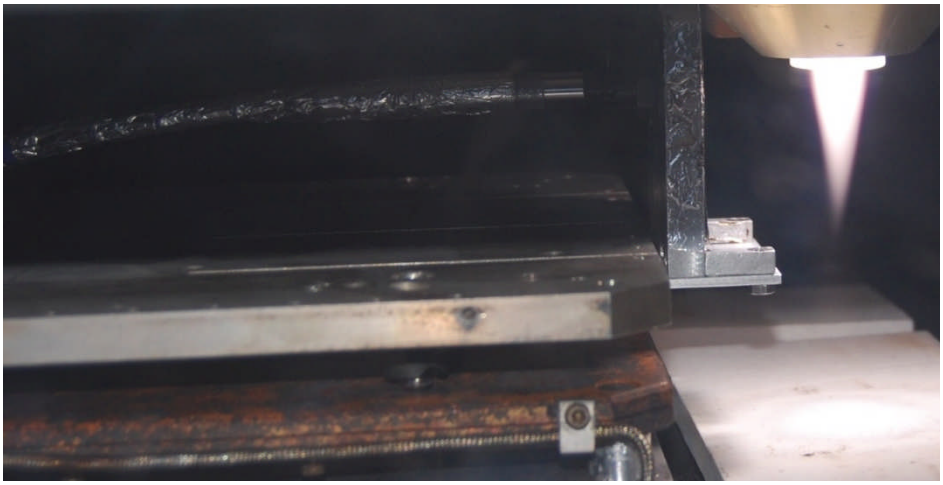

Figure 3.11 **Sampling the argon ICP, with the collimating lens mounted onto the motion stage.**

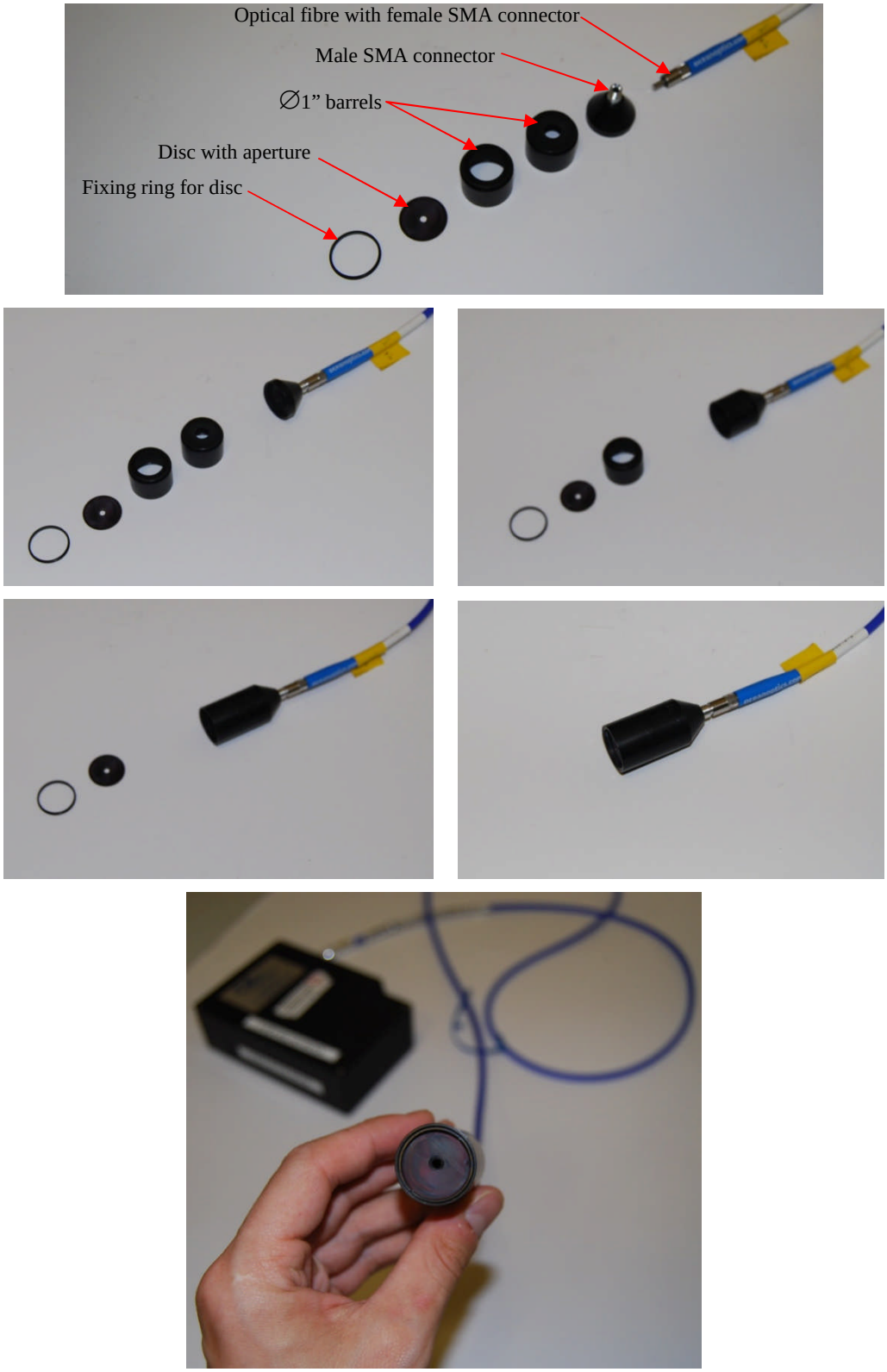

Figure 3.12 Assembling the Gershun tube.

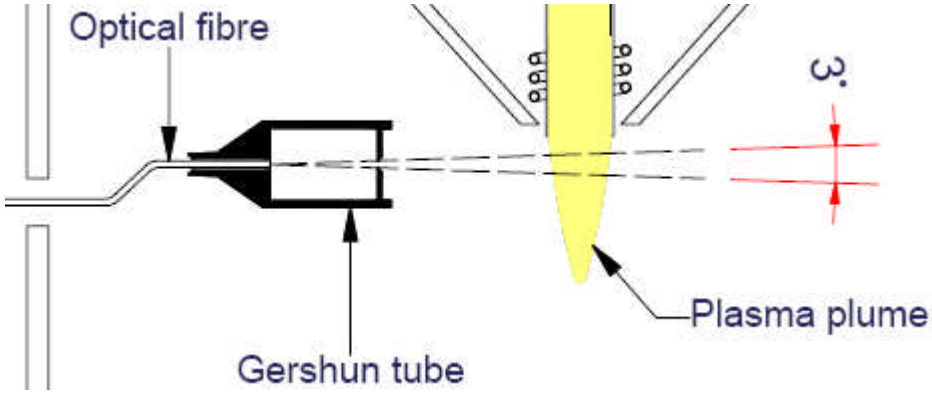

Figure 3.13 **The Gershun tube can be used to collect light from a conical volume. Although the angle shown is 3°, it can be set to view through other angles.**

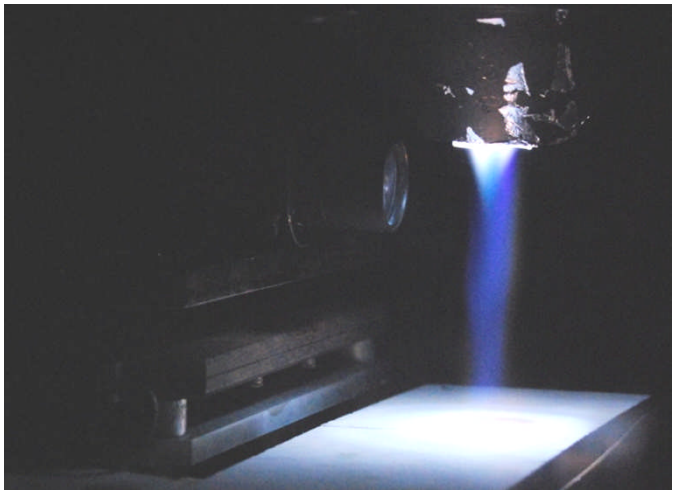

Figure 3.14 **Examining the plasma with SF_6, using a Gershun tube.**

A significant advantage of the Gershun tube method is that it can cut out a considerable amount of the stray light that might interfere with measurements.

Ocean Optics provide a software package, 'Spectrasuite', which can be used to collect and record data from their spectrometers. The user sets the acquisition period and the iteration count. The software records the selected number of samples and gives the average count of that set of measurements, compensating for random fluctuations. The readout from the linear CCD array is in arbitrary units known as 'counts'. Each count corresponds to a bundle of photons. The detective quantum efficiency of the CCD varies with wavelength. Ocean Optics declare the sensitivity of the CCD as '*130 photons per count at 400 nm, 60 photons per count at 600 nm and 100 photons per count at 800 nm*'.

Another important factor is the grating efficiency. For a given reflective grating, only a proportion of the incident light at a given wavelength reached the detector. Graphs are shown in the manufacturer's specifications as a guide.

During early trials, attempts to compensate for both the detector's and grating's efficiency were made using this information. However the accuracy of such approximations was questionable and further losses and dispersion exist within the

optical fibres and at all of the interfaces. For this reason, an Ocean Optics LS-1 calibration lamp was purchased. This tungsten filament lamp is a NIST-traceable calibration standard. By connecting the lamp to the end of the fibre and taking a single measurement, as shown in figure 3.15, the measuring system can be calibrated with the aid of the data displayed graphically in figure 3.16, which is provided by Ocean optics. Spectrasuite then makes it straightforward to produce absolute irradiance graphs. Figure 3.17c shows such a graph. All photodetectors produce a current even when no light is received, known as dark current. During the calibration procedure, the operator is asked to record a 'dark spectrum' by blanking off the end of the optical fibre. The dark spectrum can then be deducted from all spectra recorded thereafter.

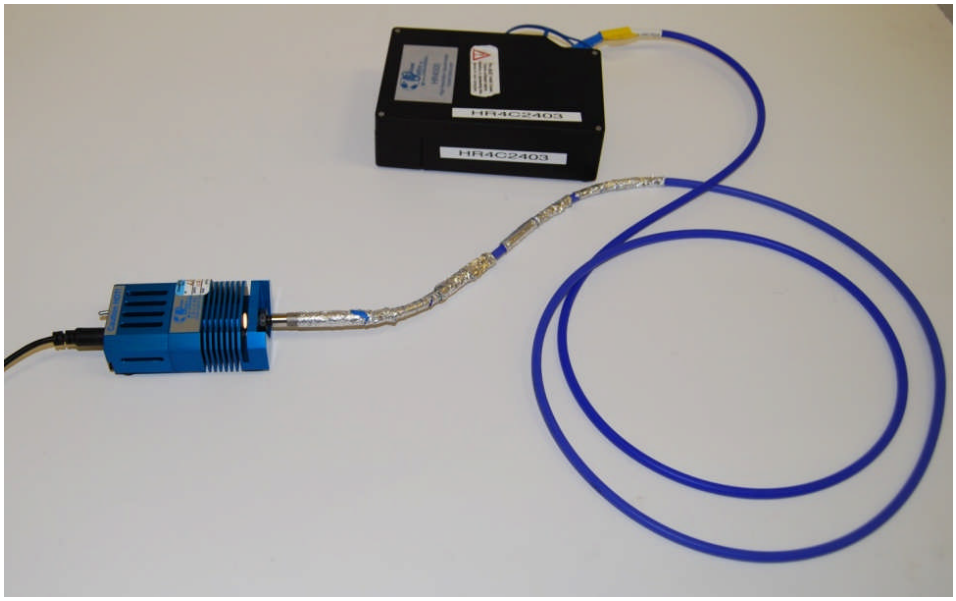

Figure 3.15 **Ocean Optics LS-1 being used to record calibration spectra. These spectra were taken so that instrumental factors could be taken into account when taking subsequent measurements.**

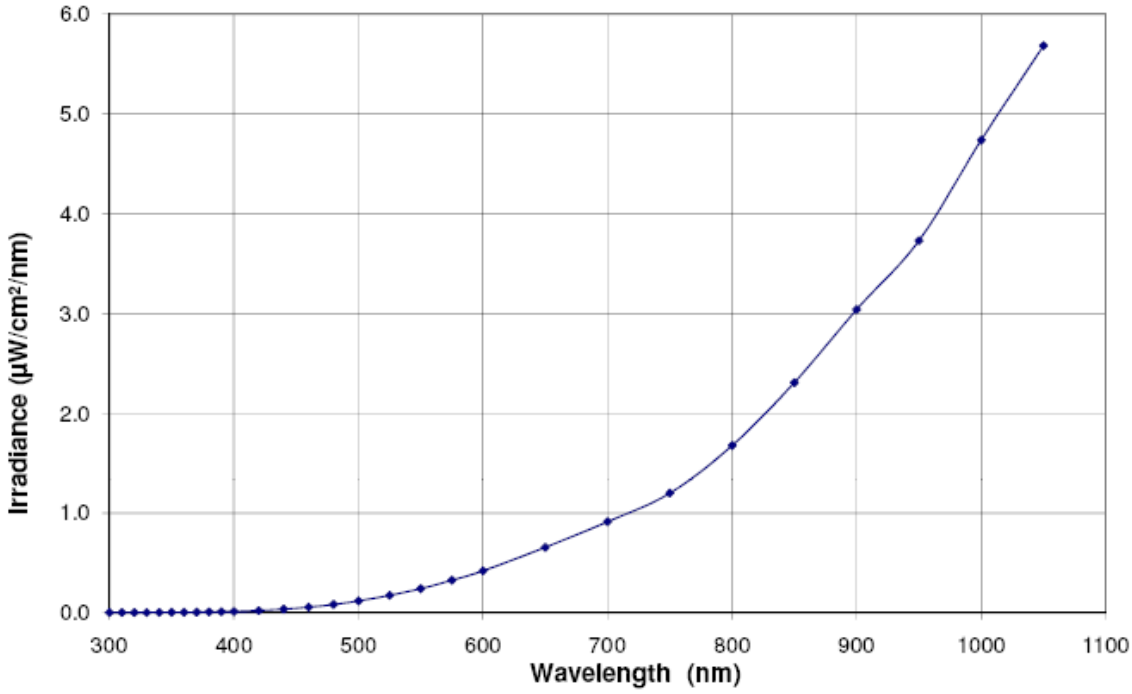

Figure 3.16 **Calibration data for the tungsten lamp, as provided by Ocean Optics, that is to be used whenever the spectrometer is coupled to a 400 µm core diameter optical fibre.**

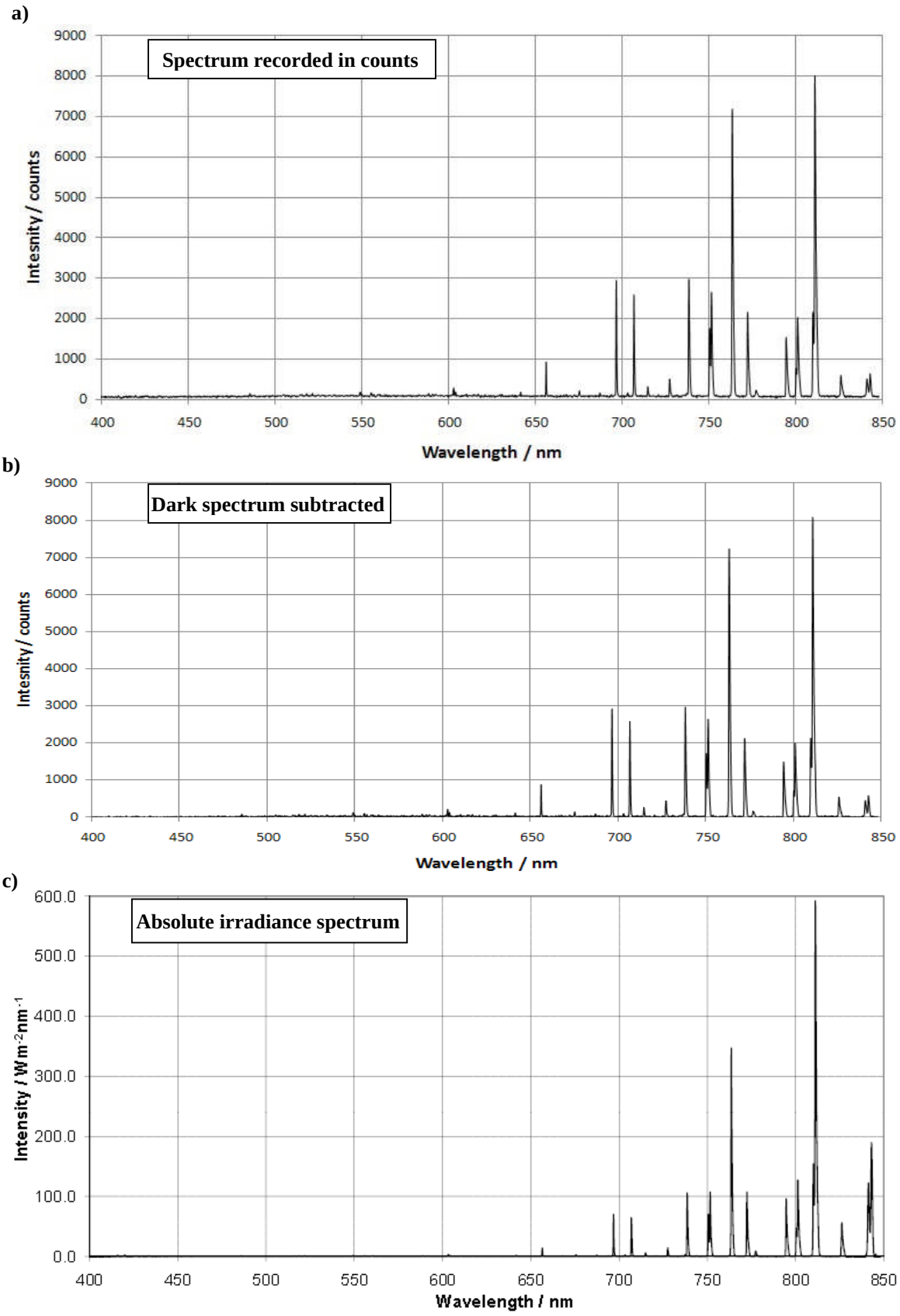

Figure 3.17 **a) A raw argon emission spectrum in 'counts'. b) The same spectrum with a dark spectrum subtracted. c) An absolute irradiance spectrum of the same plasma, produced using Spectrasuite.**

3.4 Sample surface temperature measurements

3.4.1 Mikron pyrometer

The term pyrometer was originally coined to denote an optical device capable of measuring temperatures of objects above incandescence (meaning objects that appear luminous to the human eye). The word is now used to refer to any noncontact device capable of detecting radiation from a blackbody or greybody and calculating its temperature accordingly. As was discussed in section 2.3, the overall luminosity of a blackbody source is proportional to the fourth power of its temperature.

A Mikron pyrometer capable of detecting radiation between 8 μm and 12 μm was supplied with the RAPT300 machine. Its position is shown in figure 3.2g and h. It is fitted with a '10 to 1' head so that it has a narrow viewing angle (≈6°). The user inputs the emissivity of the sample and the temperature is calculated accordingly. With this device, the maximum sampling rate is 1 Hz.

3.4.2 FLIR ThermaCAM™ SC3000

This thermal imaging camera is a much more powerful tool than the pyrometer. Instead of just reading out a single temperature, it provides the operator with a two-dimensional image (320 × 240 pixels). Much higher sampling rates can be achieved (up to 50 Hz). It includes gallium arsenide Quantum Well Infrared Photon (QWIP) detector that is sensitive to radiation between 8 μm and 9 μm. The detector is cooled to –203.15°C, heavily reducing the noise level. The camera comes equipped with a 20° aperture germanium lens[25]. Additional lenses can be fitted to alter the viewing angle. The operator enters experimental parameters (such as the source's emissivity, the distance to source, the air transmittance and humidity) using the computer software, FLIR researcher. The emissivity of the object of interest is usually the most crucial parameter to be set correctly. Should it be found, after recording, that any parameters have been set incorrectly, they can be changed retrospectively. However, the operator must be careful to select the most appropriate temperature measurement range otherwise important data might be lost. The camera carries out its own calibration, internally, using blackbody standards.

3.4.3 Resistance Temperature Detectors

A resistance temperature detector (RTD) is a small device which contains an element whose electrical resistance depends on its temperature and, provided that there is strong thermal connection between it and the medium in question, can be used as a thermometer.

Platinum sensors from Omega (part number F3101) were employed to assist with sample temperature measurements. RTDs of this type are known as Pt100 sensors, as the resistance at 0°C is ≈ 100 Ω. Platinum sensors are a very common choice, because the relationship between resistance and temperature is close to being linear between -200°C and 250°C. Signals were acquired from the RTDs, using a National Instruments CompactDAQ unit. Connections between that and the RTDs were done with screened

[25] The lenses of the ThermaCAM™ SC3000 made of germanium, which is ~50% transmissive to infrared radiation in the wavelength band concerned. Glass lenses are completely opaque within the wavelength band in question and therefore are completely useless.

cables and connectors, which were supplied by Lemo®. Screened cables were chosen to prevent RF noise from the plasma affecting the results. The CompactDAQ units measured the RTDs' resistances using four-wire measurements. When taking such measurements, a current of ~100 mA is passed through the sensor through one pair of wires and the voltage drop across the sensor is measured using the other pair. The advantage of this method over a simple two-wire measurement (in which both the current and the voltage drop measurements are made using the same leads) is that the result is not affected by voltage drop through the leads or at connections. Four CompactDAQ units were purchased (see figure 3.18). Each one is able to accommodate 4 RTDs when taking four wire measurements. The maximum sampling rates that can be achieved is dependent on the number of channels utilised per unit; these are displayed in table 3.2.

Table 3.2 **The maximum achievable sample rate depends on the number of four wire measurements being taken per CompactDAQ unit.**

Number of measurements taken per unit	Maximum sampling rates (Hz)
1	5
2	2
3	1
4	1

The measurements were visualised and recorded using the software, LabVIEW SignalExpress.

The sensors were not individually calibrated by the manufacturers. Even inexpensive Pt100 RTDs are reasonably consistent, and one can expect to determine temperatures correct to within 1°C using tabulated values. Even so, it was decided that sensors should be calibrated in house to improve the precision of the measurements and add to check that the electronics are operational. To do this, all the sensors were connected and dipped into water that had just been boiled, together with two pre-calibrated K-type thermocouples, as shown figure 3.19. A polystyrene bung was inserted into the top of the beaker which contained the water to slow the cooling rate. This was done to improve the homogeneity of the temperature within the water and increase the number of data points collected. Temperatures between 85°C and 23°C were recorded over a 15 hour period.

For the precise calibration Pt100 RTDs, the formula

$$R(T) = R_0(1 + AT + BT^2 + C(T - 100)T^3) \quad (3.4)$$

is used, where R_0 is the resistance at 0°C and A, B and C are dimensionless constants. C is nearly always set to zero above 0°C. The LabVIEW SignalExpress interface allows the user to set these values. Figure 3.20a shows the temperatures that were recorded using "default" calibration values (R_0 =100, A = 0.0039, B = 5.78×10^{-7}, C = 0). The two thermocouples gave very similar readings. The values of R_0, A and B for each sensor were then adjusted so that the temperature profile was close to that given by the Pico T-08 unit over the whole period of recording (only a small part is shown in figure 3.20). The values of C were kept at zero. The thermocouples used do not claim to be industrial calibration standards. However, adjusting the calibration values, R_0, A and B, of the individual sensors ensures a higher degree of consistency. The experiment was then repeated and the new calibration values were used to determine temperatures given

by the RTDs. The RTDs were connected to different channels on the CompactDAQ unit during the second run to investigate as to whether that might have an influence. Results are displayed in figure 3.20c. There is a spread in temperature but at any one time the temperatures are normally within 0.5°C of each other, whereas, when the default calibration values were used, the spread was more than 1°C.

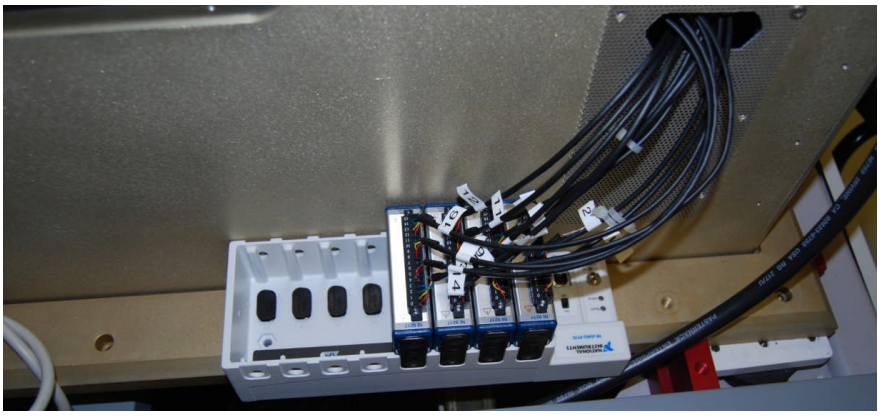

Figure 3.18 **4 National Instruments CompactDAQ units on a single chassis. The 4-wire screened Lemo® cables are connected to the Pt100 RTDs inside the RAPT300 machine.**

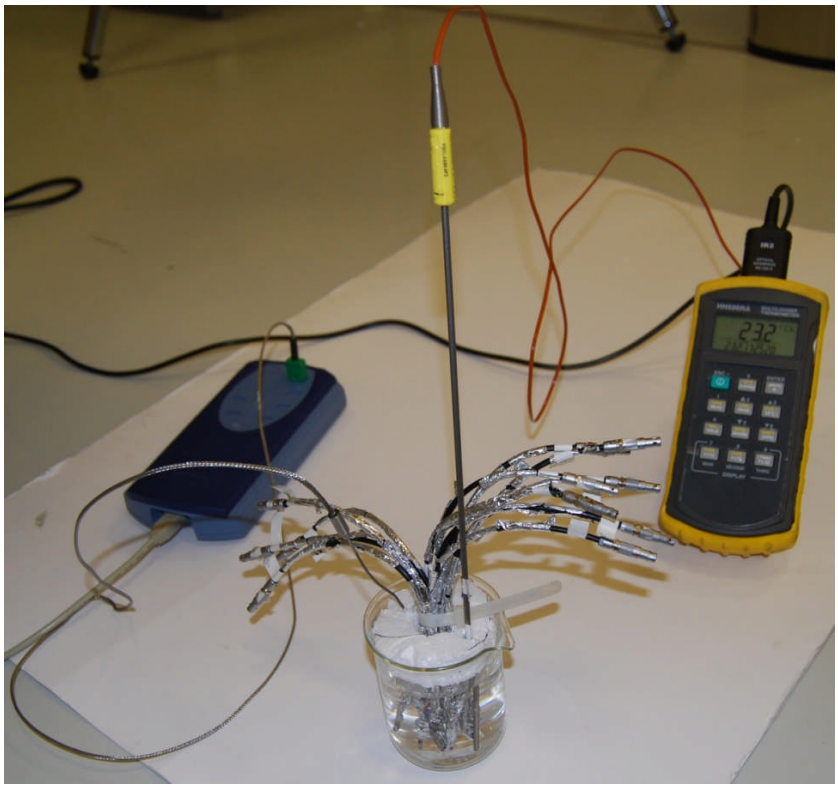

Figure 3.19 **RTD calibration kit. Two K-type thermocouples and the 11 RTDs were all held in cooling water at roughly the same depth. One of the thermocouples was connected to an Omega HH506RA hand-held measuring unit (it includes a facility for logging data onto a computer). The other thermocouple was connected to a Pico T-08 USB unit. The RTDs were connected to the CompactDAQ unit (but not in this photograph). A polystyrene bung was placed at the top of the beaker. More polystyrene was positioned around the beaker during the experimental run to slow the cooling rate and make the temperature distribution as homogenous as possible.**

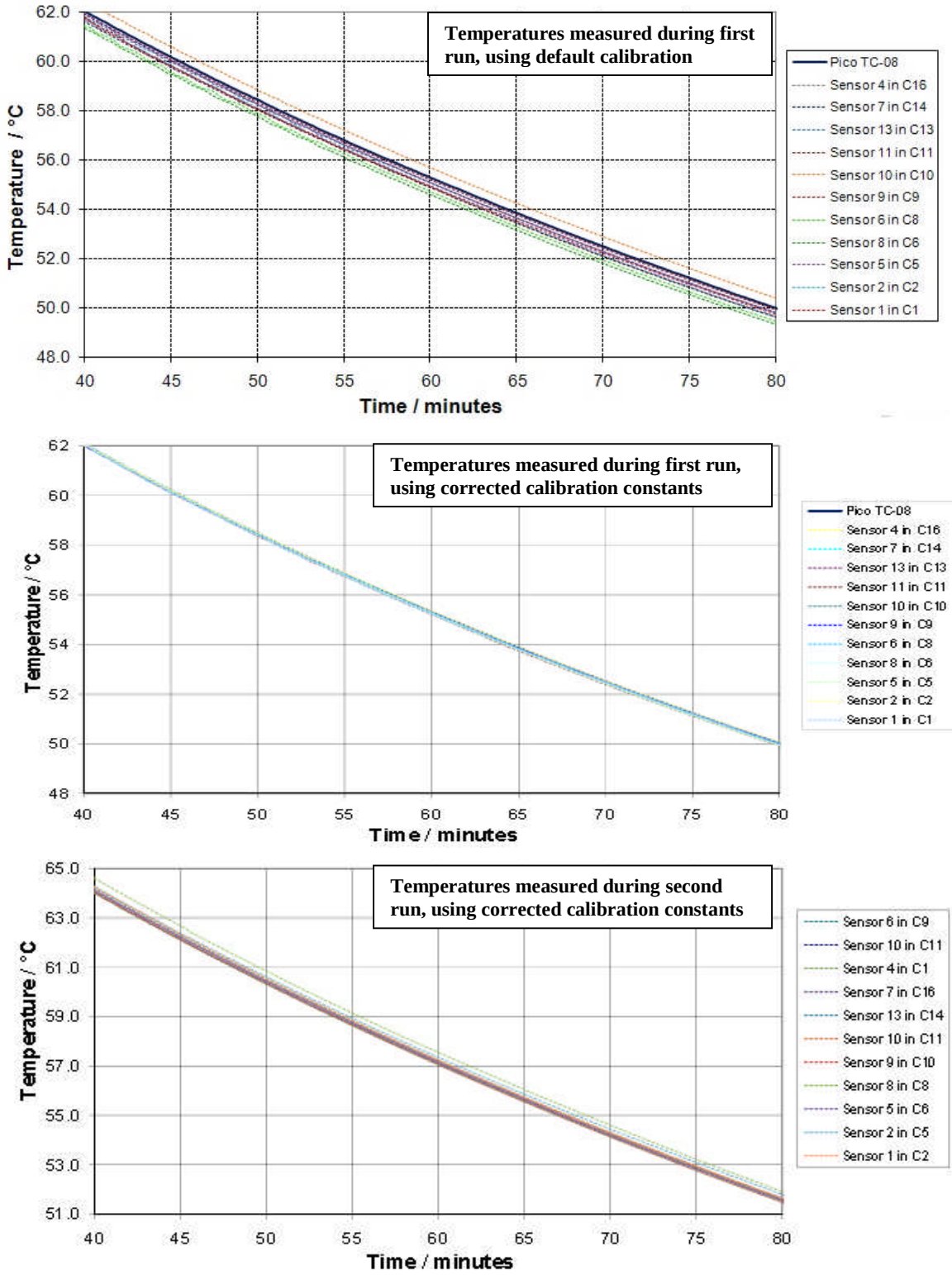

Figure 3.20 **a) Temperatures given by a K-type thermocouple attached to Pico T-08 unit and from 11 Omega Pt100 thin-film RTDs, using default calibration values, while immersed in cooling water. b) From the same experiment, but the calibration values for each RTD have been adjusted so that temperatures match that given by the thermocouple. c) Temperatures given by the RTD sensors during a repeat of the same experiment with new calibration values used. The sensors were plugged into different channels to investigate as to whether that had an influence.**

4 Material removal and surface roughness measurements

In section 2.7, some of the early experiments using the RAPT 300 machine, which had been published by Fanara *et al.* [**135**], were discussed. This included some simple material removal experiments on ULE. In this chapter, some of the experiments which immediately followed that work are described. Based on earlier work carried out at both Cranfield and RAPT Industries, it was decided that the torch power be kept at 1 kW and that the sample offset be 15 mm. Having made these decisions, an immediate objective was to define a relationship between material removal rate and torch travel speed. In doing this, faster travel speeds were used than those reported in [**135**]. A more crucial objective was to investigate the level of determinism of the process. It is important to know, for a given set of input parameters, how much material is removed from a particular point within a particular period of time. The vast majority of the work carried out at Cranfield has involved the use of NF_3 as the precursor gas. In the summer of 2009 it was decided that SF_6 be tried as an alternative, mainly because it is very much less expensive. So that direct comparisons could be made, some of the tests that had been carried out using NF_3 were repeated using SF_6.

Another important objective was to assess the evolution of the roughnesses of the etched surfaces. In large reflecting telescopes, poor surface roughness (height variations of medium to high spatial frequency) can lead to specular reflection, limiting its light gathering, focusing and resolving ability. In the manufacturing of precision optics it is usual to aim for Sa values <1 nm.

Plans were also made to investigate whether RAP could be used to etch other materials.

4.1 Material removal tests on ULE

Figure 4.1 shows an example of a trench that was etched onto a ULE sample, a result of a single pass of the plasma with a travel speed of 20 mm/s. The parameters used are shown in table 4.1. The surface graph was created by subtracting the pre-process surface height data from the post process surface height data (plus 1000 nm to make it easier to visualise in Microsoft Excel). Figure 4.2a shows a cross section through the trench, close to the centre, without the addition of 1000 nm. A Gaussian fit has been applied to it; the full width at half maximum of the fit is ≈17.5 mm. Figure 4.2b shows the pre-process and post-process profiles and surface which were used to create the profile shown in figure 4.2a. The initial surface, which was supposedly flat, was actually very slightly concave. Hereafter, the results similar subtractions will be known as "post-pre" data.

To prove beyond any doubt that the etching mechanism using RAP is purely chemical (i.e. no contribution from ionic sputtering) a pass was made across the surface, using exactly the same parameters but with no reactive gas (the parameters shown in table 4.2 were used). The results are shown in figure 4.3. As expected, no trench was visible.

a)

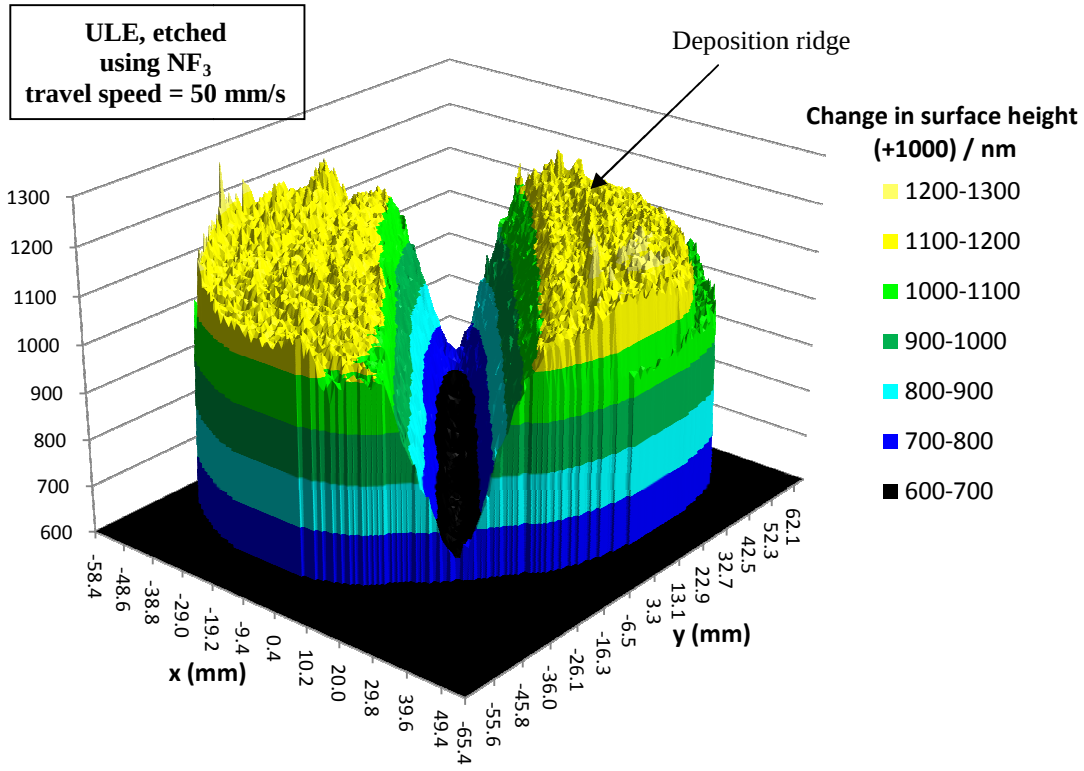

Figure 4.1 **a) A surface graph showing the 'post-pre' process data, displaying trench made on a ULE surface, using NF_3 as the etchant. The travel speed was 50 mm/s. Other parameters are shown in table 4.1. 1000 nm has been added to the height change to make it easy visualise.**

Table 4.1 **Process parameters used for all tests when using NF_3 as the etchant gas.**

Cooling gas flow (argon)	15 slm
Plasma gas flow (argon)	600 sccm
Central gas flow (20% NF_3 in argon)	400 sccm
RF power	1 kW
Sample offset (separation between quartz tube base and sample surface)	15 mm

Table 4.2 **Process parameters used for null test (no chemical etchant gas).**

Cooling gas flow (argon)	15 slm
Plasma gas flow (argon)	1000 sccm
Central gas flow	Zero
RF power	1 kW
Sample offset (separation between quartz tube base and sample surface)	15 mm

Table 4.3 **Process parameters used for all tests when using SF_6 as the etchant gas.**

Cooling gas flow (argon)	15 slm
Plasma gas flow (argon)	850 sccm
Central gas flow (10% SF_6 in argon)	150 sccm
The RF power	1 kW
Sample offset (separation between quartz tube base and sample surface)	15 mm

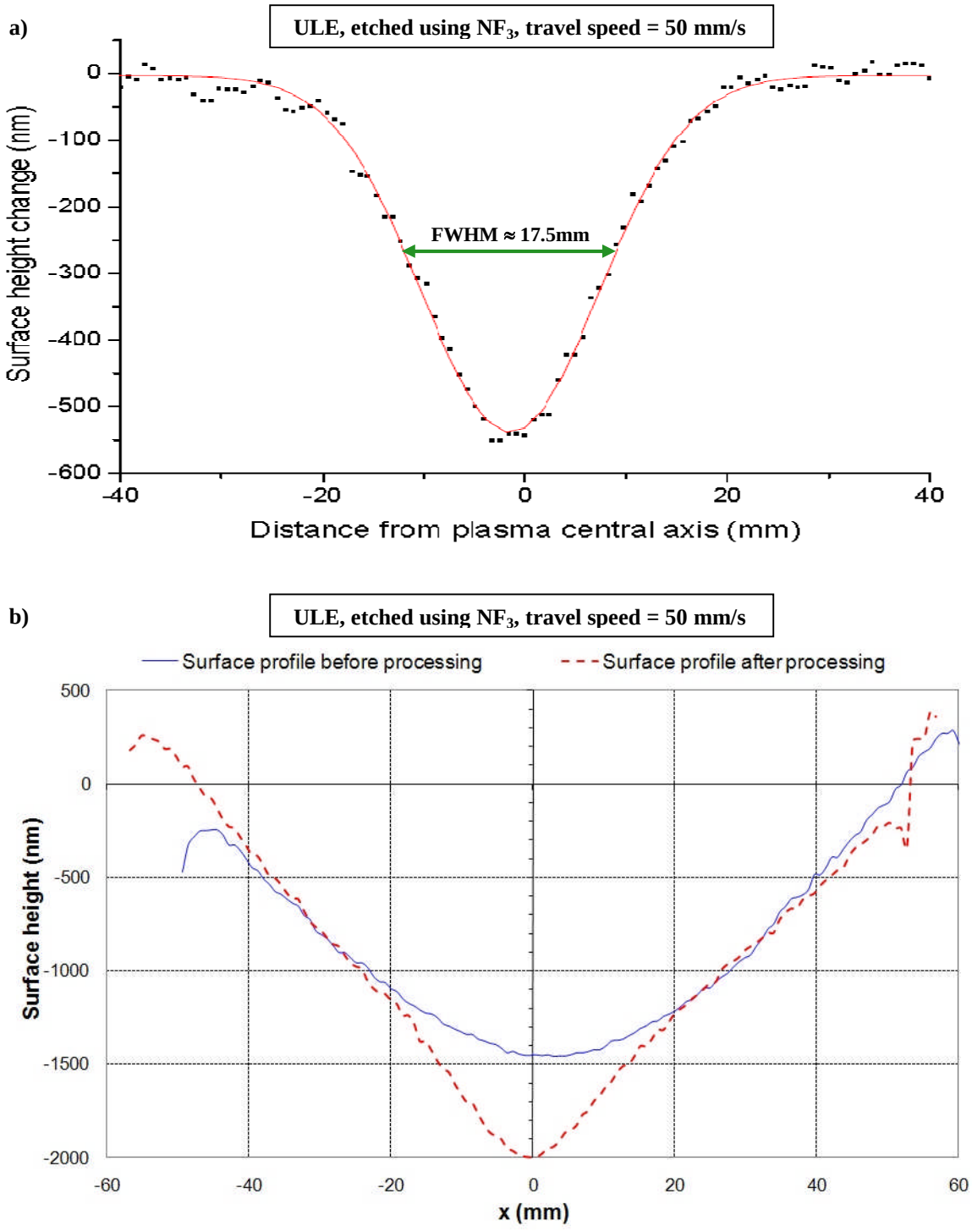

Figure 4.2 **a) A cross-section through the data shown in figure 4.1, close to the centre of the part, without the addition of 1000 nm. A Gaussian curve has been fitted to the profile; the FWHM of the fitted curve is ≈17.5 mm. The trench depth is ≈540 nm. b) The pre-process and post-process data profiles used in creating a profile shown in a).**

a)

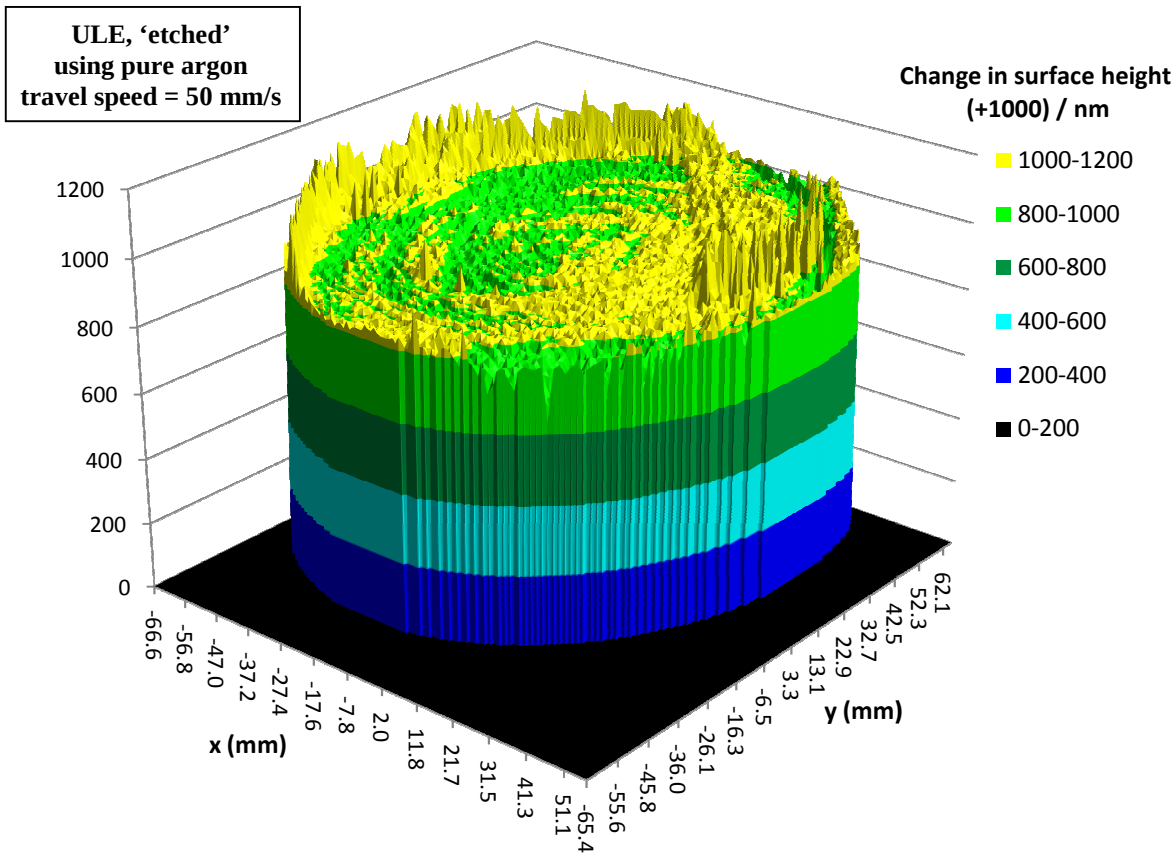

b)

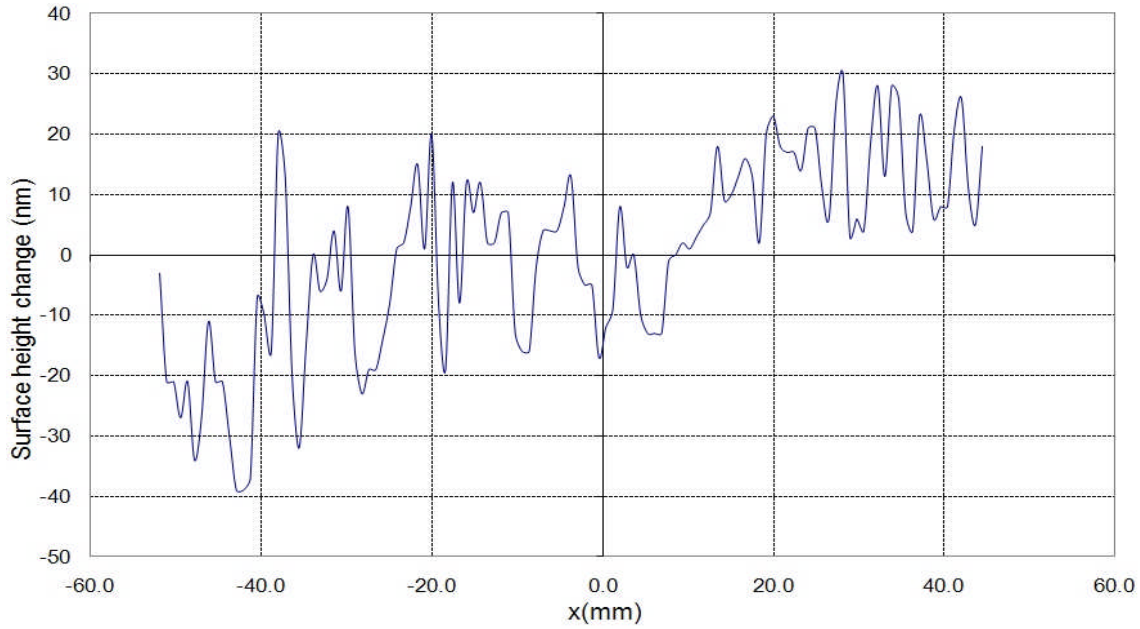

Figure 4.3 **Results of a repeat of the experiment whose data is shown in figure 4.1 and 4.2 but this time without NF_3 (process parameters are shown in table 4.2). As no trench is visible, it proves that the etching mechanism is purely chemical. The fluctuations indicate that it is not possible to accurately measure the depth of any trench shallower than about 20 nm.**

In order to obtain accurate data (and aesthetically pleasing surface graphs) when subtracting one surface profile from another, it is important that the sample be repositioned as close to its original position during examination under the interferometer after processing. This was particularly important when measuring the depth of very shallow trenches. To achieve this, three kinematic hemispheres were fixed to the sample support plate on the Zygo interferometer, in the same relative positions as those on the sample tray on the RAPT300 machine, and three 'v-blocks' were fixed to the underside of the sample support plates. Provided that the hemispheres all make contact with both sides of the V of the v-blocks and that the orientation of the V's is close to 120° of each other (the exact angle is not crucial), it should be possible to reposition the sample in the horizontal plane consistently to within 10 µm. This is an example of a kinematic coupling. Both hemispheres and the v-blocks were supplied by Bal-tec®. They are all made of hardened steel to minimise the amount of deformation at the contact points. Every effort was made to ensure that the surface was not touched by hand in between measurements.

The Zygo system includes a monitor for displaying the fringe pattern. When taking the post process measurement, it is wise to adjust the tilt so that the fringe pattern matches what it was beforehand as closely as possible. This is most important when only a small amount of material has been removed. In spite of the efforts made, it was usually necessary to make some adjustments to reposition the sample as accurately as possible. After each pre-process measurement, either a photograph of the image on the screen would be taken or a sketch of the fringe pattern would be made to aid with this repositioning strategy.

In figure 4.3a, it looks as though there is a series of concentric rings on the surface. These features are not real but are due to the instrument's error in interpreting the phase data. This leads to fluctuations of ~20 nm. It is not possible to accurately measure removal depths of smaller size. The ridges around the circumference are probably due to slight repositioning errors. In figure 4.1 there is a ridge on the right-hand side of the trench, parallel to the trench. This is due to the redeposition of titanium oxides and titanium silicates[26].

[26] Such products might include titanium IV oxide (or titanium dioxide) and titanium silicate. Titanium dioxide is a useful pigment and photocatalyst and is frequently used in making paints, sunscreen and toothpastes. Titanium silicate is used by dentists as a filling cement.

a)

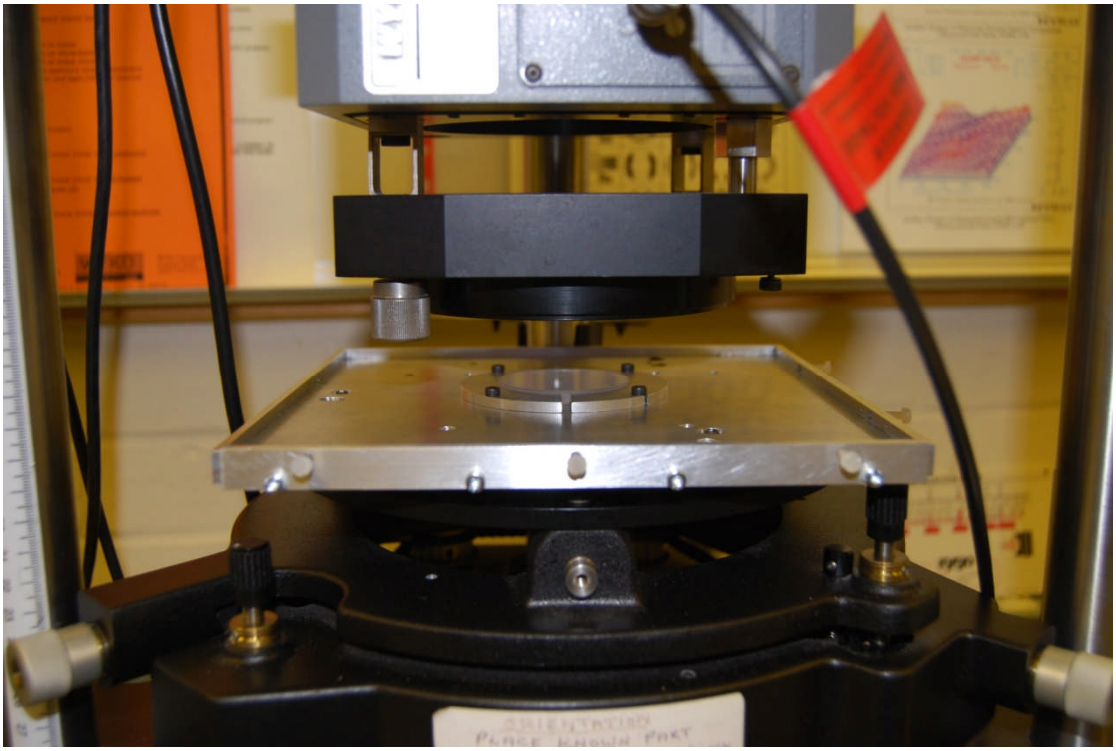

b)

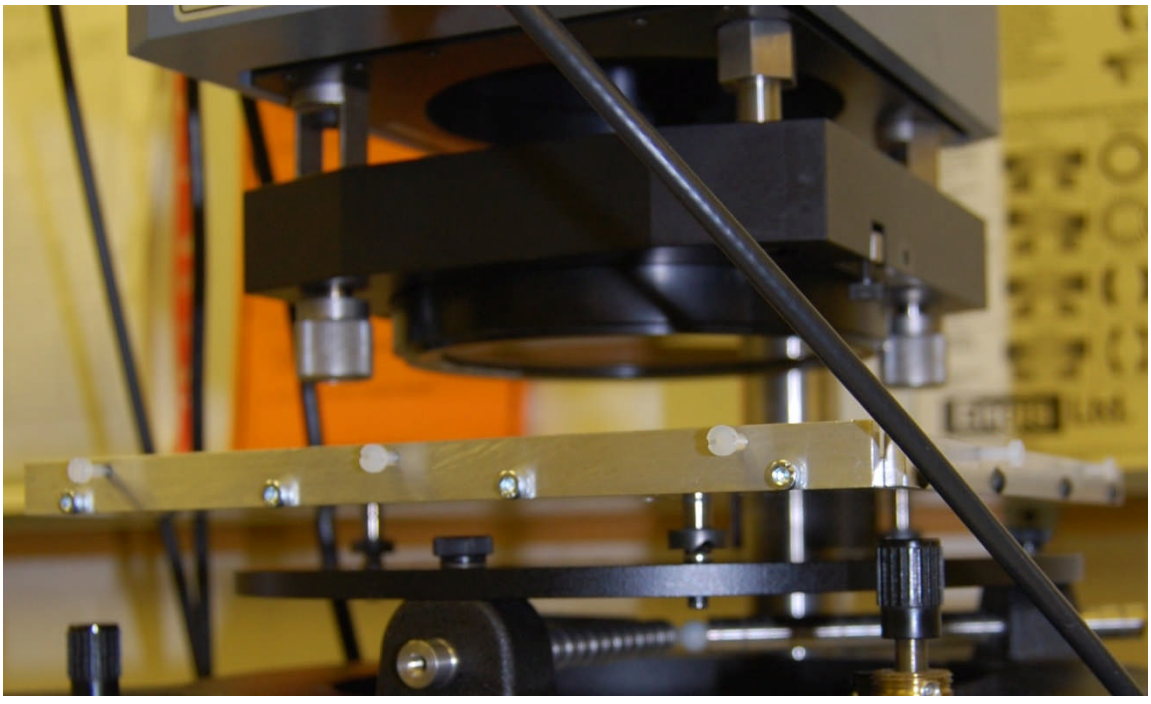

Figure 4.4 **a) a ULE disc being examined using the ZYGO PTI interferometer. b) The hemispheres and v-blocks that form a kinematic coupling to aid repositioning are visible.**

In order to establish a relationship between the depth of a single trench and the torch travel speed, a series of trenches were etched onto ULE surfaces using different torch travel speeds. The surface was measured using the Zygo PTI in between the etching of each trench. The depths of the resulting trenches are shown in figure 4.5. There was no discernible trench when using a speed of 233 mm/s. Some of the higher speed tests were repeated; there is a degree of scatter among those results. This indicates that it is difficult to predict the exact removal depths when moving the plasma at very fast speeds.

One possible explanation for the lack of repeatability might be because the exhaust fan connected to the RAPT300 machine (which removes potentially harmful gases from the laboratory) is very powerful and it is difficult to precisely regulate the exhaust flow. The flow inevitably has an effect on the ambient gas pressure in the chamber and, in turn, could affect the dynamics of the ICP. It is unlikely that the flow was set to the same value during each session.

Although pairs of points at the same speed might differ by values greater than the sizes of the error bars, the depth of these shallow trenches is generally constant along the length of the trench. Figure 4.6 shows an example of the trench etched at 133 mm/s.

Even so, the overall trend is reasonably clear. If the material removal rate were always the same, the trench depth would be directly proportional to the reciprocal of the torch travel speed (it had already been established that the widths of the trenches are invariant of the travel speed). If that were the case exactly, all the points in the graph on figure 4.5b would fall on a straight line that passes through the origin. However, as mentioned in section 2.5.2, the rate at which chemical etching takes place is temperature dependent. The surface probably has to warm up a certain amount for it to be possible for etching to initiate and then further heating increases the reaction rate. When the torch is moving at high speeds (>233 mm/s) it doesn't spend enough time over any point of the sample to create a trench. When it moves at very slow speeds, the surface warms significantly and the material removal rate becomes higher than what one might expect.

a)

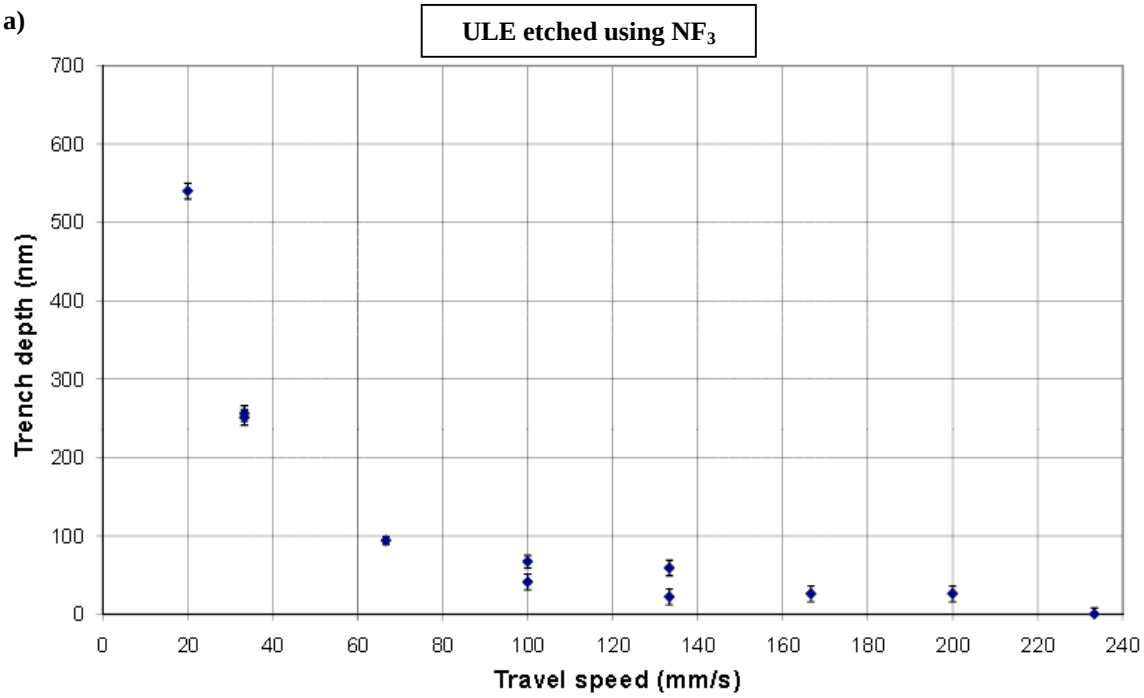

b)

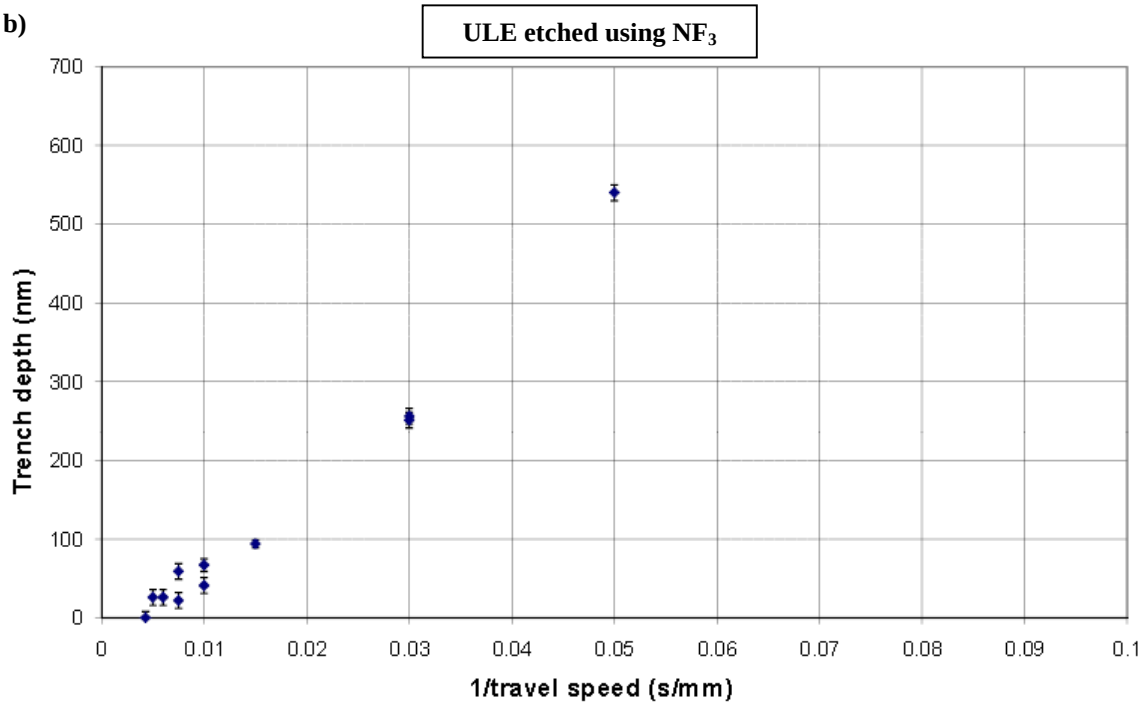

Figure 4.5 **a) The depths of trenches, etched on ULE discs, using NF_3, plotted against the torch travel speeds. b) The same data, but the trench depth is plotted against the reciprocal of the travel speed.**

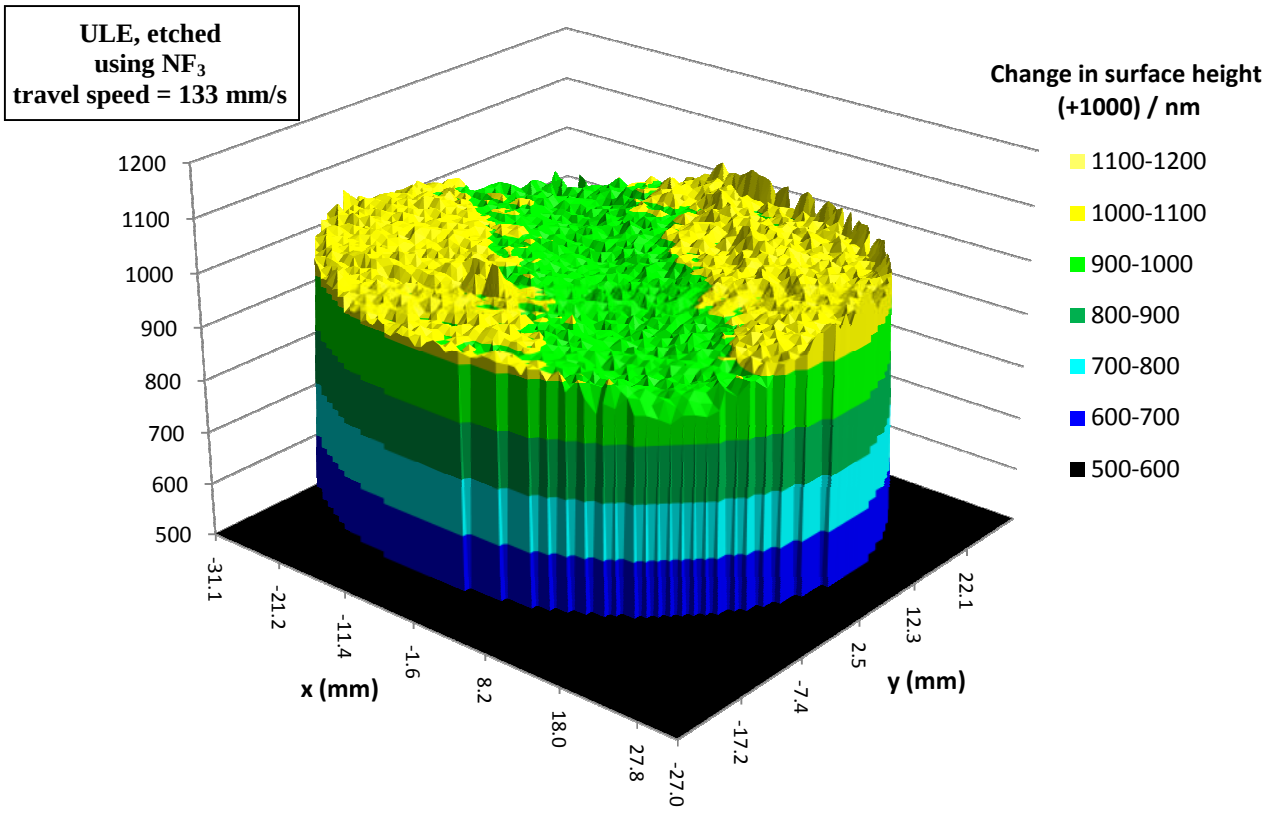

Figure 4.6 **A very shallow trench (central depth 59 ± 10 nm) etched using NF_3. The travel speed was 133 mm/s.**

Another set of depth measurements were made when etching trenches onto ULE using SF_6. The parameters used are shown in table 4.3 (on page 106) and the results are shown in figure 4.7. The flow of SF_6 used was only 15 sccm (10% of 150 sccm), very much less than that used with NF_3 (80 sccm, 20% of 400 sccm). This was done because it was not possible to achieve a stable plasma when using a higher flow with SF_6 ,the mass flow controllers could not maintain a steady flow and would cause the machine to be switched a few seconds after ignition. The material removal rate using SF_6 was lower than that obtained when using NF_3, as a result of the lower flow used. The fact that a molecule of SF_6 contains twice as many fluorine atoms as one of NF_3 compensated to a degree.

Figure 4.8 shows the same data as was shown in figures 4.5 and 4.7, but in terms of volumetric removal rate (the volume of material removed in creating the trench divided by the period in time over which the plasma was over the surface). If one were to assume that all of the material removed is a result of the following chemical reaction

$$4F\bullet(g) + SiO_2(s) \rightarrow SiF_4(g) + O_2(g),$$

the proportion of all fluorine atoms that passed through the plasma that ultimately react with the surface material in the creation of these trenches is given in Figure 4.8b.

a)

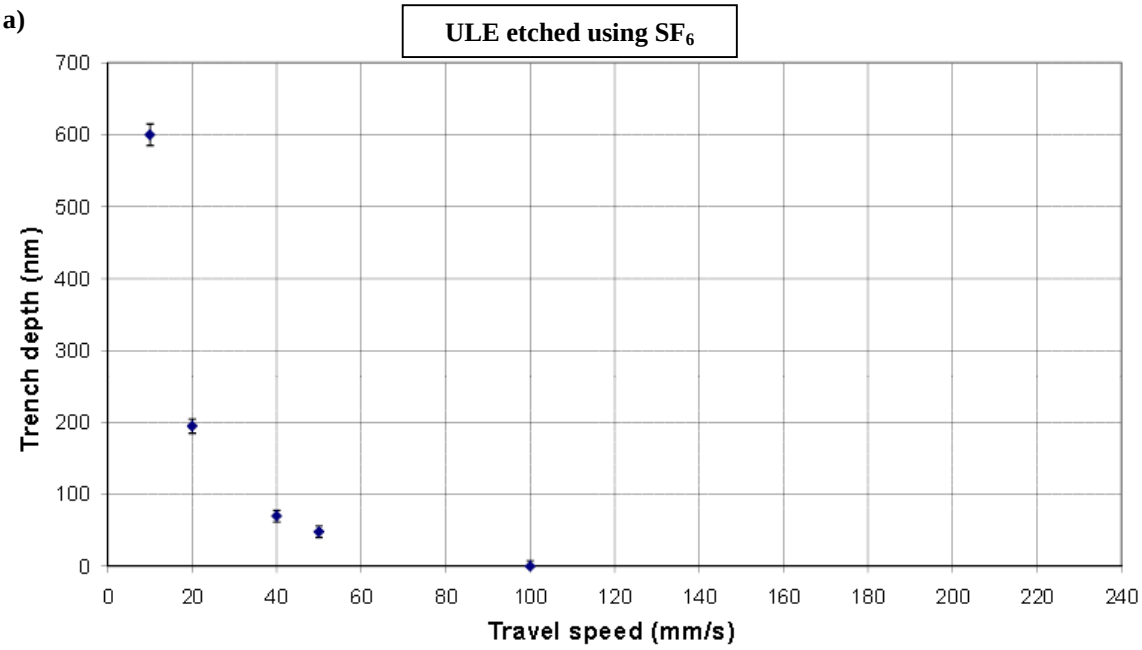

b)

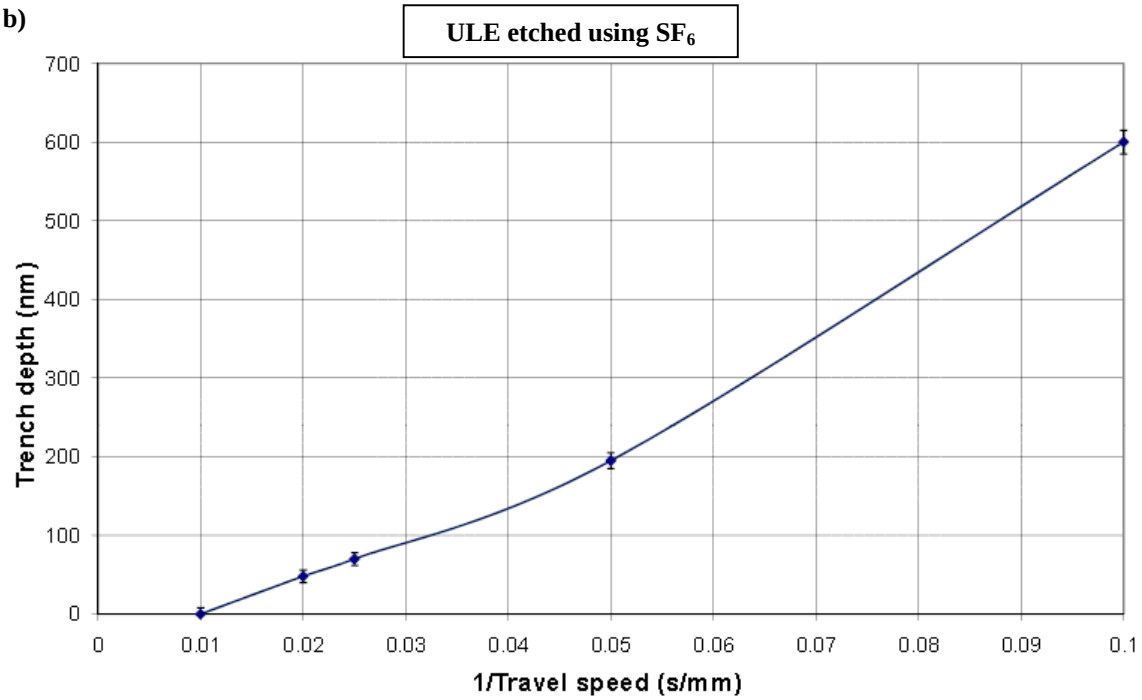

Figure 4.7 **a) The depths of trenches, etched on ULE discs, using SF_6, plotted against the torch travel speeds. b) The same data, but trench depth is plotted against the reciprocal of the travel speed.**

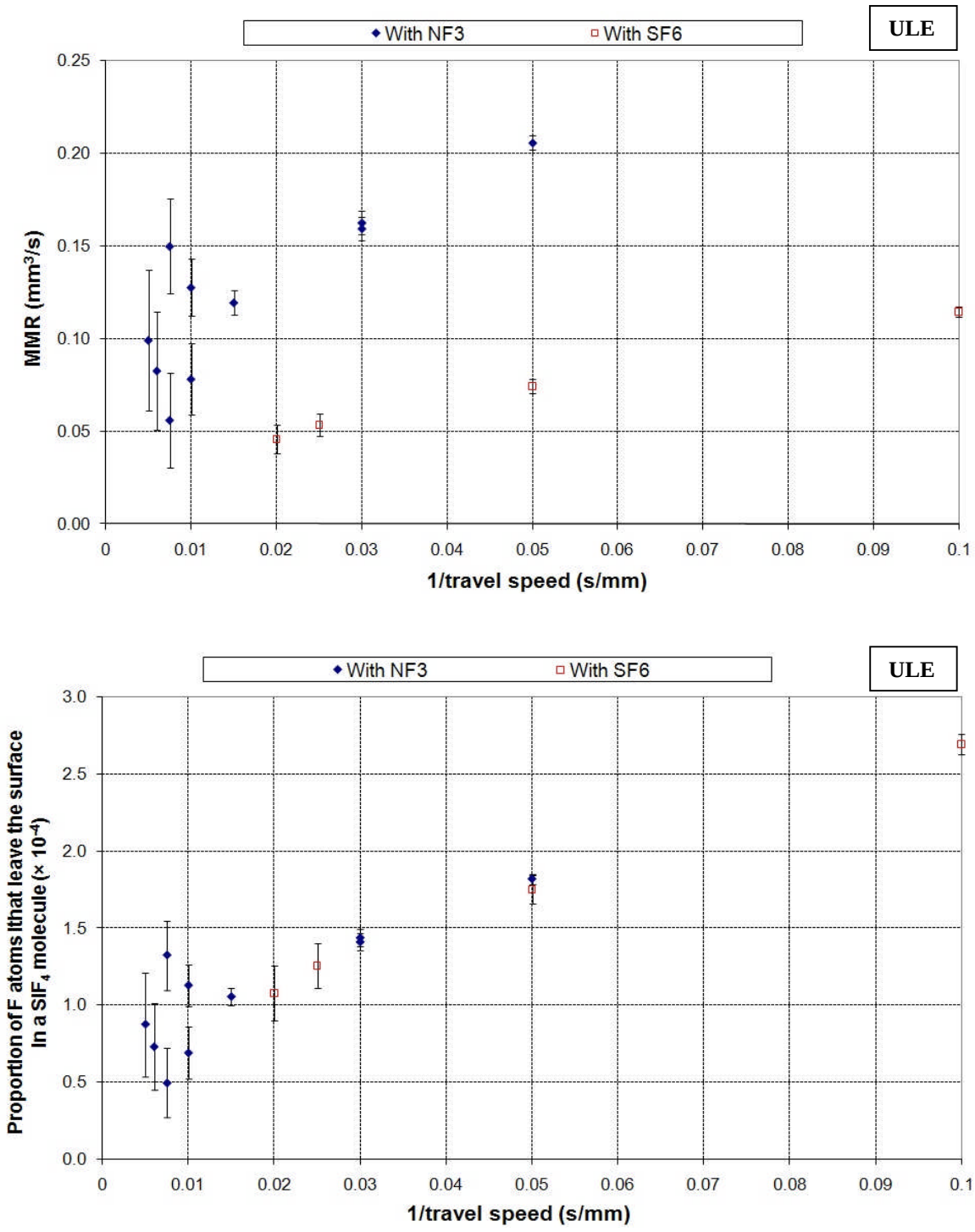

Figure 4.8 **a) The volumetric material removal rates, calculated from the single trench profiles that resulted when ULE was etched using NF_3 and SF_6. b) The proportion of all the fluorine atoms passing through the ICP that ultimately react with the surface material and leave as part of a SiF_4 molecule, assuming that that is the only gaseous product containing those atoms.**

The deposition ridges were very much more prominent alongside the trenches etched using SF_6 than those etched using NF_3. Figure 4.9 shows one such example, indeed, the ridge on one side is so steep that the interferometer was unable to cope with the gradient (hence the chasm in the surface graph). As was mentioned in section 2.5.2, using SF_6 as an etchant can lead to the formation of polymeric residues, so the mountains might not be purely due to titanium oxides and silicates. Solid sulphur or sulphur-containing compounds might be present too.

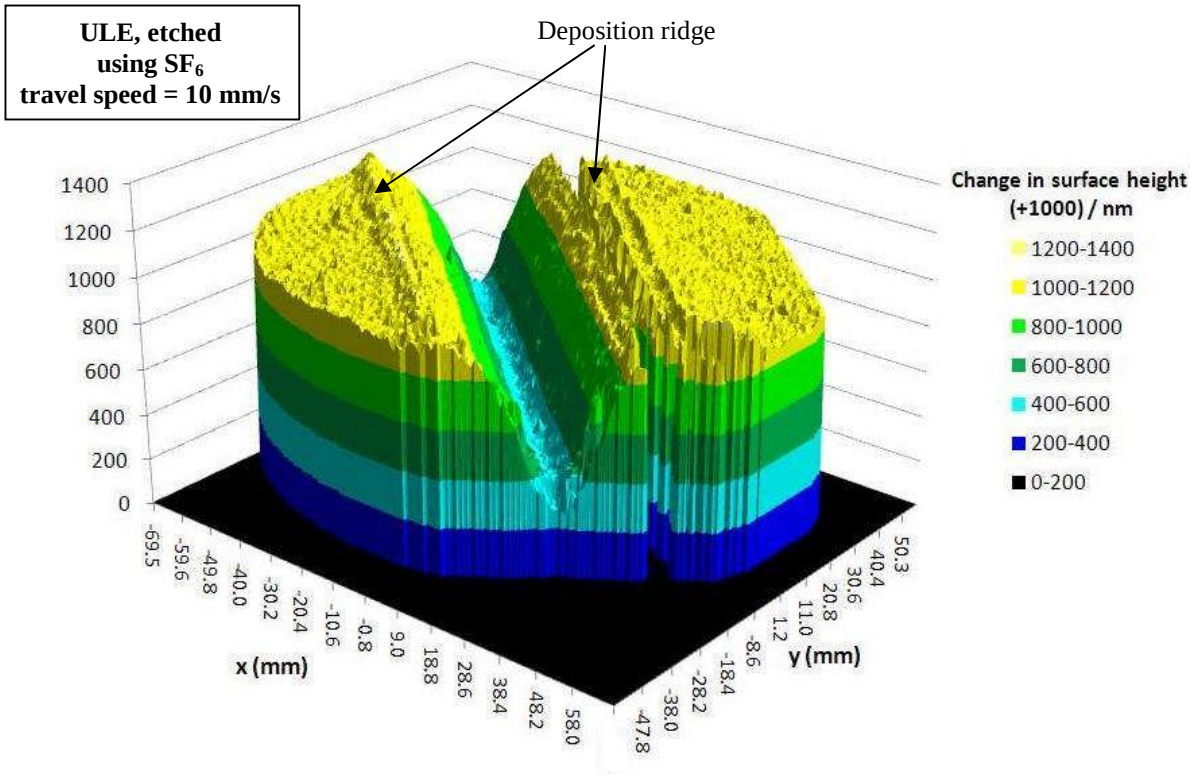

Figure 4.9 **A trench etched on ULE using SF_6. The travel speed was 10 mm/s. Steep ridges of deposited material formed parallel to the trenches, so steep that the interferometer could not cope.**

4.1.1 Neutral removal tests

A number of neutral removal tests were carried out upon 100 mm × 100 mm ULE surfaces. The plasma torch was rastered across the surface in both the serpentine and staggered fashions described in section 2.7. Copper strips were fixed along the edges of the samples, covering about 15 mm on each side, to mask those areas so that they would not be etched (these are visible in figure 4.10). This was done to make it easier to calculate the volume of material that was removed over the rest of the surface. Figure 4.11a shows a cross-section of the post-pre data that resulted when the surface was etched in a serpentine fashion (torch travel speed was 133 mm/s, 1 mm pitch). Clearly, different amounts of material have been removed from different parts of the surface. This is expected to be due to the increase in etch rate that resulted from local temperature build-up on the part. Figure 4.11b shows the result of a similar test, except that this time a staggered rastering pattern was used. The trench depth is roughly the same all the way across, although some mid-spatial features appeared on the surface.

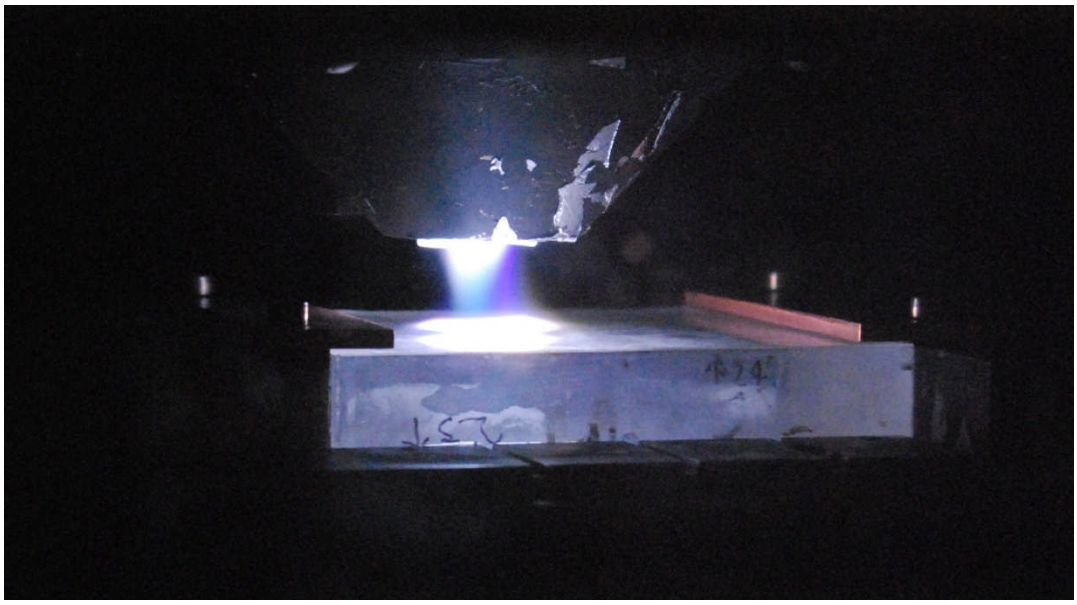

Figure 4.10 **A ULE surface being rastered. Copper strips have been fixed into position so as to mask strips of the surface. This was done so that the amount of material removed at different positions could be easily visualised in the 'post-pre' profile.**

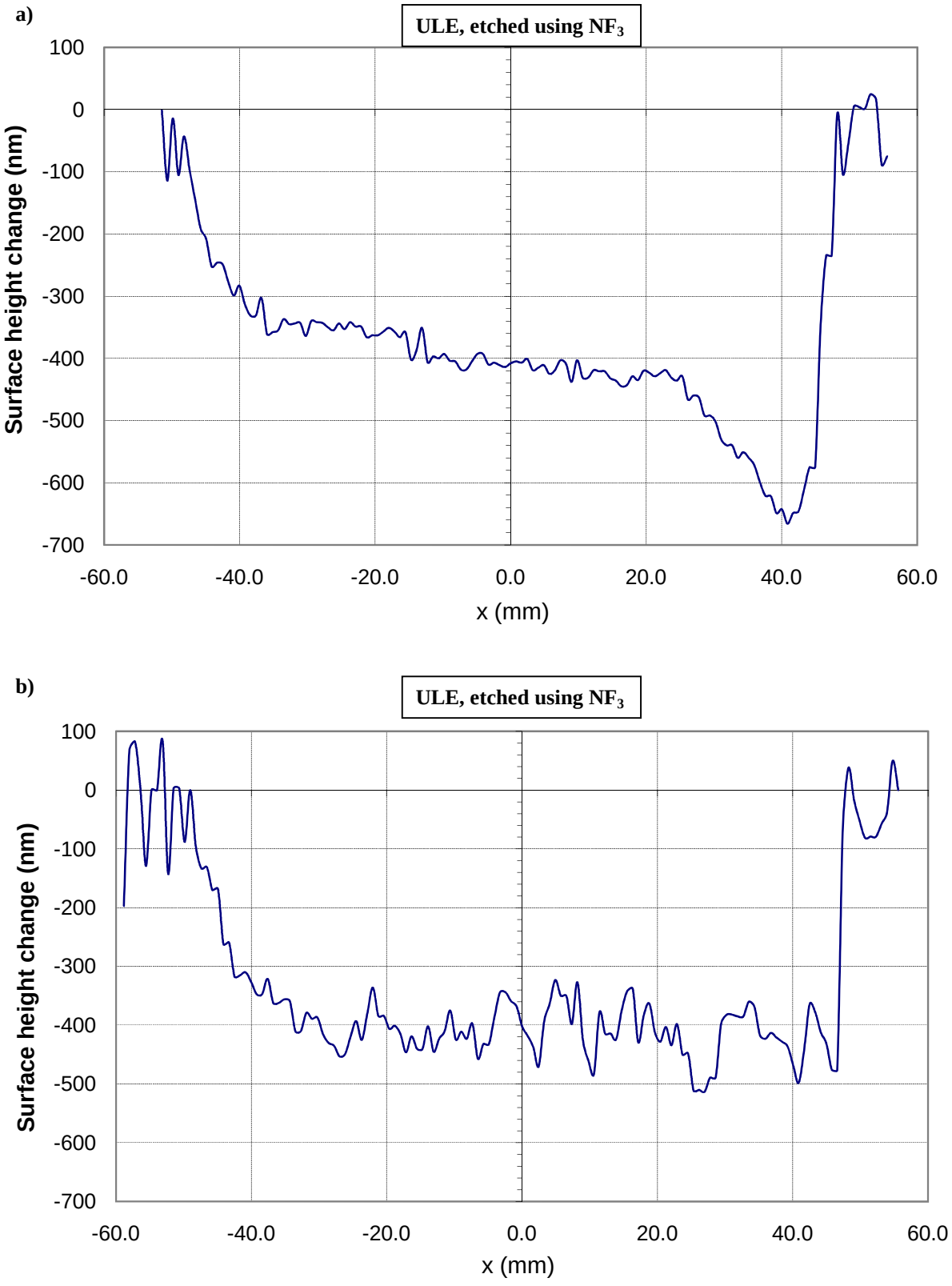

Figure 4.11 **Surface profile changes (central cross-section) that resulted after neutral removal was performed upon 100 mm × 100 mm ULE surfaces. a) The result following serpentine rastering (torch travel speed was 133 mm/s, 1 mm pitch). b) The result following staggered rastering (torch travel speed was 133 mm/s, 1 mm pitch and 15 mm stagger length).**

4.2 ULE Surface roughness measurements

The Talysurf 6000 Coherence Correlation Interferometer (hereafter known as the CCI) was introduced in section 3.2.2. It is a powerful instrument for measuring surface roughness. It was used extensively for that purpose while investigating the RAP process, frequently on the same surfaces upon which the material removal tests described in the previous section were made. Roughness measurements were made at various points on the surface to see how it was affected by the process. All of the roughness measurements given in this chapter are Sa values, the average modulus of the deviation in height from the average level from samples taken over a two-dimensional area (this is defined formally in appendix A). The values have not been filtered in the analysis. As the area examined for each sample is fairly small (0.9 mm × 0.9 mm is the largest sample area) only features of spatial size <0.9 mm contribute. Using the TalyMap Gold software, it is very straightforward to apply an 80 μm wide Gaussian filter. The Sa values of the higher frequency components (which could be referred to as the mid-spatial frequency Sa roughness) were invariably very close to the unfiltered value. The Sa values of the lower frequency components[27] were invariably much lower. In other words, it is the smaller features, of characteristic size 80 μm or smaller, that chiefly contribute to the quoted roughnesses.

Absolute roughness values frequently come under scrutiny as any determined value depends somewhat on the instrument used, the exact measurement procedure and the routines used for analysis. However, if a measurement is taken before carrying out a process on the surface (such as etching a trench) and then another measurement is taken after the process, using exactly the same procedure, a change in the calculated roughness indicates a change has taken place on the surface. It is therefore possible to assess whether the action taken improves or worsens the roughness of the surface.

In some preliminary tests, ULE surfaces (100 mm × 100 mm) were rastered in a serpentine fashion using different parameters and their roughnesses were measured before and after processing. The results are displayed in table 4.4. In each case, the results shown are the average of nine measurements taken at different positions, all within the etched region. The standard deviation values are given in brackets. NF_3 was the etchant used. The CCI was used with the 50 × objective. The method used for acquiring the data is described in appendix C. In all instances, the surface roughness roughly doubled.

Table 4.4 **Mid-spatial frequency roughness values measured upon four 100 mm × 100 mm ULE surfaces. The values quoted are Sa values (arithmetical average surface height deviation over an area from the mean over that area). The mean from nine measurements at different positions, equally spaced over the surface are displayed. The value in brackets is the standard deviation of that set of measurements.**

Surface	Travel speed (mm/s)	Pitch	Sa (nm)	
			Pre process	Post process
1	133.3	3.25	1.4 (0.1)	3.2 (1.8)
2	133.3	6.5	1.3 (0.2)	3.2 (0.4)
3	133.3	3.7	2.2 (1.0)	3.3 (1.7)
4	133.3	6.5	1.4 (0.1)	2.8 (0.5)

[27] Low spatial frequency roughness is often known as waviness.

Several of the trenches, whose depths are plotted in figure 4.5, were etched on the same ULE surface discs (∅50 mm × 5 mm thick). The order in which the trenches were etched is listed in table 4.5. The torch made the same path across the surface in all instances (the trenches were superimposed). The roughness of the surface was measured before processing, and then after trench 1, after trench 2 and after trench 5. These measurements were taken using the Talysurf Coherence Correlation Interferometer (CCI) with the 20 × objective; thus the viewing area was 900 μm × 900 μm. Figure 4.12 shows how the surface roughness (unfiltered Sa) evolved. The largest increases take place at the edges of the trenches, due to redeposition. The heat from the plasma is probably sufficient to evaporate away most of the material deposited on the trench path.

The increase in surface roughness resulting from the etching within the trench region is probably at least partly due to redeposition. Another contribution to the roughening, observed during both the rastering tests and the single trench tests, might be selectivity. As was mentioned in section 2.5.2, chemical etching processes are more selective than sputtering processes, meaning that they attack some materials very much more quickly than others. ULE primarily consists of SiO_2 and TiO_2; fluorine radicals will inevitably etch one material more favourably than the other. In section 2.6.1, investigations conducted by Kurushima *et al.* were discussed [**117**, **118**]. In their investigations, the surface roughnesses that resulted when IBF was applied to ULE were lower than those that resulted when IBF was applied to Zerodur. The difference was attributed to the fact that ULE has a more homogenous composition. In spite of its high homogeneity, it is still possible that selectivity might result in some surface roughening. This hypothesis could be tested by repeating this experiment using fused silica instead of ULE.

Surface roughnesses were also measured, in between the etching of trenches when SF_6 was used, which were described earlier and whose depths are shown in figure 4.7. The order in which trenches were etched is listed in table 4.6 and the roughnesses are shown in figure 4.13. The Sa values inside the trench region remain <3 nm, as before. The resulting roughnesses outside the trench region were so high that a logarithmic scale is shown in figure 4.13a. The depth of the trenches when etching with SF_6 were considerably shallower than those etched using NF_3 for a given travel speed, and yet levels of deposition away from the trench area are very much higher. The first pass to even leave a discernible trench was pass number 4, and yet an Sa of 19.3 was measured. It is difficult to see how this greater increase in roughness could be purely due to titanium deposits. This supports the hypothesis that polymeric substances form within the plasma and leave a residue on the surface.

Subsequent research at Cranfield has shown that it is very easy to clean small ULE sample surfaces after they have been etched by SF_6. Cleaning surfaces that have an area ~1 m^2 by hand would be a more formidable task. It appears that the heat from the plasma is effective at evaporating away redeposition, so perhaps the easiest way to remove it would be to raster the finished surface using the pure argon plasma. Another solution might be to add oxygen to the discharge, which can help suppress the formation of polymeric residues, as was mentioned in section 2.5.2.

In the RAPT Helios 1200 machine, the plasma torch etches the material from underneath so that gravity can prevent some of the non-gaseous reaction products from

settling on the surface. It would be interesting to repeat the tests on fused silica to found out whether the roughness increases after etching.

Table 4.5 **5 torch passes were made on the same ULE surface using NF_3**

	Torch travel speed (mm/s)
1	33.3
2	33.3
3	66.7
4	100.0
5	133.3

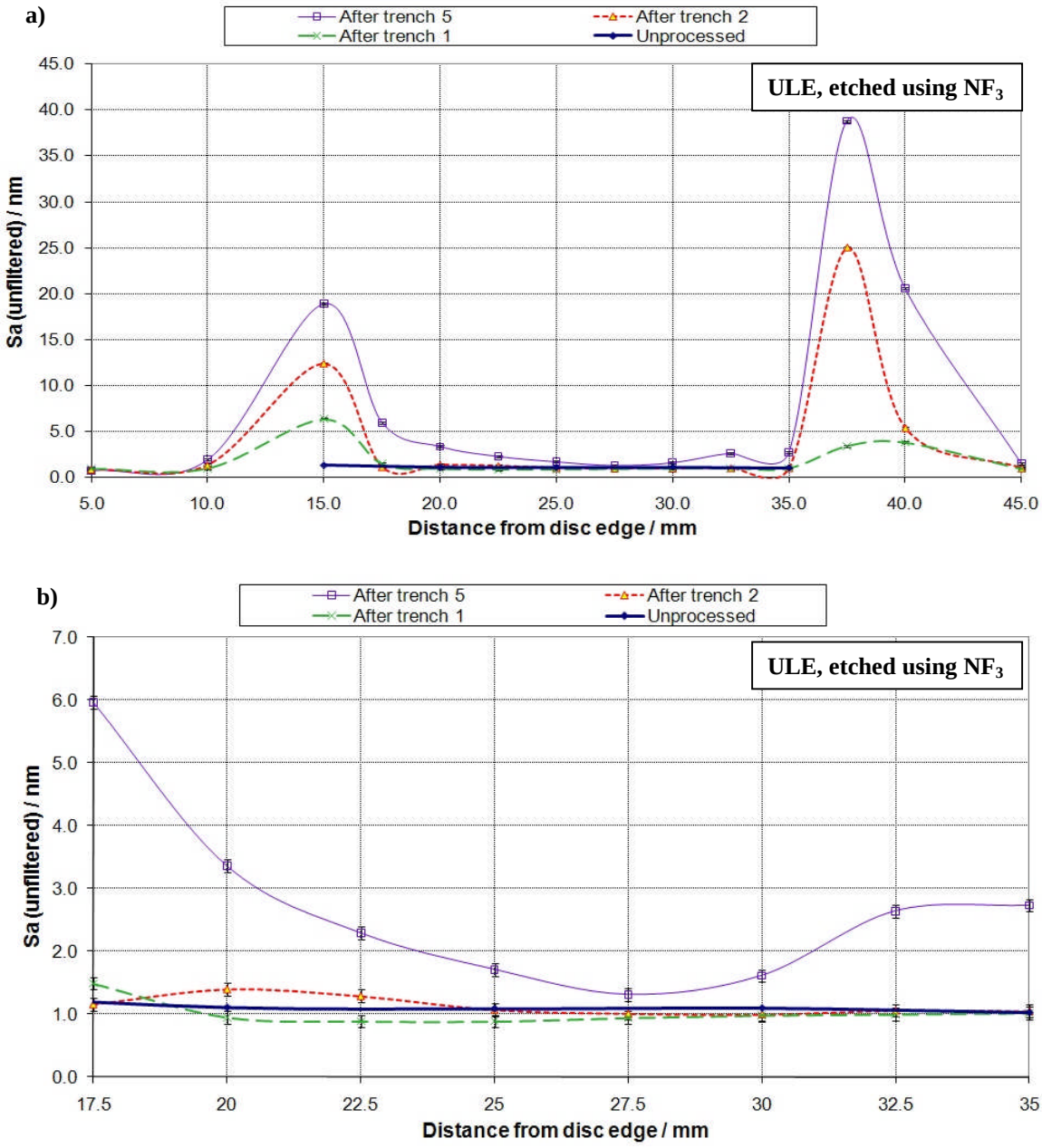

Figure 4.12 **a) The evolution of the surface roughness across the width of a ULE disc as trenches were successively etched upon it using NF_3. b) Central portion of the same profiles.**

Table 4.6 **8 torch passes were on the same ULE surface using SF_6.**

	Torch travel speed (mm/s)
1	250
2	200
3	150
4	100
5	50
6	40
7	20
8	10

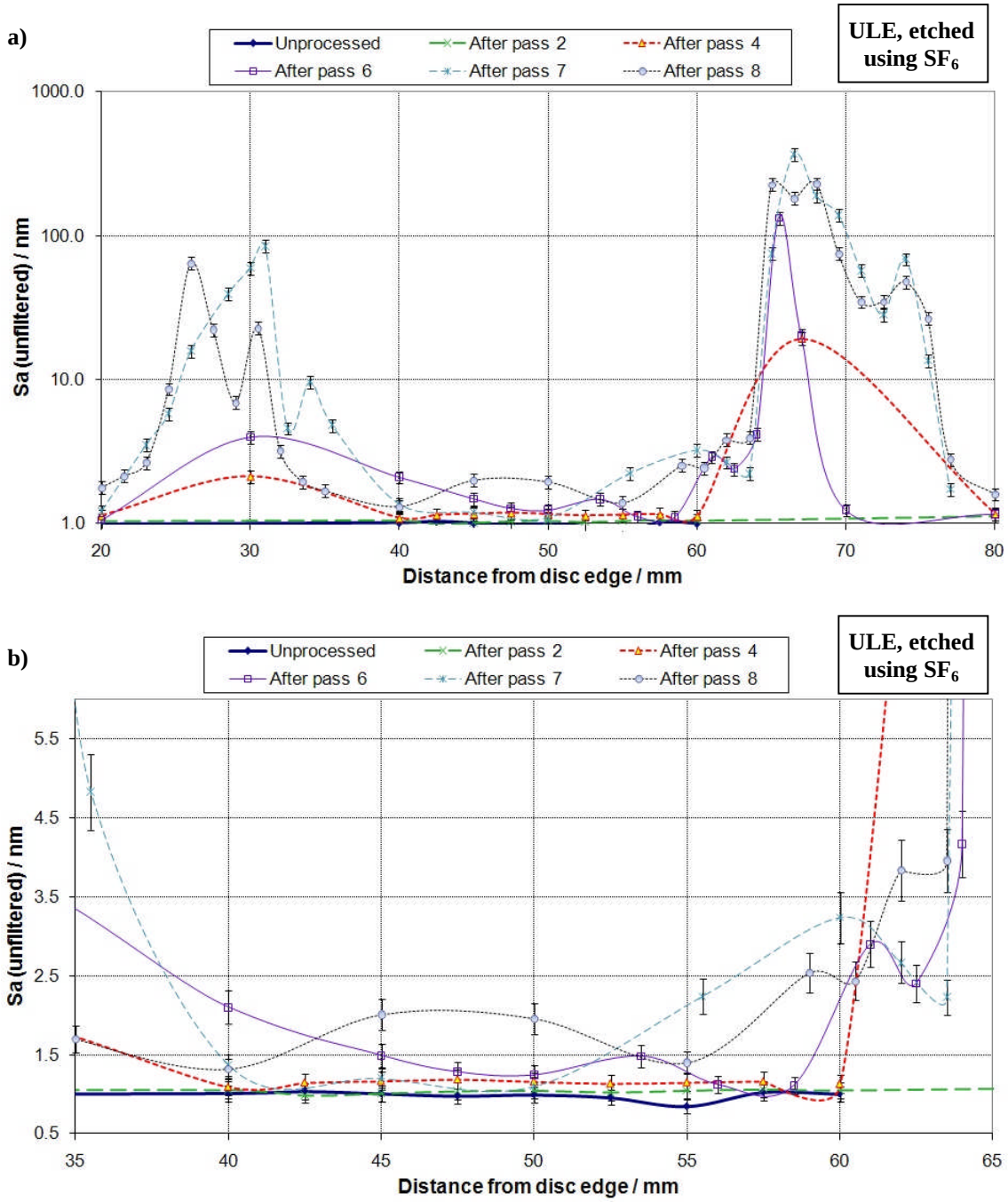

Figure 4.13 **a) The evolution of the surface roughness across the width of a ULE disc as passes were successively etched upon it using SF_6. b) Central portion of the same profiles.**

4.3 Preliminary tests on other materials

4.3.1 Silicon

Some single trenches were etched onto plates of silicon (100 mm × 100 mm × 5 mm thick). Trenches were etched using various travel speeds with NF_3 using the parameters given in table 4.1. The depths of these trenches were measured using the Fisba FST10 with the 100 mm lens and are plotted in figure 4.14. The points in the graph in figure 4.14b are rather closer to forming a straight line than those in figures 4.5b and 4.6b. The net material removal rates have been calculated from these trenches and are displayed in figure 4.15a. The MRR is more consistent than was the case with ULE, although there is a certain amount of scatter in the points resulting from faster travel speeds ($\approx$0.1 mm^3/s).

The most likely reason as to why RAP's MRR on silicon is less dependent on the travel speed than it is on ULE is because silicon has a much higher thermal conductivity (124 $Wm^{-1}K^{-1}$, as opposed to 1.31 $Wm^{-1}K^{-1}$ in the case of ULE). The heat from the plasma inevitably dissipates through silicon samples very much more quickly. As the plasma is moved on to a particular point on the surface, the temperature rises at that position to an equilibrium point very quickly. Thereafter the heat dissipation through the sample compensates for what it receives from the plasma. The samples were placed on an aluminium tray, a material with an even larger thermal conductivity. When etching ULE, it takes much longer for such an equilibrium point to be reached.

The fact that the removal rate of silicon is lower than that of ULE when using the slower travel speeds suggests that the chemical reactions are taking place at a much lower temperature when silicon is used (regarding figure 2.43). Indeed, it suggests that the temperature difference might be greater than 200°C.

The trenches concerned were etched on separate polished silicon surfaces (two on each surface, side-by-side). Surface roughnesses were measured before and after etching. The unfiltered Sa of all the unetched surfaces was 1.0 ± 0.1 nm. After etching, the Sa in the regions away from the trenches remained virtually unchanged. However, within the trench regions there were significant increases in roughness and the increase depended on the trench depth. In many instances, it was clear by simple observation that there was an increase in roughness (see figure 4.17). Figure 4.16 shows the unfiltered Sa at the base of the trench, plotted against the central trench depth. This is the result of newly exposed silicon becoming oxidised.

a)

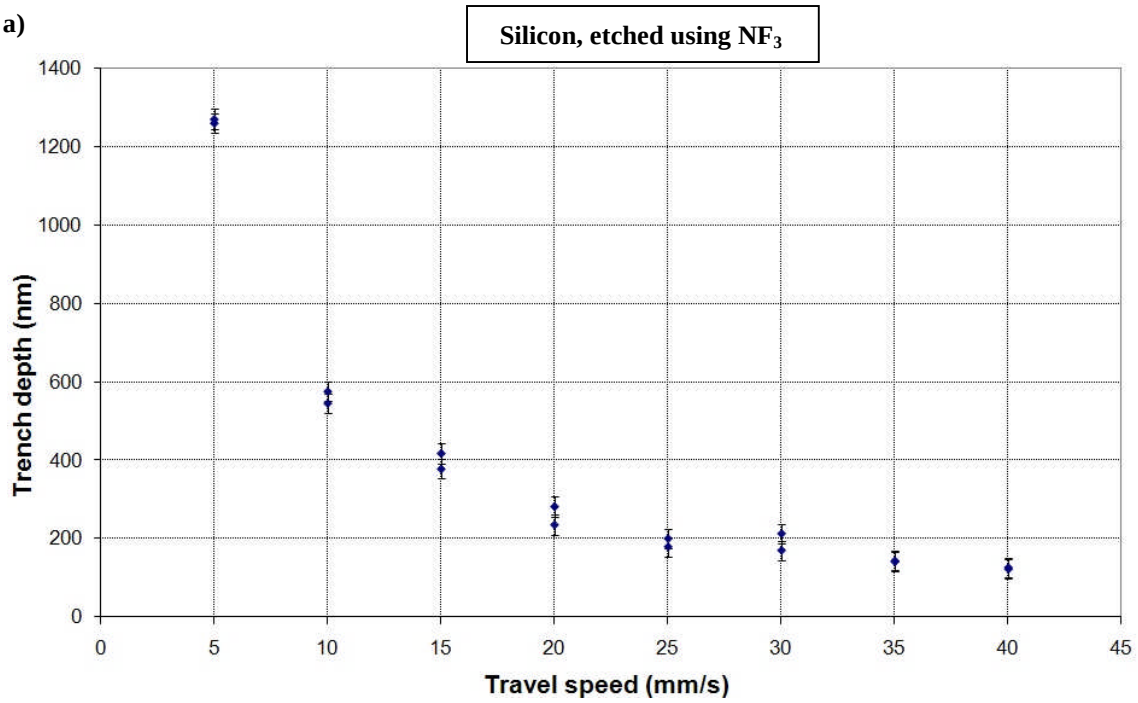

b)

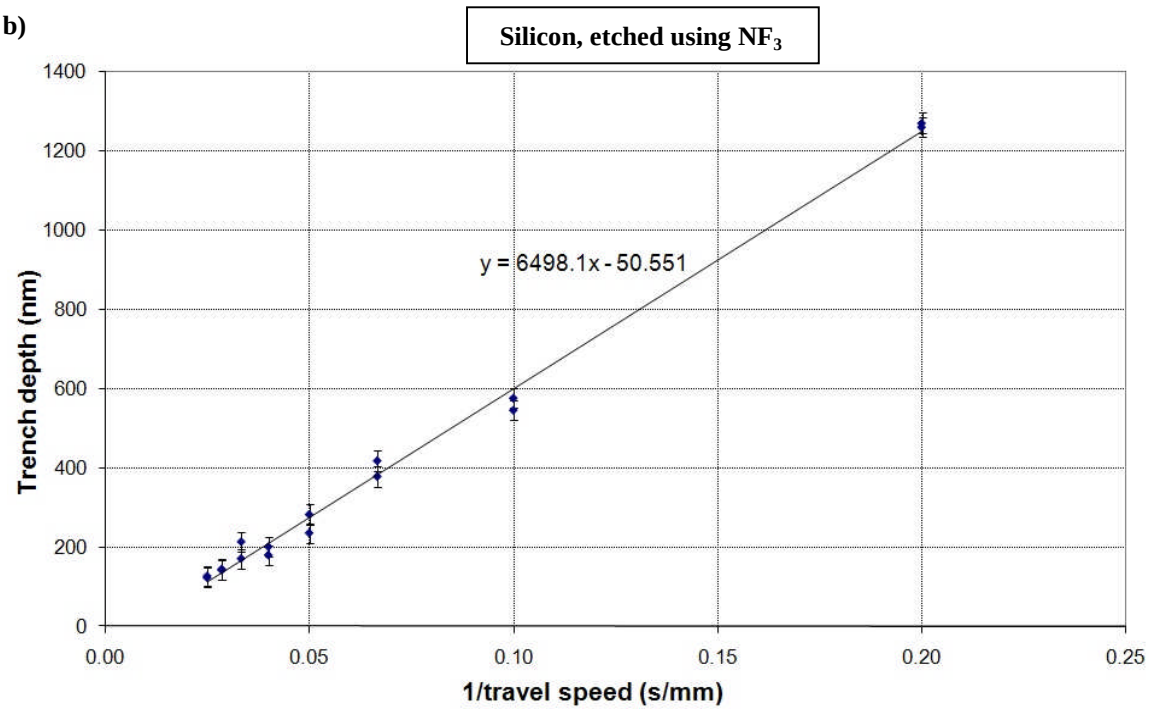

Figure 4.14 **a) The depths of trenches, etched on silicon plates using NF_3, plotted against the torch travel speed. b) The same data, but trench depth is plotted against the reciprocal of the travel speed.**

a)

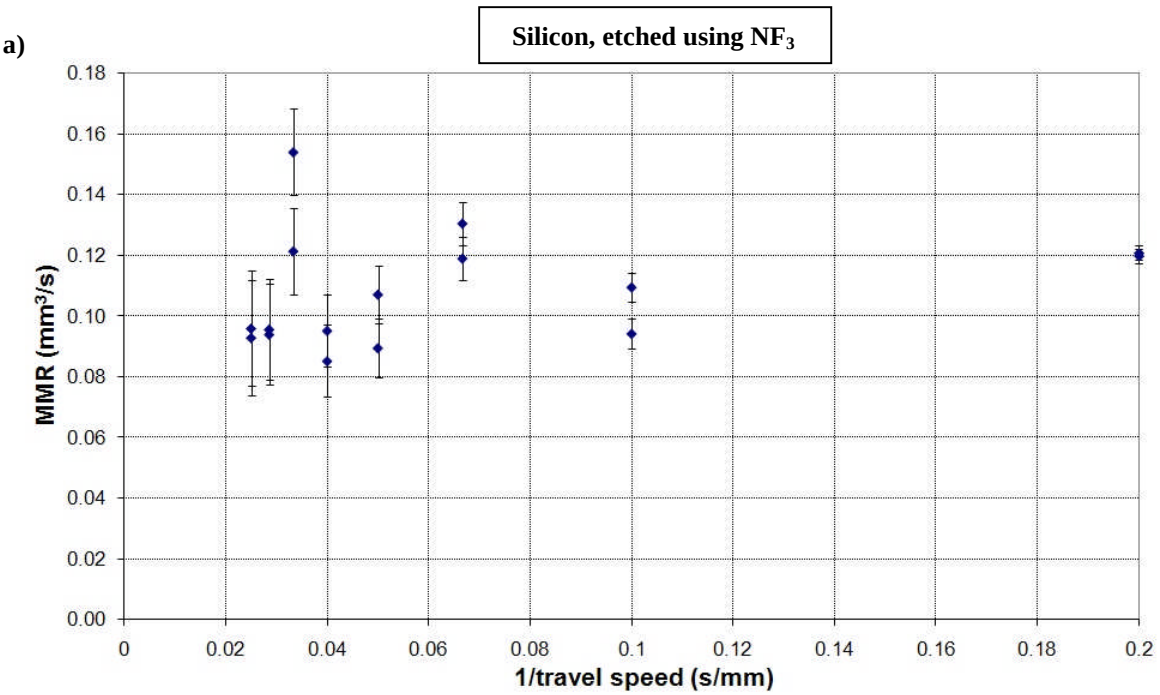

b)

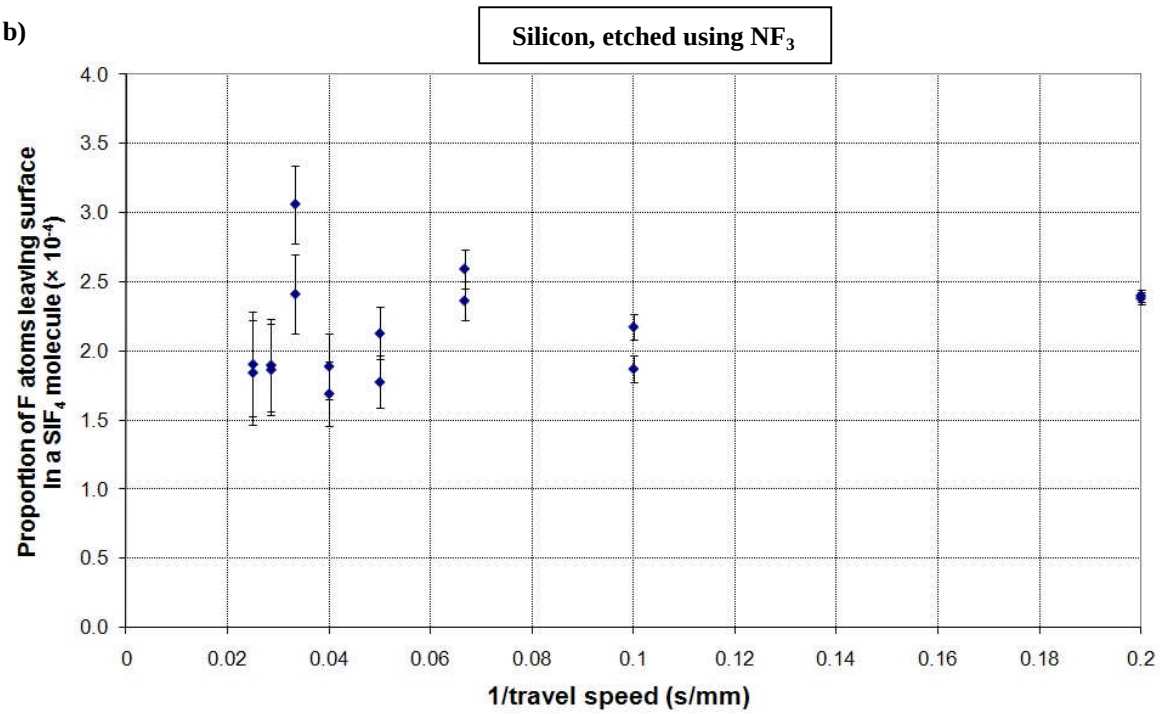

Figure 4.15 **a) The volumetric material removal rates, calculated from the single trench profiles that resulted when silicon was etched using NF_3. b) The proportion of all the fluorine atoms passing through the ICP that ultimately react with the surface material and leave as part of a SiF_4 molecule, assuming that that is the only gaseous product containing those atoms.**

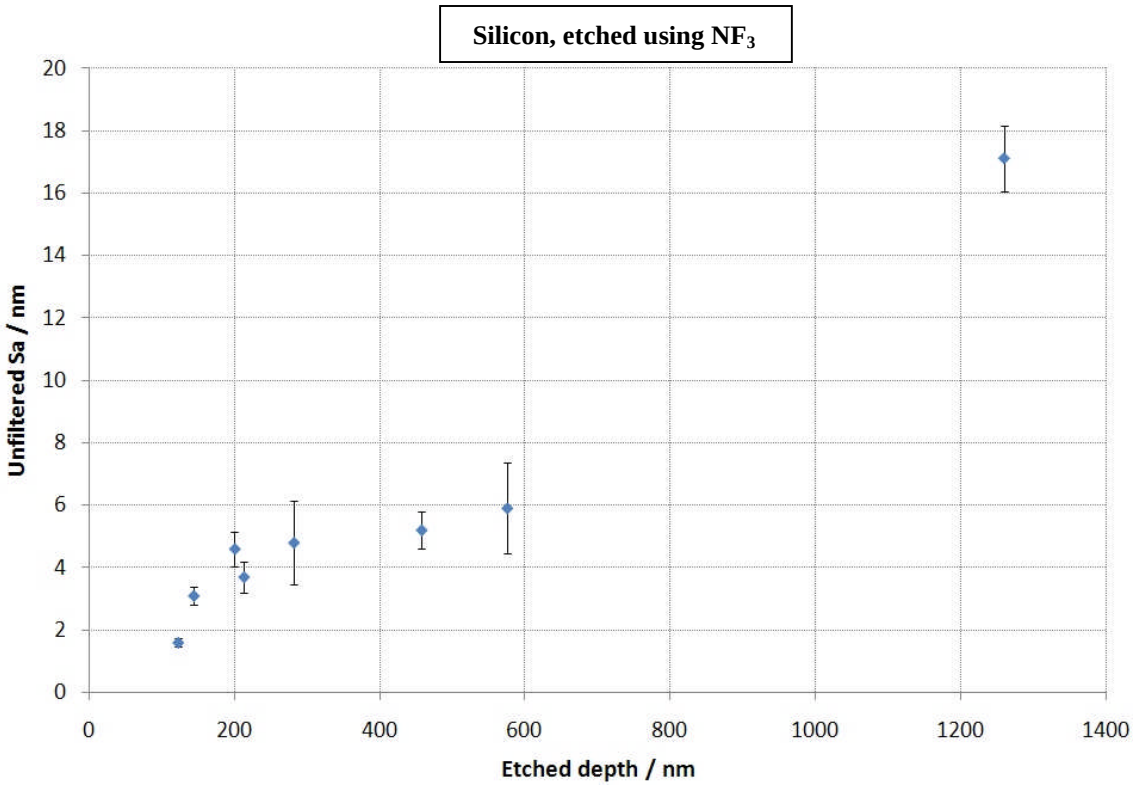

Figure 4.16 **The surface roughness (unfiltered Sa), measured after etching at the centre of trenches etched onto polished silicon surfaces. The Sa before etching was 1.0 ± 0.1 nm.**

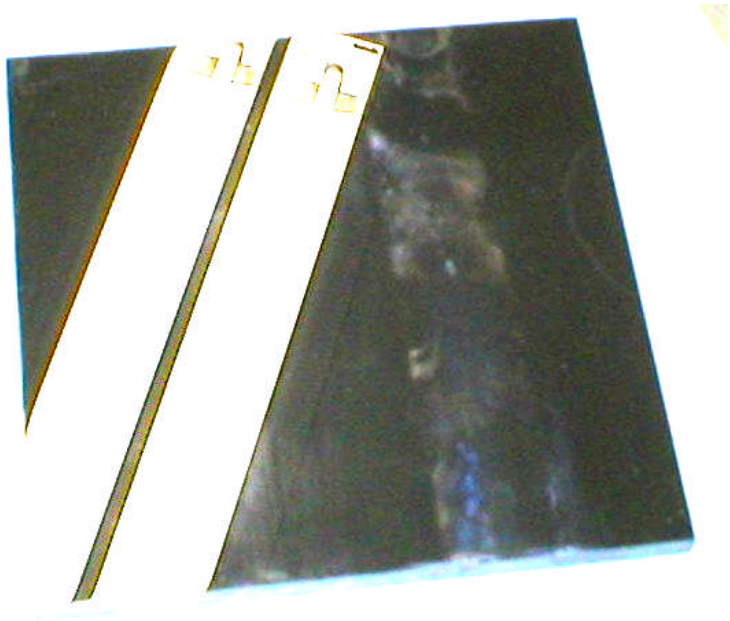

Figure 4.17 **A silicon sample after a trench has been etched upon it. The oxidation on the surface is quite apparent.**

4.3.2 Zerodur

Some tests were performed on Zerodur at Cranfield to confirm reports that RAP is ineffective at etching it because of its alumina content. Two trenches were etched side-by-side onto a ground surface with a torch travel speed of 10 mm/s (one with two passes) and the sample was pre-warmed to 200°C. The resulting surface was measured using a stylus profilometer and the profile is shown in figure 4.18. As the surface had not been polished, it was not sufficiently reflective for it to be possible to use any of the optical metrology equipment.

It was fairly clear that some material had been removed by these passes. However plateaus of visually opaque material appearwed along the centre of the trenches. The origin of all this material is not known, but it is it likely that chemical reactions are producing non-volatile (and chemically resistant) products.

This one test confirmed that RAP is not suitable for the figure correction of Zerodur optics.

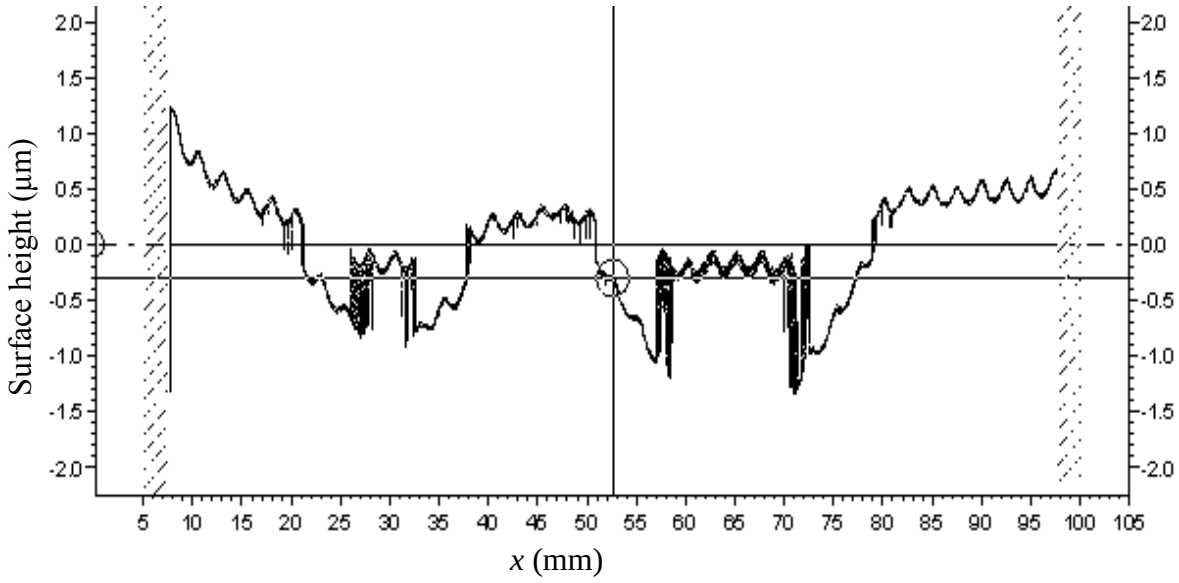

Figure 4.18 **A cross-section through the trenches etched onto Zerodur. Measurements were made using a stylus profilometer.**

4.4 Summary of material removal and roughness tests

Early research carried out at Cranfield using the RAPT300 machine concerning the material removal rates and surface roughness measurements has been discussed in this chapter. Most of these were performed on ULE and on silicon.

Some material removal experiments on ULE had been performed previously by passing the plasma torch across the surface at slow speeds, which were reported in [**135**]. Some new tests were performed, using a lower torch power 1 kW, and faster torch travel speeds to see if it is possible to establish a relationship between torch travel speed and removal depth. This was done by measuring surface profiles before and after etching and subtracting one from the other. Some removal depths <50 nm were measured. No discernible removal was measured at travel speeds above 200 mm/s when etching ULE with NF_3. When the removal depth was plotted against the reciprocal of the travel speed, there were deviations from the linear relationship that one might expect; meaning that the material removal rate is faster at slower travel speeds. This is expected to be due to increased local heating of the region immediately under the plasma. The chemical reaction rate, and hence the material removal rate, is temperature dependent. Material removal rates up to 0.2 mm^3/s were recorded. At the faster removal rates there is some scatter in the distribution of resulting removal depths. The repeatability of the process might be limited when trying to remove material depths <100 nm, at least when using the prototype RAPT 300 machine. A similar set of tests were conducted using SF_6 as the precursor gas. A significantly lower reactive gas flow rate of 15 sccm was used (80 sccm was used with NF_3); the material removal rate was lower as a result. It was not possible to maintain a stable plasma with a flow rate of SF_6 higher than 15 sccm.

The effects that the process has on the roughness of ULE surfaces were investigated using both NF_3 and SF_6. Such work was often done in parallel with the material removal tests (i.e. the same surfaces were used). The unfiltered Sa of the surfaces before etching were ≈1 nm. This value approximately doubled within the regions where material was removed. This might be primarily the result of the redeposited material. It might also be due to selectivity, meaning that the fluorine atoms might react with SiO_2 more favourably over TiO_2, or vice versa. It was noticed that a significantly larger quantity of material was deposited outside of the trench region when SF_6 was used. It could be that, in addition to the deposition of titanium oxides and silicates, polymeric residues (containing sulphur and fluorine) formed within the plasma are deposited as well.

The material removal rate of the process when applied to silicon was found to be very much less dependent on the torch travel speed than was the case of ULE. This is expected to be because silicon has a much higher thermal conductivity. As the plasma is moved on to a particular point on the surface, the temperature rises to an equilibrium point much more quickly; heat is then dissipated through the material as fast as it is received from the plasma and so the removal rate remains constant.

No discernible material removal was observed when the process was tried upon Zerodur using slow torch travel speeds, confirming reports from RAPT Industries that the process is not effective on Zerodur.

5 Spectroscopic Measurements

In chapter 4, material removal tests were carried out upon silicon and ULE. It was found that in the case of ULE, the material removal rate was dependent upon the speed at which the plasma was moved over the sample. In the case of silicon, the material removal rate remained more or less constant. The difference is expected to be due to the different rates at which heat transfers through the material. In this chapter, results from spectroscopic work are discussed in which the plasma's temperature is measured and estimates of the heat flux delivered to the sample material are made.

5.1 Data Acquisition and Calibration

The spectroscopic instruments utilised for atomic emission spectroscopy measurements of the ICP were discussed in section 3.3. An Ocean Optics LS-1 lamp was used for calibration so that the instrumental losses within the fibre, spectrometer and CCD could be taken into account. In principle, the absolute intensity given at all wavelengths should be independent of the acquisition time used, provided that the acquisition time is sufficiently small that saturation does not occur within any wavelength bin. A test was performed whereby absolute irradiance measurements of the same argon plasma were taken simultaneously using various calibrations that had been created using a range of acquisition periods. It was found that the resulting intensities did vary; the results are displayed graphically in figure 5.1. The largest discrepancies occurred closest to extremes of the spectrometer's measurement bandwidth. It was a decided that emission lines below 430 nm and above 830 nm should not be used in any analysis.

The resulting emission spectra were found to be most accurate when the acquisition time used for recording the spectrum matched the acquisition times used when taking the original calibration measurements. It was decided that, for all subsequent measurements, each recorded measured spectrum should be referenced against the original calibration measurement whose acquisition period was most similar.

Ultimately, tungsten lamp spectra were recorded using the acquisition periods and iteration numbers shown in table 5.1. It was not possible to use an acquisition period longer than 500 ms as that led to saturation.

Table 5.1 **Acquisition periods and iteration numbers used when taking measurements from a tungsten lamp for calibration purposes.**

Acquisition period	Iterations
500 ms	20
200 ms	50
100 ms	50
50 ms	200
20 ms	500

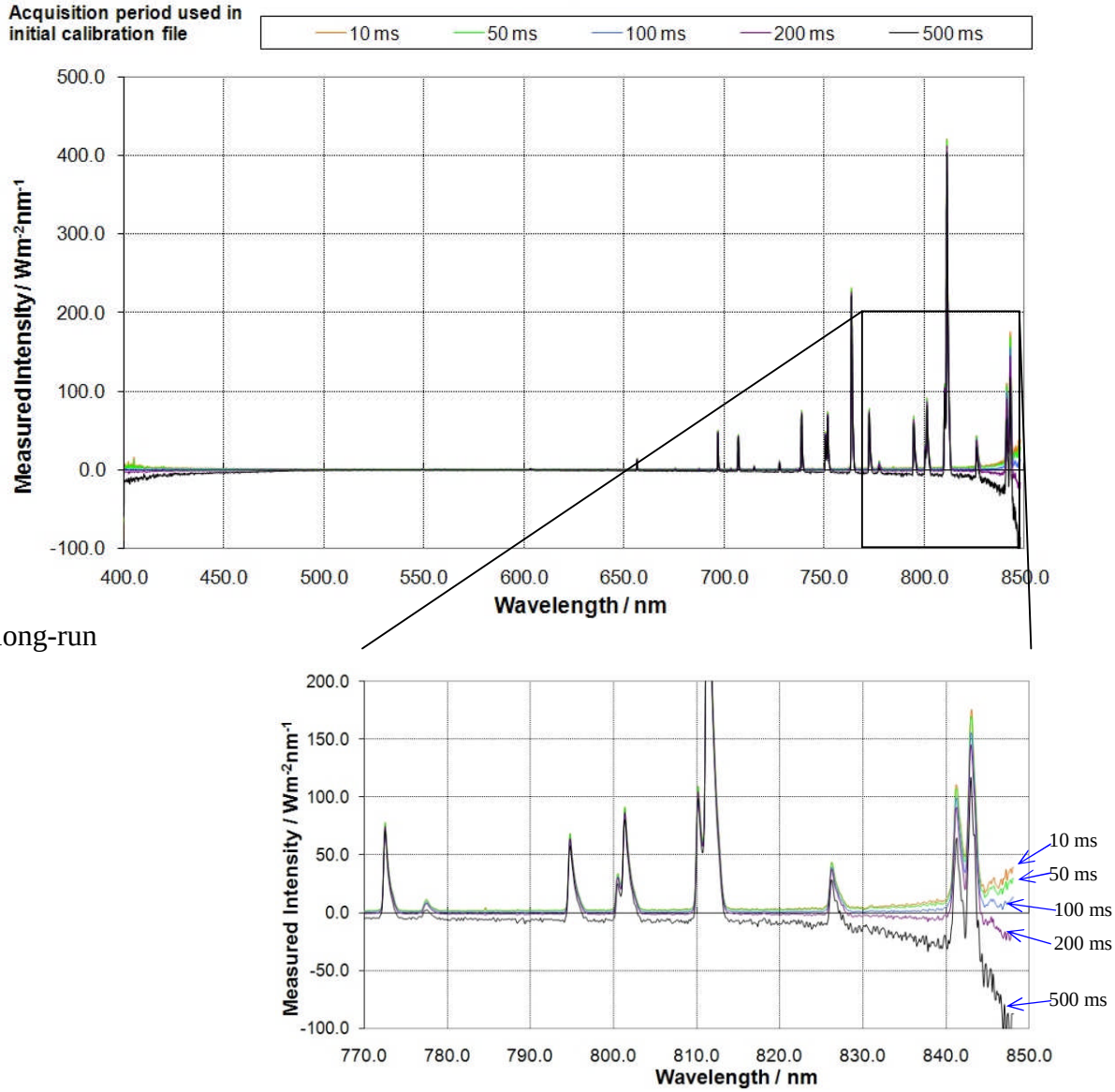

long-run

Figure 5.1 **Five spectra recorded (a dark spectrum has been subtracted) from the same acquisition, but each referenced against a different calibration measurement. The calibration files were created using different acquisition settings. The lower graph shows a region of the spectra expanded to make the differences clearer.**

5.2 Plasma sampling techniques

As discussed in section 3.3, two different sampling techniques were employed. Initially the collimating lens technique was tried (see figure 5.3).

During the early trial experiments, it became evident that a significant amount of unwanted light was being collected during acquisitions. Much of this stray light was light from the plasma that was reflected off the chamber walls. This was apparent because significant intensities were measured even when the lens was pointing along lines of sight that did not intersect the plasma or were not even close to doing so.

To suppress these reflections, all of the internal walls were coated with either black spray paint or folded black cardboard. Figure 5.2 shows how the intensity of readings of a particular line within the plasma with NF_3 were suppressed as a result.

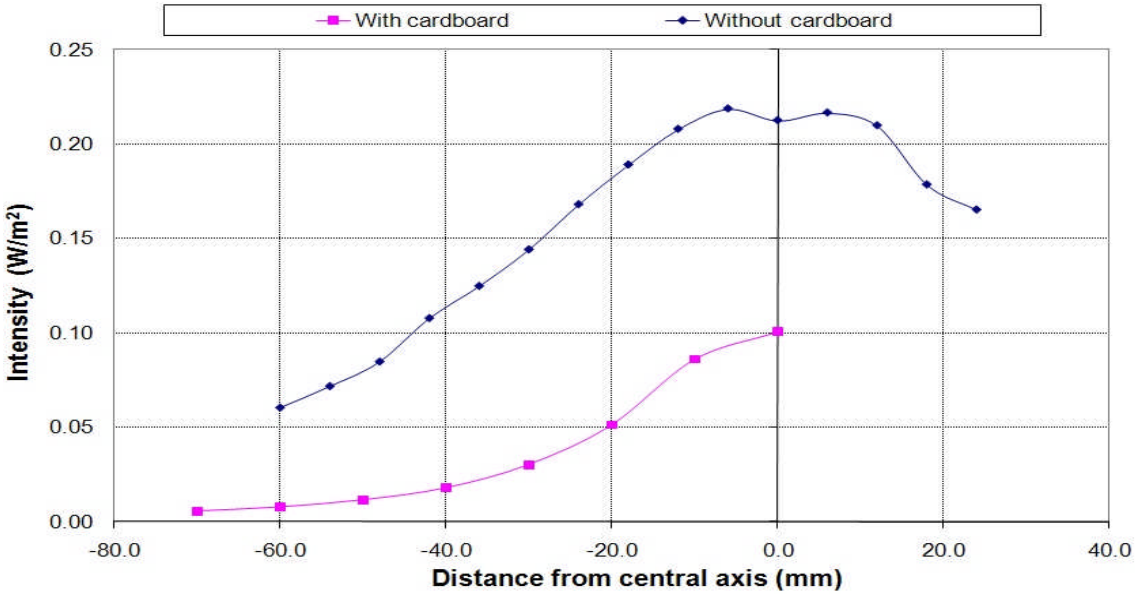

Figure 5.2 **The measured intensity of the Ar I emission line at 696.54 nm before and after the walls inside the chamber were covered with black cardboard or black spray paint. The reduction in the measured intensity after the covering of the walls, indicates that much of the light received during the measurements without the walls covered was the result of reflections within the chamber.**

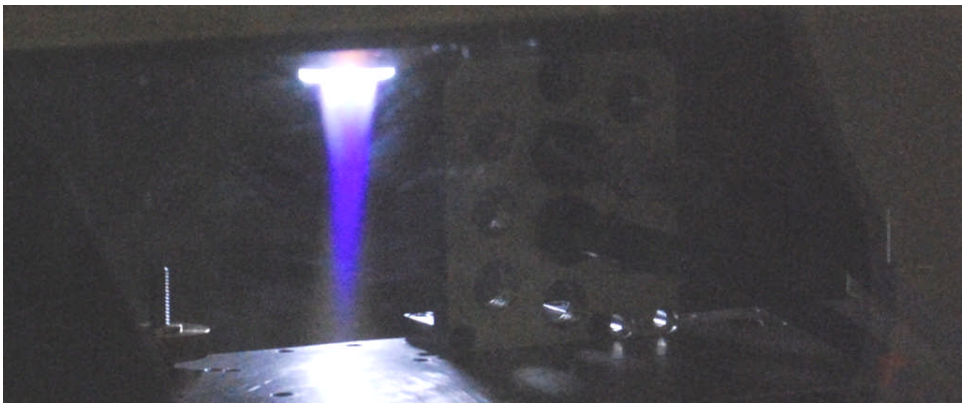

Figure 5.3 **The plasma with NF_3 being examined using collimating lenses.**

Even with the black cardboard shields in place, the noise level was high. It was suspected that off-axis light was being received directly from the plasma even when the lens was pointing along a line-of-sight that did not intersect the plasma. An alternative strategy was tried, using the Gershun tube set up. In the order to achieve maximum resolution, the smallest aperture size, 1º, was tried initially but, when initial measurements were analysed, it was decided that the received signals were generally too weak. The 3º aperture was utilised instead.

Figure 5.4 shows two spectra recorded, both examining the same region of the reactive plasma. Figure 5.4a was taken using the collimating lens and figure 5.4b with the Gershun tube with the 3º aperture. Both spectra include a series of lines centred around 440 nm, which are responsible for the violet colour seen in the plume. In the spectrum shown in figure 5.4b, these peaks dominate over the argon emission lines. Visual inspection suggested that, in the examined region, this ought to be the case. This spectrum shown in figure 5.4a, taken using the collimating lens, suggests otherwise.

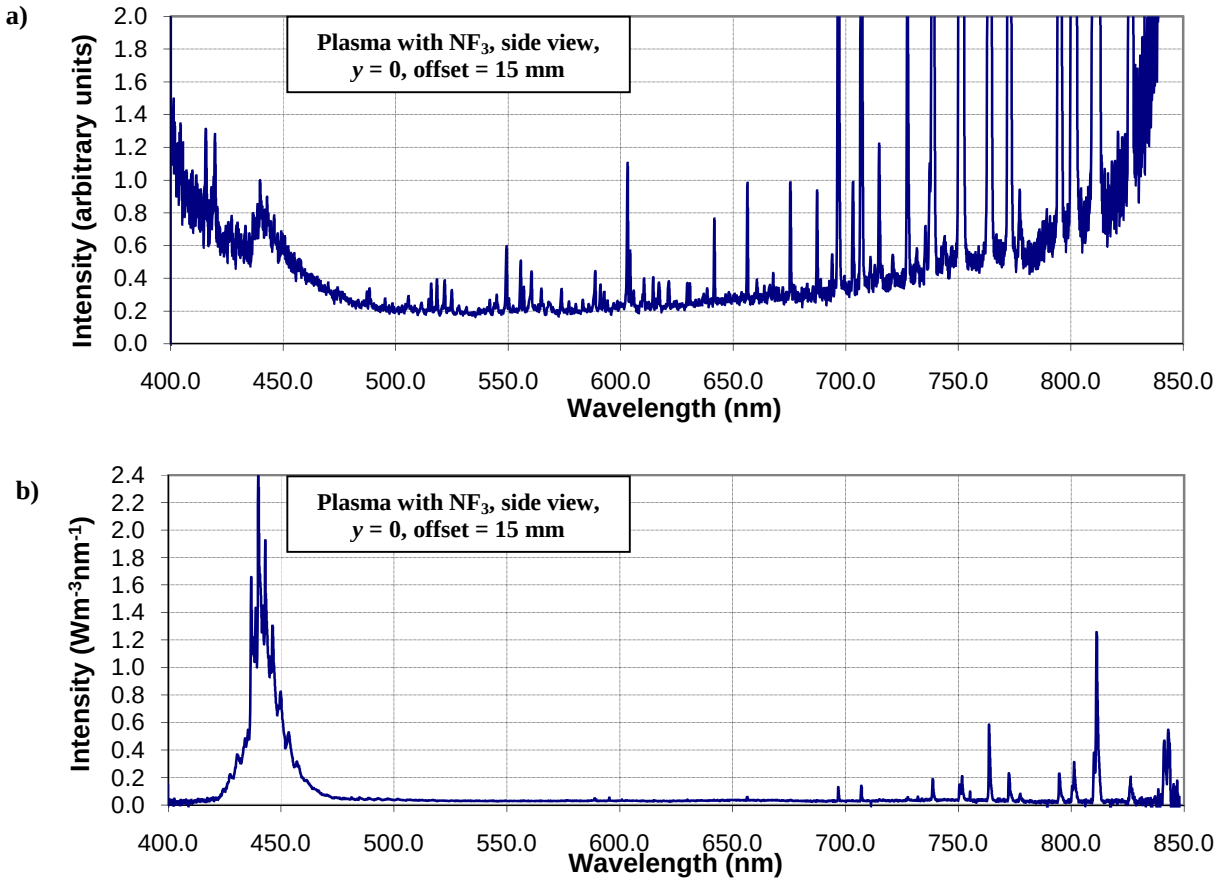

Figure 5.4 **Spectra taken of the same region of the plasma with NF_3 (looking along a line towards the central axis of the plume, 15mm below the base of the quartz tubes from the side of the chamber). a) Spectrum taken using the collimating lens set-up and b) using the Gershun tube set-up. Arbitrary units are quoted in a) (with the highest point within the peaks around 440nm being set unity) because the measurement system used was found to be unreliable.**

It was concluded that, when using the collimating lens, the volume of plasma being measured at any one time was much larger than intended. Although it is possible

to adjust the position of the collimating lens relative to the end of the optical fibre, and hence adjust the viewing angle, it was not possible to achieve satisfactory resolution using the lens. Only measurements taken using the Gershun tube will be discussed hereafter.

5.3 Choice of temperature measurement technique

Several methods of measuring the temperature in the plasma are discussed in section 2.2.4. As the temperature within the plasma plume was expected to be well below 10,000 K throughout, the Fowler-Milne method was not considered suitable. Determining temperature from the continuum emission was also considered unsuitable. This was mainly because its intensity is very low within the temperature range of interest. There are also difficulties involving the various assumptions and approximations that are required and in separating the continuum emission from all the emission lines and from noise. The resolution of the HR4000 spectrometer is not nearly sufficient for the detection of Doppler broadening. As indicated in table 2.1, the FWHM of Doppler broadened profiles would only be ~100 pm which itself is smaller than the resolution of the spectrometer.

Therefore, it was therefore decided that it would best to employ absolute or relative lines methods, which are described in sections 2.2.4.2 and 2.2.4.3. The use of relative methods offers big advantages, but has the disadvantage of having to measure the intensity of several emission lines, rather than just one, to make a single temperature measurement with reasonable accuracy. However, using the Ocean Optics spectrometer and software, an entire spectrum can be recorded very quickly and it is relatively straightforward to write a computer program that can calculate the intensities of a large number of emission lines automatically. Therefore, having to measure the intensities of several emission lines for each temperature measurement is not necessarily such a big task.

So perhaps the best solution would be to measure the intensities of as many lines as reasonably possible and create a Boltzmann plot. The accuracy of this method depends on the extent to which LTE (local thermal equilibrium) exists. As was mentioned in section 2.1.4, significant departures from LTE have been observed in atmospheric ICPs within the coil zone. If LTE is absent, atoms in different electronic configurations are effectively at different temperatures; the atoms in states of higher excitation having higher temperatures than those in states of low excitation. This can result in the points in a Boltzmann plot not falling on a straight line.

Therefore, having determined the temperature at a particular point, its significance should be questioned. In this study of the plasma torch, the aim is to understand how much heat is being implanted into the substrate material. The Dulong and Petit theory of equipartition states that, in a non-degenerate substance, the heat contained within a single particle, U, can be calculated using the simple formula

$$U = {}^{n}\!/_{2}\, kT\,, \qquad (5.1) \quad [\mathbf{82}]$$

where n is the number of degrees of freedom. In an argon plasma, all particles have just 3 degrees of freedom (translational motion in three dimensions).

Therefore, the heat contained per unit volume in an argon plasma is

$$U = \tfrac{3}{2} k\left(N_e T_e + N(ArI)T(ArI) + N(ArII)T(ArII) + N(ArIII)T(ArIII) + ...\right) \quad (5.2)$$

where N_e is the electron density, T_e the electron temperature and *N(Ar_)* and *T(Ar_)* the particle density and temperature of the bracketed argon species. As the ionisation fraction in the plasma is expected to be very low it should be acceptable to reduce equation 5.2 to

$$U \approx \tfrac{3}{2} k\left(N(ArI)T(ArI)\right). \quad (5.3)$$

It is therefore the neutral atomic temperature which is of most interest. In order to attain a temperature as close to this as possible, one could try determining the temperature using the absolute line method, using lines corresponding to transitions between lower energy levels. Fortunately, the strongest lines in the spectral range studied correspond to Ar I transitions, which result from electrons transfering between the 4p and 4s levels.[28]

It was decided that temperatures be determined using a combination of both the absolute line and Boltzmann plot methods. As stated in section 2.2.4.2, determining temperature from a single line requires knowledge of the Einstein transition probability and the degeneracy of the upper energy level of the transition and the partition function and particle density of the emitting species. For argon, the transition probabilities and degeneracies for all the important atomic transitions (and for very many of the ionic transitions) are well documented in the NIST database [**141**], for example. As was mentioned in section 2.2.4.2, estimates of the partition function have been calculated for an argon plasma at atmospheric pressure for temperatures above 5000 K by Olsen [**83**]. These values were used in the analysis.

5.4 Argon emission line choice

In order to create useful Boltzmann plots, it is necessary to measure the intensity of emission lines that correspond to transitions which originate from a wide spread of upper energy levels. The details of all selected lines are listed in appendix B. The criteria for selecting these lines are:

1 The plasma is optically thin to radiation at that wavelength, such that the use of an Abel inversion is valid.

2 The lines are not significantly occluded by neighbouring lines of comparable intensity.

3 The central wavelength must be between 430 nm and 830 nm, for reasons described in section 5.1.

Previous studies of argon plasmas have shown that at all temperatures, such plasmas are transparent to radiation between 400 nm and 750 nm. Emission from lines of wavelength >750 nm have shown a high level of self-absorption in argon plasmas above 10,000 K. However, below 10,000 K, these lines show negligible self-absorption, particularly in a plasma so narrow (see figure 5.5). Therefore, it was

[28] In an unexcited argon atom, the electron shells are filled up to the 3p level. The 4s and 4p levels are the lowest empty energy levels in the unexcited atom.

deemed acceptable to include these lines as well. The line chosen for the absolute methods was the line at 696.54 nm.

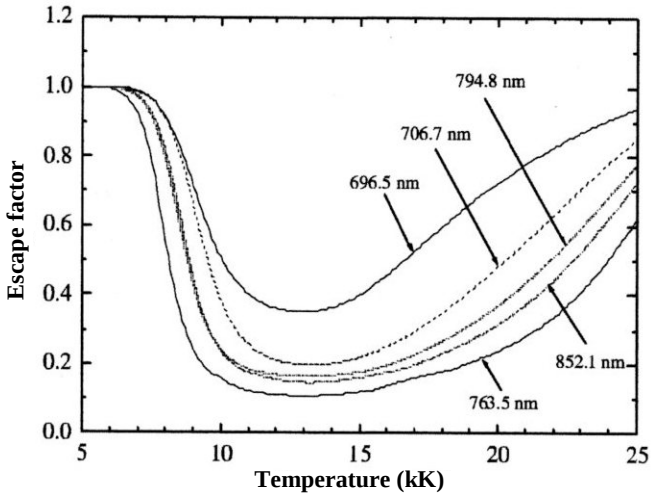

Figure 5.5 **The escape factors of the emission of several of the emission lines corresponding to 4p-4s transitions in an argon plasma, 5 cm in diameter, as a function of temperature [90].**

5.5 Temperature measurements of the pure argon plasma plume

Spectroscopic Measurements were taken of the pure argon plasma plume at the following distances below the base of the quartz tube: 1 mm, 3 mm, 6 mm, 9 mm, 12 mm, 15 mm and 18 mm. The base of the tube is ≈20 mm below the central plane of the RF coil.

In principle, if the central position were known precisely and the plasma were radially symmetric (a necessary assumption if an Abel inversion is to be performed) it would only be necessary to take measurements from one side and to only examine half of the plume. However, initial investigations indicated that there is a departure from symmetry, particularly when measuring close to the nozzle. This was not unexpected. Previous research carried out elsewhere on atmospheric ICPs has shown similar asymmetry, a result of the helical shape of the RF coil [**69**]. Therefore, it seemed wise to take measurements across the whole width of the torch and from orthogonal directions. Measurements were taken using the Gershun tube with a 3º aperture, positioned both in front of the plasma and from the left-hand side with respect to the viewing window. Measurements were taken at spatial intervals of 0.5 mm across the full width of the plasma. Diagrams showing the viewing positions are displayed in figure 5.6.

At each position a spectrum was captured and an ASCII file containing the data was created. In addition, a reference spectrum was recorded. This was taken by moving the sampling set-up such that it looks along a line that is ~15 mm away from the plasma's central axis (so that it 'just misses' the plasma). This was done to estimate the amount of noise received due to reflections. This reference spectrum was subtracted from each of the measured spectra.

a)

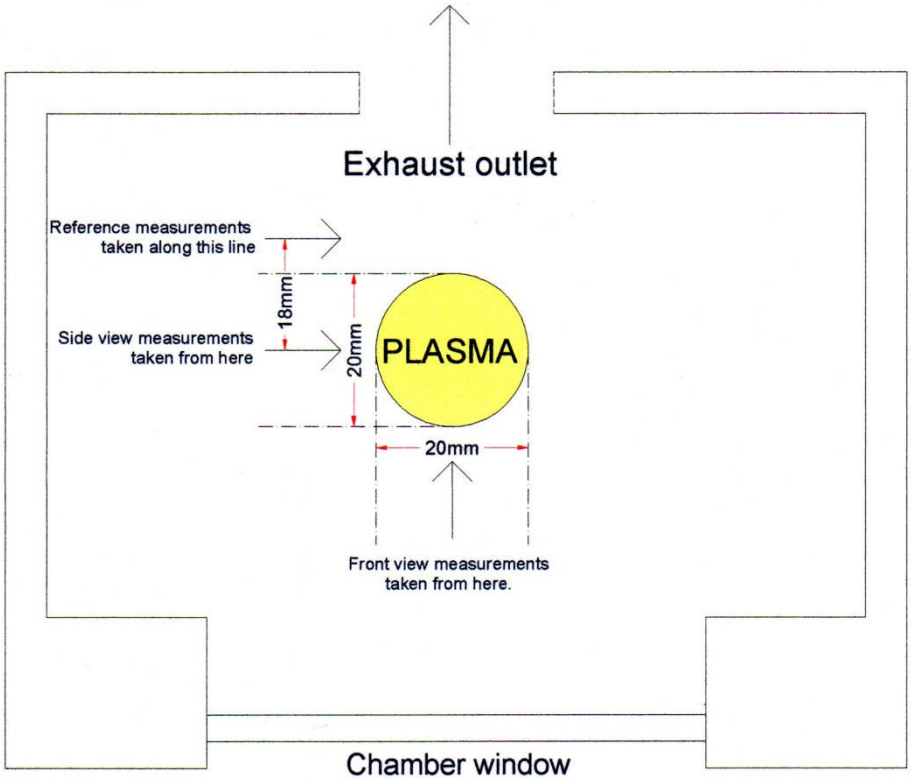

b)

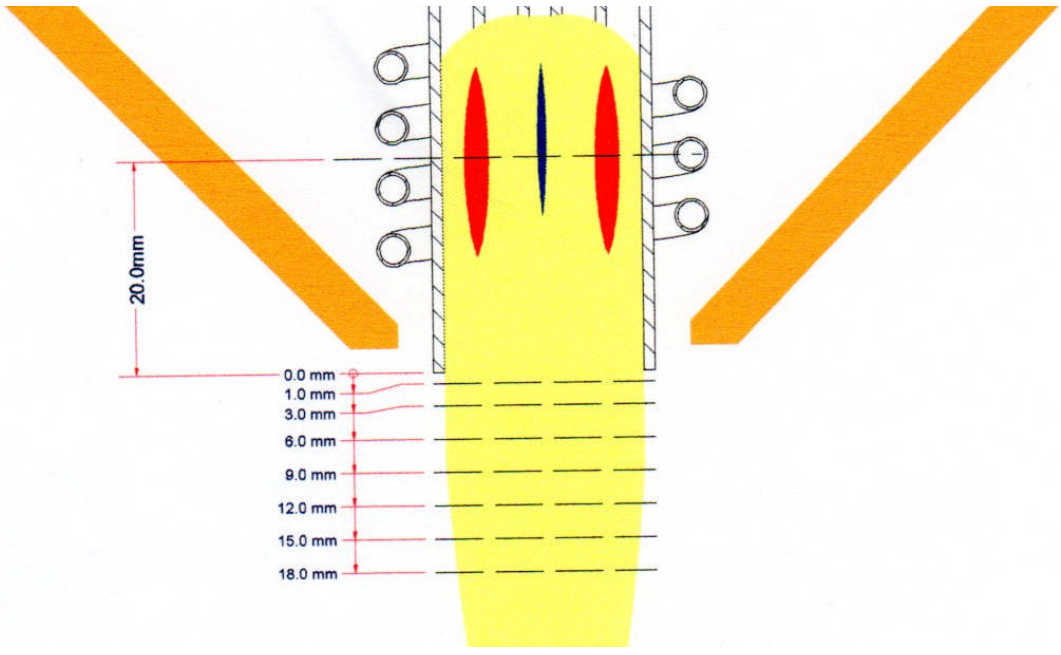

Figure 5.6 **a) Intensity measurements were taken from the front and from the side of the chamber (this drawing is not to scale). b) Measurements were taken looking into the plume across planes at the heights shown.**

A computer program was written, in C++ to handle the data files. The program first pools all of the recorded spectra that have been recorded along a single plane into a single file. The programme then calculates the intensities of a series of emission lines. Start and end wavelengths were pre-defined for each of the selected lines. The program integrates the intensity between these two wavelengths to best determine the overall intensity of the line. In doing so, an estimate of the contribution from the continuum emission (or noise), which is assumed to be linear across the base of the peak, was subtracted. An example of how an emission profile is corrected, using this process, is shown graphically in figure 5.7. Any negative values within the wavelength range that result after the baseline subtraction were disregarded.

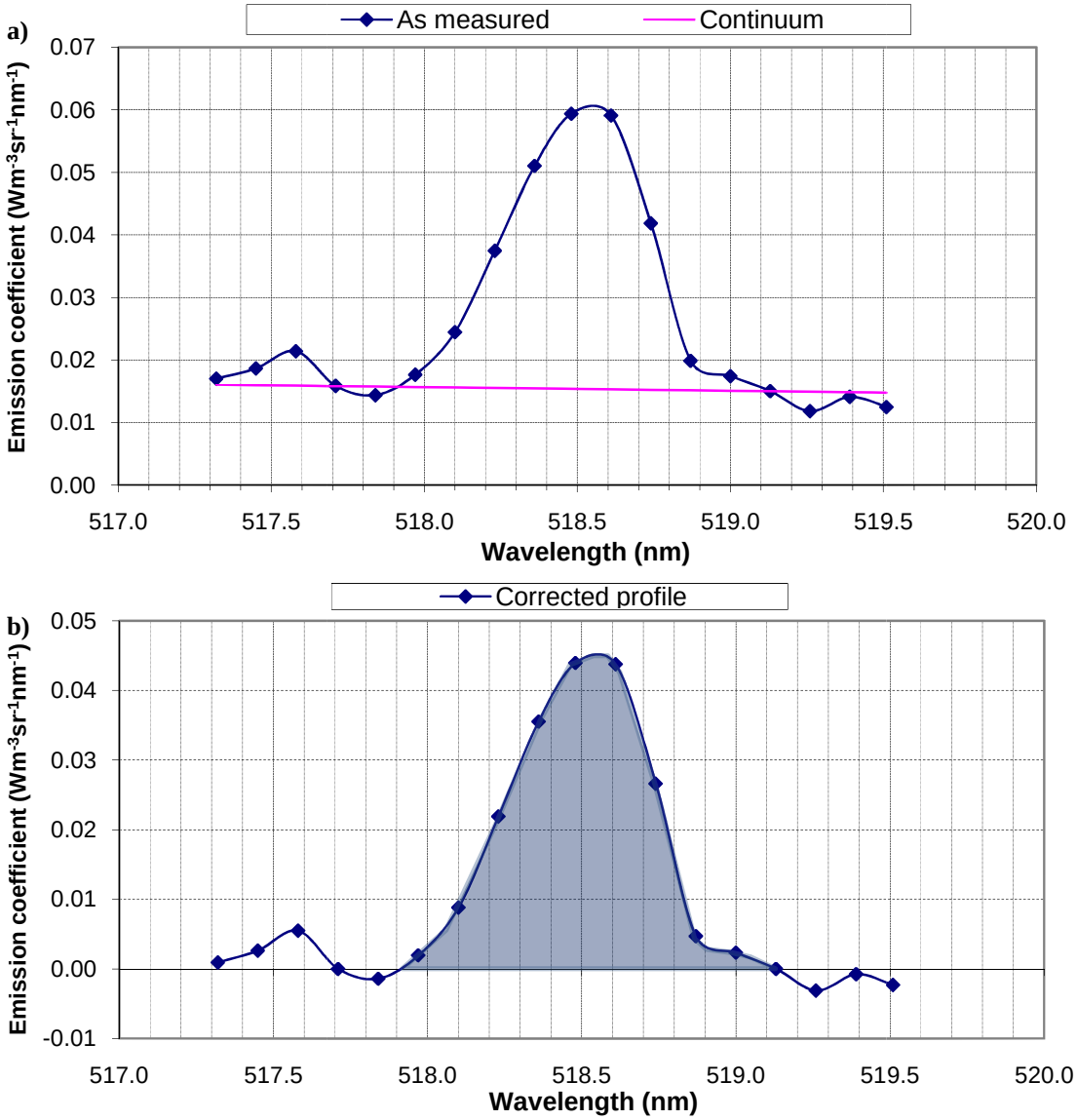

Figure 5.7 **a) Profiles of the measured intensity profile of the line at 518.775 nm and the estimated contributions from continuum and noise. b) The corrected peak profile (measured intensity minus continuum). The peak margins were set to 517.8 nm and 519.2nm for this particular peak. All emission coefficient values outside that range are disregarded when the calculating the emission coefficient for the whole peak. The inferred emission coefficient of the emission line is made equal to the shaded area.**

Having calculated the line of sight peak intensities, the programme performs an Abel Inversion (using the solution devised by Nestor, described in section 2.2.3.2). This converts the integrated measured line intensities into a radial distribution of the emission coefficient for each line. Nestor's method was used as it is straightforward to implement. Because measurements were taken across the full width of the plasma torch, it effectively produces two radial distributions. The graphs in figure 5.9 show the result following an inversion of the data shown in figure 5.8.

During the data analysis, profiles of the emission coefficient similar to figure 5.9a generally have been produced. This is somewhat erroneous as the distribution is supposed to be radial and so one might consider the graph in figure 5.9b, in which the two distributions are overlaid, to be more appropriate. Indeed, if the measurements were absolutely precise, the plasma were 100% symmetric and the '0' point were precisely defined, these distributions would be identical. In practice, that is never completely the case although, in this instance, the two distributions are almost certainly within each other's error margins.

For reasons of convenience, only graphs of the type shown in figure 5.9a will be displayed hereafter and such data profiles will be referred to as **emission profiles**. The temperature distributions calculated from emission profiles will be referred to as **temperature profiles**. The raw, line-of-sight distributions will be referred to as **intensity profiles**.

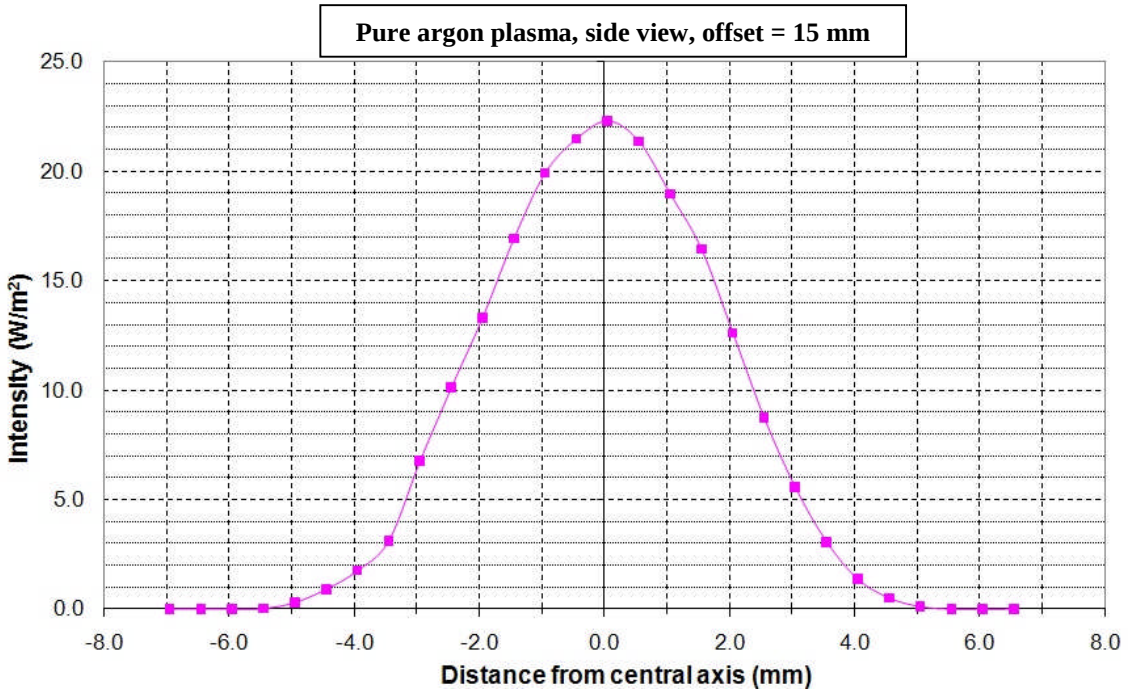

Figure 5.8 **a) Integrated intensity of the 696.54 nm emission line in the pure argon plasma as measured across the width of the plasma along a plane 15 mm below the base of the torch, viewed from the side of the chamber.**

a)

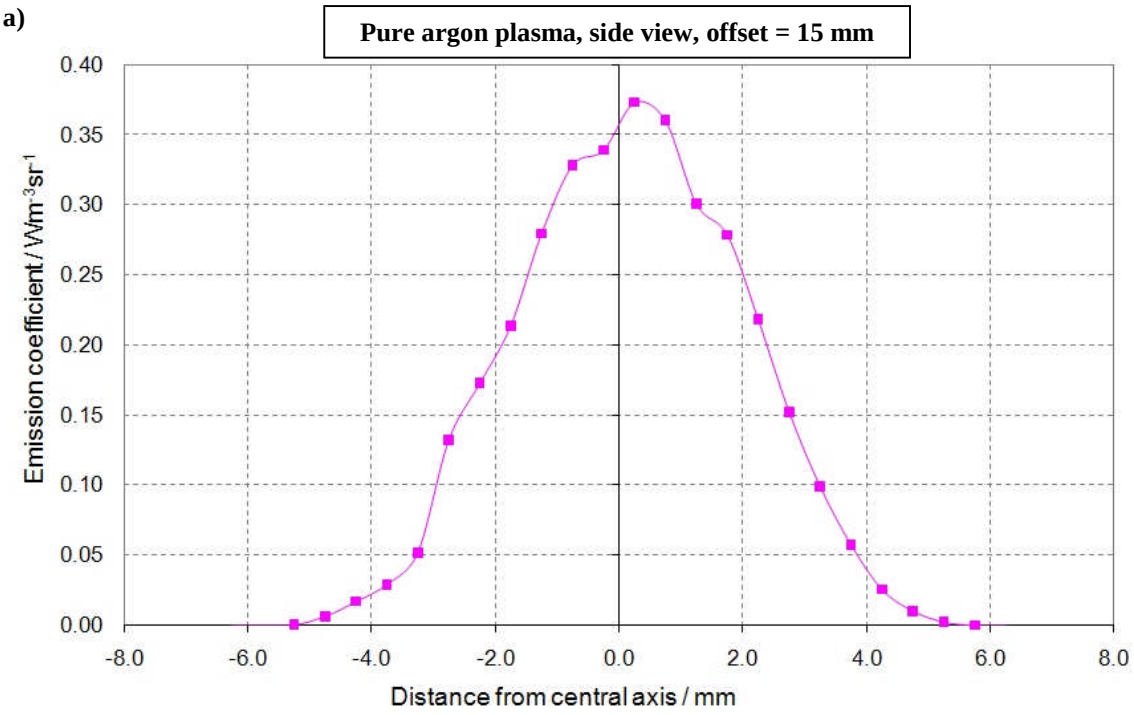

b)

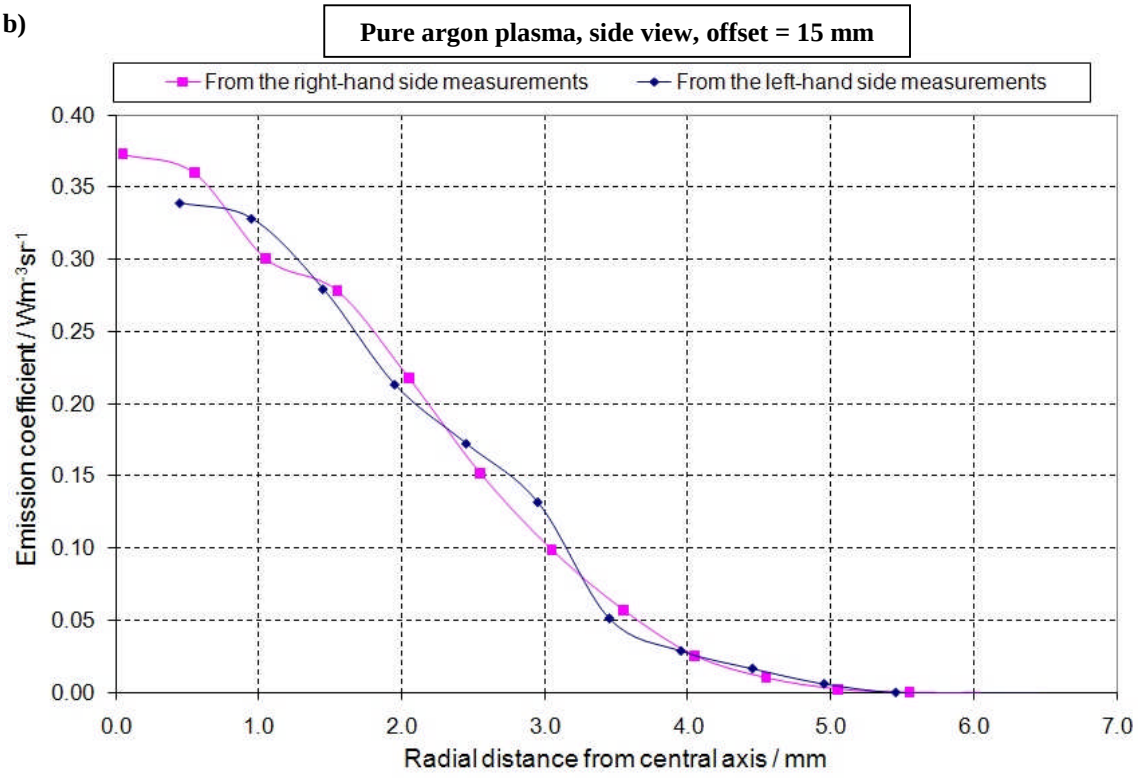

Figure 5.9 **a) A radial distribution of the emission coefficient (ε) as determined from the measured data shown in figure 5.8. b) Same data but with the two distributions superimposed.**

5.5.1 Temperature evaluation using the 696.5nm line

The temperature at a particular point can be evaluated from the emission coefficient of a single transition using the following equation, which is a rearrangement of equation 2.40,

$$T = \frac{E_U}{k}\left(\ln\left(\frac{N(T)g_U A_{UL} h f_{UL}}{4\pi Z(T)}\frac{1}{\varepsilon_{UL}}\right)\right)^{-1} \quad (5.4).$$

The following information has been tabulated for the 696.5431 nm line in the NIST database [**141**]:

E_u (upper energy level) = 107496.4166 cm^{-1} = 13.3279 eV = 2.13536 × 10^{-18} J.

g_U (degeneracy of upper energy state) = 3.

A_{UL} (Einstein transition probability) = 6.39 × 10^6 s^{-1}.

Figure 5.10 shows the temperature profile that results from the data shown in figure 5.9. The plasma was assumed to be at atmospheric pressure and the particle density (N) at each position was deduced by an iterative process. A temperature value was calculated at each position, using an initial guess for the particle density. A revised particle density would then be calculated from that temperature (according to the data in figure 2.28b). A revised temperature would then be calculated and the process would be repeated until both values converged to their final values. Z was set to unity throughout.

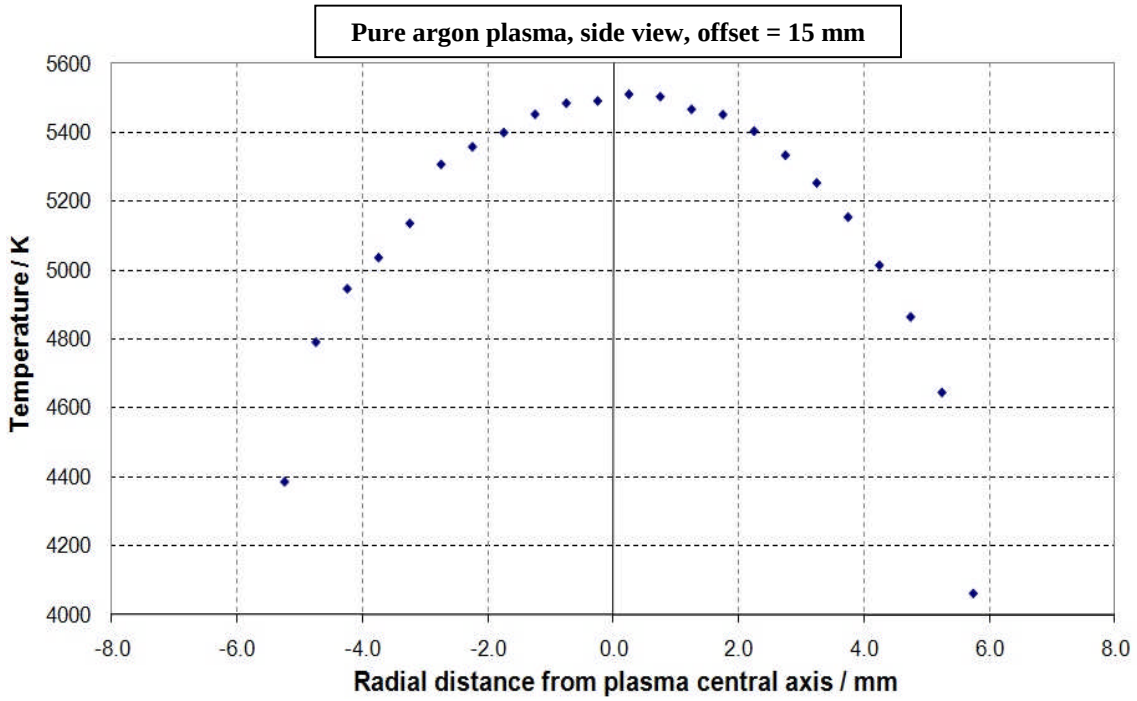

Figure 5.10 **Temperature profile as calculated from the data shown in figure 5.9, using equation 5.4.**

5.5.2 Temperature evaluation using Boltzmann plots

Temperature calculations of the argon plasma plume were also made by measuring the intensity of 17 Ar I atomic emission lines and creating Boltzmann plots. The details of these lines are listed in appendix B.

It was possible to produce high quality Boltzmann plots from measured data covering most of the plume. Figure 5.11 shows an example. The gradient of the linear fit is -1.88 eV^{-1}, which corresponds to a temperature of 6830 K.

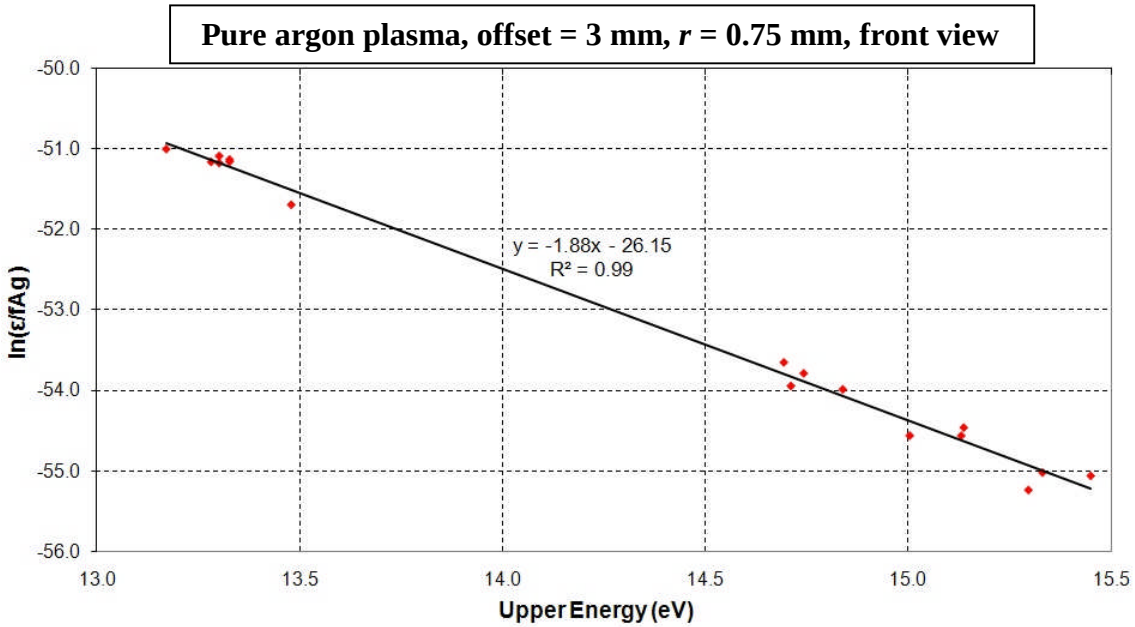

Figure 5.11 **A Boltzmann plot, taken from data looking very close to the central axis of the plasma (0.75 mm away) and 3 mm below the base of the quartz tube, viewed from the front of the chamber.**

For the data shown in the above Boltzmann plot, the emission coefficient of the most intense line, the 763.5 nm line, was 2950 $W/m^3/sr$. That of the weakest line, the 667.7 nm line, was 3.55 $W/m^3/sr$; smaller by a factor of 800. The computer program and the statistics used to determine the intensities are not foolproof, and the inaccuracies might be greater than 100% in determining the intensity of the weaker lines. The programme includes a facility that allows the user to check and adjust these intensities, but to check them all would be a very time-consuming process. In spite of that, the gradient of the linear fit in most of the plots can be determined accurately to within ~5%.

In the cooler regions of the plume, the quality of the Boltzmann plots degrades and it becomes increasingly difficult to determine the gradient. Figure 5.12 shows a Boltzmann plot of the data lower down in the plume, 17 mm below the nozzle and 2.45 mm from the central axis. In this instance, it is difficult to estimate the gradient to within ~15%. The gradient of the fit shown, -2.15 eV^{-1}, corresponds to a temperature of ~5400 K. However, the error on that might be ~700 K. In even cooler regions, it becomes virtually impossible to apply a meaningful linear fit to the data. Therefore, the range over which the Boltzmann plot method can be applied is restricted.

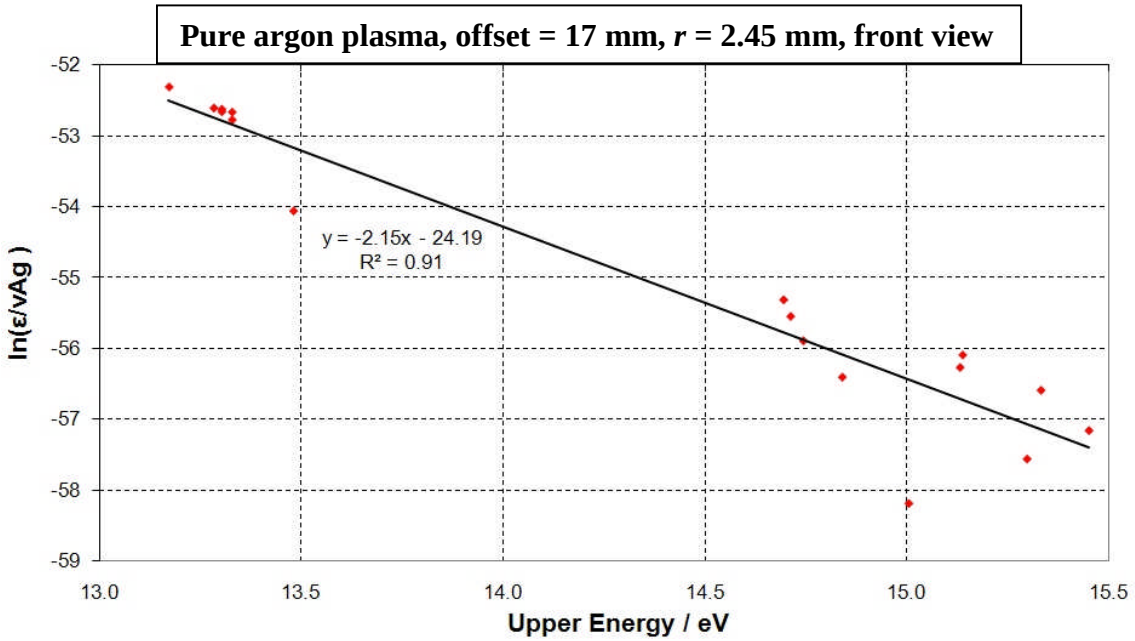

Figure 5.12 **A Boltzmann plot, taken from data taken looking 17 mm below the base of the torch, 2.45 mm away from the central axis, front view. A linear fit like this is perhaps as poor as can be tolerated.**

The graphs in figure 5.13 shows three temperature profiles: one from the side view data, along the plane 3 mm below the torch base, and two from the front view measurements, along the planes 3 mm and 17 mm below the torch base. In each case, one profile shows temperatures determined from Boltzmann plots, the other just from the intensity of 696.5 nm line. The error bars on the Boltzmann plot data are the result of the uncertainty in measuring the gradient.

Discrepancies exist between the two profiles in both instances, but allowing for the error margins, the profiles are sufficiently similar to suggest a reasonable level of consistency. The profiles determined from the single line measurements are much smoother. The fluctuations in the profiles produced from the temperatures deduced from Boltzmann plot gradients are probably not real. Overall, it seems more sensible to use temperatures taken from single line measurements. The Boltzmann plots are useful nonetheless; if there were bigger discrepancies, it could indicate that a systematic error had been made during the analysis.

If the intensity measurements and the linear fit were exactly right, a particle density could be deduced. Let us suppose that the linear fit on a Boltzmann plot is extrapolated back to the vertical axis and it crosses at the point *I*. The particle density could be inferred from this value, using the equation

$$N = \frac{4\pi Z}{h} e^{-I} \quad (5.5).$$

For the plot in figure 5.11, the intercept is at -26.15. Setting *Z* equal to one, *N* turns out to be 8.34×10^{22} m^{-3}. This value is rather less than what would be expected if the plasma were at atmospheric pressure (1.2×10^{24} m^{-3}). This might mean that the atmospheric pressure assumption is invalid. However, the uncertainty on the intercept is large, leading to an inferred uncertainty in the determined particle density of about a factor of 5.

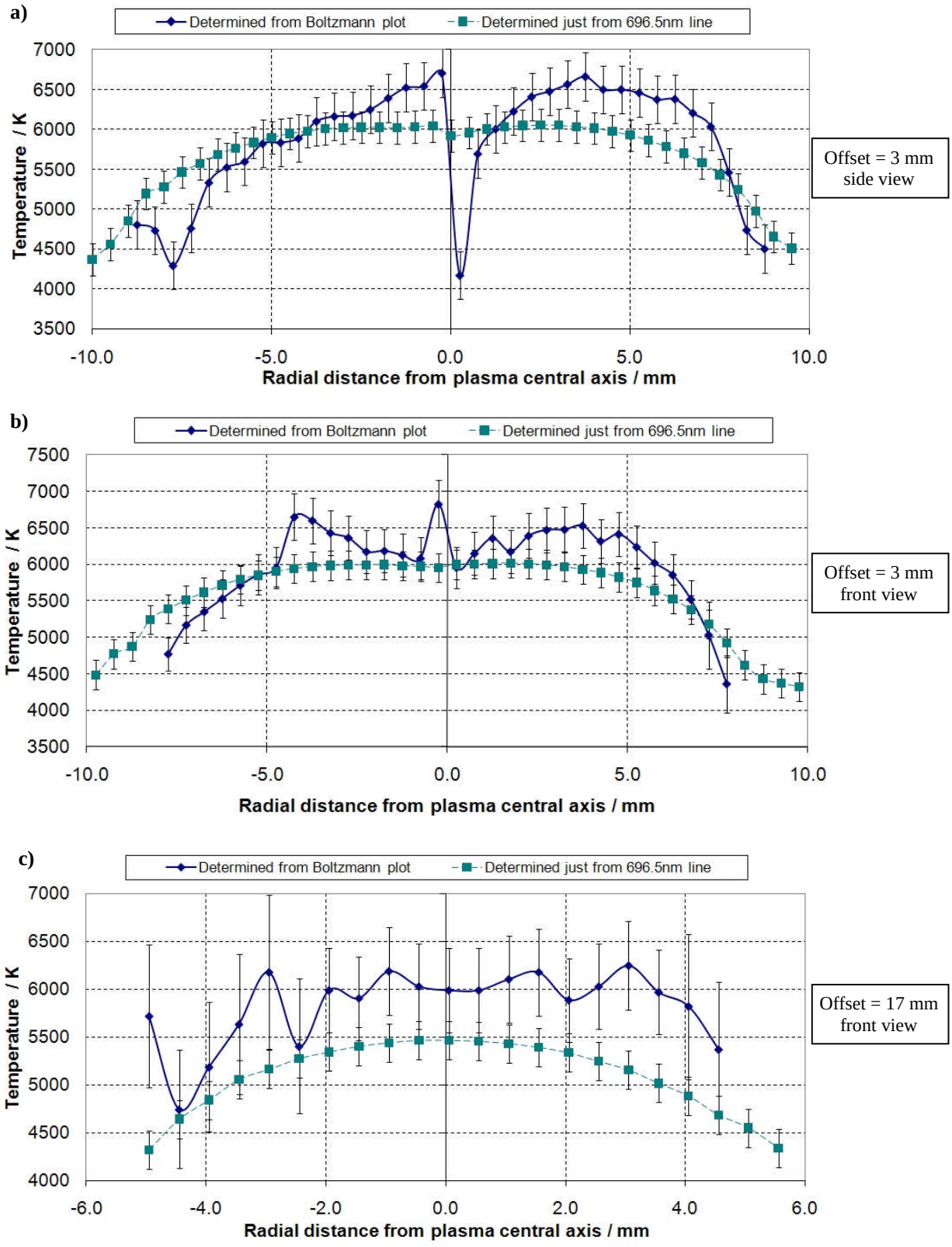

Figure 5.13 **Radial temperature profiles calculated from both Boltzmann plots and from just the 696.5nm line at a) 3 mm below the base of the torch, side view, b) 3 mm below the base of the torch, front view and b) 17 mm below the base of the torch, front view.**

5.5.3 Temperature maps

It was decided that for making temperature maps of the plasma, temperatures calculated using the 696.5 nm line only should be used. It was thought that to produce a Boltzmann plot at every sampled position would greatly increase the amount of effort required for limited benefit and useful only over a restricted region of the source. Figure 5.14 shows measured intensity maps (of the 696.5 nm line) for the measured regions of the pure argon plasma plume. Maps of the emission coefficient are shown in figure 5.15 and temperature maps are displayed in figure 5.16.

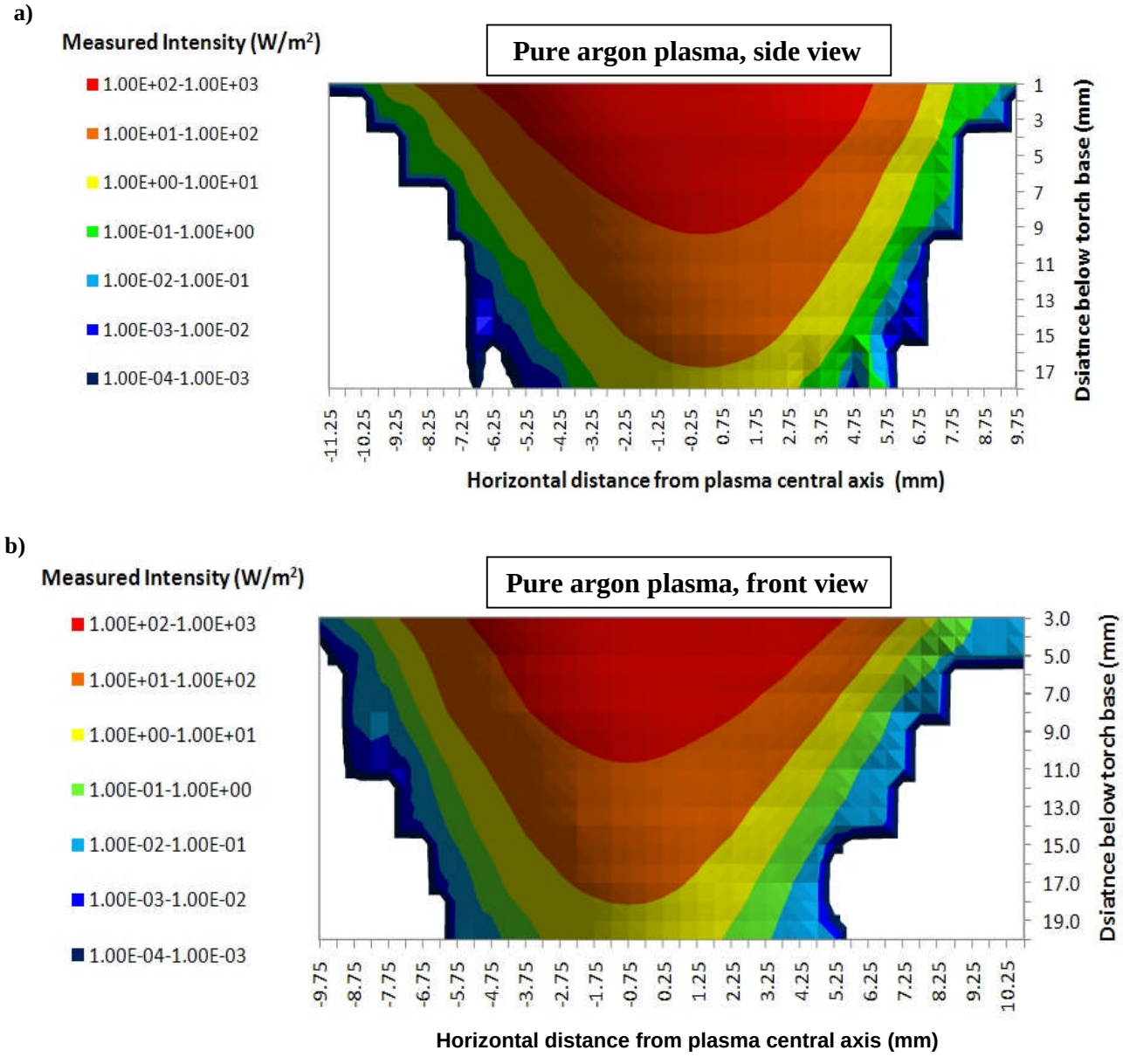

Figure 5.14 **a) Side view intensity map of pure argon plasma. b) Front view intensity map of pure argon plasma.**

a)

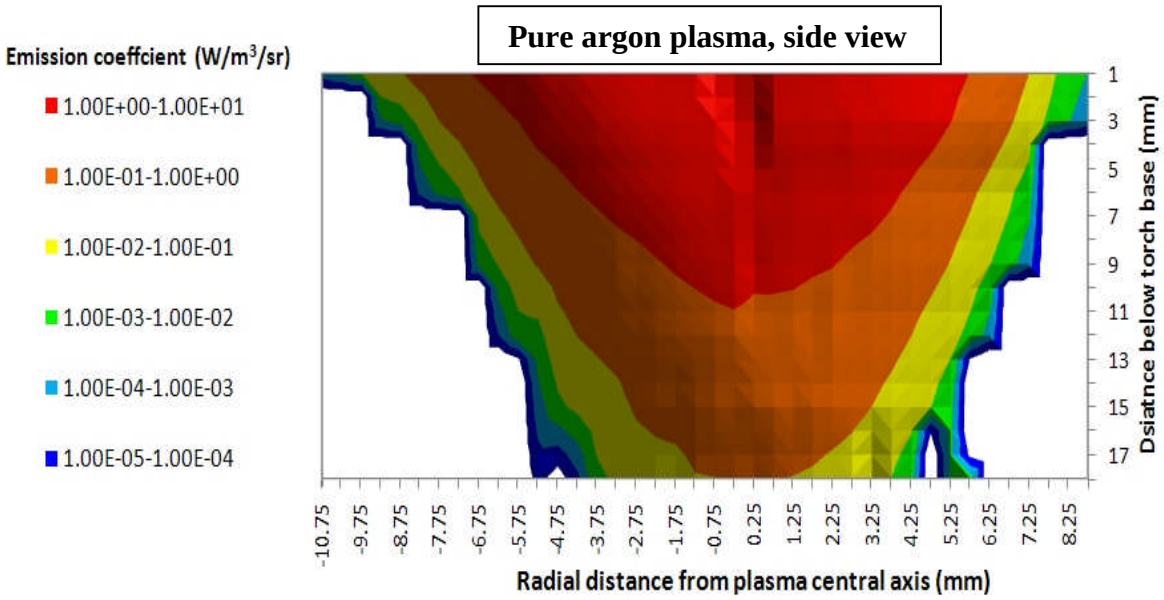

b)

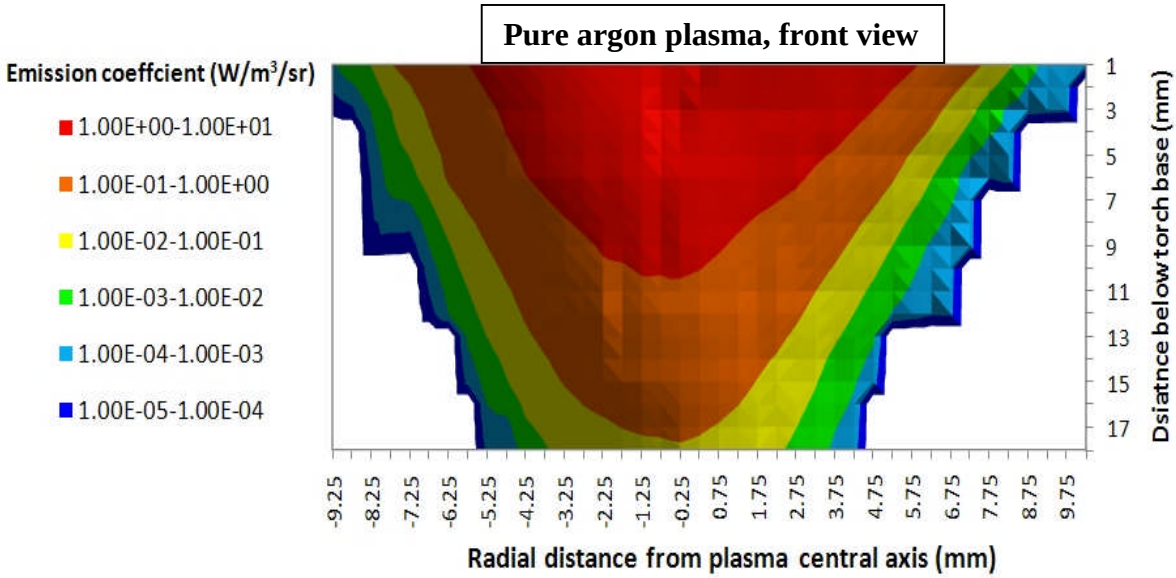

Figure 5.15 **a) Side view emissivity map of pure argon plasma. b) Front view emissivity map of pure argon plasma.**

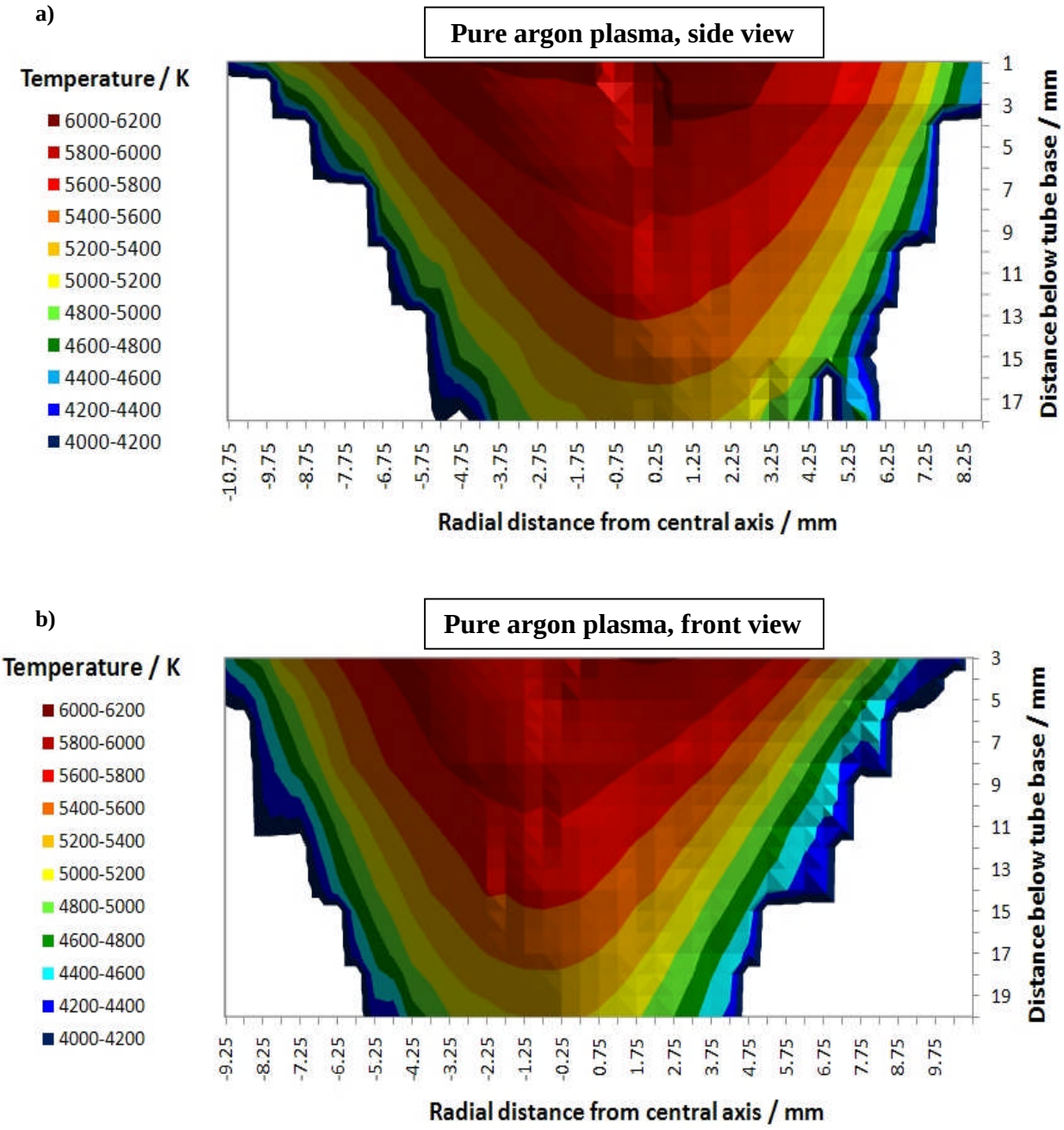

Figure 5.16 **a) Side view, temperature map of pure argon plasma. b) Front view temperature map of pure argon plasma.**

The reader might be interested to note that while the emission coefficient varies by a factor >1000 over the region measured, the temperature varies only between 4000 K and 6200 K. In other words, within the temperature range concerned, a small change in temperature results in a big change in luminosity of an emission line. In regions where the plume is below 4000 K, the line intensity is too weak and the temperature cannot be determined reliably using this method with this AES set-up.

5.5.4 Temperature measurement uncertainties

At this point, it might be prudent to discuss the uncertainties in the temperature values presented that were based on measurements just taken using the 696.54 nm. Uncertainties exist in both the original measurements and the analysis.

5.5.4.1 Shot noise

Shot noise describes the statistical fluctuations that exist in measurements when a number of discrete events are recorded over a period of time. In this instance, the events are the 'counts' recorded by each element on CCD; each count is a response to a bundle of photons. Let us suppose that an experiment were to be conducted in which the number of counts is recorded over a given period and then that experiment be repeated a large number of times with exactly the same conditions. If the average number of counts over that set of experiments is N, the standard deviation should be $\approx\sqrt{N}$, as given by the Poisson distribution. Therefore, the signal to noise ratio is equal to

$$\frac{N}{\sqrt{N}} = \sqrt{N} \qquad (5.6).$$

A spectrum was taken of the pure argon plasma, 12 mm below the torch, side view, looking close to the centre of the plume. The acquisition period was 100 ms and the iteration count was 20, typical parameters for such measurements. The overall number of counts used in recording the intensity of the 696.5 nm line was 85978 (following the subtraction of a reference spectrum and the continuum emission). The signal to noise ratio for that measurement was therefore 293.2. A ratio as large as this results in a temperature inaccuracy of ~0.3 K, which is minute.

5.5.4.2 Torch intensity fluctuations

It is expected that uncertainties in the intensity measurements due to instabilities in the plasma itself are much larger than those due to shot noise. This could primarily be due to turbulence, variations in the outputs of the mass flow controllers and slight distortions within the plume due to the RAPT 300 machine's exhaust.

To investigate this, measurements were taken at five positions along a plane in the argon plasma plume, 12 mm below the torch base, side view, and each acquisition was repeated 20 times. The resulting line intensities, as given by the in-house written program, were compared. The results are summarised in table 5.2. The positions are in millimetres relative to the plasma central axis.

Table 5.2 Summary of results from the measurement fluctuations test

Position	P / ms	N	Mean over 20 measurements / W / m^2	SD over 20 measurements / W / m^2	SNR	Fractional error on ε	Temperature Inaccuracy / K
-5.5	6000	1	2.8	0.05	51.5	0.027	4.4
-4.5	2000	3	18.0	0.40	45.6	0.041	3.7
-3.5	500	5	48.5	0.62	78.6	0.044	2.7
-1.5	200	5	179.1	1.45	123.3	0.044	2.2
0.5	100	20	211.0	2.72	77.7	0.051	3.6

P = Acquisition period N = Number of samples taken per measurement.
SD= Standard deviation SNR = Signal to noise ratio ε = emission coefficient

The calculated signal to noise ratio is just the mean divided by the standard deviation. In calculating the fractional error on the emission coefficient, an allowance has been made for the fact that, when using an Abel inversion, the error made on a single measurement affects the determined emission coefficient at all positions closer to the centre.

Even 5.5 mm away from the centre, the signal to noise level on the measured 696 nm line intensity is very good. The temperature inaccuracies from this source are still very small.

5.5.4.3 Choice of calibration file

As was stated in section in 5.1, the processed spectrum depends, to some extent, on the acquisition settings used when taking measurements with the tungsten calibration lamp. Attempts were made to minimise such inaccuracies by, for each measurement, using the calibration file data whose acquisition is most similar. However it is possible that, on occasions, the most appropriate choice was not made. To investigate the influence of this, eight acquisitions were taken at the same position (100 ms acquisition, 20 samples) and five different spectra were processed for each acquisition, one to each of the calibration files created. The intensity of the 696 nm line was then calculated in the usual manner. The spectra displayed in figure 5.1 are the five spectra taken from the first acquisition.

Once again, the signal to noise ratios are very high and so while the choice of calibration file has a noticeable influence on a spectrum's noise level, it should have very little influence of the temperature measurements.

Table 5.3 The influence of the choice of calibration file on measured line intensity

Acquisition period used in calibration file / ms	Mean / W / m^2	SD / W / m^2	SNR
500	169.1	3.9	43.7
200	166.5	3.8	43.3
100	161.5	3.8	43.0
50	167.6	3.9	42.6
10	167.9	3.9	42.7
Overall	166.5	3.9	43.1

5.5.4.4 Interference from other emission lines

The computer program that was written for calculating the intensity of the 696.5nm line integrates between 695.6 nm and 698.1 nm. This range includes emission from the line at 696.025nm. However, this line is very weak (their relative intensities are listed in the NIST database) and only increases the calculated emission coefficient by 0.07%. This results in a change in temperature of ~0.2 K.

5.5.4.5 Inaccurate definition of the central axis

In order for the use of an Abel inversion, using Nestor's solution, to be completely correct, a series of parallel line-of-sight measurements should be taken along a plane at equally spaced lateral intervals. If measurements are to be taken right through to the plasma's central axis, the position of that central axis must be known.

Let us consider the intensity profile shown in figure 5.17a from measurements taken along a plane 14 mm below the base of the torch, front view. One could probably pinpoint the central axis to within 0.25 mm. Let us suppose that the zero point were moved 0.5 mm to the left. Figure 5.17b shows how the emission profile is affected and figure 5.17c shows how the temperature profile is affected. The emission profile at radii >3 mm is affected very little by the choice of zero position. At smaller radii, the deviation is more significant. However, figure 5.17c suggests that the uncertainty is ±40°C, at worst.

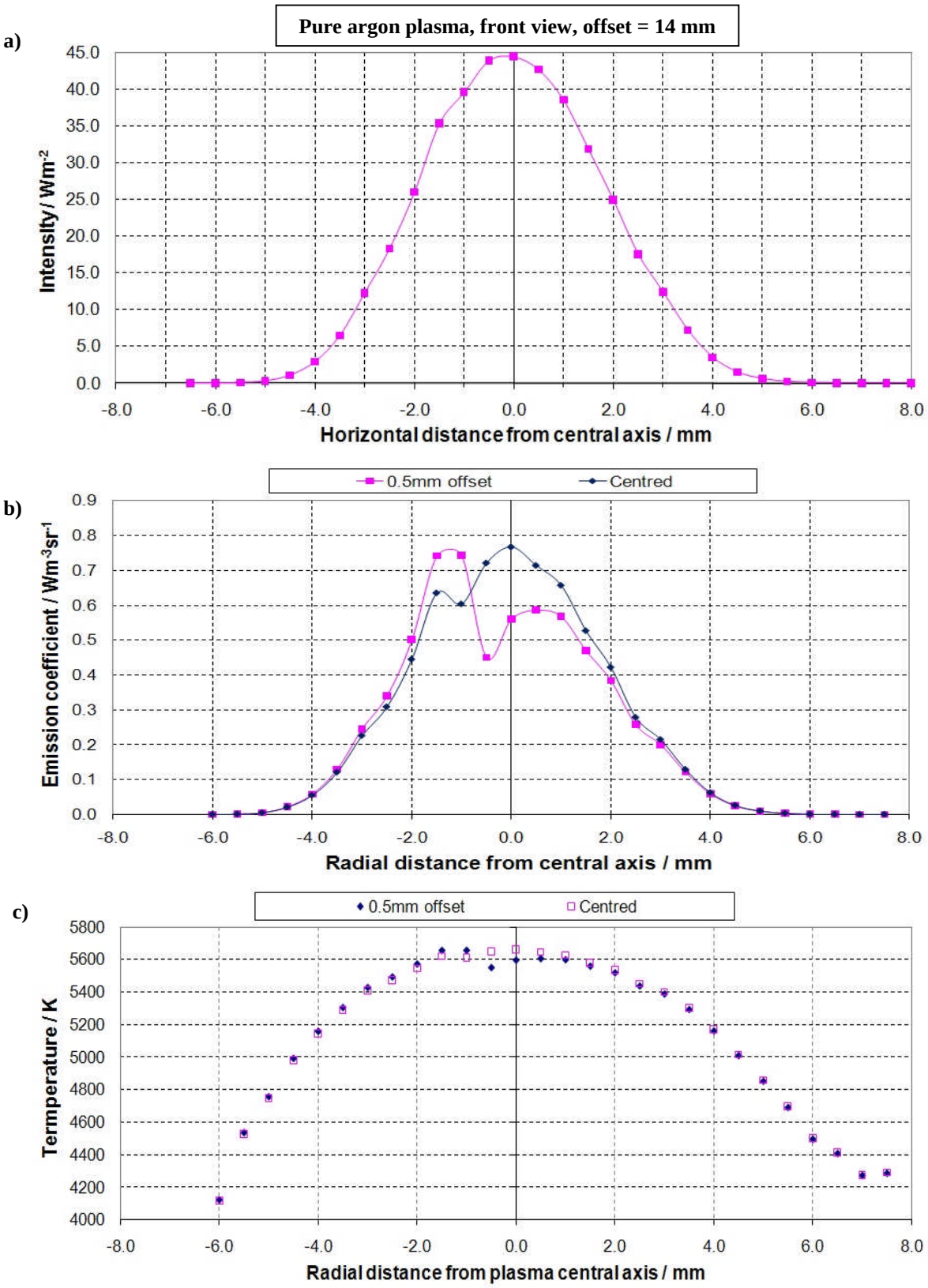

Figure 5.17 **a) A near symmetric intensity profile, b) the affect on the emission profile if the envisaged zero point were to be shifted 0.5 mm to the left and c) the affect on the temperature profile resulting from the same shift.**

5.5.4.6 Asymmetric profiles

In some of the measured intensity profiles close to the base of the torch were significant deviations from radial symmetry. Figure 5.18 shows the intensity profile of the 696.5 nm line, side view, 1 mm below the base of the torch. The 'zero position' is close to the torch's central axis. Experimental studies and simulations of similar torches have shown that, within the coil zone, a cylindrical torus of high electron density and temperature forms. Because of the helical shape of the coil, the torus is slightly lop-sided. This is the most likely cause of the profile's shape.

It is reasonable to question whether putting the zero point at the torch's central axis is most appropriate; it might make more sense to take the profiles maximum as the zero point. Figure 5.19a shows two emission profiles, one calculated using the torch's geometric centre as the zero point and the other using the intensity maximum as the zero point. In both instances, there are sharp deviations which are probably not real. As of yet no information exists to suggest that, in an overall sense, one profile is more correct than the other. Figure 5.19b shows the temperature profiles that result from each of the emission profiles shown in figure 5.19a.

The system used in creating the temperature maps shown in figure 5.16 was to make two emission profiles, such as in figure 5.19a, and use the average of the two to create the temperature profile, such as the one shown in figure 5.19c. The uncertainty in temperature measurements close to the centre is perhaps ±50°C. This is still very acceptable for a spectroscopic study of this nature.

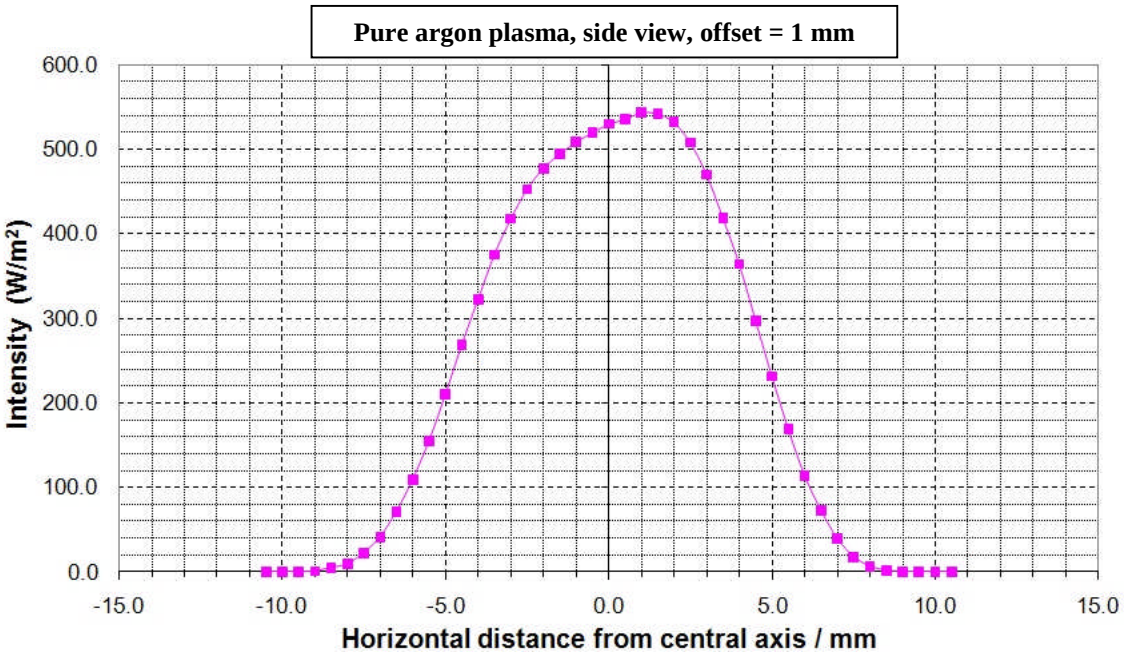

Figure 5.18 The intensity profile of 696.54 nm line, side view, 1 mm below the base of the torch.

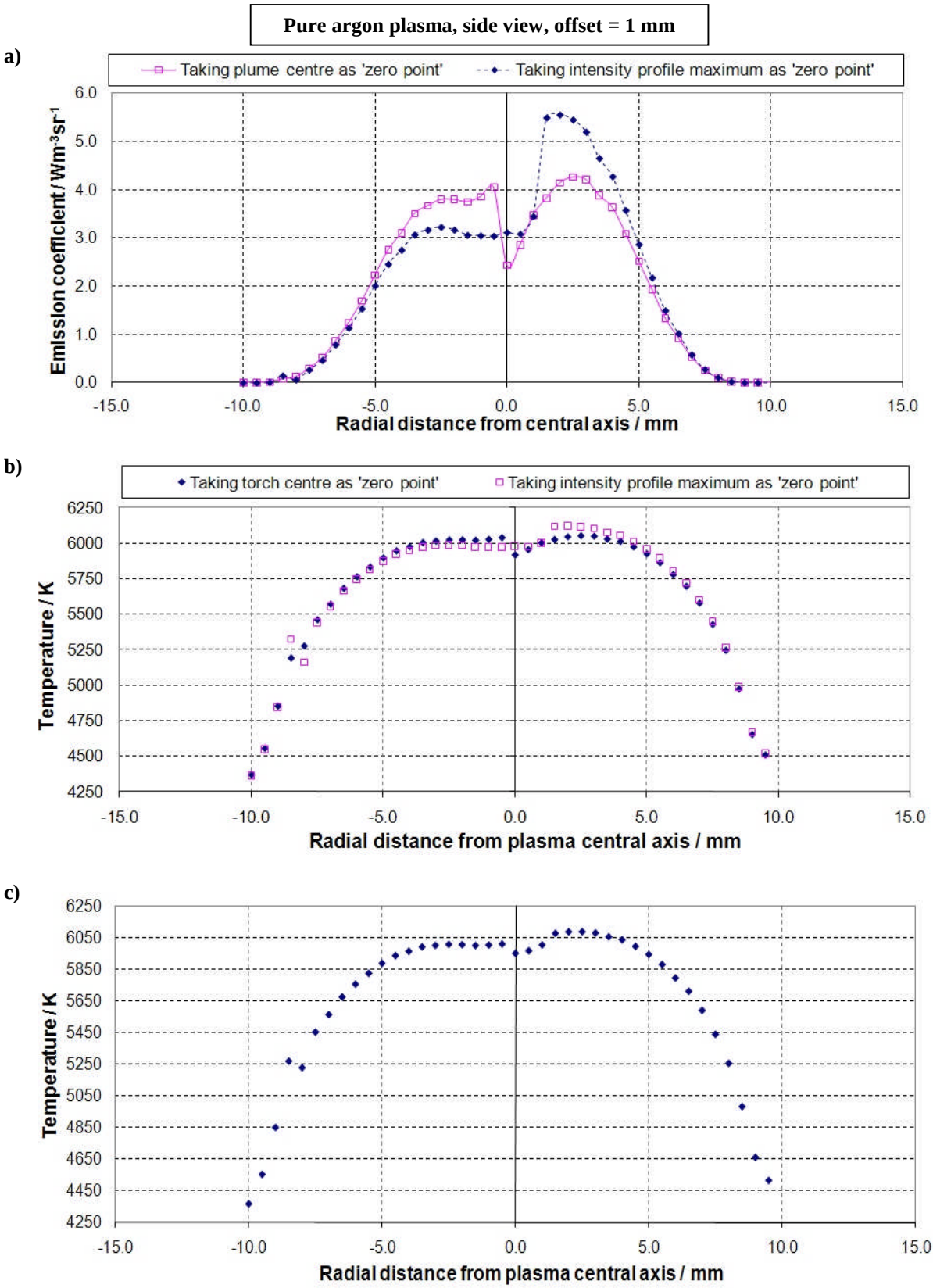

Figure 5.19 **a) Emission profiles of the data shown in figure 5.18, one calculated using the torch's geometric centre as the zero point and the other using the intensity maximum as the zero point. b) The temperature profiles that result from those emission profiles. c) The temperature profile that results from the average of the two emission profiles.**

5.5.4.7 Line choice

The chosen emission line was the 696.54 nm line. Several other strong lines could have been chosen. Figure 5.20 shows the same temperature profile as shown in figure 5.10 with five other profiles which result from alternative line selections. All six lines originate from 4p-4s transitions. Towards the centre of the plume, the overall spread is less than 70 K, increasing to ±200 K in the periphery.

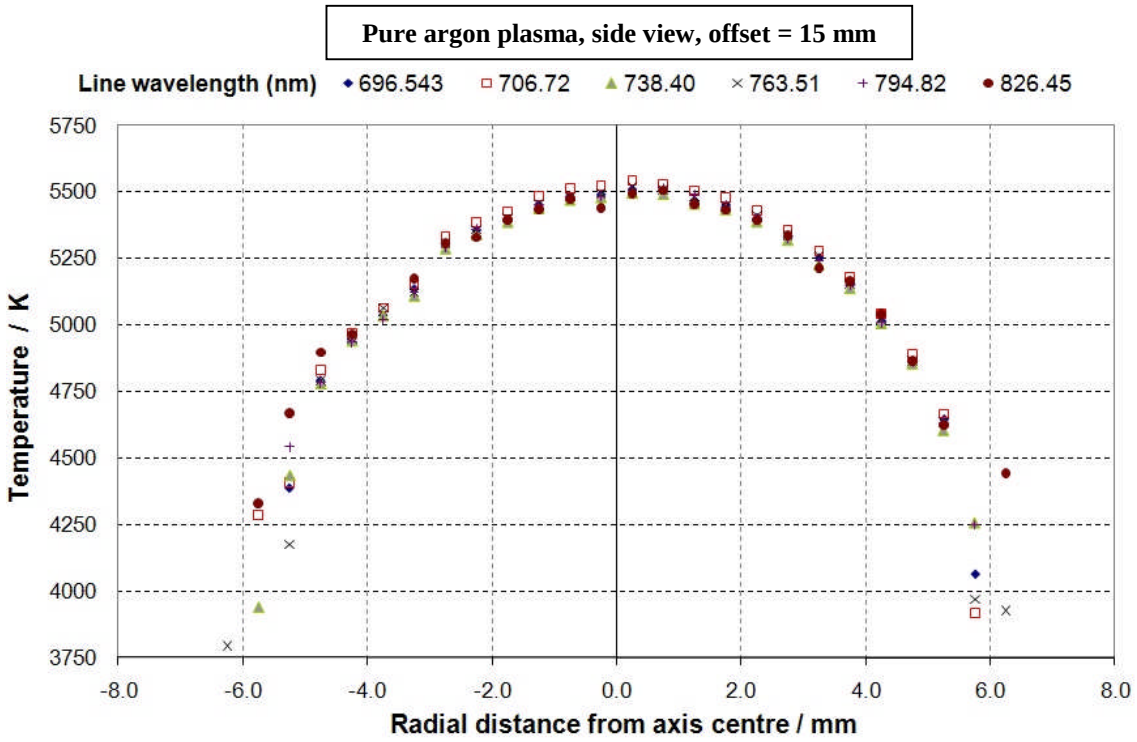

Figure 5.20 **Temperatures of the pure argon plasma determined from the intensities of different strong lines, 15 mm from the torch base, side view data.**

5.5.4.8 Estimation of particle density

When estimating the particle densities, the gas pressure was assumed to be at 1 atm (= 101,325 Pa). The argon was admitted to the mass flow controllers at ≈2 atm. As the argon passes through the torch the pressure must drop. The air in the chamber is rarefied by the exhaust, which means that ultimately it drops below atmospheric pressure. As the argon gas mixes with air in the plume, the argon particle density must drop further still. It is difficult to state exactly what the partial pressure of the argon is at any particular position in the plasma plume.

Figure 5.21 again shows the temperature profile that was first shown in figure 5.10, with alternative profiles showing how the temperature is affected by a change in argon gas pressure. If the plasma is assumed to be an ideal gas, the particle density at a given position is directly proportional to the pressure. A factor of 10 difference in pressure results in a temperature change of 500 K at most, less sensitive than one might expect.

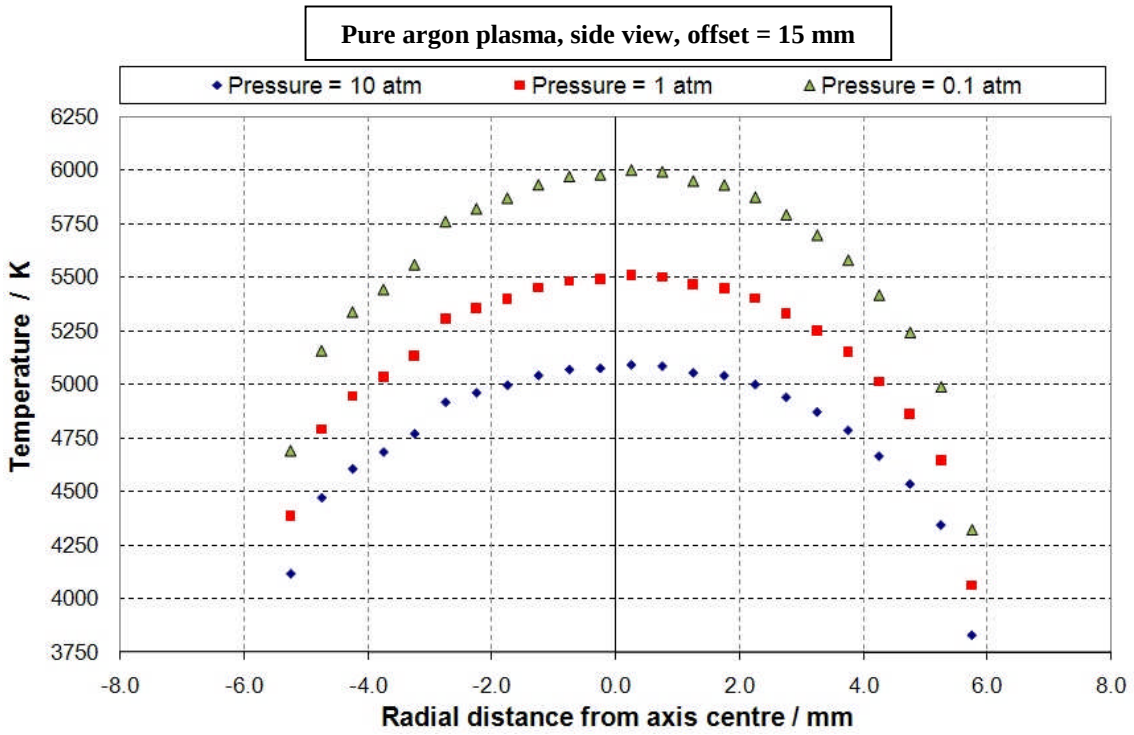

Figure 5.21 **The effect on the calculated temperature profile when the estimated pressure is adjusted.**

5.5.4.9 Inaccuracies summary

Many sources of inaccuracy exist in both the taking of measurements and the analysis. Because the relationship between temperature and the emission coefficient is logarithmic, the errors due to measurement inaccuracies are not as large as one might expect. Larger inaccuracies exist in the analysis; those resulting from the particle density estimations are probably the largest. Overall, it seems reasonable to suggest that temperature measurements within the plume of the argon plasma are correct to within ±500 K at worst. Such a figure is very satisfactory for an investigation of this type.

5.5.5 Extrapolation

Measuring the plasma temperature helps us estimate the amount of heat output from the torch. However, it has only been possible to measure the temperature in regions where it is > 4000 K. There is likely to be a significant contribution to the heat output in the cooler gas in the periphery of the plume. One way to compensate for this is to apply a fit to the existing data on each plane and extrapolate. Many of the emission profiles, such as the one shown in figure 5.22a are close to being Gaussian, so that might be a good starting point. A perfectly Gaussian emission profile, whose maximum is at $r = 0$, can be written

$$\varepsilon(r) = A\exp\left(-{}^{r^2}\!/_{\sigma^2}\right) \qquad (5.7)$$

where A is the central (maximum) emission coefficient and σ is the radius at which the emission coefficient drops to the value ^{A}/e. Equation 5.7 can be rewritten in terms of the full width half maximum (*FWHM*)

$$\varepsilon(r) = A\exp\left(-{}^{4r^2\ln 2}\!/_{FWHM^2}\right) \qquad (5.8).$$

Equation 5.4, for calculating the temperature, may be rewritten

$$T = \frac{B}{\ln\left(\frac{CN}{\varepsilon(r)}\right)} \qquad (5.9)$$

where B and C are constants, $B = \frac{E_U}{k}$ and $C = \frac{g_U A_{UL} h f_{UL}}{4\pi Z}$.

If the emission profile were a perfect Gaussian distribution, equation 5.8 could be substituted into equation 5.9

$$T = \frac{B}{\ln\left(\frac{CN}{A}\right) + \frac{4r^2\ln 2}{FWHM^2}} \qquad (5.10).$$

Figure 5.22b shows a temperature profile (9 mm below the torch, side view, using the +ve side data). Also displayed is the temperature profile that would be observed if the emission profile were a perfect Gaussian distribution (by setting A = 0.38 W/m^3/sr and *FHWM* = 4.4 mm).

The distribution produced from a Gaussian emission profile is a good fit at small radii. Above 3.5 mm it starts to deviate and so a correction to the fit is required. A similar deviation is observed at all of the other heights. It could be that the larger temperature gradient at high radii is due to the high cooling gas flow rate.

a)

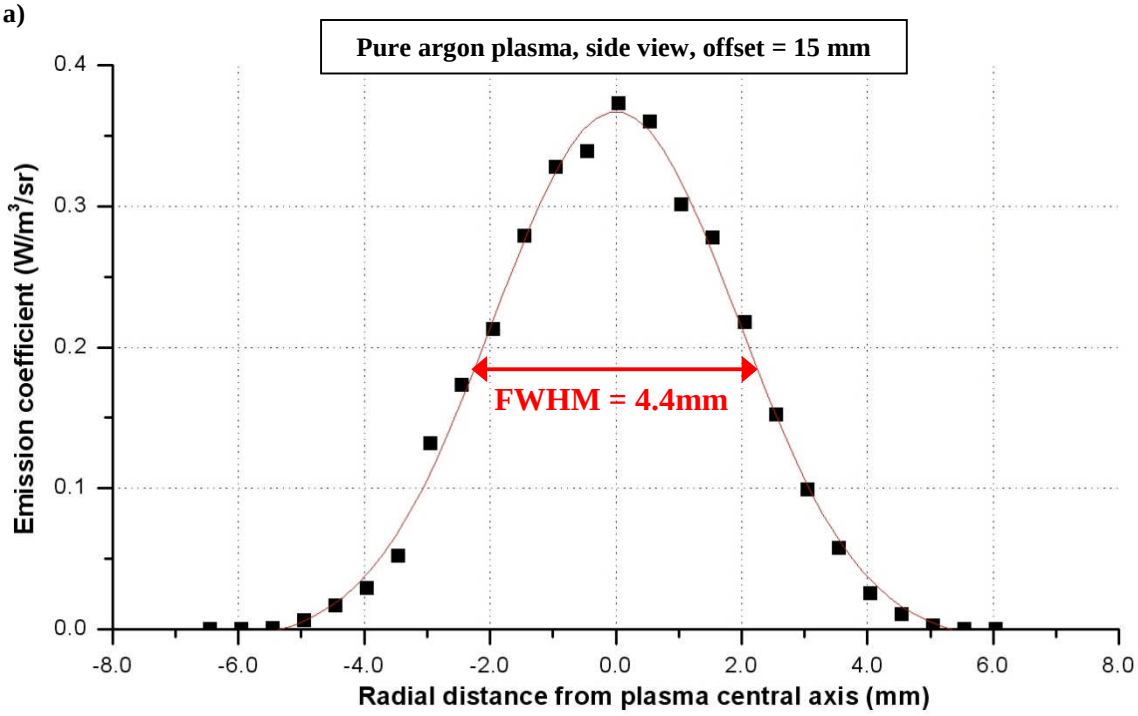

b)

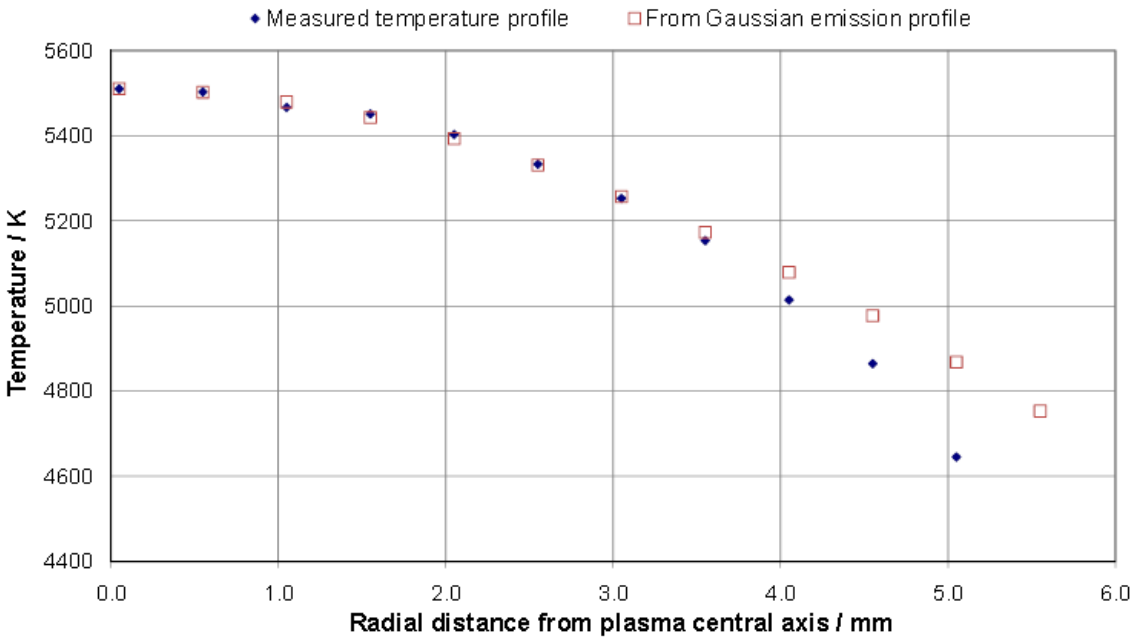

Figure 5.22 **a) A Gaussian fit is applied to the emission profile (the 696.5 nm line, 15 mm below the torch, side view). b) The measured temperature profile (from +ve side data) with that deduced from the Gaussian fit for comparison.**

A suitable correction could take many different forms. The chosen form must ensure that the temperature continues to decrease at larger radii. One suitable form could be a power law. If X is the transition radius, then a power law correction to the temperature could take the form $\Delta T = -Y(r-X)^Z$, where Y and Z are positive numbers. Equation 5.10 would therefore become

$$T = \frac{B}{\ln\left(\frac{C}{A}\right) + \frac{4r^2 \ln 2}{FWHM^2}} \quad \text{for r < Y}$$

$$T = \frac{B}{\ln\left(\frac{C}{A}\right) + \frac{4r^2 \ln 2}{FWHM^2}} - Y(r - X)^Z \quad \text{for r > Y} \qquad (5.11)$$

Figure 5.23 shows the same distributions as shown in figure 5.22b but includes the additional correction (X = 3.95 mm, Y = 57.9 and Z = 1.55).

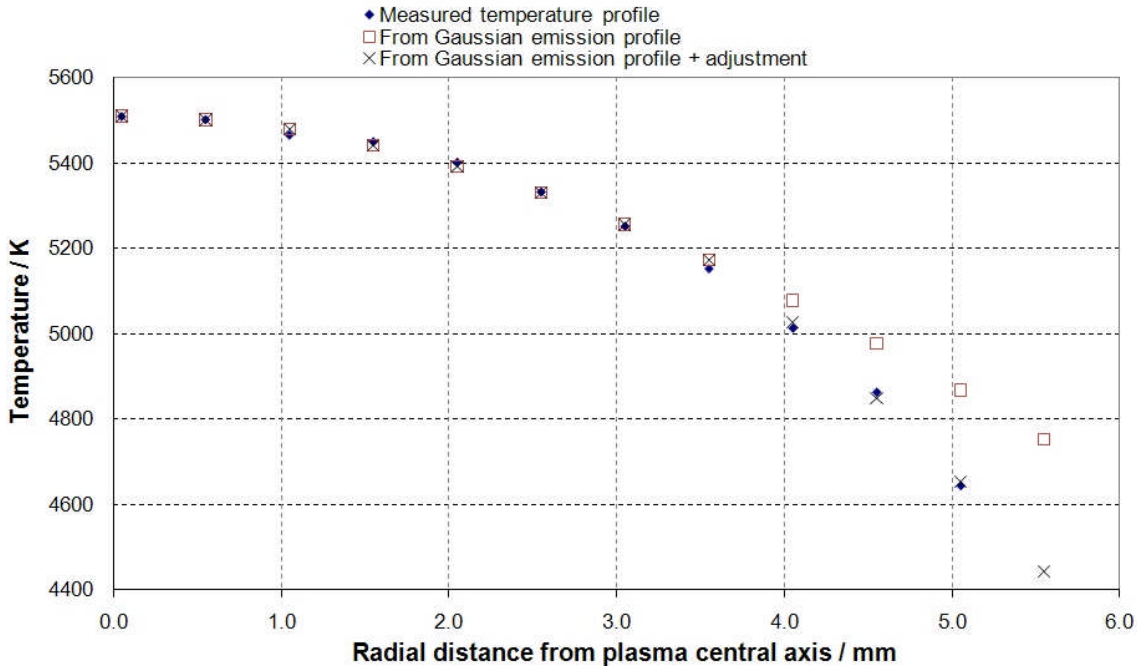

Figure 5.23 **As figure 5.22b but with an additional curve, which results from the Gaussian emission profile and a power law correction.**

Figure 5.24 shows the same temperature maps as were shown in figure 5.16 except that these have been made using data from the extrapolations.

a)

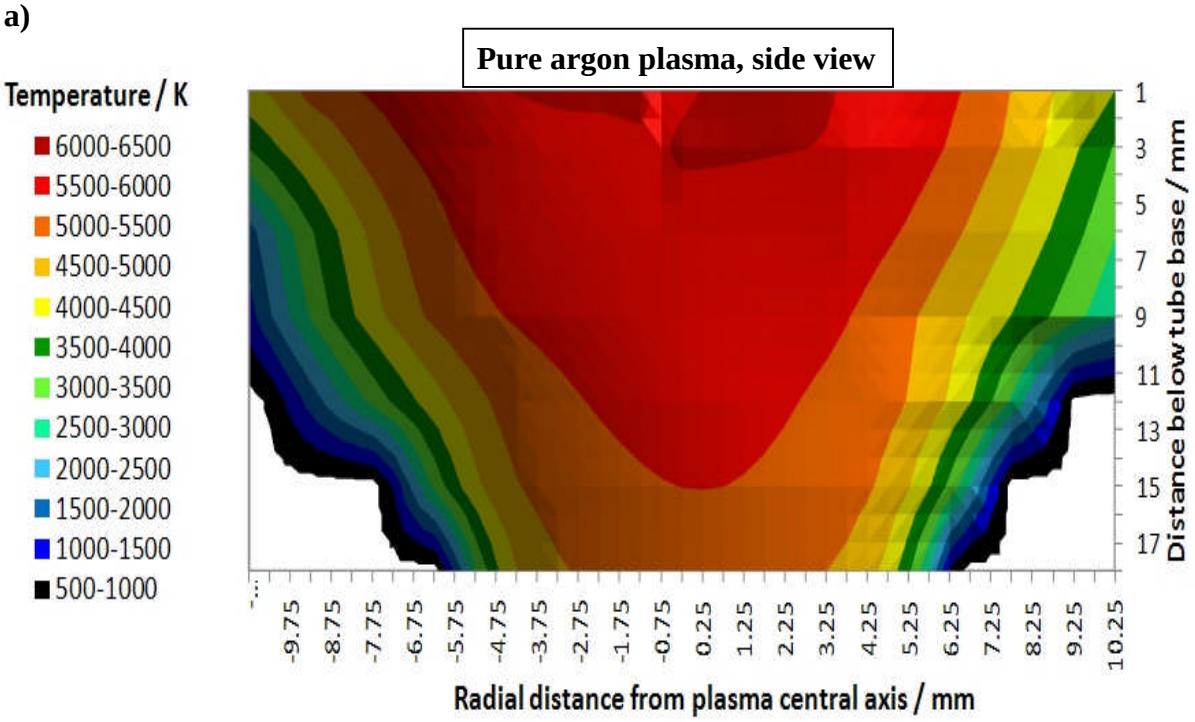

b)

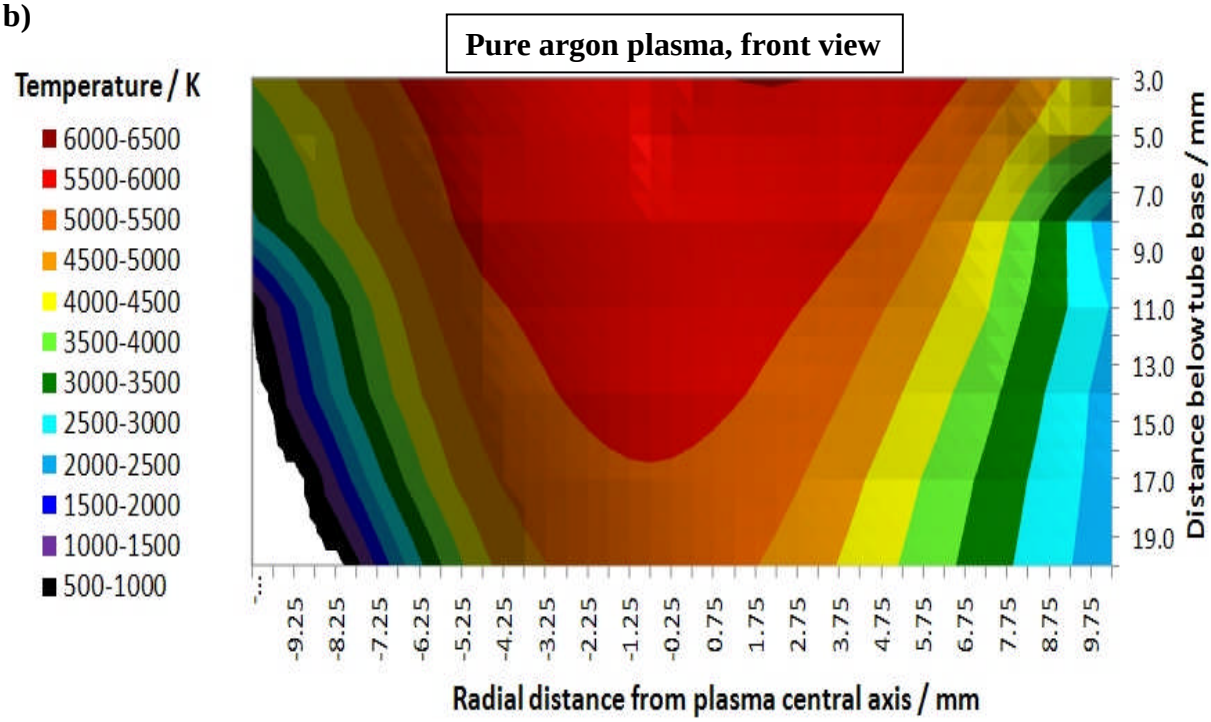

Figure 5.24 **a) Side view temperature map of pure argon plasma. b) Front view temperature map of pure argon plasma. Extrapolated data had been included in both instances.**

The endeavour is to calculate the amount of heat a substrate material receives while being etched. It perhaps goes without saying that the closer the material is to the base of the torch, the more heat flux it will receive. The gas heat that the sample receives per unit time, when positioned at a particular height, is equal to be instantaneous energy density integrated across the cross section of the plasma at that height multiplied by the gas flow speed at that height. If the sample is initially at room temperature (T_R), the plasma temperature profile is $T(r)$, the radius of the plasma is R and the vertical gas speed is equal to v, the heat input is approximately equal to, using equation 5.3

$$\tfrac{3}{2} k \int_0^R v(r) N(r) \left(T(r) - T_R\right) dr \,. \qquad (5.12)$$

Figure 5.25 shows how the heat flux received by a substrate material varies when positioned at different heights, using the data shown in figure 5.24. Values for the gas speed in the plume have been adopted from those calculated for a similar ICP by another research group using three-dimensional simulations (which peak at around 12 m/s). Equation 5.12 assumes that the temperature distribution is radially symmetric. This is not the case everywhere. However, having effectively measured four radial profiles (two from two different directions), this can be averaged out to a degree.

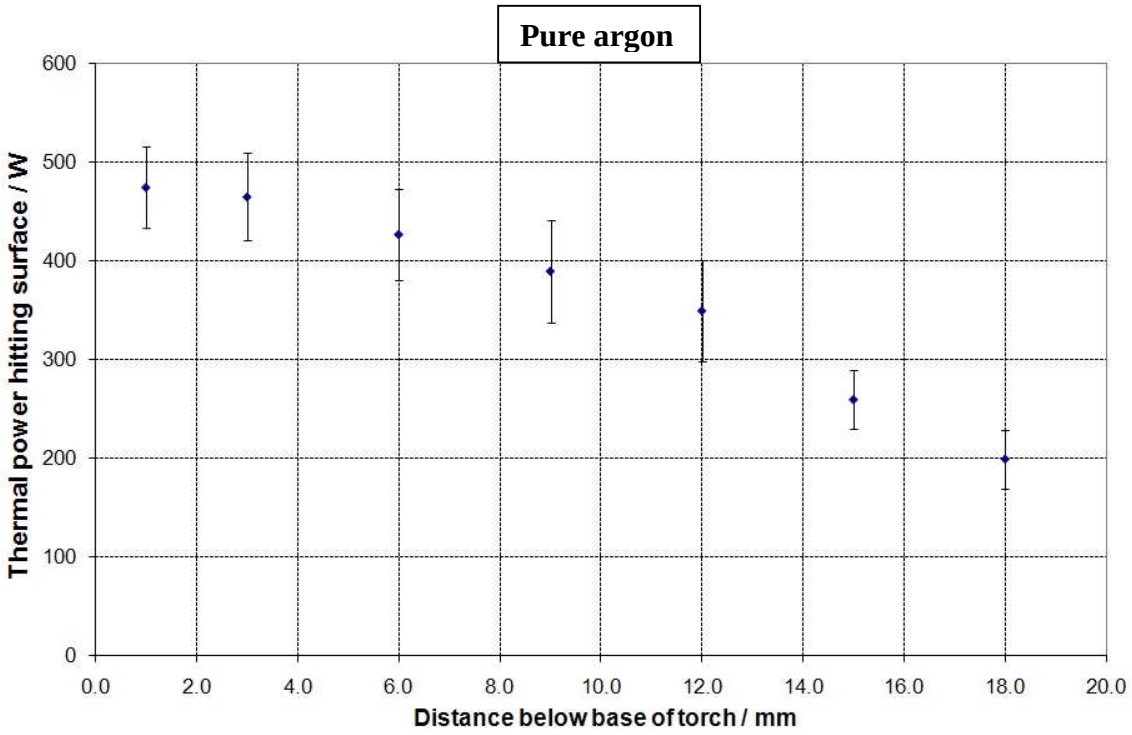

Figure 5.25 **A graph showing how much heat a substrate material receives when positioned at different heights below the torch.**

5.6 Measurements of the reactive atom plasma

Although the pure argon plasma could be useful as a heat source, it is useless as an etching tool. The spectroscopic work on the pure argon ICP was performed to help verify that the acquisition and analysis techniques are of sufficiently good quality. To the author's knowledge, no spectroscopic study of an atmospheric argon ICP with a fluorine-containing reactive gas has ever been made. However, very many spectroscopic studies of pure argon ICPs have been carried out, some of which are described in section 2.2.

Gao *et al.* used a 300 W, 40 MHz ICP whose diameter was 18 mm. [**69**]. In their study, a plasma image was projected onto the entrance slit of a 1 m-long monochromator to take measurements and relative line techniques were used for temperature calculations. They deduced temperatures between 4000 K and 5500 K in the plasma plume. As can be seen in figure 2.30, the measurements in that plume extended over a 20 mm range. The temperatures measured here are not dissimilar (the plasma studied here is slightly hotter, possibly due to the greater input power used).

The violet colour of the NF_3 plasma is the result of a cluster of broad lines of wavelength between 430 nm and 460 nm, visible in figure 5.26a. The emission responsible for the blue colour in the SF_6 plasma is less obvious in the observed spectrum (see figure 5.26b).

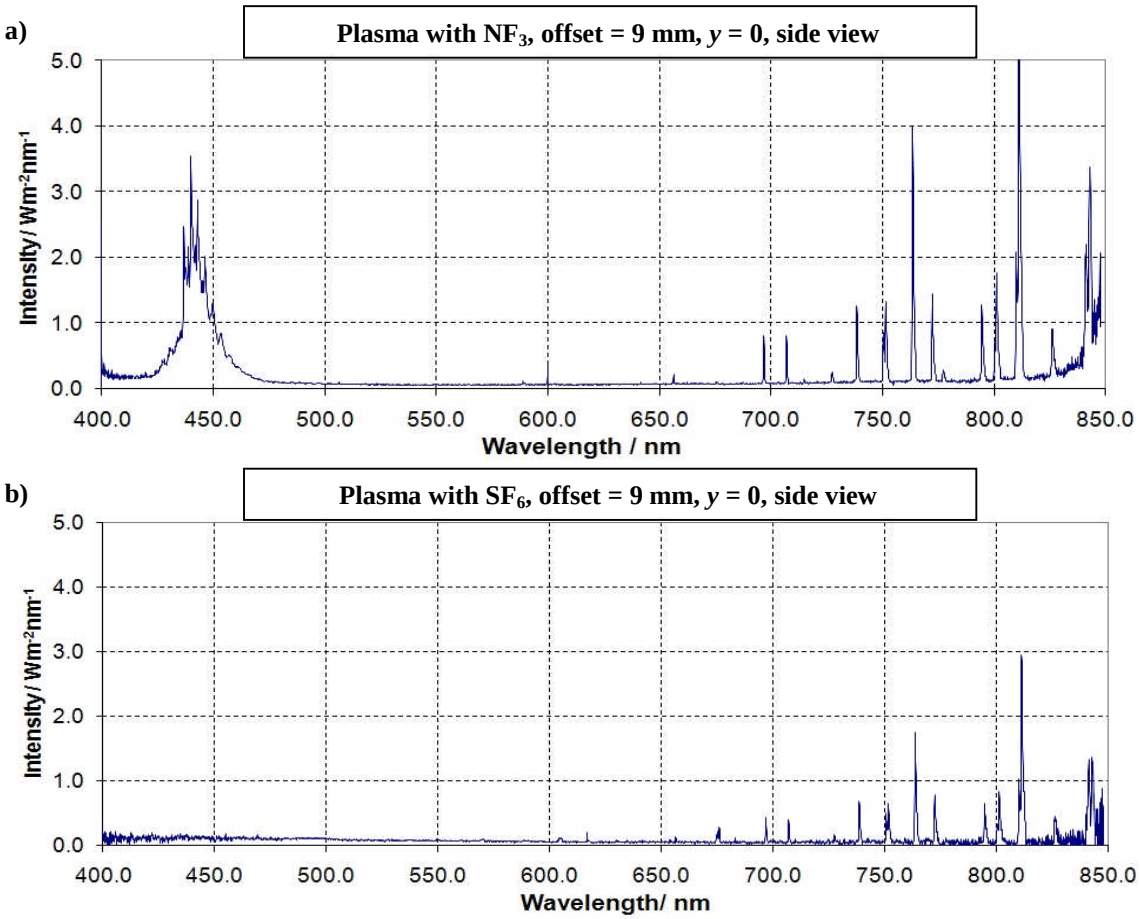

Figure 5.26 **Spectra taken of the plasma with a) NF_3 and b) SF_6. Both were recorded when looking along a line towards the central axis of the plume, 9 mm below the base of the quartz tubes from the side of the chamber.**

In the NF_3 plasma, measurements were taken from both the front and from the side at torch offsets between 3 mm and 17 mm. In the SF_6 plasma, measurements were only taken from the side and were only taken down to an offset of 9 mm. At greater offsets there were barely any emission lines at all. In both instances, measurements in the horizontal direction were separated by 0.5 mm.

Measured intensities of the 696.5 nm line in the SF_6 plasma are shown in figure 5.27. Temperature maps deduced from those intensities are shown in figures 5.28; the map shown in figure 5.28b includes temperatures extrapolated in a similar manner to that described in section 5.5.5. Similar maps for the NF_3 plasma are shown in figures 5.29 and 5.30. Graphs showing the amount of heat that a substrate surface receives at different heights when exposed to both plasmas are displayed in figures 5.31 and 5.32. Integrated measured intensity maps of the cluster of lines between 430 nm and 460 nm, hereafter referred to as the 'lines at 440 nm,' in the NF_3 plasma are shown in figure 5.33.

These calculations, it has been assumed that the relative proportions of argon and the reactive gas remain uniform throughout the plume. For the NF_3 calculations, the proportions by volume were 92% argon and 8% NF_3; for the SF_6 calculations, the proportions were 98.5% argon 1.5% NF_3. As the reactive plasma contains a mixture of gases, it is possible that the argon atom number densities, used in these calculations might be inaccurate due to demixing. When NF_3 is used, it is expected that many molecular species exist within the plasma, including NF_3, NF_2, NF, N, F, plus positively and negatively charged version of some of those. In the case of the SF_6, there are many more possibilities. As described in section 2.1.3, demixing can take place in regions where temperature is hot enough dissociate a significant fraction of the molecules of any gas present. Computing the deviations in mass fraction that result from demixing between argon and the reactive gas for this ICP would be a formidable task. To the author's knowledge, no research investigating demixing phenomena within an atmospheric ICP has been performed. The majority of work research into demixing processes, both practical and computational, has been based upon welding arcs. All demixing processes are driven by temperature gradients. The temperature gradients within welding arcs are generally very much steeper than those which have been presented for the ICP studied here; there is no reason to assume that a significant amount of demixing takes place within the plasma plumes when a reactive gas is included. In section 5.5.4.8 it was demonstrated that even a large error in the estimation of the particle density results in only a small error in the estimate of the temperature so, even if the amount of demixing were significant, it is expected the resulting inaccuracies in the temperature measurements would be negligible.

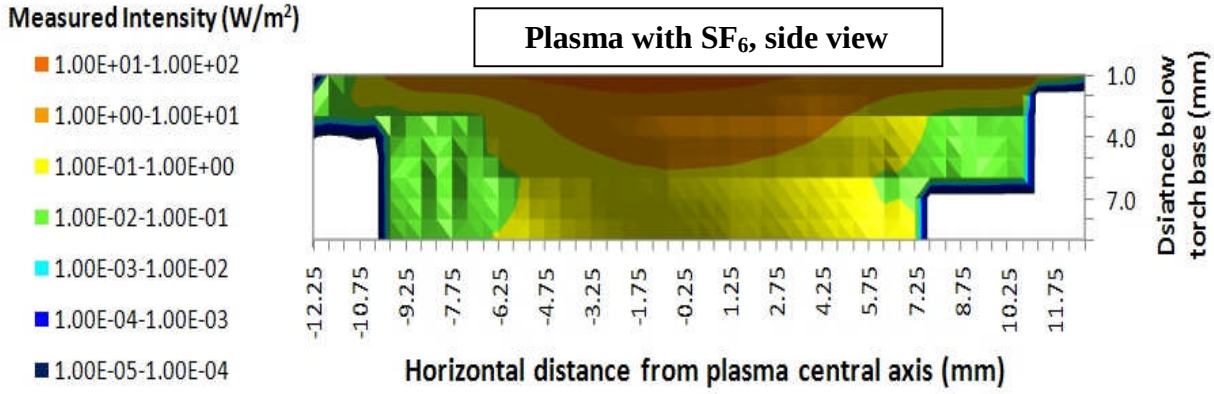

Figure 5.27 **Intensity map of the 696.5 nm line in the SF_6 plasma plume, side view.**

a)

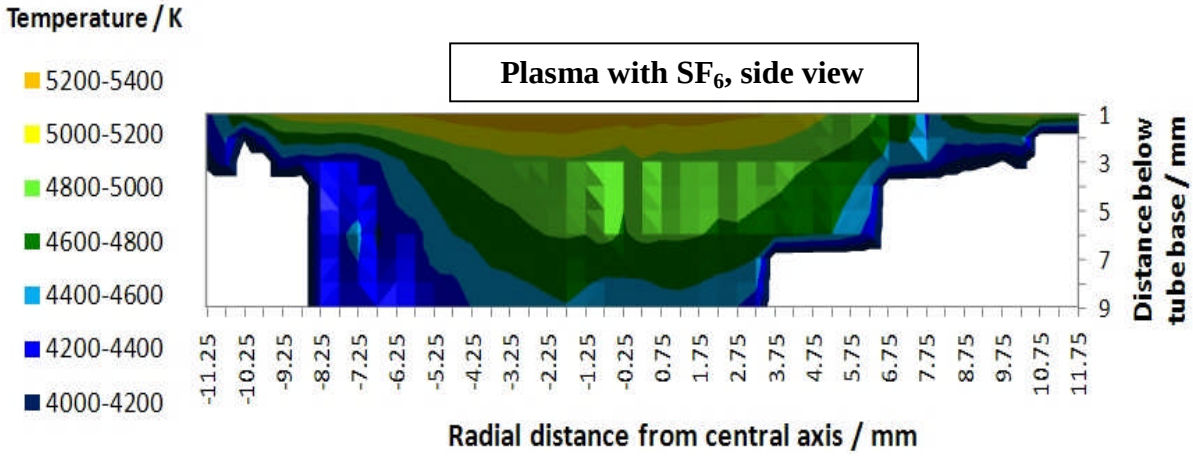

b)

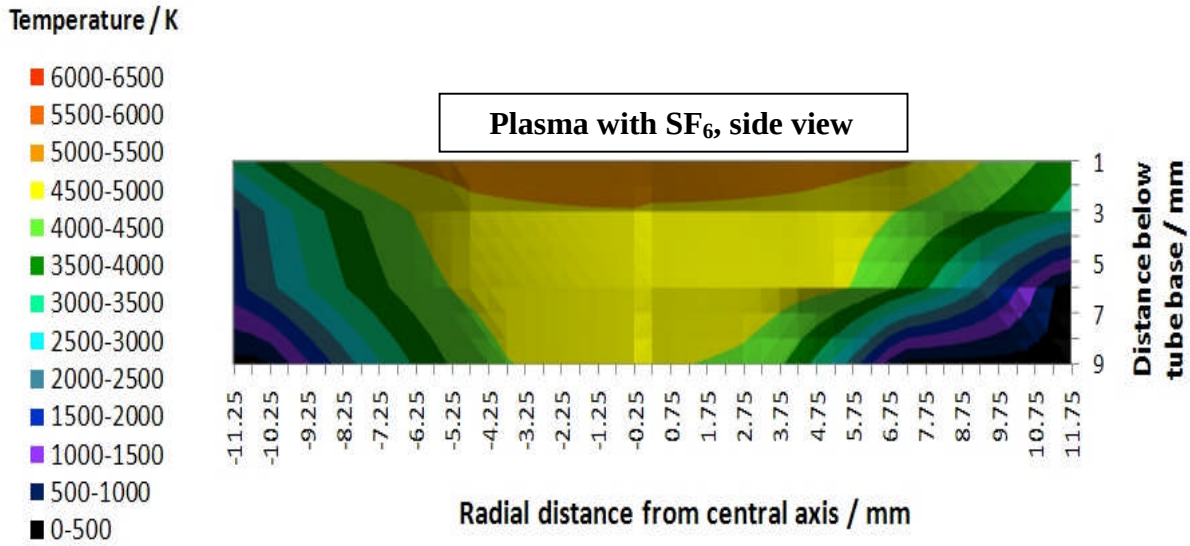

Figure 5.28 **Temperature maps of the SF_6 plasma plume, deduced from side view intensity measurements of the 696.5 nm line. In b), the temperatures in the cooler regions have been estimated by extrapolation.**

a)

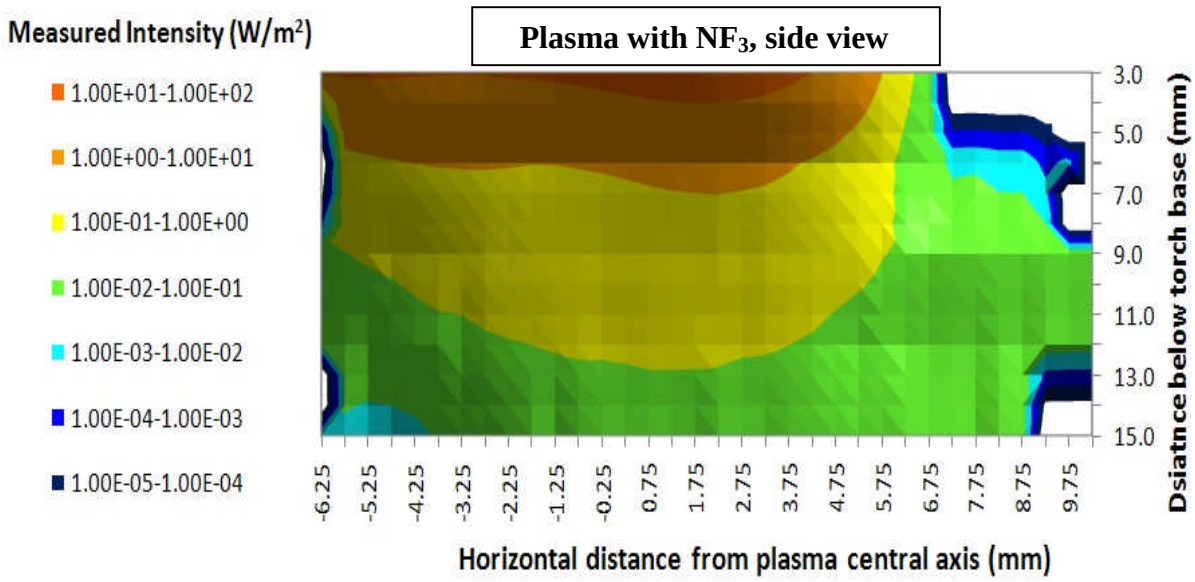

b)

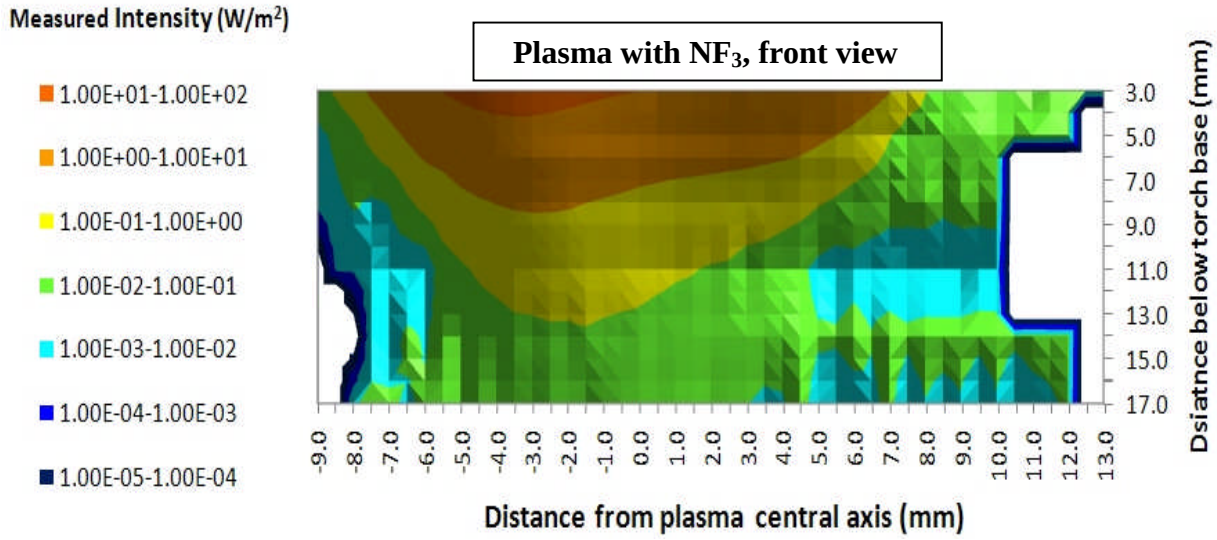

Figure 5.29 **Measured intensity maps of the 696.5 nm emission line, looking at the reactive plasma (with NF_3), a) side view and b) front view.**

a)

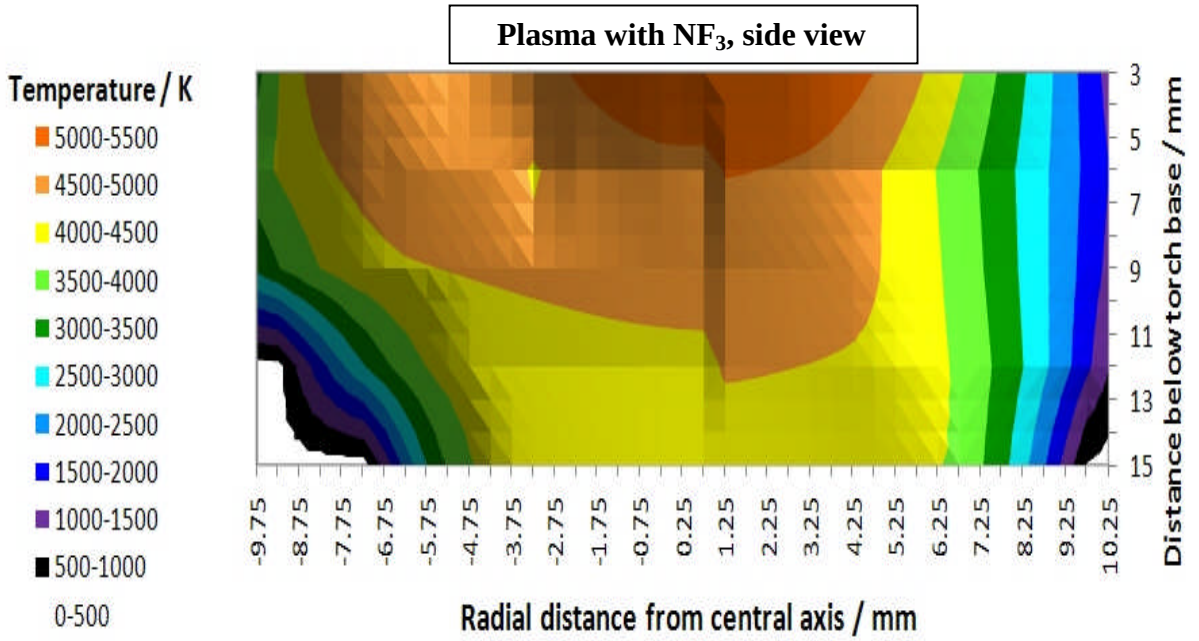

b)

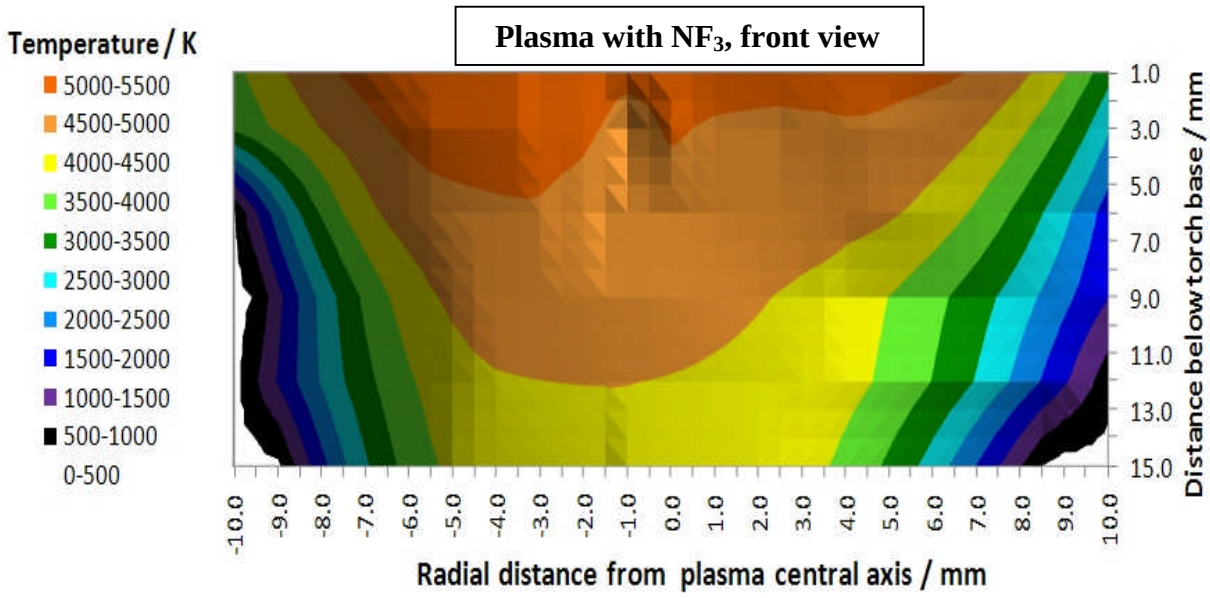

Figure 5.30 **Temperature maps deduced from intensity measurements of the 696.5 nm emission line, looking at the reactive plasma (with NF_3), a) side view and b) front view. Temperatures in the cooler regions have been estimated by extrapolation.**

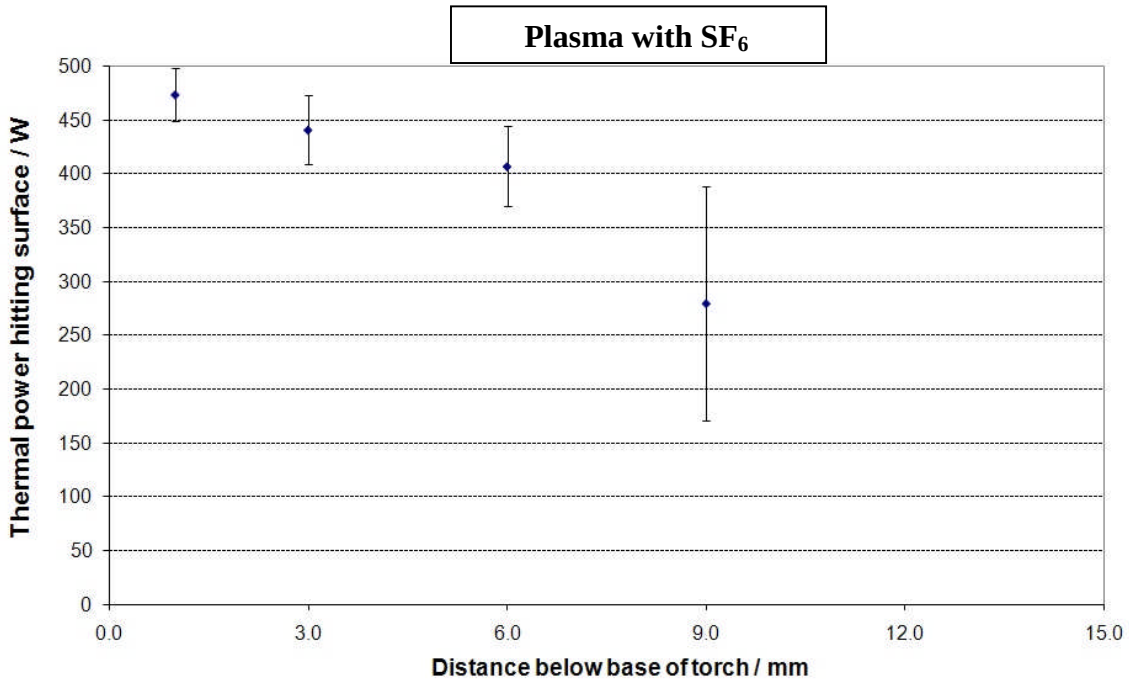

Figure 5.31 **The amount of heat a substrate material receives when positioned at different heights below the torch, when using the SF_6 plasma. Measurements taken looking from both the front and from the side of the chamber have been used.**

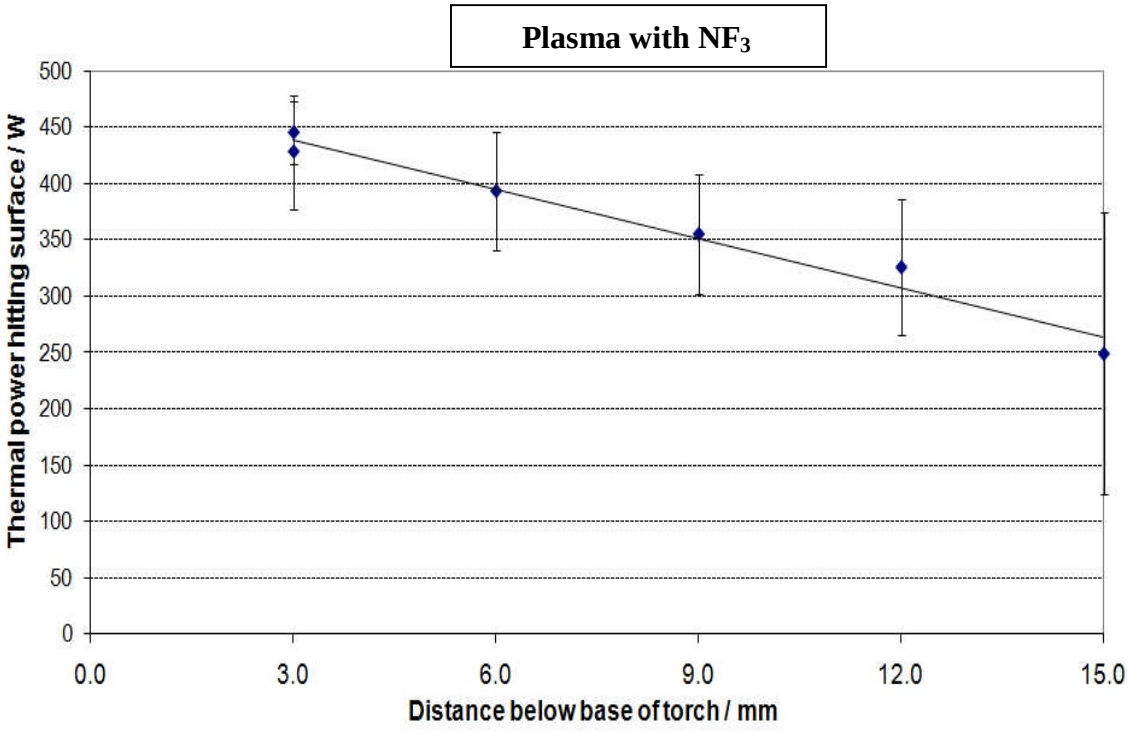

Figure 5.32 **The amount of heat a substrate material receives when positioned at different heights below the torch, etched using the NF_3 plasma. Measurements taken looking from both the front and from the side of the chamber have been used.**

a)

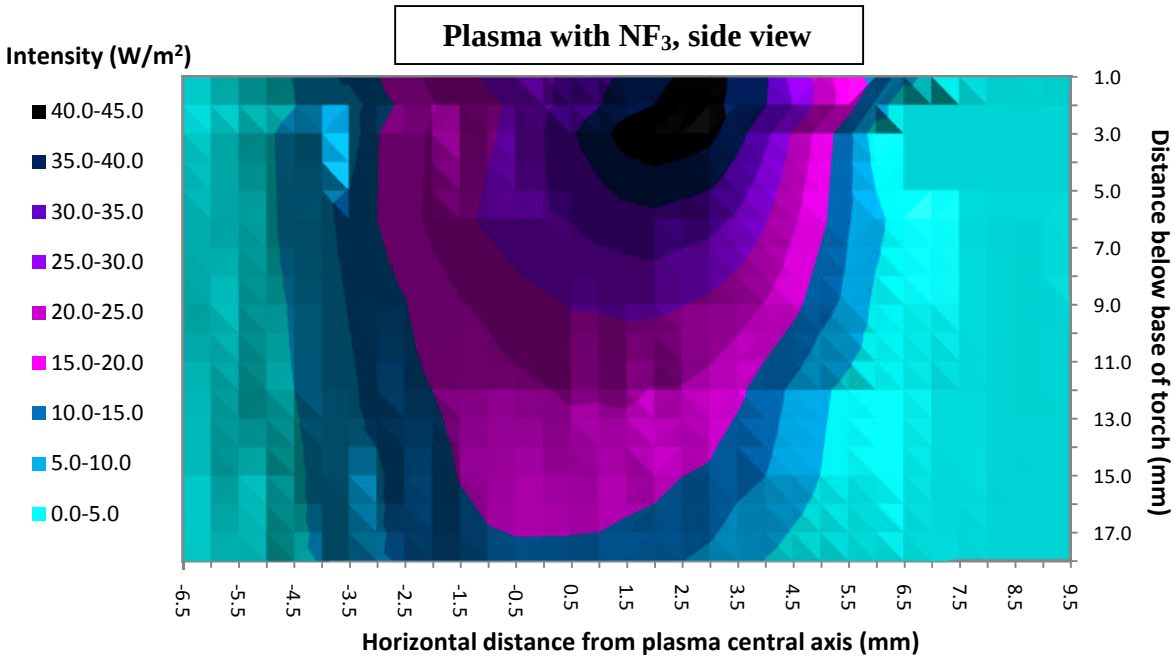

b)

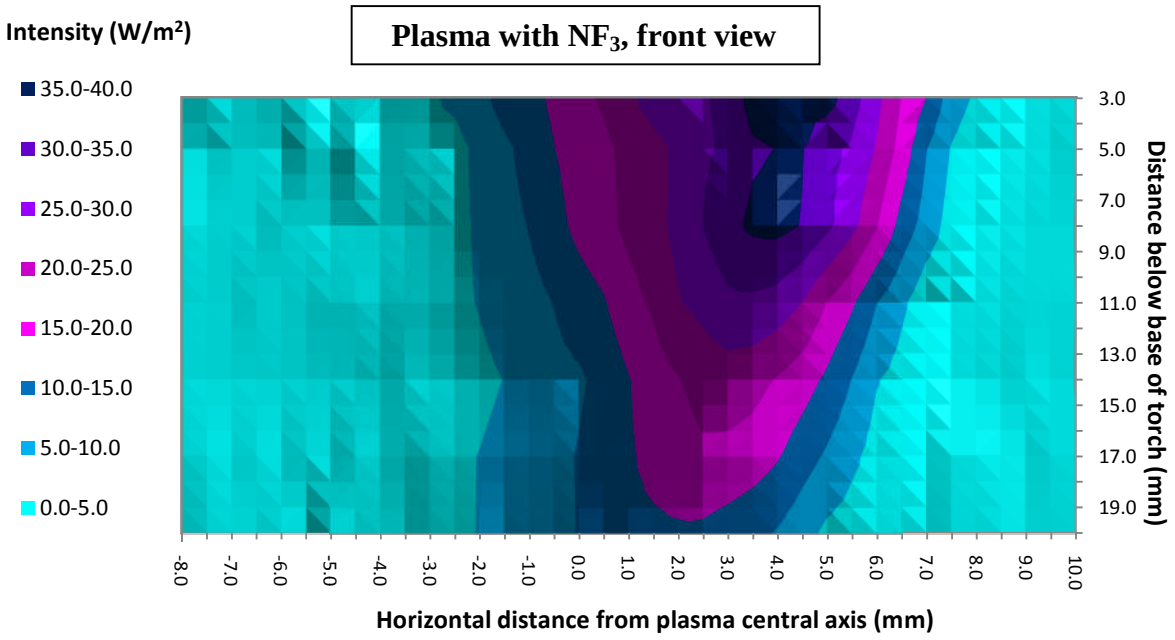

Figure 5.33 **Maps displaying the integrated intensity of the lines at 440 nm from a) side view measurements and b) front view measurements.**

The intensity of the argon emission lines generally drops by a factor of ~20 when the reactive gas is introduced.

In the NF_3 plasma, it is clear from the intensity profiles of the 696.5 nm line that it is far from being radially symmetric. The regions where the intensity of the 696 nm line is greatest do not coincide with the regions where the intensity of the 440 nm lines are greatest. This is fairly obvious when comparing the two front view maps.

As was mentioned in section 2.6.4, the activation energy for the reaction

$$NF_3\,(g) \rightarrow NF_2\,(g) + F\,(g)$$

is 125.9 kJ/mol. One would expect the ratio of the concentration of fluorine radicals [*F*], divided by the concentration of NF_3 molecules, [NF_3], would be temperature dependent and given by the equation

$$\frac{[F][NF_2]}{[NF_3]} \approx \exp\left(-\frac{126kJ/mol}{RT}\right) \qquad (5.13)$$

where R is the molar gas constant, 8.31 J/mol/K. The dissociation takes place in the coil zone, where temperature is above 9,000 K (see section 5.8). Assuming that the NF_3 molecules spend enough time in this warm region (so that equilibrium is reached) about 80% of the NF_3 molecules are dissociated. When using NF_3, the flow rate of that gas was 80 sccm, equivalent to 6.0×10^{-5} mol/s. A mere 7.5 W are needed to achieve such dissociation. Between 4000 K and 8000 K, the ratio increases with temperature almost linearly.

The torch heat output graphs derived from the data of the reactive plasmas do not show a big reduction compared to that of the pure argon plasma data. And, allowing for the error margins, one cannot assert from these graphs that there is any reduction at all. Profiles high up in the plume of the NF_3 plasma, at least those from the side view, include two maxima of different height. It could be that hot argon gas near the centre is pushed aside slightly when the NF_3 is introduced and not evenly in all directions. The centre of the plasma becomes cooler as a result, but the reduction in overall heat content is not so great.

If it were possible to identify fluorine emission lines in the spectrum of this plasma, it might be possible to determine the temperature (and maybe concentration) of fluorine radicals in the plume, and thus determine where the most chemically active part of the plume is. Unfortunately, it has not been possible to recognise any fluorine emission lines in any spectrum that has been taken. This is not a surprise; it is well known that inferring the existence of non-metallic atoms by ICP-AES is usually a challenge and fluorine is one of the hardest of all as its first ionisation energy is larger than that of argon [**31**]. In section 2.6.4, research on Plasma Chemical Vaporization Machining (PCVM) [**127**] and Atmospheric Pressure Plasma Polishing (APPP) [**129**] were discussed. In those instances, it was possible to identify atomic fluorine spectroscopically. However, in both of those instances the plasma gas was helium, whose highest first ionisation energy is our highest of all the elements. This means that it should be much easier to observe fluorine emission lines within a helium plasma than it is within an argon plasma.

It might seem reasonable to assert that the emission lines at 440 nm are the result of fluorine and nitrogen atoms recombining. NF_3 cannot be synthesised from N_2 and F_2,

therefore it is unlikely that nitrogen and fluorine atoms are recombining to make NF_3. It is rather more likely that N_2 and F_2 are being formed. In any case, it is a reasonable to hypothesise that these emission lines are due to fluorine atoms reacting with something before they have the opportunity to react with the surface material. The variation of intensity of these lines might give us an indication of how much useful fluorine is present at particular heights. Figure 5.34 shows a plot of the intensity of the lines at 440 nm, integrated across the cross-section of the plasma, against the height below the base of the outer tube. The decay is approximately linear. The linear fit reaches zero at a height of 26.5 mm; if the substrate material were positioned at a lower height, presumably no etching would take place. If achieving the fastest possible etch rate is desired, it makes sense to position the substrate close to the torch. However, if achieving a symmetrical (Gaussian), material removal profile is the priority, it would be better to position substrate lower down, where the intensity profile of the lines at 440 nm is more symmetric (see figure 5.35). The offset used in all tests that were described in chapter 4, was 15 mm, which is a reasonable compromise.

The SF_6 plasma appears to be very much more symmetric than the NF_3 plasma (although measurements of the SF_6 plasma were only taken from one direction). When SF_6 was used a central flow used was only 200 sccm (10% SF_6 in argon); when NF_3 was used, the central flow was 400 sccm (20% NF_3 in argon). The lower central flow used with SF_6 might be less disruptive.

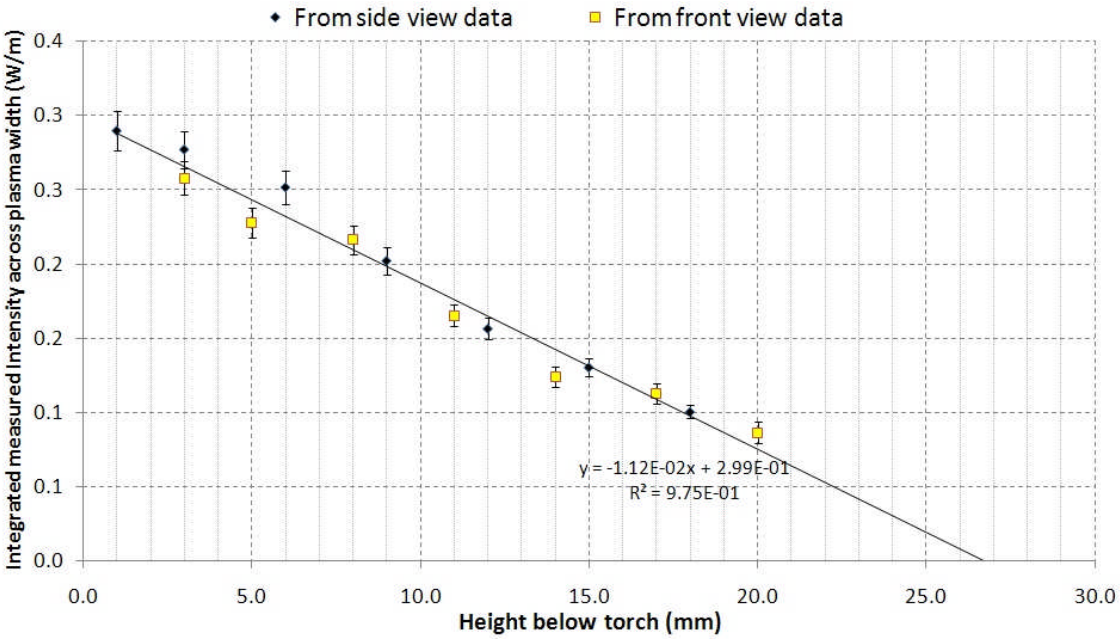

Figure 5.34 **Variation in the total measured intensity integrated across the width of the plasma at all measured distances below the torch base in the NF_3 plasma plume. A linear fit has been made to the data. If the hypothesis is correct, all of the fluorine atoms have recombined to form molecules by the time they have reached a distance of 26.5 mm below the torch base.**

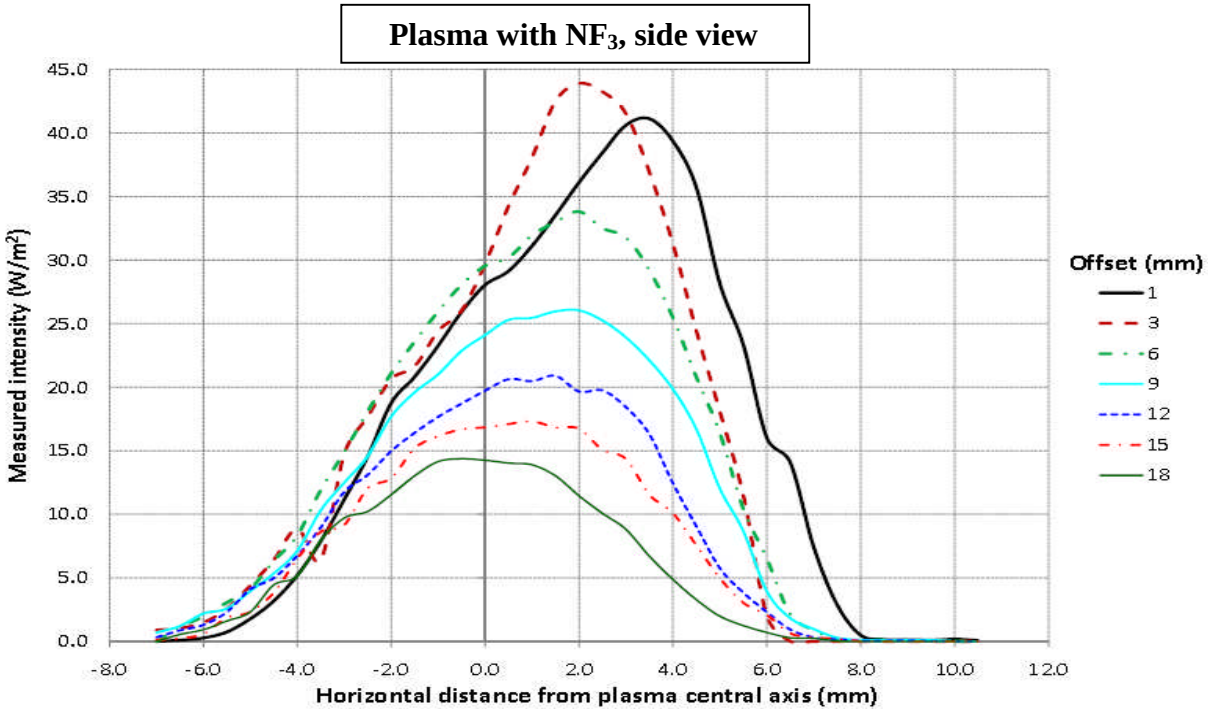

Figure 5.35 **Integrated intensity of the lines at 440 nm, side view measurements. The data display here is the same as in figure 5.33a. The variation in the symmetry of the profiles is more obvious when shown in this way.**

5.7 Spectra taken while etching substrates

Spectra were recorded while examining the plasma whilst it was over the substrate material. The Gershun tube was mounted onto the sample stage (see figure 5.36) and samples were taken at 2 mm increments horizontally across a 60 mm width. Spectra were recorded of both the plasma with NF_3 and the plasma with SF_6.

Figure 5.38 shows spectra that were recorded when looking at NF_3 etching ULE, SF_6 etching ULE, SF_6 etching silicon and the pure argon plasma over ULE. When ULE is being etched, a bright white disc appears on the surface. As can be seen in figures 5.38a and b, a plethora of emission lines are apparent which had not been visible in any spectra when looking at the naked plumes. The continuum level is much higher when ULE is etched. A number of strong titanium atomic emission lines have been identified between 400 nm and 530 nm and many weaker lines are found right across the wavelength range observed. There are also some broad spectral lines which probably derive from molecular transitions. These lines must be the result of chemical activity as when the pure argon plasma was placed over the sample, none of these lines appeared. These lines were also absent when silicon was etched using SF_6.

The ULE surface was held under the plasma for about half an hour. Consequently, a considerable amount of redeposition, which most likely consists of titanium IV oxide, was left behind on the surface, appearing as a white powder.

Rather surprisingly, the lines at 440 nm were not visible in the naked SF_6 plasma plume but were visible when that plasma was held over both silicon and ULE. A violet colour can be seen on the surface (it appears in the short exposure photograph shown in figure 5.37). As was briefly discussed in section 2.5.2, when silicon is etched using a fluorinated gas, one of the reaction steps produces SiF_3 in an excited state. This radical then drops back to its ground state, emitting a broad violet peak in the process. The reason why the NF_3 plume's spectrum contains this peak is not known, although it might be the result of the quartz tubes being etched by the plasma.

Figure 5.39 and 5.40 show the integrated measured intensity profiles of the lines at 440 nm line and that of the titanium emission line at 468 nm that resulted when ULE was being etched by NF_3 and SF_6 respectively. They are, more or less, in proportion with each other. The shapes of these profiles are approximately Gaussian (slightly skewed in the NF_3 plasma data). Therefore, it seems reasonable to infer that the radial distribution of the number of fluorine radicals striking the surface per unit area and per unit time is also Gaussian, leading to the Gaussian footprints that the plasma torch produces. It also suggests that fluorine reacts with the titanium in ULE as well as the silicon, and perhaps more readily.

a)

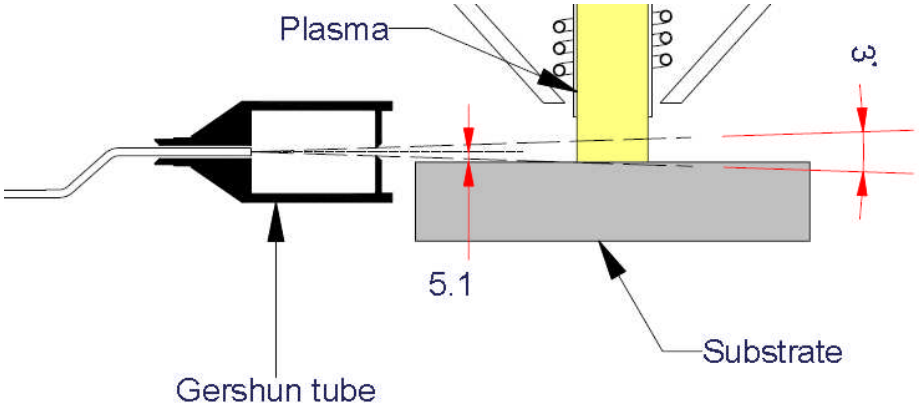

b)

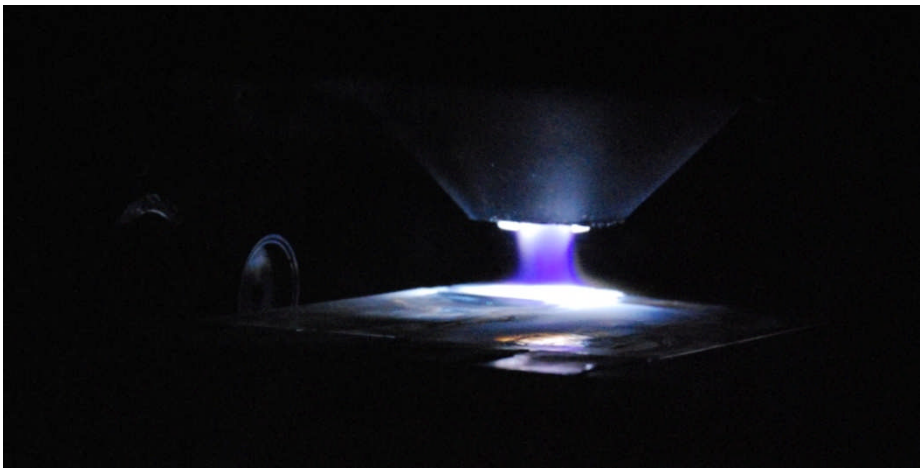

Figure 5.36 **Taking spectroscopy measurements of the plasma while it is etching ULE. The Gershun tube was mounted on the side of the motion stage. In the photograph, the reactive gas was NF_3.**

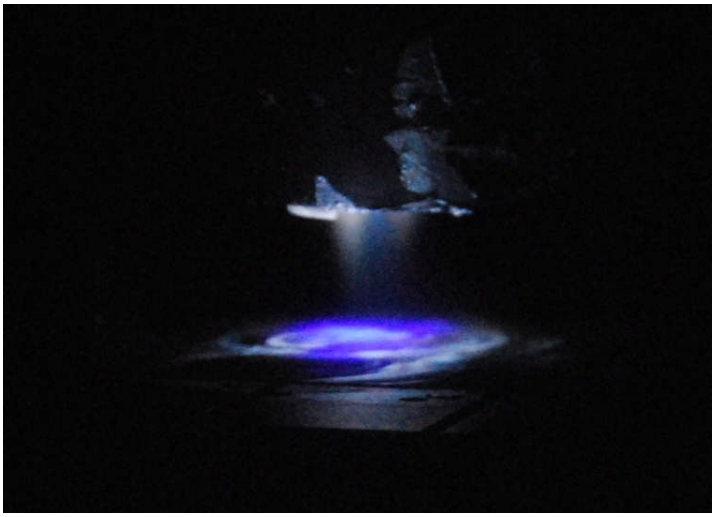

Figure 5.37 **Measurements were also taken while silicon was being etched using SF_6.**

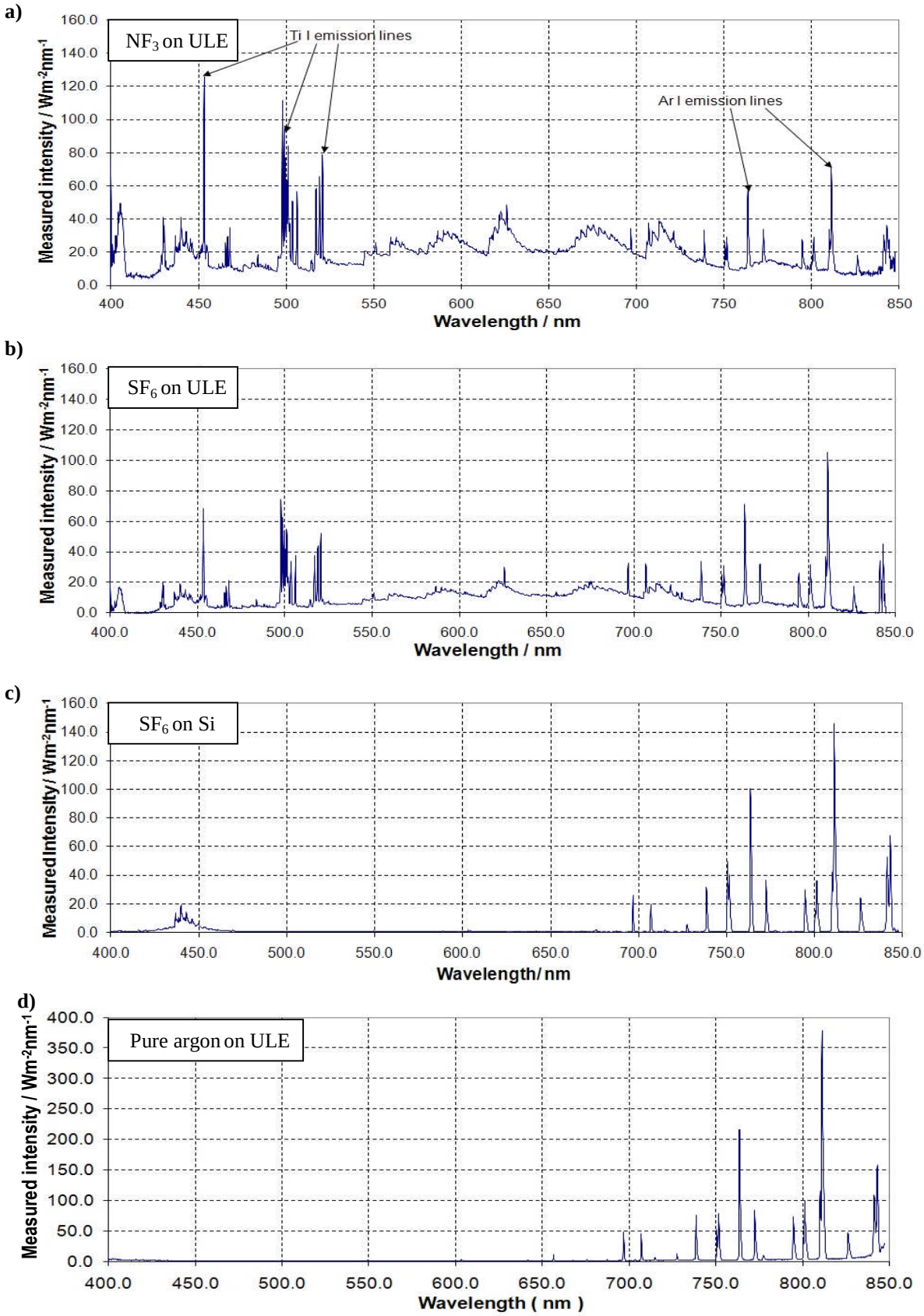

Figure 5.38 **Spectra observed when looking at a) ULE being etched using NF_3, b) ULE being etched using SF_6, c) silicon being etched using SF_6 and d) the pure argon plasma over ULE.**

a)

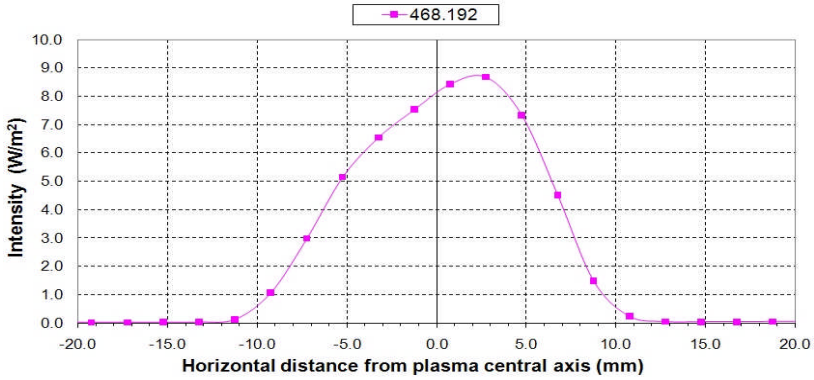

NF_3

b)

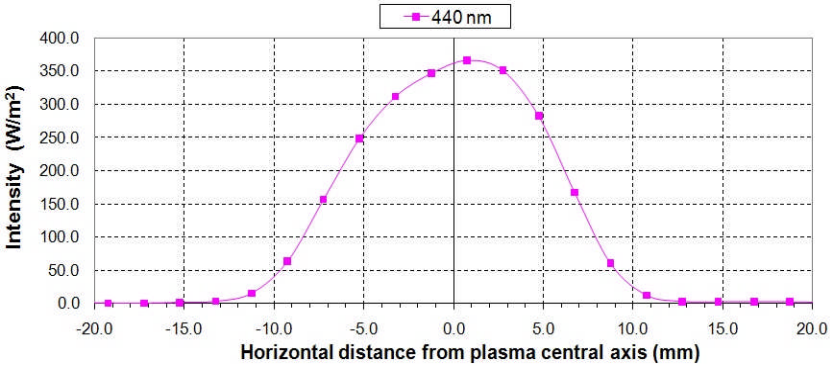

NF_3

Figure 5.39 **Integrated intensity profile of a) the titanium line at 468 nm and b) the integrated intensities of the lines at 440nm, taken when looking at ULE being etched using NF_3, side view.**

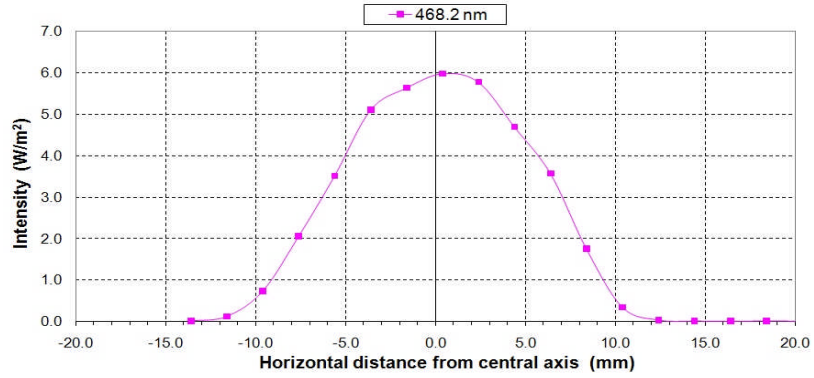

SF_6

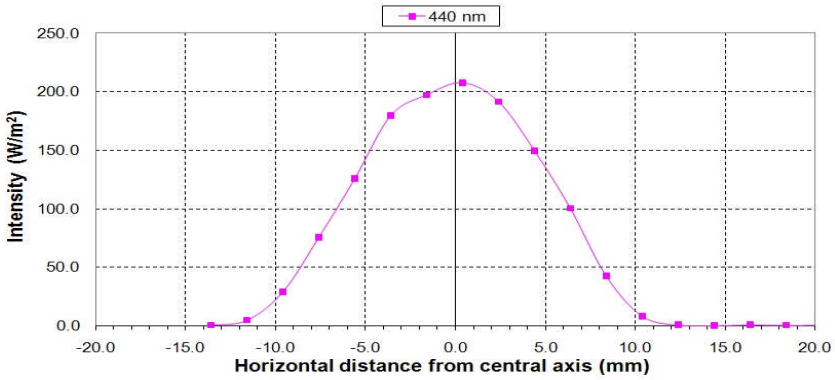

SF_6

Figure 5.40 **Integrated intensity profile of a) the titanium line at 468 nm and b) the integrated intensities of the lines at 440nm, taken when looking at ULE being etched using SF_6, side view.**

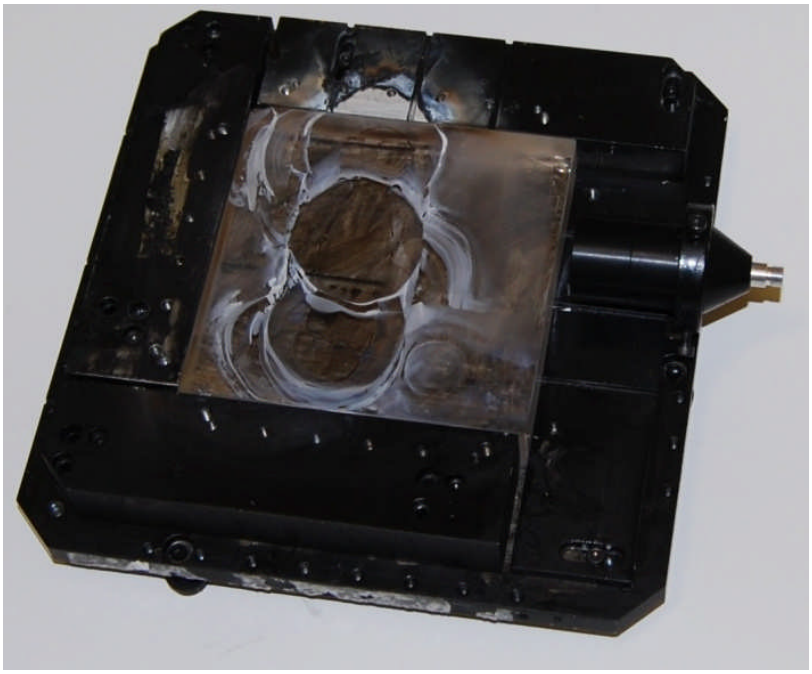

Figure 5.41 **The ULE surface used during the spectroscopic measurements. After such a long etching period (~30 minutes) a considerable amount of white powder has been deposited on to the surface, which is probably titanium dioxide.**

It seems that when the plasma with a reactive gas is held over ULE, a titanium-enriched plasma forms in a thin layer above the surface. The titanium emission lines could be used to calculate a temperature in the same way that the argon lines had been used. Determining this temperature is difficult to achieve using a single emission line as estimating the particle density, in this instance, is not possible. Boltzmann plots have been made using eleven emission lines, whose details are listed in appendix B. Figure 5.42a shows a sample Boltzmann plot. The quality of the linear fit is not remarkable; the cluster of points around 3.3 eV spoil it somewhat. This implies that departures from LTE exist. Figure 5.42b shows the same plot with two linear fits. The blue solid line is the best fit through the points of upper energy between 2.40 eV and 2.70 eV (i.e. a cluster on the left-hand side of the graph and a cluster in the middle). The red dotted line is the best fit through the points of upper energy between 2.70 eV and 3.32 eV (i.e. a cluster on the right-hand side of the graph and a cluster in the middle). The blue solid line implies a temperature of 2251 K; the red dotted line implies a temperature of 3712 K. Boltzmann plots taken from data at other positions display a similar pattern. It appears that this titanium plasma cannot be characterised as having a single, unambiguous temperature anywhere. Figure 5.43 shows temperature profiles determined from Boltzmann plots made from 'hot' data (using the emission lines whose upper energies are between 2.70 eV and 3.32 eV) and from 'cold' data (using the emission lines whose upper energies are between 2.40 eV and 2.70 eV). The temperature profile of unexcited titanium atoms would be similar to or lower than that of the cold data temperature profile, although probably not much lower. The populations of excited atoms are at higher temperatures. The ionic and electron temperatures will be above the hot data temperature profiles. It would have been of interest to calculate ionic temperatures. Unfortunately, there are no strong ionic

titanium lines between 400 nm and 900 nm, the range detectable by the spectrometer. There are some strong ionic emission lines in the ultraviolet, between 300 nm and 400 nm.

Using the intercept points from the 'cold' Boltzmann plots and equation 5.5, the titanium atom density can be estimated to be ~4.2×10^{16} m^{-3} ($\pm$ 1×10^{16} m^{-3}) at the centre while etching with NF_3. When using SF_6, this value was larger, ~8.8×10^{16} m^{-3} ($\pm$ 2×10^{16} m^{-3}). The internal partition function, *Z*, has been set to 12 for this calculation [**142**]. The ionisation fraction of this titanium plasma, when applying Saha equation (equation 2.6), is ~10%, very much higher than that in the argon plasma.

Although it has not been possible to define an unambiguous temperature for the titanium plasma disc, it is clearly lower than that of the naked reactive plumes at that height (the temperatures at the same height were about 1000 K higher than the hot data temperature profiles) but higher than that of the ULE surface. ULE melts at around 1900°C and starts to soften at the 1490ºC. Although no melting has been observed, evidence of deformation has been observed in one of the samples used in these tests.

a)

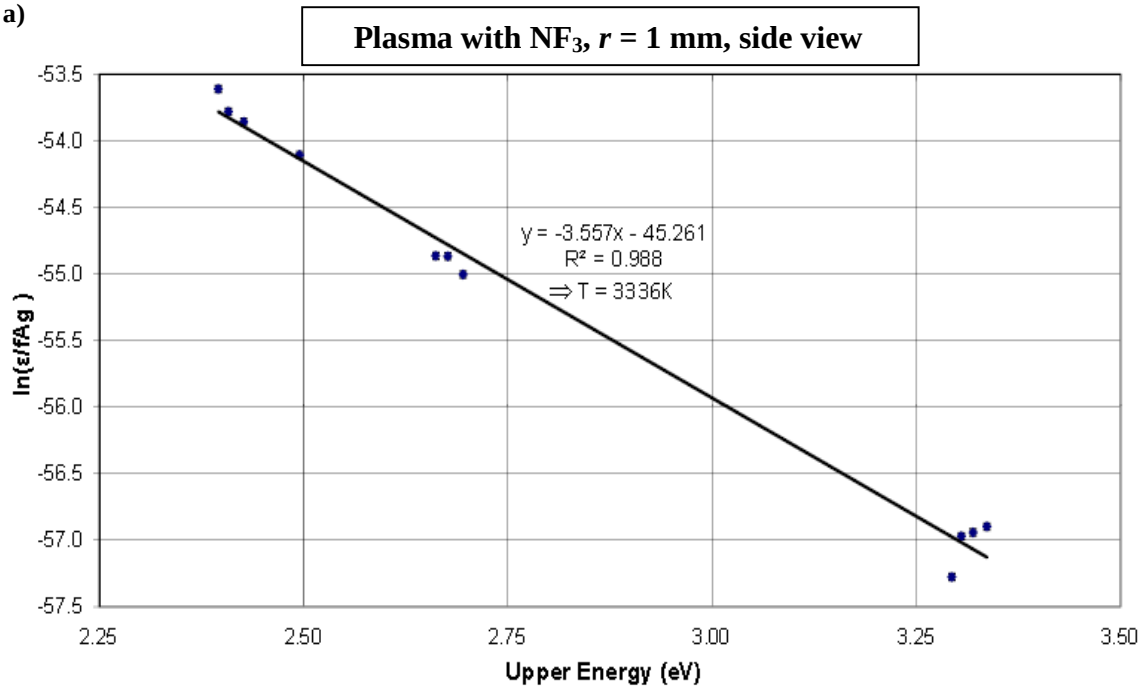

b)

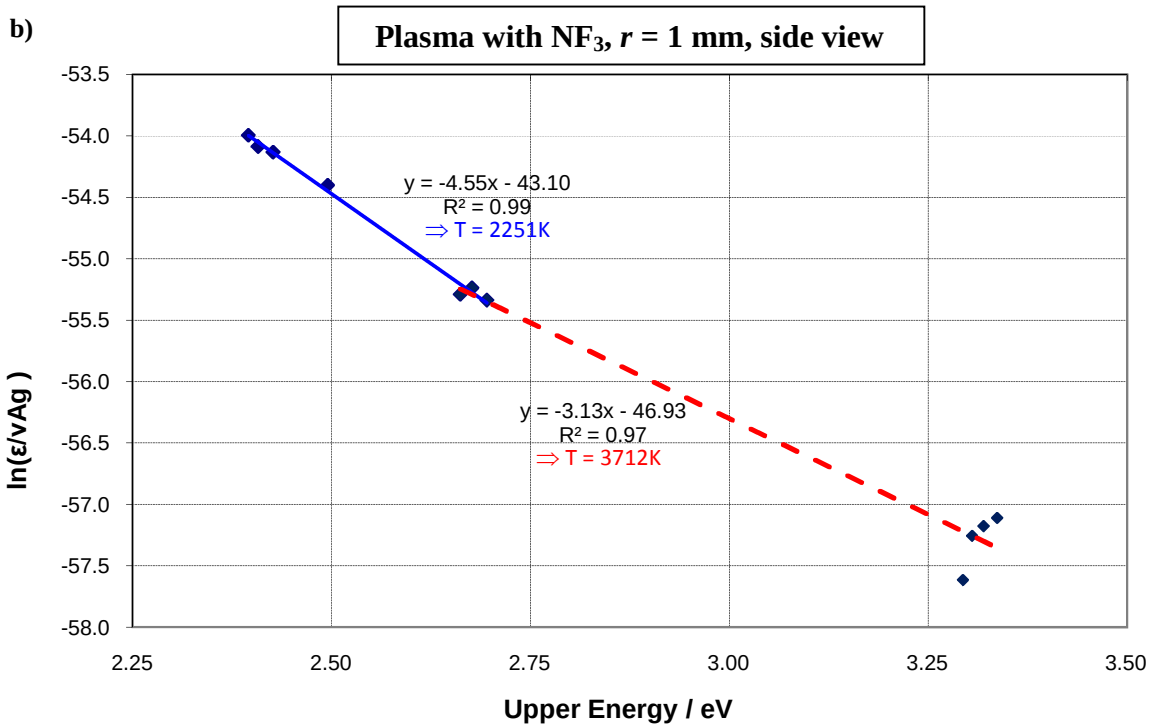

Figure 5.42 **Boltzmann plots made from the intensities of titanium emission lines observed just above the surface of ULE being etched using NF_3, side view, looking 1mm away from the plasma central axis. In b) two straight lines that have been made between adjacent clusters of points. The two gradients correspond to significantly different temperatures.**

a)

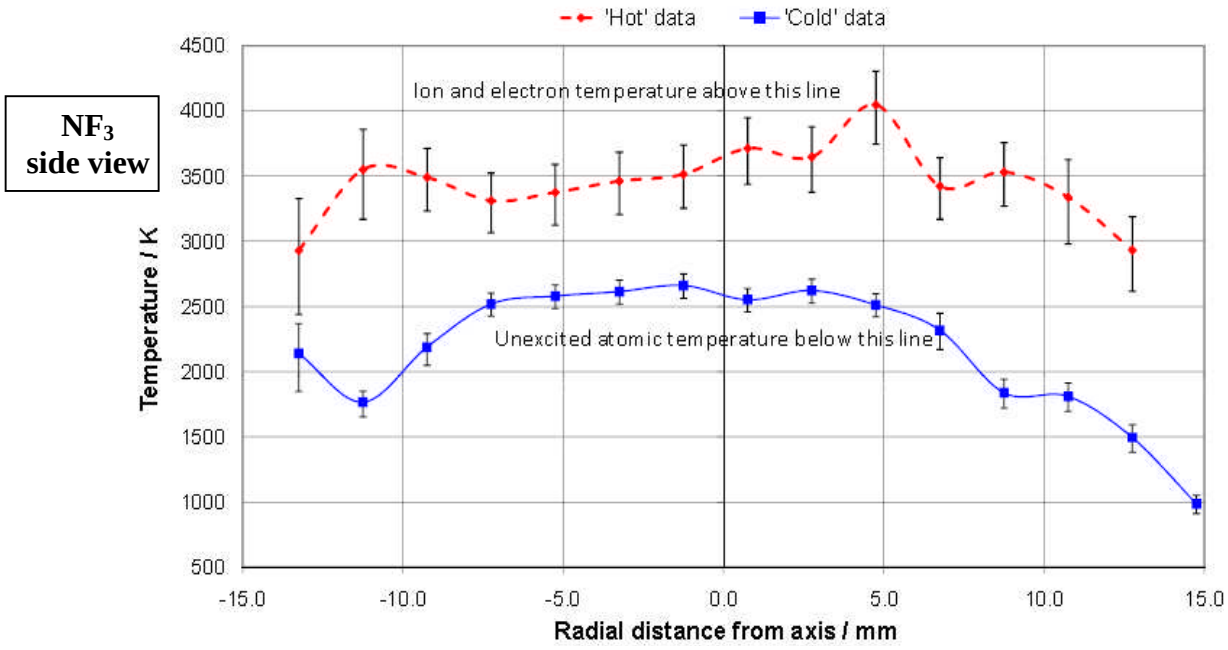

b)

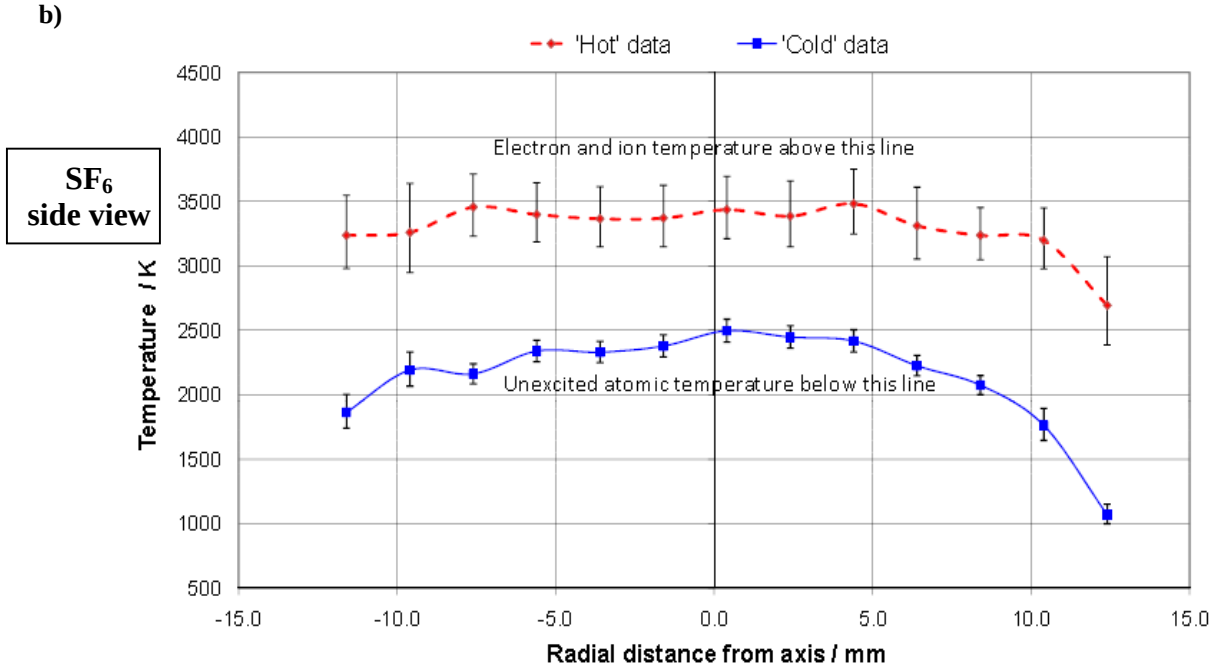

Figure 5.43 **Temperature profiles deduced from Boltzmann plots that were derived from the intensities of titanium atomic emission lines, looking just above the surface of ULE being etched using a) NF_3 and b) SF_6, viewed from the side of the chamber. Local thermal equilibrium does not appear to exist anywhere in this plasma, so it is not possible to define an unambiguous temperature at any position. The solid line plots are taken from emission lines of upper energy between 2.40 eV and 2.70 eV ('cold' data). This could be regarded as the upper limit to the neutral atom temperature. The dotted red line plots are taken from emission lines of upper energy between 2.70 eV and 3.32 eV ('hot' data). This could be regarded as a lower limit to the ionic and electron temperature.**

5.8 Measurements within the coil zone

The last spectroscopic measurements were made while examining the coil zone. Measurements were taken looking along just one plane in the lower part of the coil zone, viewed from the side of the chamber (see figure 5.44). A set of measurements was taken first with just the pure argon plasma, and secondly, looking at the plasma with SF_6. The temperature profiles shown in figures 5.45 were all created from Boltzmann plots. The peak value, around 9300 K, is consistent with values measured by other research groups on similar ICPs. Temperatures of the same region derived from just the 696.54 nm were found to be more than 2000 K lower than those shown in figure 5.45. This is most likely due to the fact that the viewing area when taking measurements may have been partially obscured by the coil. The temperature profile of the plasma with SF_6 is noticeably flatter. It could be a result of central gas flow pushing the hot plasma gas outwards. As was mentioned in section 2.1.3, departures from LTE have been observed in the coil zone of some atmospheric ICPs with greater departures at larger radii. Such departures are not apparent here. However such departures are generally more apparent in broader ICPS.

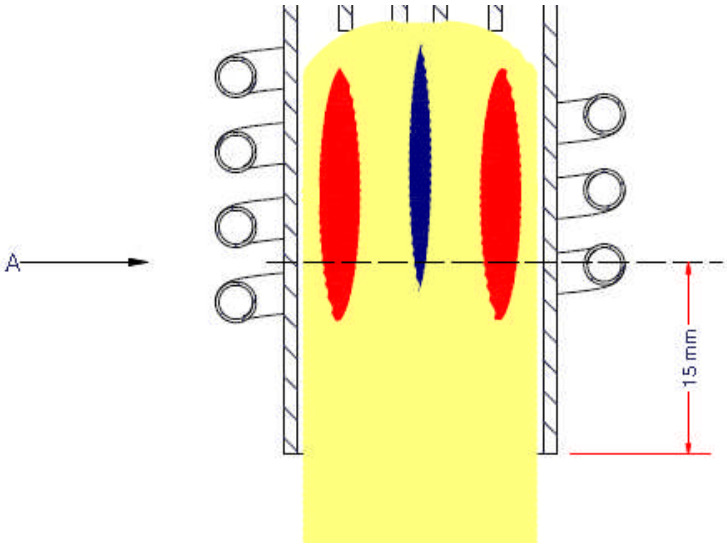

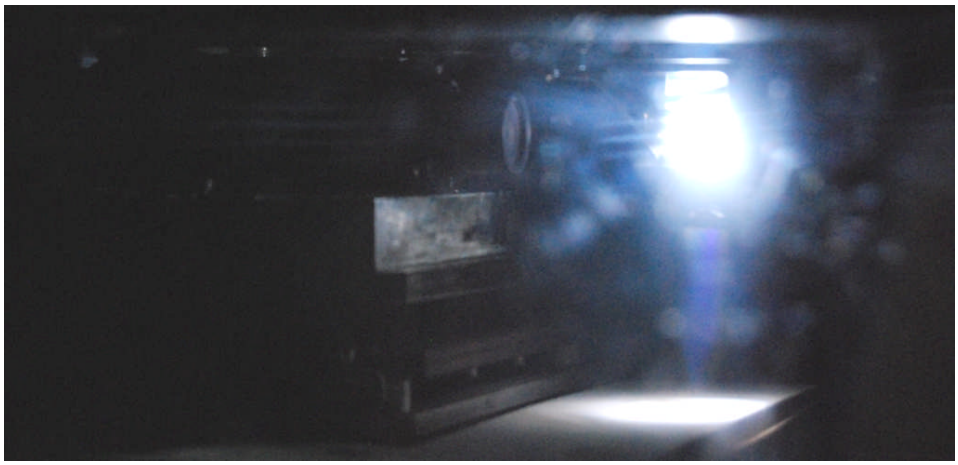

Figure 5.44 **Measurements were made looking into the lower region of coil zone of the plasma on a single plane, looking along viewing line A in the diagram.**

a)

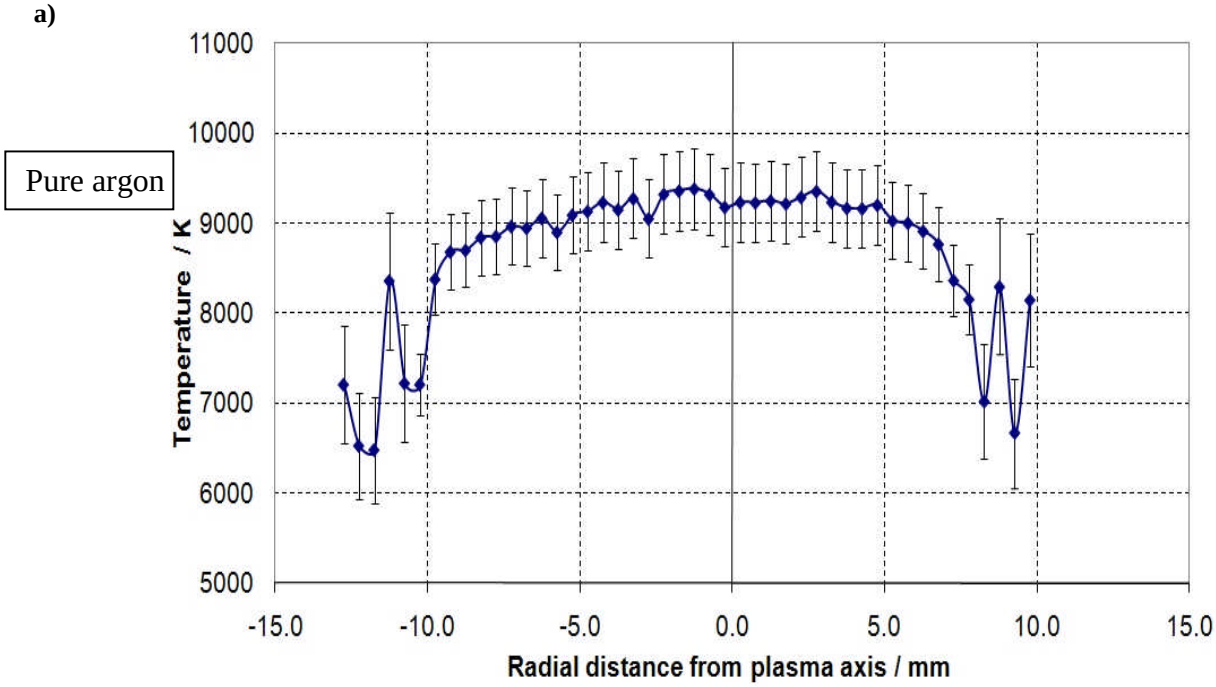

b)

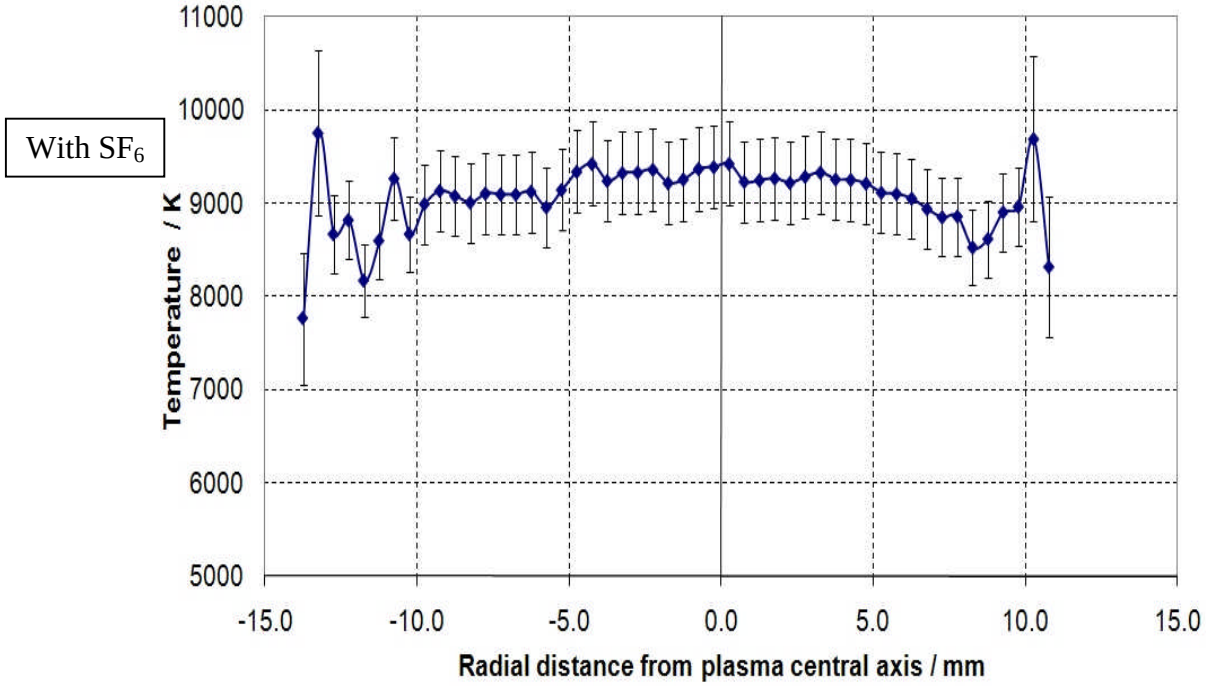

Figure 5.45 **Temperature profiles when looking into the coil zone of a) the pure argon plasma and b) the plasma with SF_6.**

5.9 Summary of spectroscopy results

A considerable amount of effort has gone into producing temperature maps of the plumes of both the pure argon and reactive plasmas. Measurements were taken within the plumes at heights between 1 mm and 20 mm below the base of the outer tube of the plasma torch. The intensity profiles of the argon emission lines in the pure argon plasma were close to being radially symmetric, although there were some deviations from radial symmetry close to the base of the torch due to the helical shape of the coil. It was considered acceptable to use an Abel inversion for converting the measured intensity profiles into emission profiles from which temperature can be calculated. Some corrections were made for those profiles where asymmetry was observed near the central axis.

Temperature measurements were made using two methods, using the absolute intensity of a single strong emission line (696.5 nm) and using Boltzmann plots. The Boltzmann plots created from data taken when examining the more luminous parts of the plume were mostly of good quality, indicating that the plasma is close to being in local thermal equilibrium (LTE) throughout most of the plume. It was decided that it was best to create temperature maps using the intensity of the 696 nm line. Calculating the temperature at all positions using Boltzmann plots would have been much more time-consuming and it does not work in the cooler regions where the emission lines which originate from a higher upper energy states are too weak. Temperatures between 4000 K and 6200 K were measured in the pure argon plasma plume. These values are in reasonably good agreement with those published by other authors examining similar ICPs. Many sources of uncertainty exist in the determination of these temperatures, most significantly in the estimation of neutral argon particle density within the plasma (the gas pressure was taken to be equal to 1 atm everywhere). However, these values are expected to be correct to within 500°C, and probably rather better than that.

The NF_3 plasma was rather less symmetric than the pure argon plasma. It appears that the additional central gas flow disrupts the symmetry. This did not appear to happen in the SF_6 plasma, in which the central gas flow was halved. The temperatures in the reactive plasmas peaked at around 5400K (800K lower than in the pure argon plasma). For each of the plasma plumes, the heat flux to which a substrate material would be subjected when positioned at particular heights was estimated. This was done using the measured temperatures and temperatures determined by extrapolation in the cooler regions of the plume. In the pure argon plasma, values calculated were between 470 W (1 mm below the torch base) and 200 W (18 mm below the torch base). The uncertainty in each of these measurements is ~50 W, due to the uncertainties on the measured temperatures and extrapolation techniques. Even though the peak temperatures in the plumes of the reactive plasmas are lower than those in the overall heat content within the reactive plasmas, the heat flux appears to be very similar. It appears that the heat is spread out over a wider volume when the reactive gas is introduced. Measurements of the intensity of a cluster of lines at 440 nm imply that high up in the plume, the population of fluorine atoms is relatively high, but asymmetric.

Spectra were taken in looking at samples of ULE and silicon while they were being etched using the NF_3 and SF_6 plasmas. The spectra produced when ULE was being etched indicated the presence of atomic titanium and a higher continuum level.

All of the additional lines observed were due to chemical activity. Temperature profiles were created using Boltzmann plots, derived from the emission of some of the stronger Ti I emission lines. The points in these plots did not all fall on straight lines, indicating significant departures from LTE. When using NF_3, within a 30 mm diameter, the temperature of the excited atoms was found to be between 1000 K and 2500 K. The temperatures of highly excited atoms and ions are probably in excess of 3500 K. Similar results were found when using SF_6. There are broad lines in the titanium-enriched plasma spectrum, whose origins have yet to be identified.

Temperatures within the coil zone in the pure argon and SF_6 plasmas were measured along a single plane. Temperatures in excess of 9000 K exist in the central region of both plasmas. Local thermal equilibrium appears to exist at all measured positions. The temperature profile of the plasma with SF_6 is noticeably flatter than that with pure argon. It is expected that this is the result of central gas flow pushing the hot plasma gas outwards.

The work performed here has been challenging and interesting and has revealed some surprises. It is hoped that the work here will encourage chemists and engineers to carry out research, using experiments in computer simulations, in order to understand the thermodynamic and chemical processes involved in etching of these materials using the RAP process.

6 Sample temperature measurements

In chapter 4, some experiments investigating the material removal rate and surface roughness measurements that were performed on ULE and on silicon were discussed. In chapter 5, spectroscopic temperature measurements of the ICP plume were described. Using this information, it has been possible to calculate the energy density within the plasma and the heat flux received by sample materials. In this chapter, temperature measurements of the sample themselves are discussed. Measurements have been taken using platinum RTDs, a pyrometer and a thermal imaging camera. The aim of these tests was to examine how the material responds to the heat that it receives.

As was mentioned in chapter 4, when the removal depths of trenches etched upon silicon were plotted against the reciprocal of the travel speed, the relationship was close to being linear. For the trenches etched onto ULE, the relationship was not linear. A hypothesis was made that this is due to the difference in the thermal conductivities of the respective materials.

To examine this more closely, the 1-dimensional heat conduction equation is

$$Q(x) = -k\frac{\partial T}{\partial x}(t) \qquad (6.1)$$

where $Q(x)$ is the heat flow at position x and k is the thermal conductivity of the medium concerned. An incremental change in temperature, ΔT, at a point is related to the change in internal energy, ΔU, by the equation

$$\Delta U = C_P \rho \Delta T \quad (6.2).$$

where C_P is the specific heat capacity at constant pressure and ρ is the density of the material. If Δx represents a small change in the x-direction, it is easy to show that

$$\frac{dT(x)}{dt} \approx -\frac{k}{C_P\rho}\frac{\partial}{\partial x}T(x+\Delta x) + \frac{k}{C_P\rho}\frac{\partial}{\partial x}T(x-\Delta x)$$

$$\Longrightarrow \frac{dT(x)}{dt} = -\frac{k}{C_P\rho}\frac{d^2T(x)}{dx^2}$$

$$\text{or} \quad \frac{dT(x)}{dt} = -D\frac{d^2T}{dx^2} \quad (6.3)$$

where D is the thermal diffusivity (= $k/(C_p\rho)$). The thermal properties of silicon and ULE are listed in table 6.1.

Table 6.1 Thermal properties of silicon and ULE [99].

	Silicon	**ULE**
Thermal conductivity ($Wm^{-1}K^{-1}$)	124	1.31
Specific heat capacity ($Jkg^{-1}K^{-1}$)	702	745
Density (g/cm^3)	2.32	2.21
Thermal diffusivity (m^2/s)	8.6×10^{-5}	7.9×10^{-7}

Suppose that one wished to simulate the evolution of the temperature distribution through a slab of material (of infinite cross-sectional area). This could be done by dividing the slab into layers of equal thickness and calculating the changes in temperature at the boundaries in between the slabs, the nodes (see figure 6.1). If the initial temperature distribution is defined and the boundary conditions at $x = 0$ and $x = L$ are specified for all values of t, it's fairly straightforward to write a computer program, or use finite element analysis (FEA) software, to calculate the incremental temperature changes for $t > 0$.

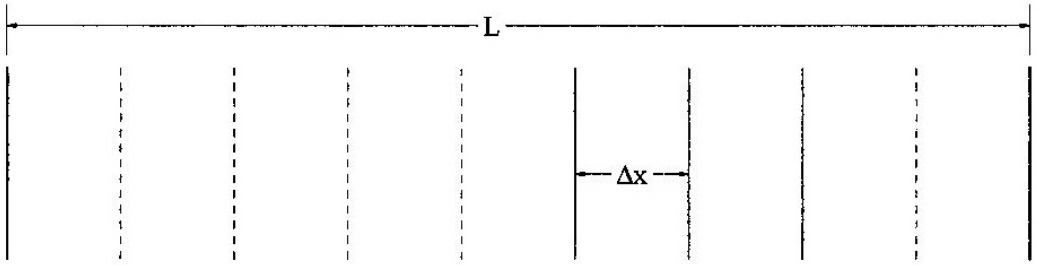

Figure 6.1 **When calculating a one-dimensional heat transfer problem through a slab of material, it is common to divide the slab into slices of equal thickness, Δx, and calculate the temperature at the nodes (denoted by vertical lines).**

Looking at figure 6.1, in order to calculate the temperature change, ΔT, at position x within the time interval Δt, one needs to estimate d^2T/dx^2. As long as Δx, is reasonably small compared to the characteristic length of the overall temperature variations,

$$\frac{d^2T(x)}{dx^2} \approx \frac{T(x+\Delta x)-T(x)}{\Delta x^2} - \frac{T(x)-T(x-\Delta x)}{\Delta x^2}$$

$$= \frac{T(x+\Delta x)+T(x-\Delta x)-2T(x)}{\Delta x^2}. \quad (6.4)$$

On substituting equation 6.4 into equation 6.3,

$$\Delta T(x) \approx -D\frac{T(x+\Delta x)+T(x-\Delta x)-2T(x)}{(\Delta x)^2}\Delta t\,. \qquad (6.5)$$

The equation that would be included in a computer program for calculating the temperature at position x and at time t (for $0 < x < L$ and $t > 0$) is

$$T(x,t) = -D\frac{T(x+\Delta x,t-\Delta t)+T(x-\Delta x,t-\Delta t)-2T(x,t-\Delta t)}{(\Delta x)^2}\Delta t + T(x,t-\Delta t) \quad (6.6).$$

Let us consider a 5 mm thick sample of silicon whose temperature is initially at 20°C at all depths. The top face is heated at a constant rate to 250°C within 0.5 seconds and is held at that temperature thereafter. Figure 6.2a shows how the temperature distribution evolves. In this model, heat is lost from the opposite face (the one that is not heated) by radiation, using equation 2.56. Figures 6.2b shows the same thing, but for a ULE sample of the same thickness. The responses of the two materials are very different. The temperature through silicon is almost completely uniform within a second. The temperature through the ULE sample, by contrast, is not close to reaching uniformity even after 10 seconds.

When performing a simulation like this, the accuracy can be improved by shortening the time increment, Δt, although, if it were too short, the running time might become unnecessarily long with little benefit. Values ~10^{-6} s were used. Making the space increment, Δx, smaller can also increase accuracy. However, it was found that if it were too small, the simulation resulted in unfeasibly large local temperature gradients developing, which were obviously unphysical, and these increased in magnitude as the programme continued to run. A suitable compromise needed to be found. Ultimately, the imaginary samples were divided into just 14 slices (making $\Delta x = {}^1/_3$ mm).

This is, of course, an extremely idealised situation. The cross-sectional area of the plasma is much smaller than the area of any surface that we are likely to want to etch, so heat conducts laterally through the material. Some allowance for heat dissipating away from the surfaces by radiation has been made, but convection is likely to be significant as well. In chapter 5, graphs showing how much heat samples receive from the plasma were shown, based on the plasma temperature measurements and estimates of the velocity of the gas. However, the high temperature gas is unlikely to donate all of its heat to the sample on contact. It is expected that a lot of the hot gas retains much of its heat and moves out to the sides after hitting the sample. If one were to carry out a more detailed simulation, one might want to consider plasma radiation losses and heat loss by convection.

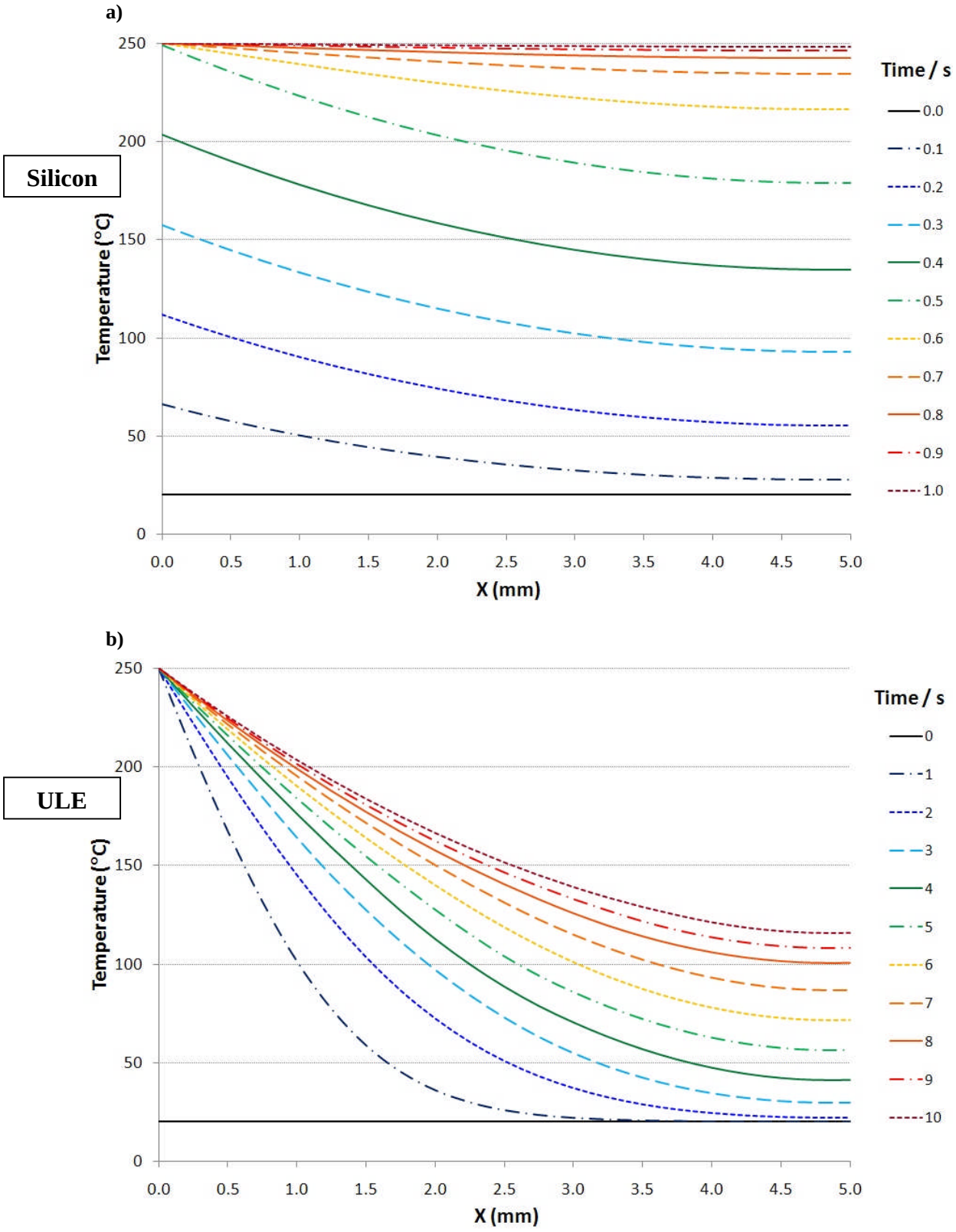

Figure 6.2 **Computed time-varying temperature profiles through 5 mm thick samples of a) silicon and b) ULE using a simple one-dimensional heat conduction simulation.**

6.1 Tests using RTDs

Although the one-dimensional conduction model might be an oversimplification, it was believed that by placing an RTD (resistance temperature detector) under a silicon wafer it might be possible to easily infer what the peak temperature reached on the top surface as the plasma torch passes across.

Several methods for attaching the Pt100 RTDs to the surface and retaining a strong thermal link were tried. The method that was ultimately chosen was to smear the underside of the sensor with a thermally conducting paste, a non-adhesive silicone grease known as Omegatherm® “201”, supplied by Omega, and then hold in place with a short piece of aluminium adhesive tape (as shown in figure 6.3). Other methods were tried, some using epoxy resins, but the quality of the thermal link was not improved and the epoxy made it very difficult to reposition the sensors. Adhesive cable tie pads were adhered to the underside of the wafers where possible and were used to restrain the cables and prevent accidental dislodging of the sensors.

A simple test was carried out in which a sensor was positioned close to the centre on the underside of a ∅200 mm × 0.8 mm thick wafer and the torch was passed directly over the top surface at various speeds. The plasma with NF_3 was used with the parameters given in table 4.1. Four-wire measurements were taken using the National Instruments CompactDAQ unit set-up. In figure 6.4a the highest temperatures measured are plotted against the torch travel speed used. In each experiment, the measured temperature started to increase before the plasma reached the wafer, and by a different amount in each case (they varied between 29.3°C and 40.3°C). To compensate for this, the maximum temperatures plotted have been "normalised"; the increase in temperature while the plasma was on the wafer has been added to the average of all the temperatures measured just before the plasma reached the wafer.

a)

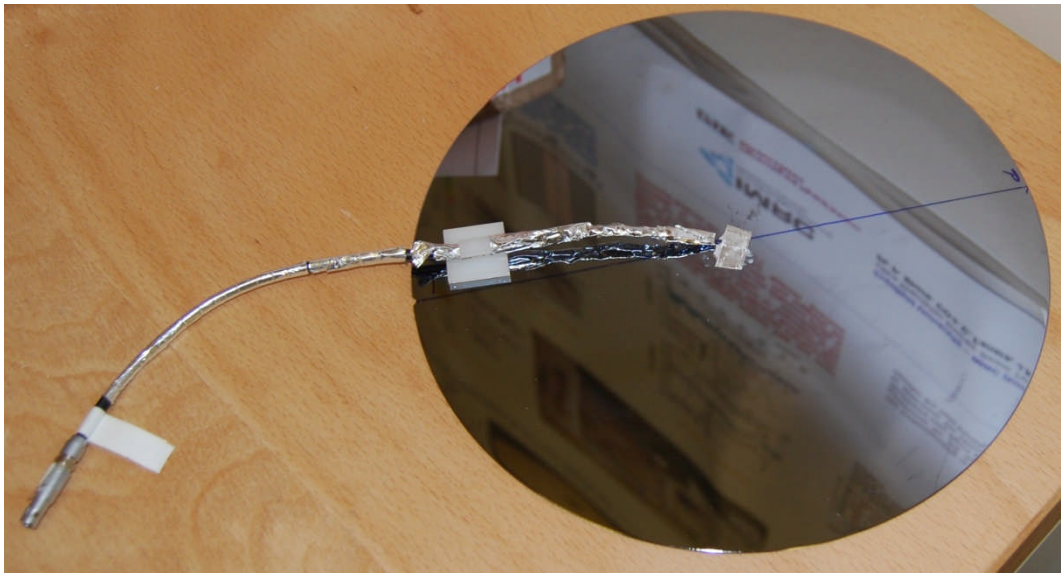

b)

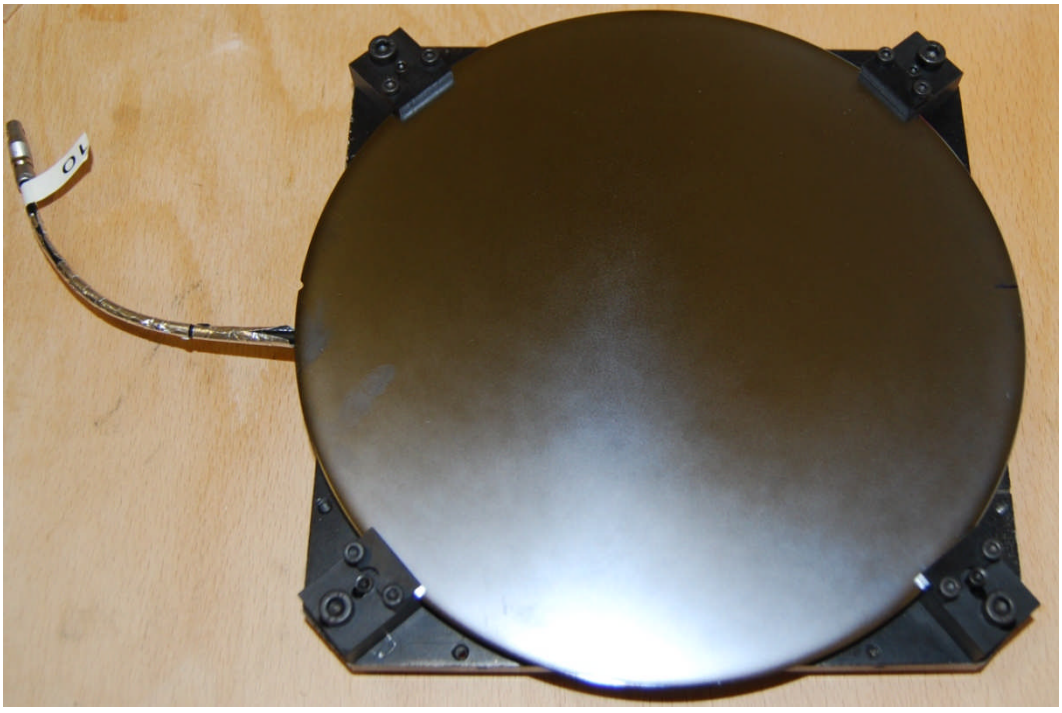

Figure 6.3 **a) An RTD adhered to the underside of a silicon wafer. b) The wafer is held in position.**

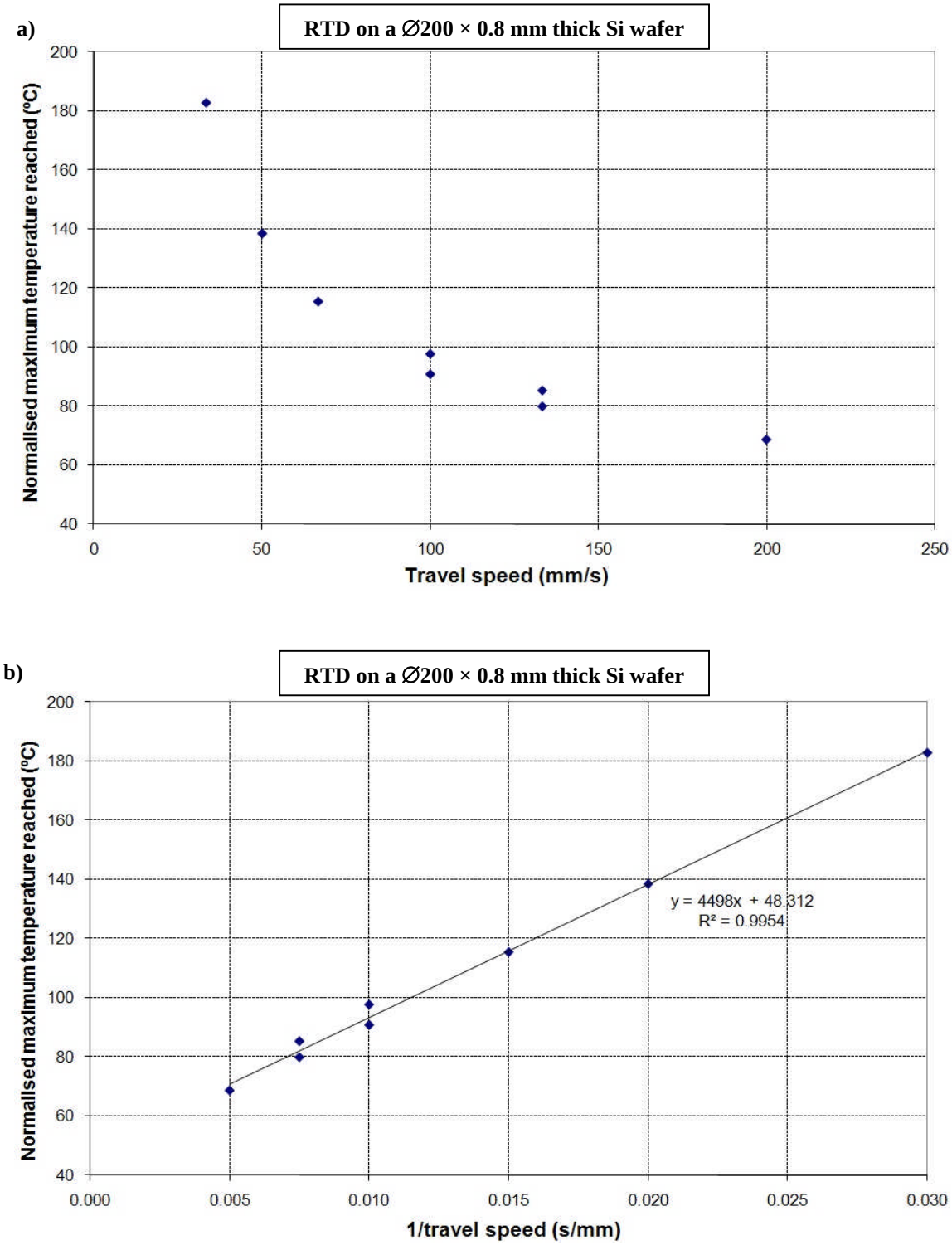

Figure 6.4 **The maximum temperatures measured using a Pt100 RTD position at the centre on the underside of a silicon wafer, while the plasma torch is passed directly overhead on the top surface, plotted against a) the travel speed used and b) the reciprocal of the travel speed. These maximum temperatures have been "normalised" to allow for the fact that the temperature measured before the plasma reached the wafer was different in each case; the measured change in temperature has been added to the average start temperature.**

Another test was carried out using a wafer of the same size, ∅200 mm × 0.8 mm thick, but with seven sensors measuring temperature simultaneously at seven different positions on the underside. The purpose was to estimate the power absorbed by the wafer as the torch makes a single pass over it. One sensor was positioned at the centre. The others were positioned on a PCD (point centre diameter) of 151 mm, or as close to as reasonably possible. Figure 6.5 shows the wafer divided into seven zones of equal area by dotted lines. The PCD of 151mm (= 2 × 200 mm/√7) was chosen so that the sensors would be close to the centre of these imaginary zones. The temperature given by each sensor was taken to be the average within each section. In order to maximise the sampling rate, no more than two sensors were connected to the same National Instruments CompactDAQ unit; the sampling rate was 2Hz (see table 3.1). Knowing the wafer's weight (53g) and the specific heat capacity of silicon, the amount of heat needed to raise the temperatures by the measured amounts during the time in which the plasma was over the wafer could be calculated, and hence the power absorbed.

The results are given in table 6.2. The estimated absorbed powers when using the plasma with NF_3 were slightly larger than when the pure argon plasma was used. As was suggested in chapter 5, although the peak temperature in the pure argon plasma plume is higher than that in the plasma with NF_3, the overall heat content is much the same but distributed over a wider area.

The reaction of fluorine with silicon is exothermic. It might be of interest to estimate how much heat has evolved from the chemical reactions. If the predominant reaction of NF_3 with silicon is

$$4NF_3 + 3Si(s) \rightarrow 3SiF_4 + 4N_2,$$

the enthalpy change, using tabulated values at standard temperature and pressure[29] is -1398 kJ/mol of silicon. For the typical material removal rates of the tests described in section 4.3.1, this corresponds to about 12 mW of heat evolved, which is minute.

The power values given in table 6.2 are higher than those deduced from the plasma temperature measurements. The values at a 15 mm offset in graphs in figures 5.25 and 5.32 suggest values ~260 W. The small number of tests described here, in which several simplifications and assumptions have been made, do not in themselves render the values deduced from the spectroscopy work invalid, but they should not be ignored and further investigation may be required to define more exact values.

[29] 'Standard temperature and pressure' means 298 K at 1 atm pressure.

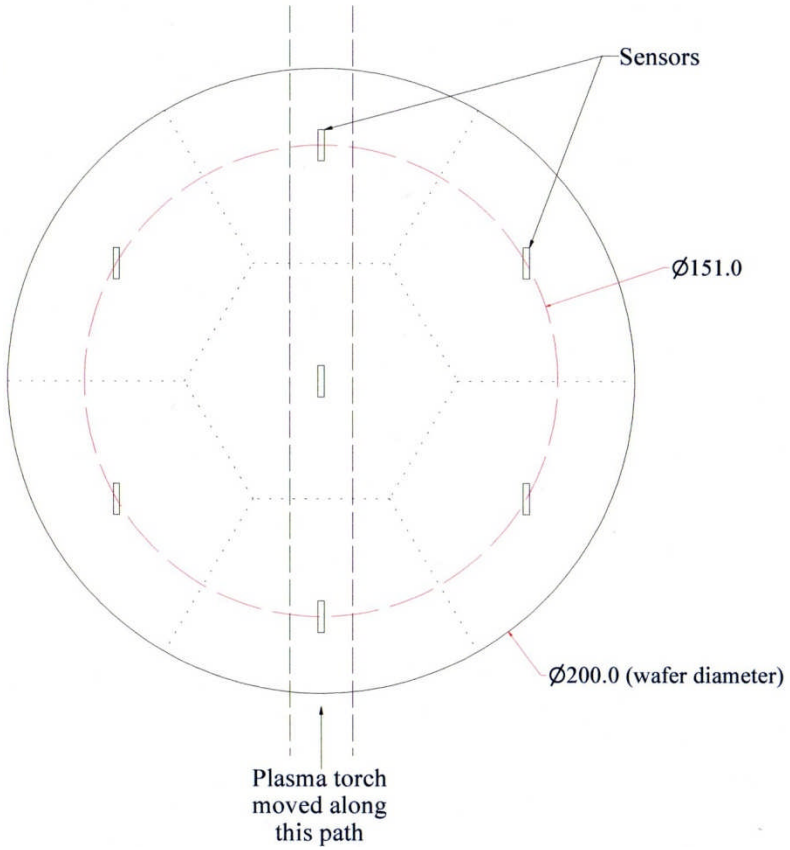

Figure 6.5 **In an experiment to measure the power absorbed by a silicon wafer from the plasma as it passed across, 7 sensors were adhered to the underside at equal distances from their nearest neighbours. The temperature measured by each sensor was considered to be representative of a particular region. The regions are divided up by the dotted lines.**

Table 6.2 a) **Results from the experiment with 7 sensors equally spaced on the underside of a ∅200 mm silicon wafer.**

	Pure argon or with NF_3	**Travel speed (mm/s)**	**Power received (W)**
1	With NF_3	100	596.7
2	With NF_3	100	620.4
3	Pure argon	100	549.6
4	Pure argon	100	588.1
5	Pure argon	66.7	591.4

b) **Results summary.**

	Average power (W)	**Standard deviation (W)**	**Error on average (W)**
With NF_3	608.6	16.7	11.8
Pure argon	576.4	23.2	16.4

In another set of tests, the torch was passed over a ∅200 mm silicon wafer many times at 100 mm/s, but along different paths relative to the RTD. This was done to find out how quickly the temperature distribution decreases away from the torch path. The results are shown in figure 6.6; normalised maximum temperatures are displayed. A similar set of tests was performed upon a silicon disc, 1 inch (25.4 mm) in diameter and 2 mm thick. The results are shown in figure 6.7. The temperatures are generally lower than those recorded on the wafer. The distribution is somewhat distorted. It could be that the quality of the thermal contact between the RTD and the disc changed between tests, even though the same wafer and the same sensor were used throughout.

A similar experiment was carried out upon wafers that were thinner and of smaller diameter (∅100mm × 0.5mm). In this instance, three RTDs were used measuring temperatures at different positions. These positions are shown in figure 6.8a. The temperatures measured when the torch was passed directly over sensor A are displayed in figure 6.8b. This experiment was repeated, passing the torch along different lines, to extend this radial distribution. Unfortunately the results of the subsequent tests were unreliable. This is probably because the quality of the thermal contacts between the sensors and the wafer degraded during successive torch passes.

The temperatures measured on the thin wafers (0.5 mm thick) are generally higher than those measured on the thicker wafers, which are higher than those measured on the 2 mm thick discs. In all instances, some passes were made at 100 mm/s. At the time in which the experiments were performed, it was believed that these differences were due to a temperature gradient in the material. It was believed that the temperature measured on the underside of the thinnest wafers would be the best representation of the temperature at the surface and that the temperature at the surfaces would be the same in all instances. However, the one-dimensional model described at the start of this chapter suggests that there should be almost no temperature gradient within such thin pieces of silicon. An alternative explanation is to believe that in all instances the temperature measured on the underside of the wafer is almost equal to that of the top surface. The reason why higher temperatures were measured underneath the thinner wafers is due to the fact that the heat builds up within a smaller volume, raising the final temperature more greatly.

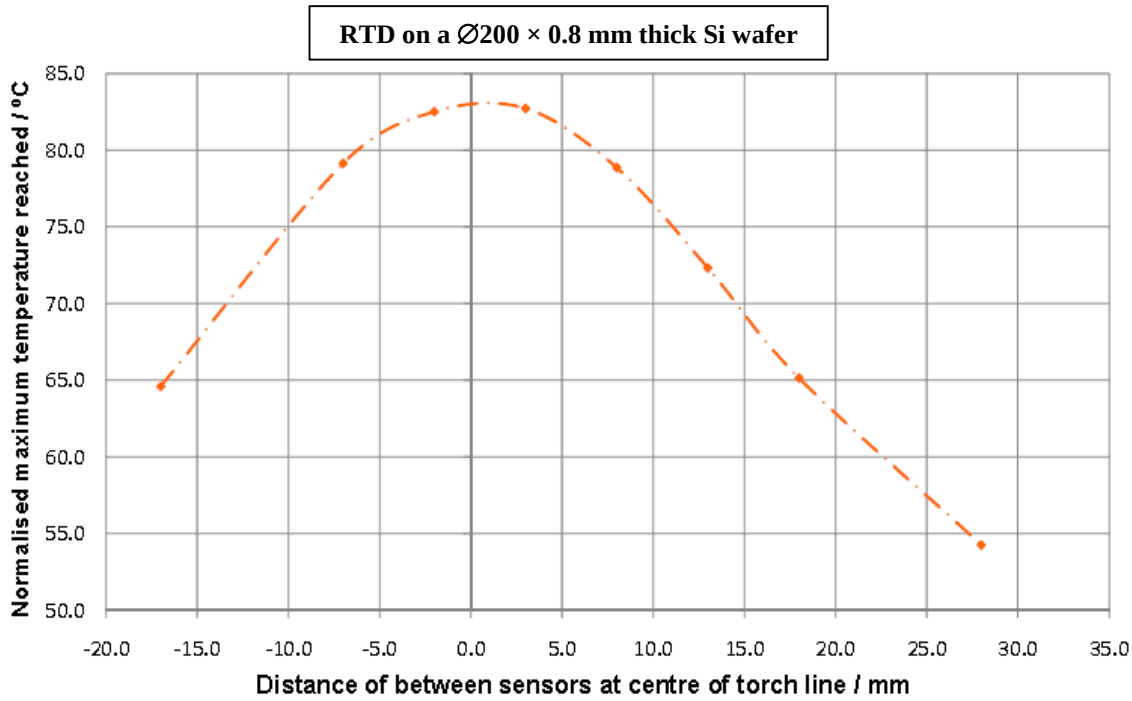

Figure 6.6 **The maximum temperature measured using a single Pt100 RTD at the centre of a ∅200 mm × 0.8 mm thick silicon wafer as a function of the position of the sensor relative to the centre line of the torch pass. Normalised maximum temperatures are shown (temperature added to the average of the start temperatures).**

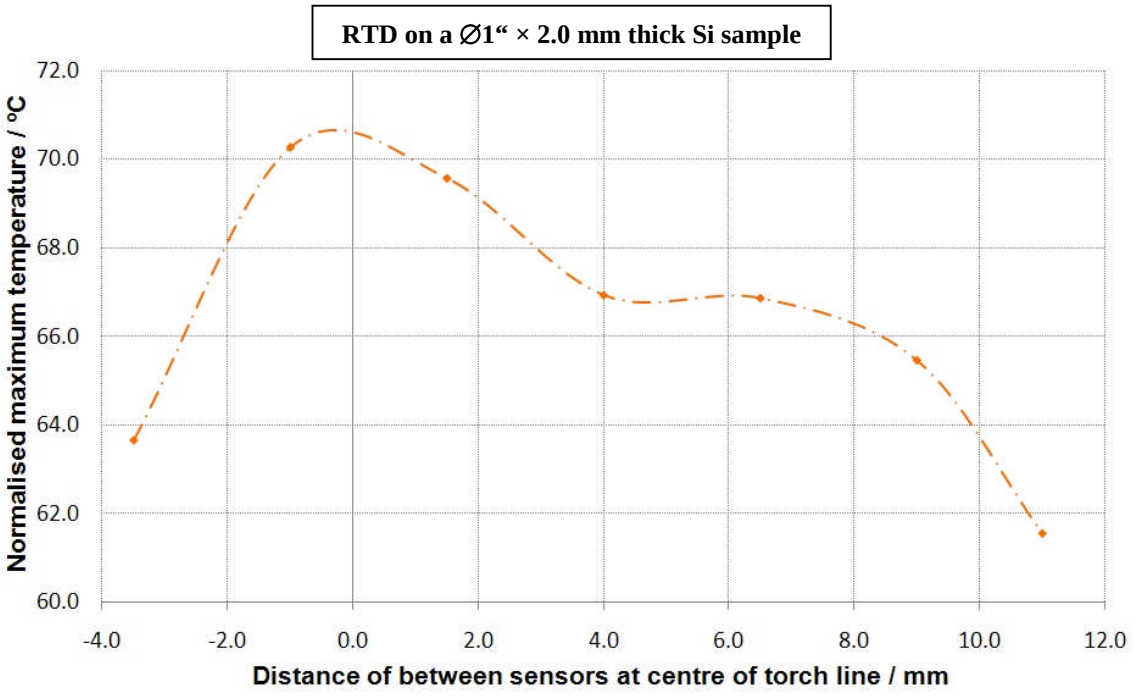

Figure 6.7 **The maximum temperature measured using a single Pt100 RTD at the centre of a ∅25.4 mm × 2.0 mm thick silicon wafer as a function of the position of the sensor relative to the centre line of the torch pass. Normalised maximum temperatures are shown (temperature added to the average of the start temperatures).**

a)

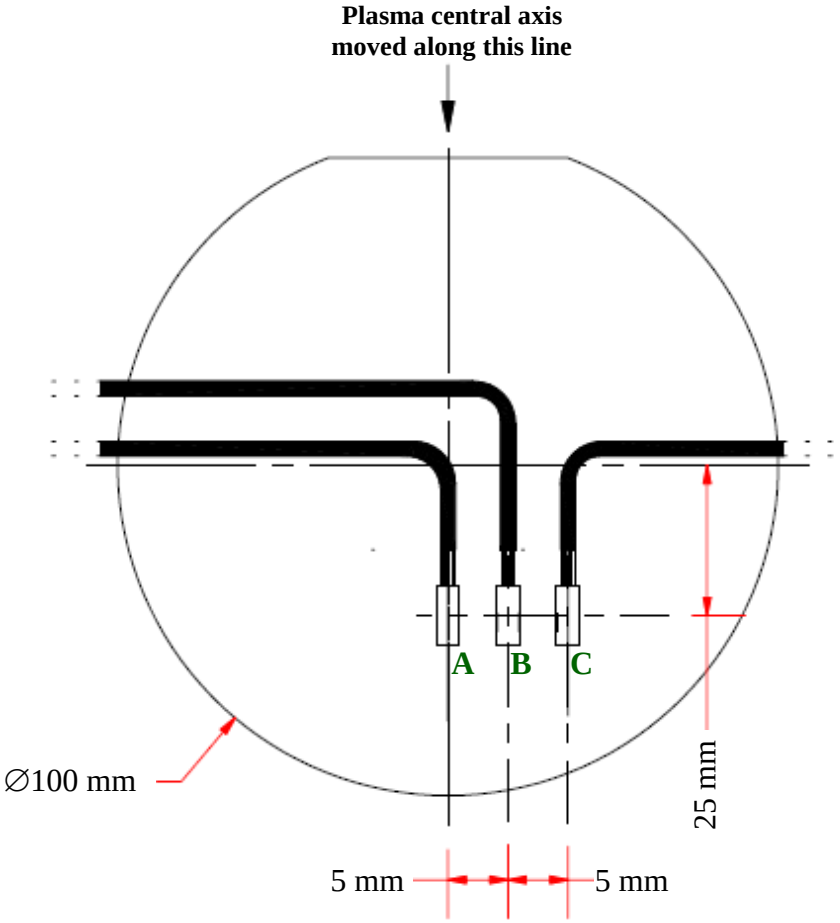

b)

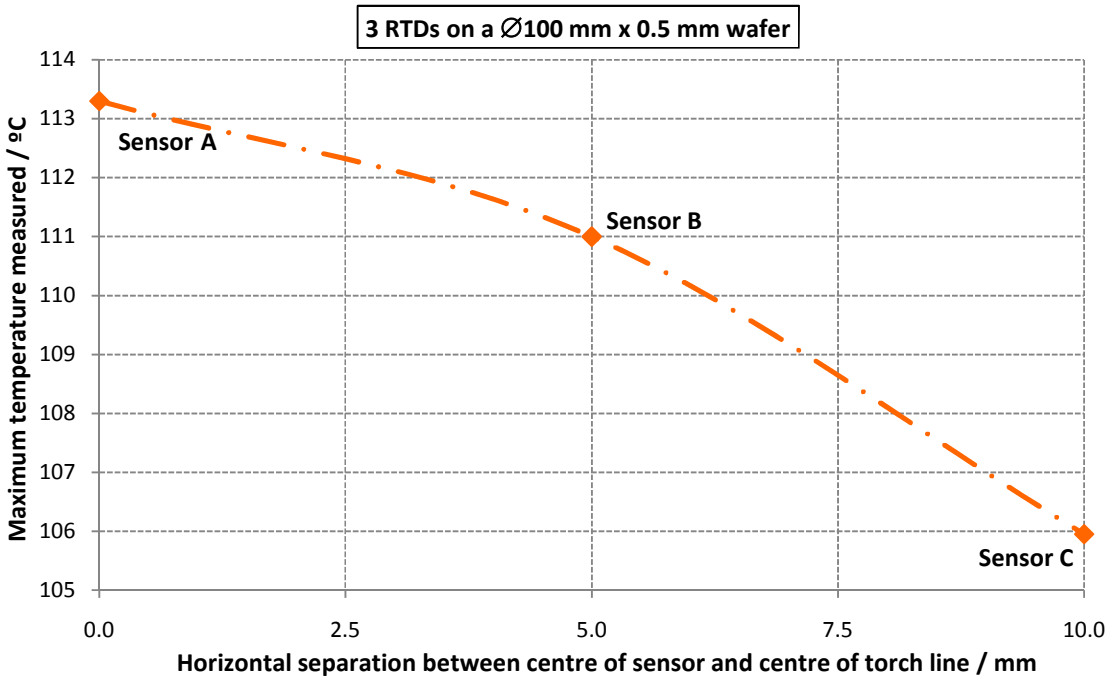

Figure 6.8 **a) The positions of the sensors that were placed on the underside of a ∅100 × 0.5 mm thick wafer. The torch was passed directly over sensor any at 100 mm/s. b) The maximum temperature measured using the sensors as the torch was passed overhead.**

6.2 Pyrometer measurements

Temperature measurements of ULE surfaces were taken using the machine's Mikron pyrometer. The pyrometer was positioned at an oblique angle in order to examine the sample's surface immediately under the plasma torch. The viewing angle of the pyrometer is ≈6.3°, which meant that an elliptical area of surface, 24.4 mm along the major axis and 11 mm along the minor axis was examined (see figure 6.9). When the RTDs were used for temperature measurements, they always measure the temperature at the same point on the sample. The pyrometer, on the other hand, is in a fixed position relative to the plasma. Passes were made across 100 mm × 100 mm ULE surfaces at different speeds. The same sample was used; it was allowed to cool down between experimental runs.

In figure 6.10a, the maximum steady temperature measured in each test is plotted against the travel speed used. Figure 6.10b shows the same data, but this time plotted against the reciprocal of the travel speed. Unlike the data shown in figure 6.4b, the relationship isn't quite linear. As the temperatures given by the pyrometer are averaged over a wide area, the measurement resolution is not particularly good and the real maximum temperature might be higher. There were, on occasions, spurious-looking spikes and the measured temperature profiles, which is why the word 'steady' was used earlier. For these reasons, it was considered worthwhile to repeat these experiments using a thermal imaging camera instead.

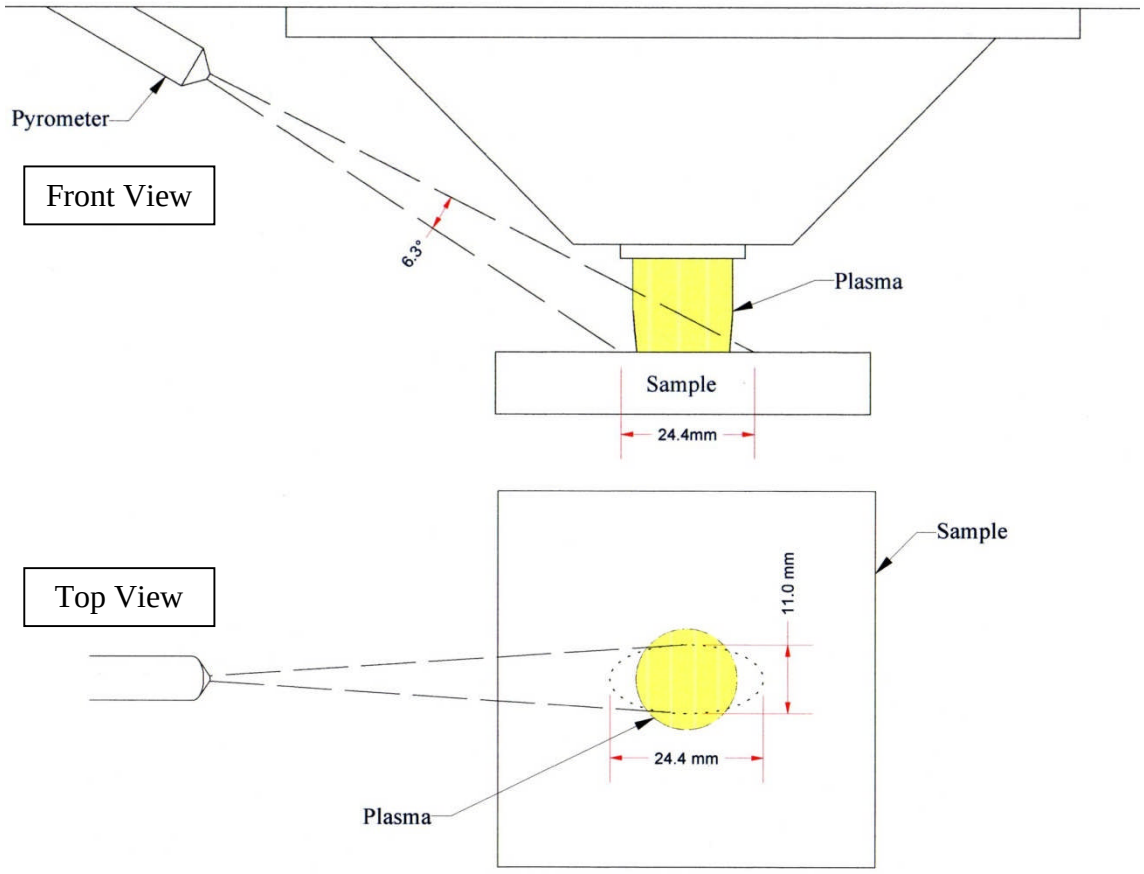

Figure 6.9 **The pyrometer detects infrared radiation from an area of surface immediately under the plasma torch. The area of surface examined is elliptical and the pyrometer outputs a single temperature (the average value over that region).**

a)

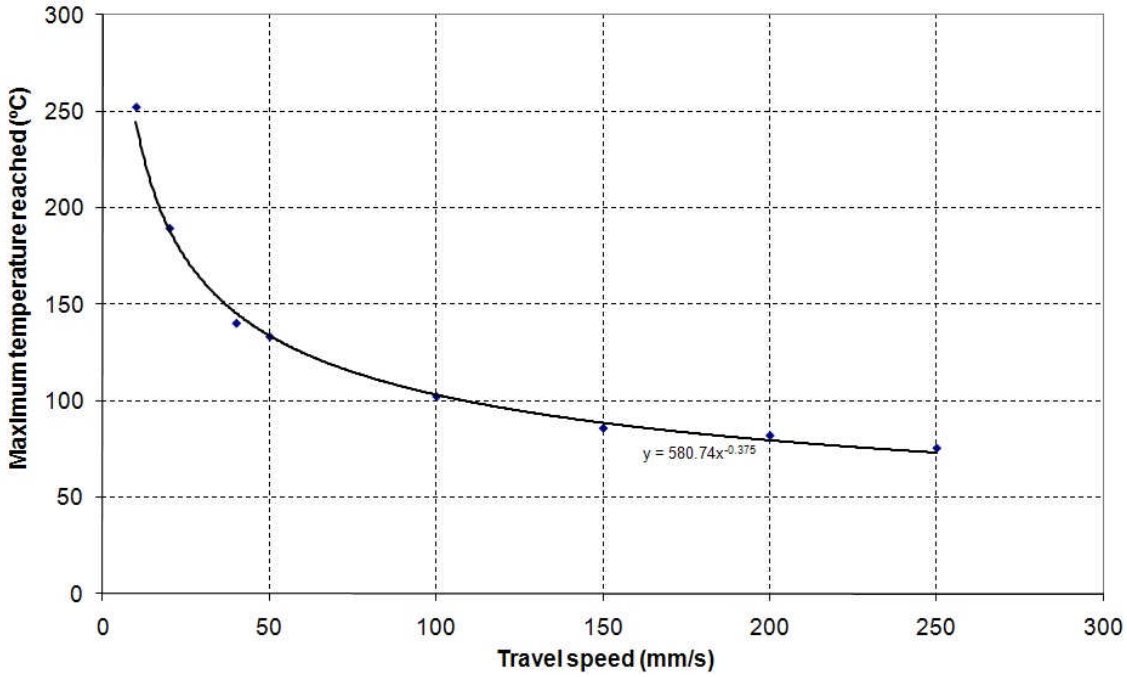

b)

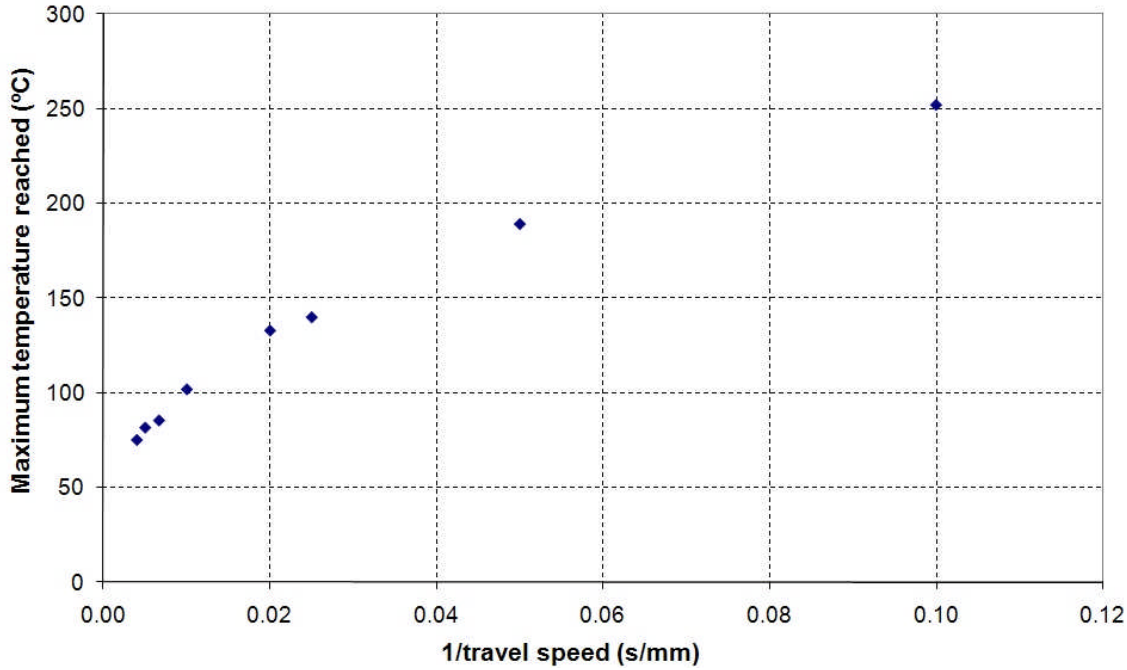

Figure 6.10 **a) The maximum temperature measured on ULE surfaces using the pyrometer as a function of the torch travel speed. b) The same data, but plotted against the reciprocal of the torch travel speed.**

6.3 Measurements using FLIR ThermaCAM™ SC3000

The FLIR ThermaCAM™ SC3000 was introduced in section 3.4.2. The RAPT300 machine's health and safety requirements meant that a Perspex guard has to be positioned over the front of the chamber and doors, with windows made of Perspex, affixed to the outer chamber. As with many materials that are transmissive to visible light, they are almost completely opaque in the mid to far infrared, including the wavelength band within which the ThermaCAM™ SC3000 is sensitive. It was decided that the best way to view samples inside the machine was to remove the pyrometer and position the camera so that it could examine through the pyrometer's porthole, as shown in figure 6.11. An indication of the camera's view from this position is shown in figure 6.12.

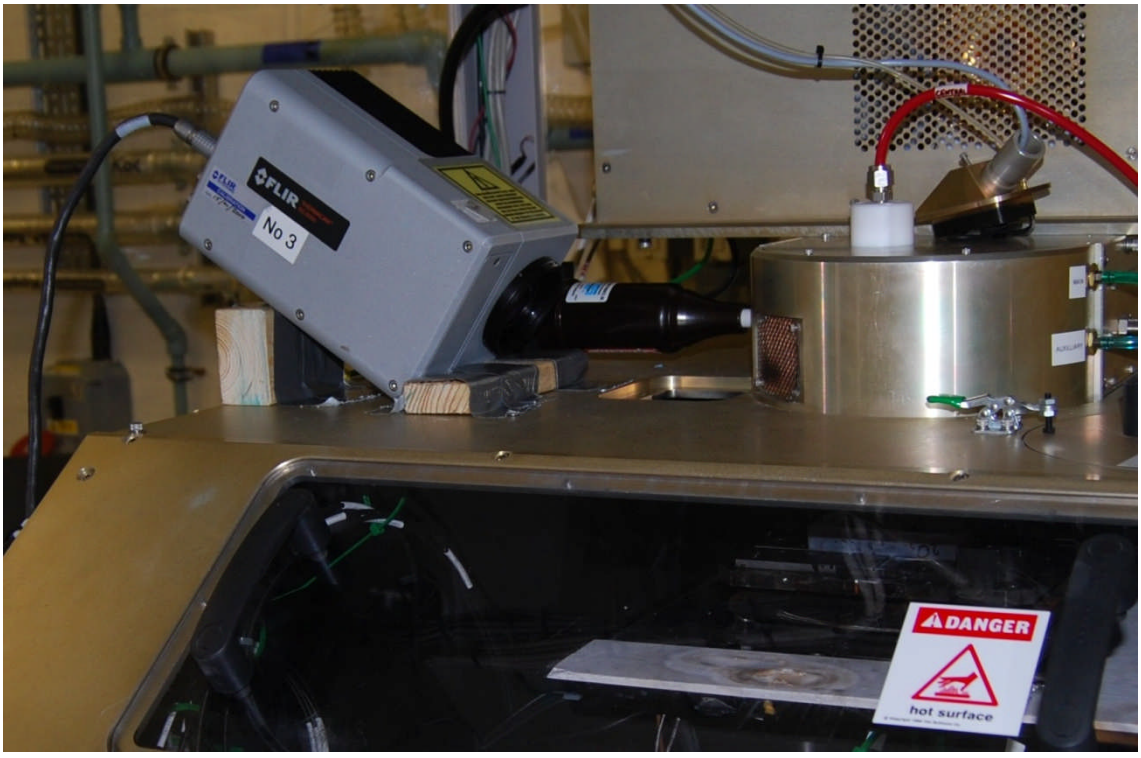

Figure 6.11 **The FLIR ThermaCAM™ SC3000 being used to measure temperatures on the surface of a ULE block.**

Figure 6.13a shows a typical thermal image of a ULE block while it is moving into the plasma. Of the parameters that the 'Researcher' programme uses in determining temperature, the emissivity of the material of interest is most important. In order to choose the most appropriate emissivity value for ULE, one of the Pt100 RTDs was connected and positioned on the surface of a ULE sample in position (though not adhered to the surface) to measure the ambient temperature. That same sample was then examined using the thermal imaging camera and the emissivity adjusted so that the temperature determined matched that given by the RTD. An emissivity value of 0.9 was found to be most appropriate. It should be emphasised that the emissivity of any material is temperature dependent, to some degree, so the uncertainty of the temperature measurements might be larger at elevated temperatures. The other parameters include the camera to object distance (0.3m), the transmittance and the humidity of the intervening material. The transmittance was set to unity, as air was the only intervening

material. The humidity was set to the default value of 0.5, but this value had little influence on the results.

Figure 6.13a shows an example of a thermal image, taken as a ULE sample is moving into the plasma, roughly in the position shown in figure 6.12. The view of the sample is somewhat oblique. A test was carried out to help create a two-dimensional temperature map of the surface using real distances. A measuring block was warmed, so that it would be easily visible in a thermal image, and was placed on top of a surface in a position where it could be imaged. It was first positioned with its measuring axis parallel to the '*x*'-axis on the map produced by the camera, at various positions on the *y*-axis and, in each case, the number of pixels covered was counted. As the length of the block was known, a horizontal distance in terms of pixels on the *x*-axis of the image could be converted into a real distance on the *x*-axis of the surface (in the direction parallel to the direction of motion) using this information. The block was then placed parallel to the *y*-axis, at various *x*-positions so that a vertical distance in terms of pixels on the *y*-axis of the image could be converted into a real distance on the *y*-axis of the surface, in the direction perpendicular to the direction of motion. This information was used to create temperature maps, such as the one shown in Figure 6.13b. The *x* and *y* distances are distances relative to the central axis of the plasma torch. The large hotspot, which appears just below the torch line, is due to a reflection of the outer quartz tube of the torch off the surface of the sample.

Modelling work conducted by a group at the University of Bologna showed that the temperature of the outer quartz tube in a similar ICP reached 600 K, in spite of the cooling gas. This offers an explanation as to why, on occasions, 'spikes' of spuriously high temperature were recorded when using the pyrometer; infra-red light from the outer tube of the torch was reflected off the surface and interfered with the measurements.

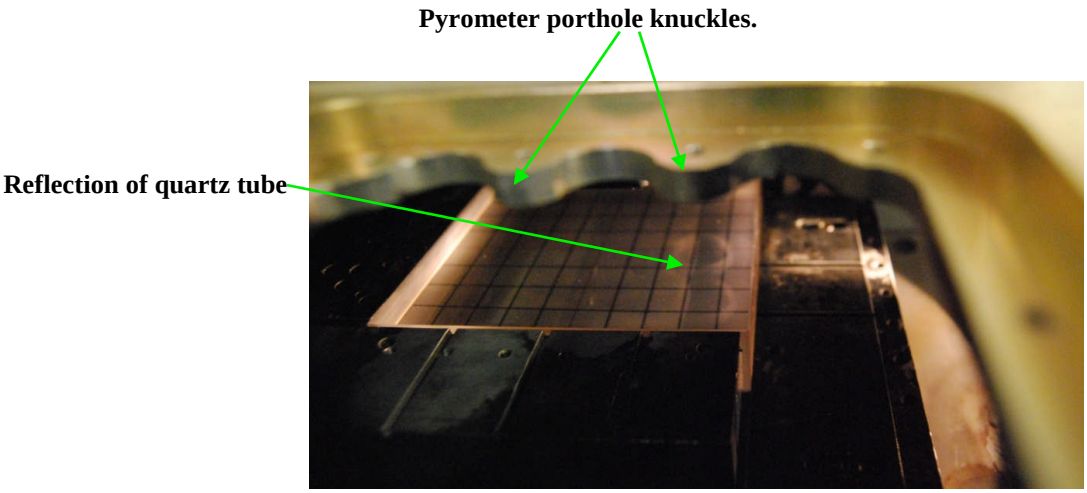

Figure 6.12 **The SC3000's view.**

a)

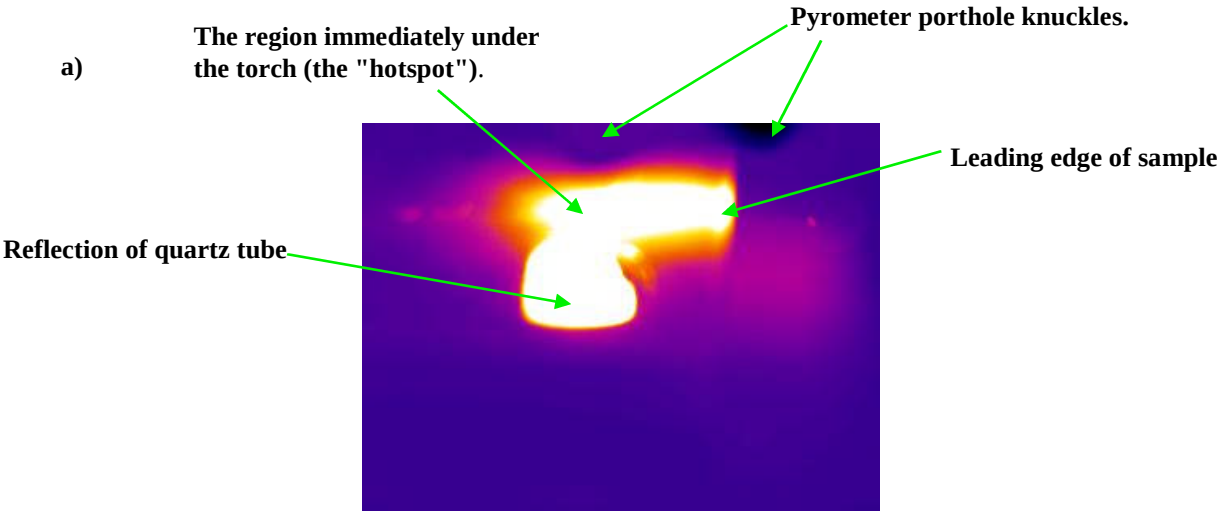

b)

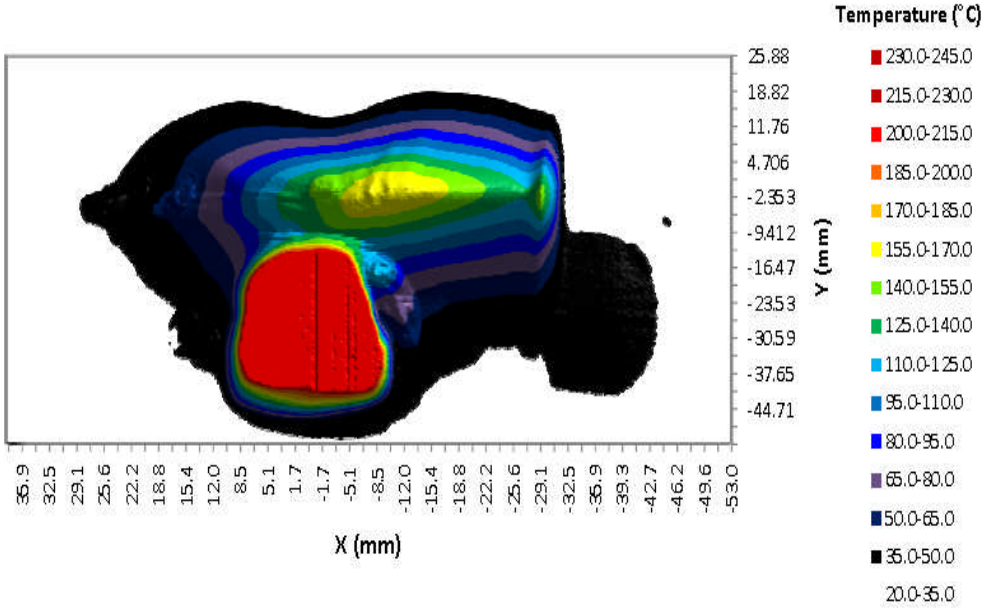

Figure 6.13 **a) A thermal image taken as a block of ULE was moved into the plasma. The sample is moving to the right, as we see it. b) A reconstruction of the thermal image with *x* and *y* dimensions relative to the central axis of the plasma torch.**

In figure 6.14, temperatures measured at the "hotspot" (the point on the surface that lies immediately under the central axis of the torch) as a ULE sample was moved through that point are shown. This was done using the pure argon plasma; the sample was moved at 40 mm/s. A steady maximum temperature was reached within 0.6 s. Figure 6.15 shows the same thing when a speed of 10 mm/s was used. In this instance the rise in recorded temperatures took 2.5 seconds. In both instances, rises in measured temperature were complete after a sample had moved ~25 mm. The removal depth within the first 25 mm is expected to be lower as a result.

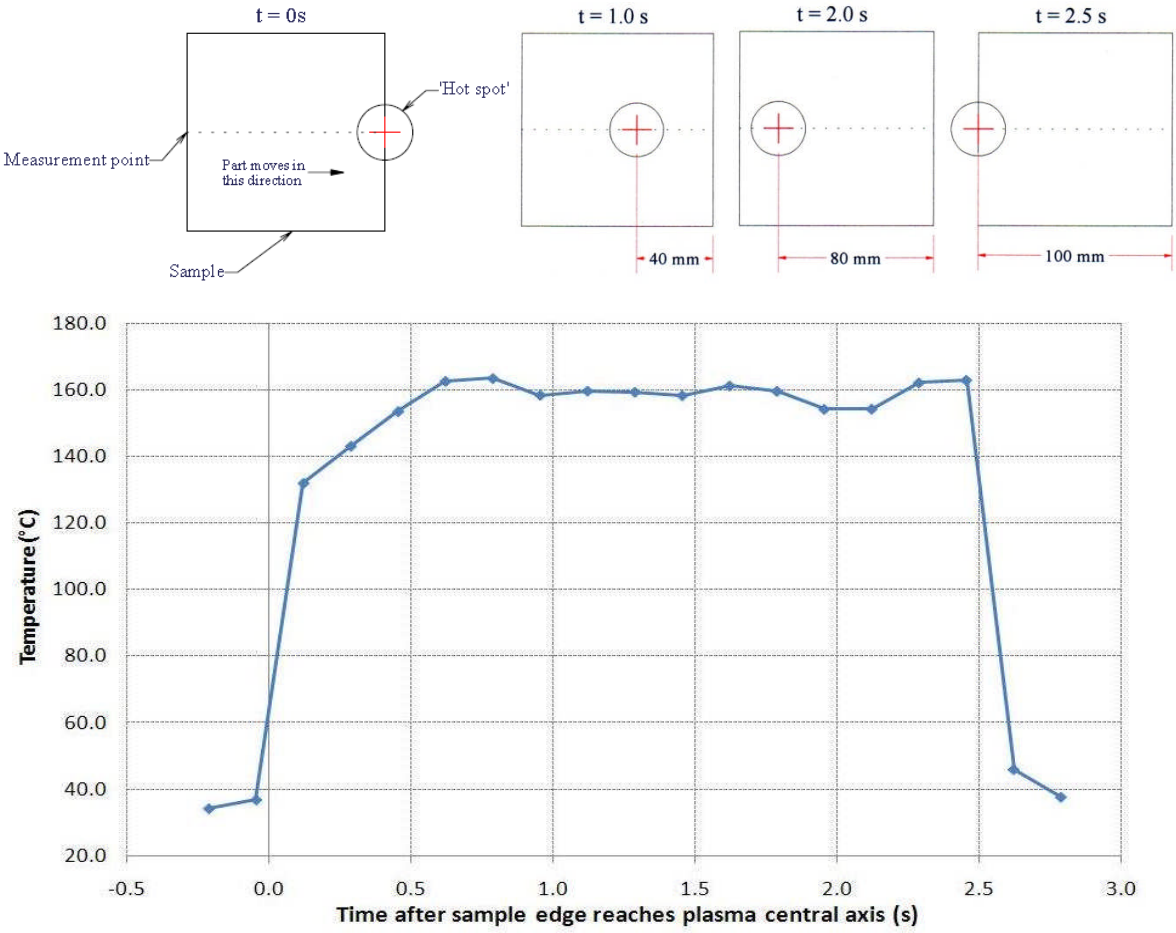

Figure 6.14 **Temperatures measured at the centre of the hot spot (where the surface meets the central plasma axis) as a block of ULE was passed through the plasma at 40 mm/s. The pure argon plasma was used in this instance. The diagrams above the graph show the relative positions of the part, the plasma (circle) and the measuring point (crosshairs) at different times of measurement (i.e. each measurement was taken at a point on the surface).**

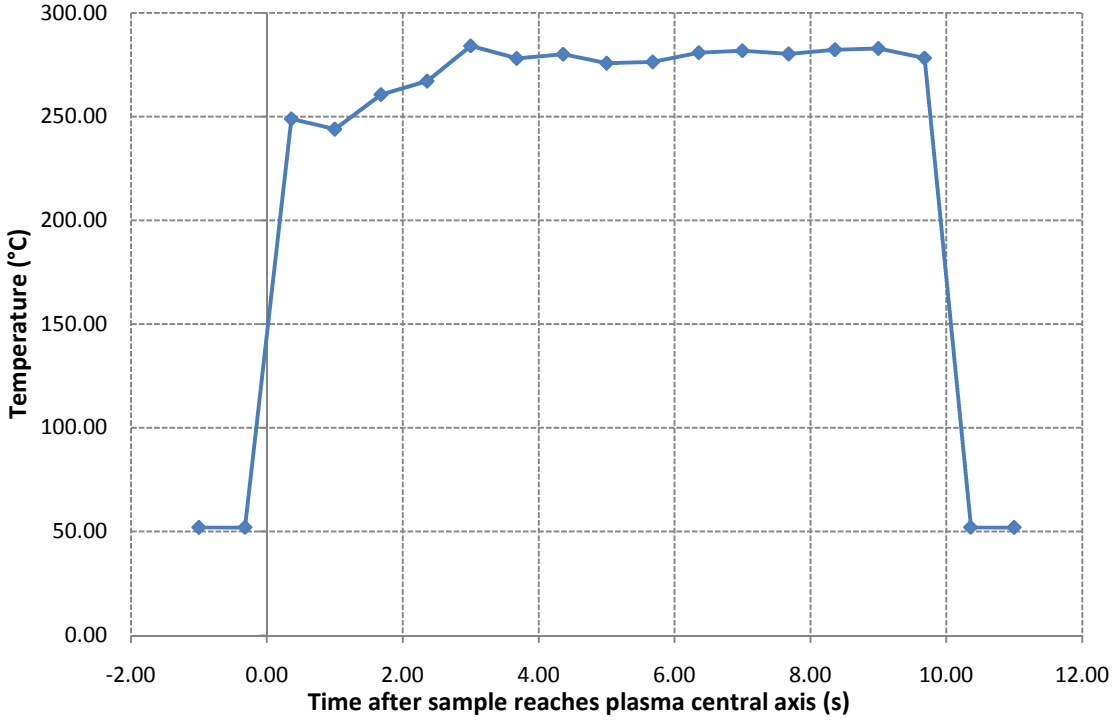

Figure 6.15 As figure 6.14, but from an experiment in which the travel speed was 10 mm/s.

Figure 6.16 shows a series of temperature profiles taken along the same section of the surface as it moved through the plasma. The temperature measurement range was set so that it was possible to record the highest temperatures, but meant that temperatures below 52°C could not be recorded. Negative X distances have been quoted for those plots in which that plane on the surface has not yet reached the centre of plasma. Positive X distances have been quoted for those plots in which that plane on the surface has passed the centre of the plasma. As expected, for any point on the surface the warming period before it reaches the plasma centre is much shorter than the cooling period after it has reached the plasma centre.

Figure 6.17 shows the '5.3s' profile in figure 6.16. The temperature gradient on the right-hand side is distorted due to the shape of the porthole (the knuckles visible in figure 6.12). The temperature gradient on the left-hand side is believed to be real, as the view is unobstructed, and averages at ≈7°C/mm. This is not expected to be a problem on glassy materials which have a low coefficient of thermal expansion. It might be a greater concern on crystalline or porous materials. Indeed, when the process was applied to quartz samples at Cranfield, several samples shattered.

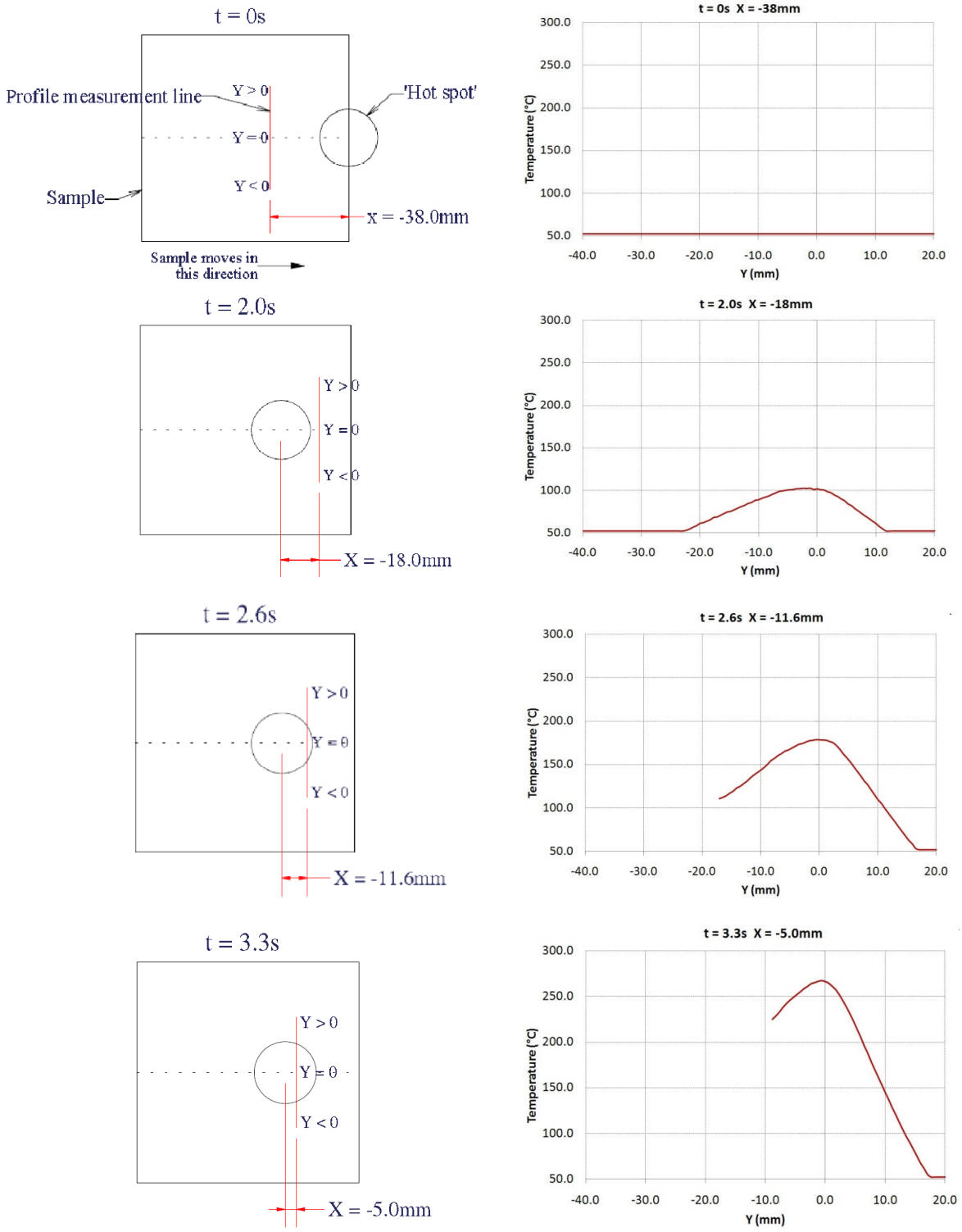

Figure 6.16 **Measured temperature profiles along the same section of a ULE surface at different times as it was passed through the plasma at 10 mm/s. The diagrams show the relative positions of the 'hotspot' (region immediately under the plasma) and the line of measurement for the first four profiles. Later profiles are shown on the next page without diagrams. Negative X distances have been quoted for those plots in which that plane on the surface has not yet reached the centre of plasma. Positive X distances have been quoted for those plots in which that plane on the surface has passed the centre of the plasma.**

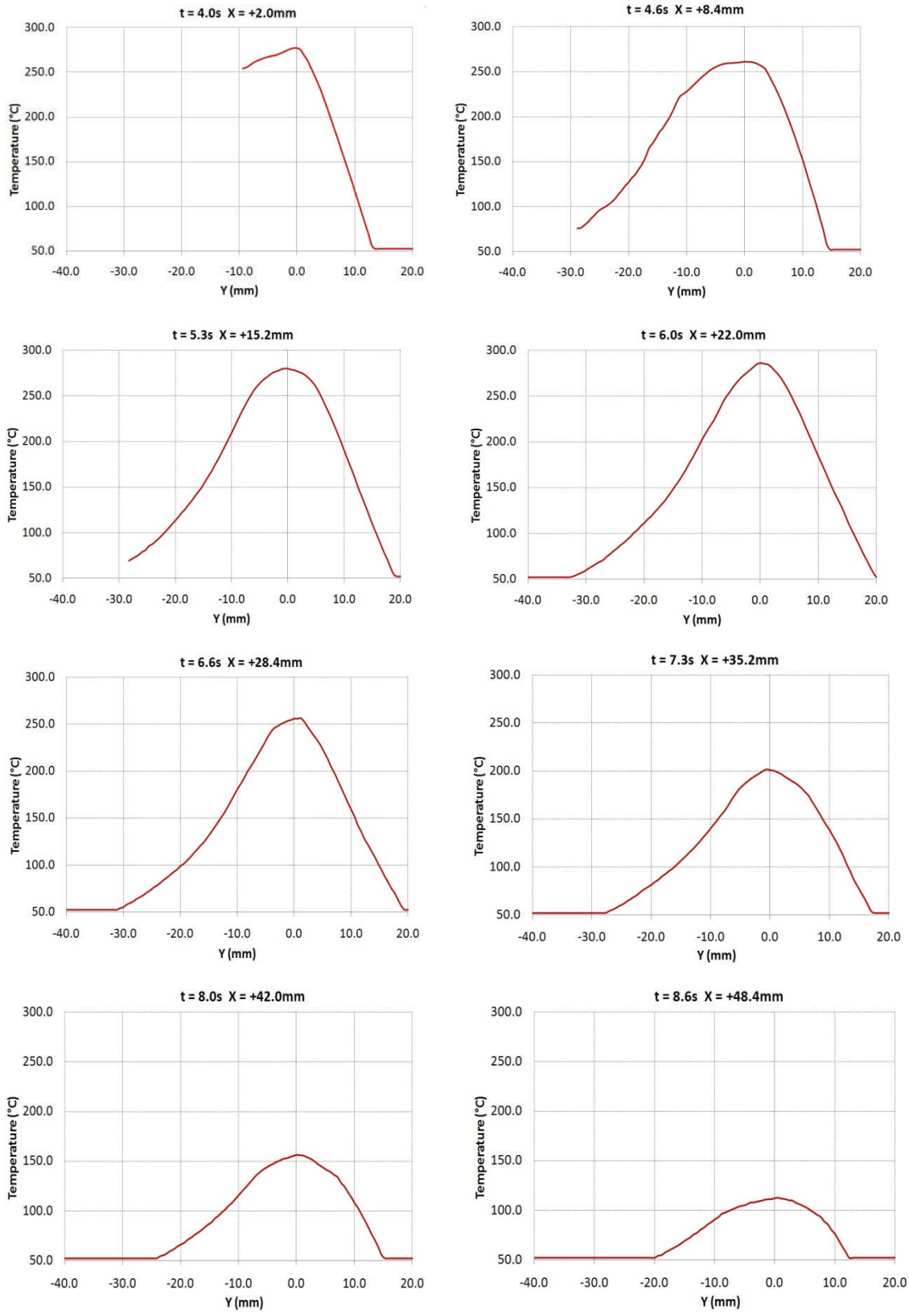

Continuation of figure 6.16

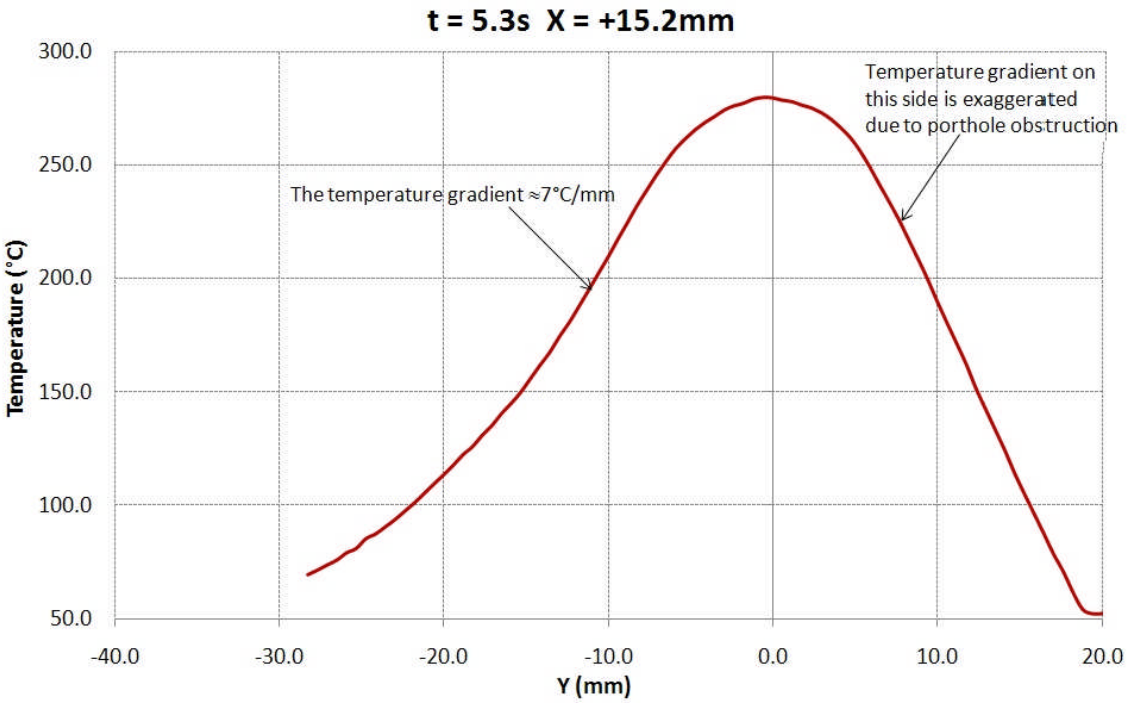

Figure 6.17 **The t = 5.3 s profile from figure 6.16. The temperature gradient on the left-hand side of the maximum averages at ≈7°C/mm.**

An experiment was performed in which single passes were made across a ULE sample at different speeds and thermal images were recorded. The maximum temperature recorded is plotted against the travel speed used in Figure 6.18. The error margins are due to uncertainties in the emissivity. The values are higher than those recorded using the pyrometer (the data shown in figure 6.10). This is believed to be because temperatures given by the pyrometer are the result of emission over a wide area of surface; the thermal imaging camera's resolution is very much better. Most of the measurements taken using the reactive plasma with NF_3, but some additional measurements were taken using the pure argon plasma. Those additional measurements fit into the same distribution, again implying that there is little difference in the overall heat output between the two plasmas. Figure 6.19a shows how the etch rate predicted using equation 2.57 varies with travel speed (relative to its value at 250 mm/s) if the temperatures shown in figure 6.18 are correct. For comparison, figure 6.19b shows how the observed material removal rate varied with the reciprocal of the torch travel speed, based on data discussed in section 4.1 (again relative to its value at 250 mm/s). The degree of variation in the observed etch rate is not as big as the degree of variation in the predicted etch rate. This might indicate that equation 2.57 is an oversimplification in this context.

The highest temperatures might be sufficient to induce thermal distortion in the material (thermal distortion has been reported in Zerodur at temperatures above 180°C [**119**]).

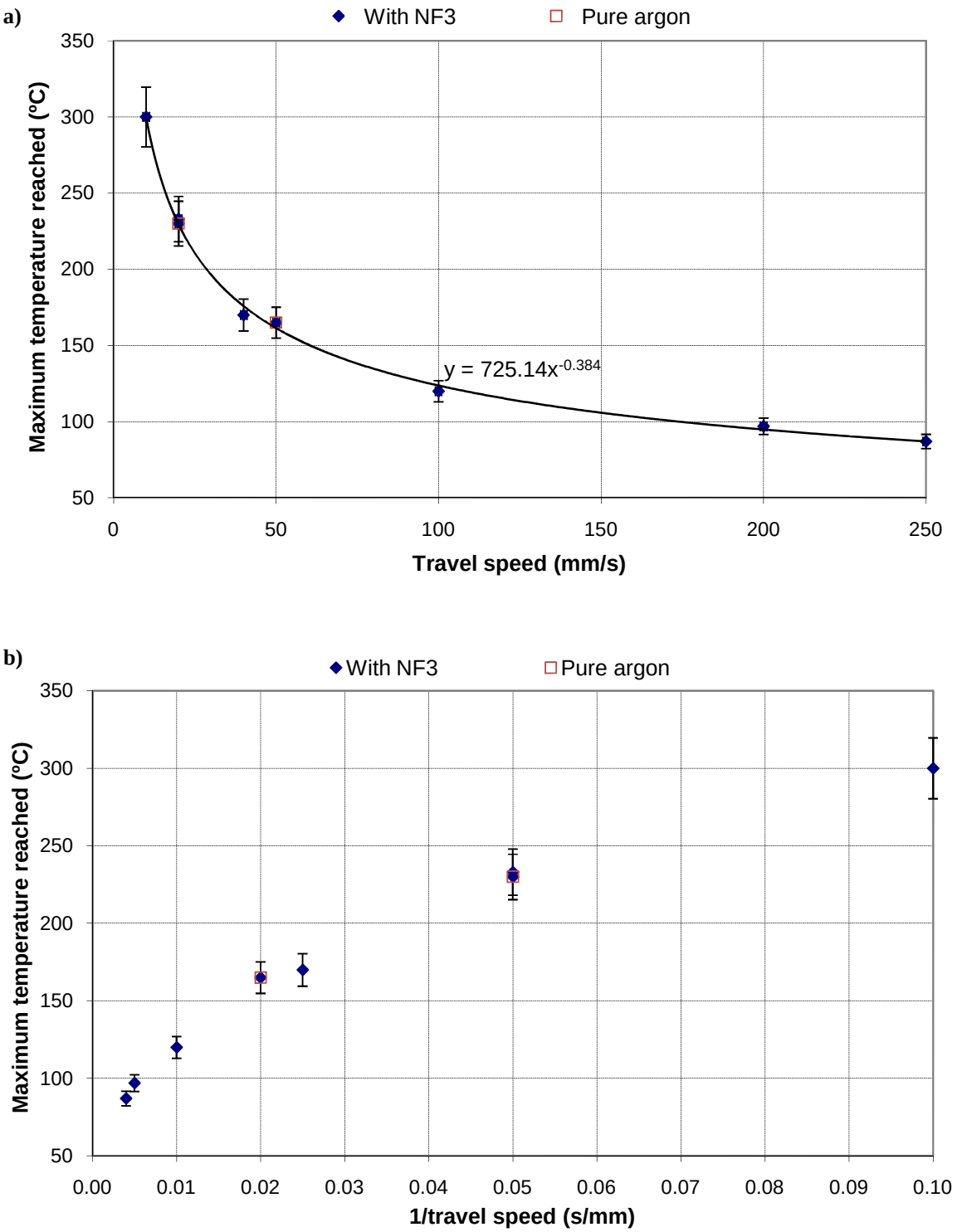

Figure 6.18 **a) The maximum temperature measured on ULE surfaces using the ThermaCAM™ SC3000 as a function of the torch travel speed. b) The same data, but plotted against the reciprocal of the travel speed.**

a)

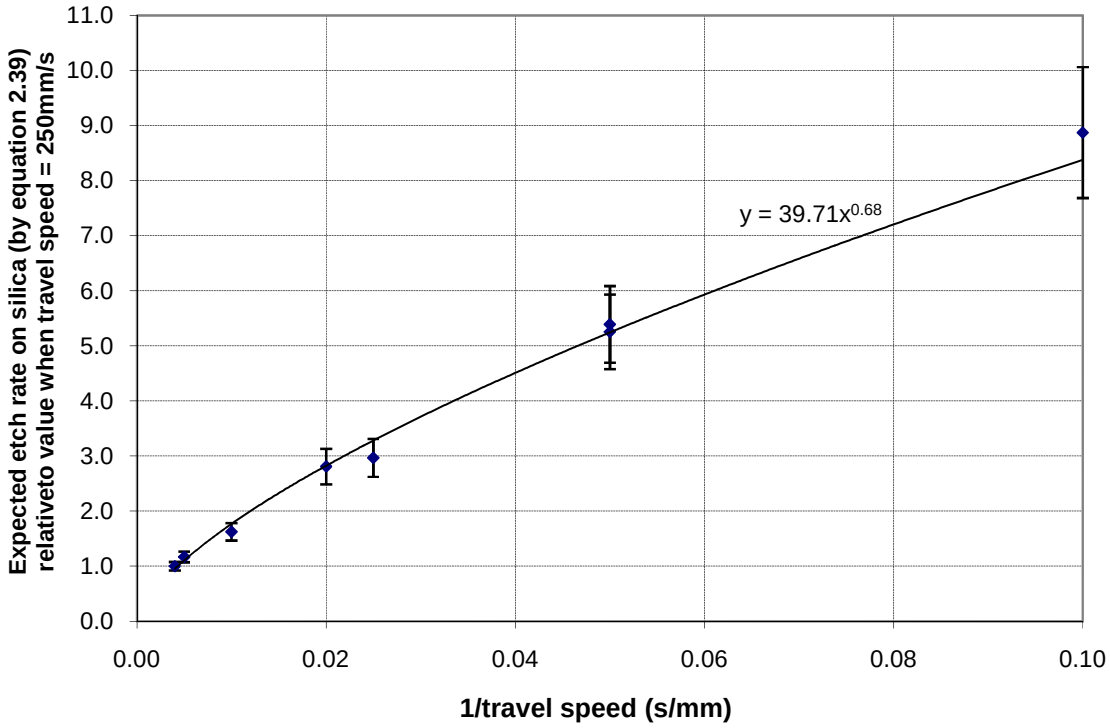

b)

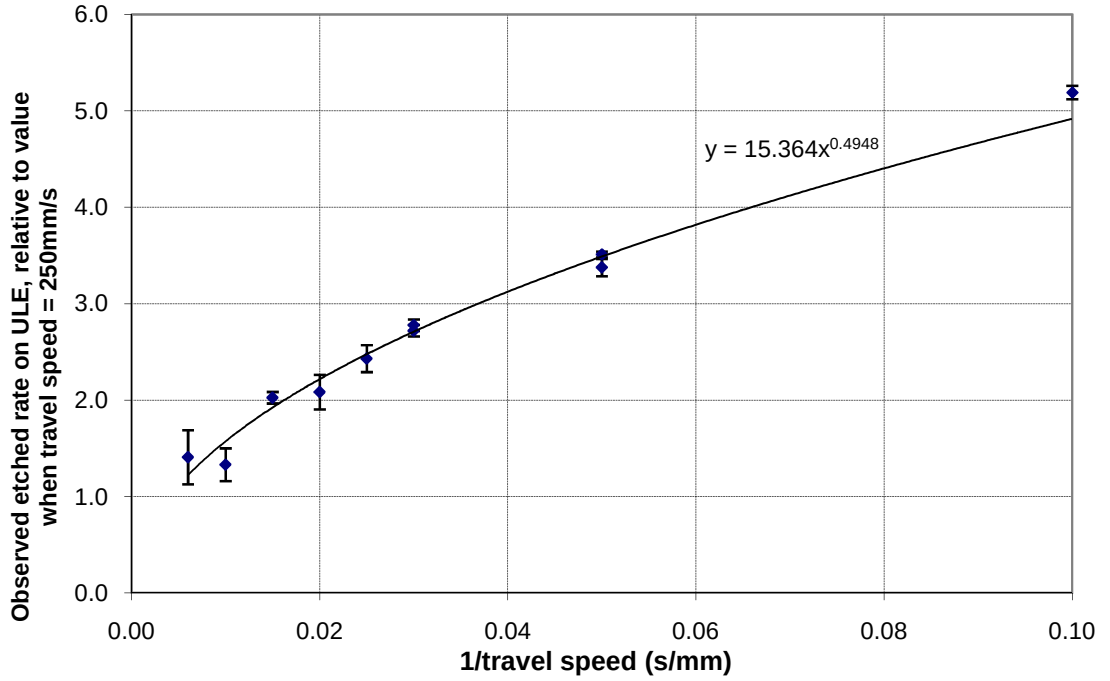

Figure 6.19 **a) The variation in the predicted etch rate on ULE (relative to its value when the travel speed = 250 m/s) with the reciprocal of the travel speed. This has been calculated using the temperatures shown in figure 6.18 and applying equation 2.57 (using the values for silica in table 2.2). b) The variation in the observed etch rates in ULE, based on data discussed in section 4.1 (again relative to its value when the travel speed = 250 m/s).**

A material's response to a heat source can be characterised by the Péclet number. The Péclet number, when applied to heat transfer, is a dimensionless quantity and is the ratio of the thermal energy advected to a fluid to the thermal energy conducted within a fluid. It is used in heat transfer in general and forced convection calculations in particular. The Péclet number is equal to the Prandtl number multiplied by the Reynolds number [**143**]. In fluid dynamics, the Prandtl number of fluid (Pr) is given by the formula

$$Pr = \frac{\nu}{D} \qquad (6.6)$$

where v is the kinematic viscosity and D is the thermal diffusivity. The Reynolds number (Re) is applied to situations where a fluid is in motion relative to a solid object and is given by the formula

$$Re = \frac{VL}{\nu} \qquad (6.7)$$

where V is the velocity of the fluid and L is a characteristic length. The Péclet number can be calculated using the formula

$$Pe = Pr \times Re = \frac{VL}{D} \quad (6.8).$$

When the plasma is passed over ULE, the advection of heat to the surface dominates over the diffusion of heat away from the surface, implying a large Péclet number. When the plasma is passed over silicon, the diffusion of heat away from the surface dominates over the advection of heat to the surface, implying a small Péclet number.

The problem of a heat source moving over a material has been investigated by Jaeger. He has carried out extensive work with regards to finding a relationship between the temperature rise on a surface and the velocity of the heat source. Jaeger's approach has been used as a basis to model the thermal characteristics of many engineering situations including material removal processes such as abrasive machining. The movement of a confined grinding zone which inputs heat to a workpiece surface can be considered analogous to the movement of the plasma torch across the workpiece surface. If the material has a large Péclet number (at least 20), the temperature rise that results, ΔT, can be estimated using the formula

$$\Delta T \approx \frac{0.754\ QL}{\sqrt{VLkC_P\rho}} \quad (6.9)$$

where Q is the thermal power dissipated at the surface per unit area and L is the width of the tool [**144**]. If L is set to the plasma radius, 10 mm, and V is the torch travel speed, Péclet numbers for ULE and silicon are show for a variety of velocities, V.

Table 6.3 **Péclet numbers for of silicon and ULE at various torch travel speeds (V). L = 10 mm.**

Torch travel speed (mm/s)	Silicon	ULE
10	1.2	127
50	5.8	633
100	12	1266
250	29	3165

These numbers imply that it should be acceptable to apply equation 6.9 to the situation where the plasma is passed over ULE at all of those travel speeds. In the case of silicon, it might only valid at the higher speeds.

Figure 6.20 shows the rise in temperature (ΔT), plotted against the reciprocal of the square root of the travel speed V. The data suggests that $\Delta T \propto V^{-0.5}$ which is consistent with equation 6.9. For comparison, values predicted using equation 6.9 have been shown with L = 10 mm and Q = 260 ± 30 W. The error bars on the predicted values are a reflection in the uncertainty in the heat flux. The discrepancy between the two graph lines might indicate that a significant fraction of the heat in the plasma is not absorbed by the surface; much of the heat remains in the plasma gas that bounces off the surface.

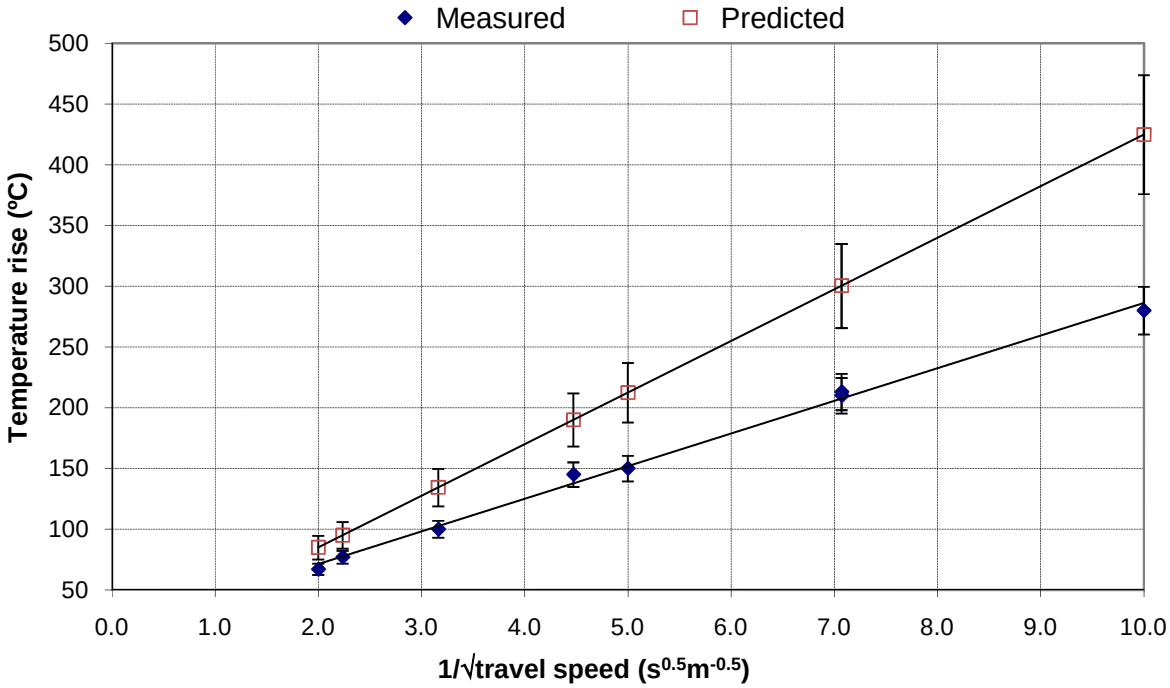

Figure 6.20 **The measured temperature rises on surfaces of ULE using the ThermaCAM™ SC3000 as a function of the reciprocal of the square root of the torch travel speed compared to values predicted using equation 6.9.**

6.3.1 Thermal imaging of neutral removal tests on ULE

Thermal images were taken while a block of ULE (100 mm × 100 mm × 25 mm) was undergoing neutral removal. The neutral removal was done while using both serpentine and staggered rastering programmes. The same number of passes was made in both instances and all at a constant speed of 133 mm/s. Figure 6.21a shows how the temperature at the hotspot increased during the process. As expected, the temperatures measured when serpentine rastering was used were very much higher than when staggered rastering was used. The staggered rastering temperature did increase slowly and so the resulting removal rate might not be as consistent as desired. The time interval between separate passes was ~2 seconds, not nearly enough to allow the sample to cool down properly in between passes. If the periods in between passes were increased, the steady temperature rises would be lower and the removal rate would be more constant. Whether that compensates for the increase in the time over which the machine has to run, when figuring optics or otherwise, is up to the operator.

Figure 6.21b shows data from the same tests, but this time the average temperature over the whole surface (excluding the 'tube reflection' region) are plotted. Temperatures recorded during the cooling down period after etching are included in both cases.

It should perhaps be stressed that these neutral removal tests were performed on small ULE parts. The RAP process is being investigated for use on large optics (>0.5 m). On such parts, local heating is expected to be a less serious problem as there will be a longer period until the plasma arrives back at the same spot.

a)

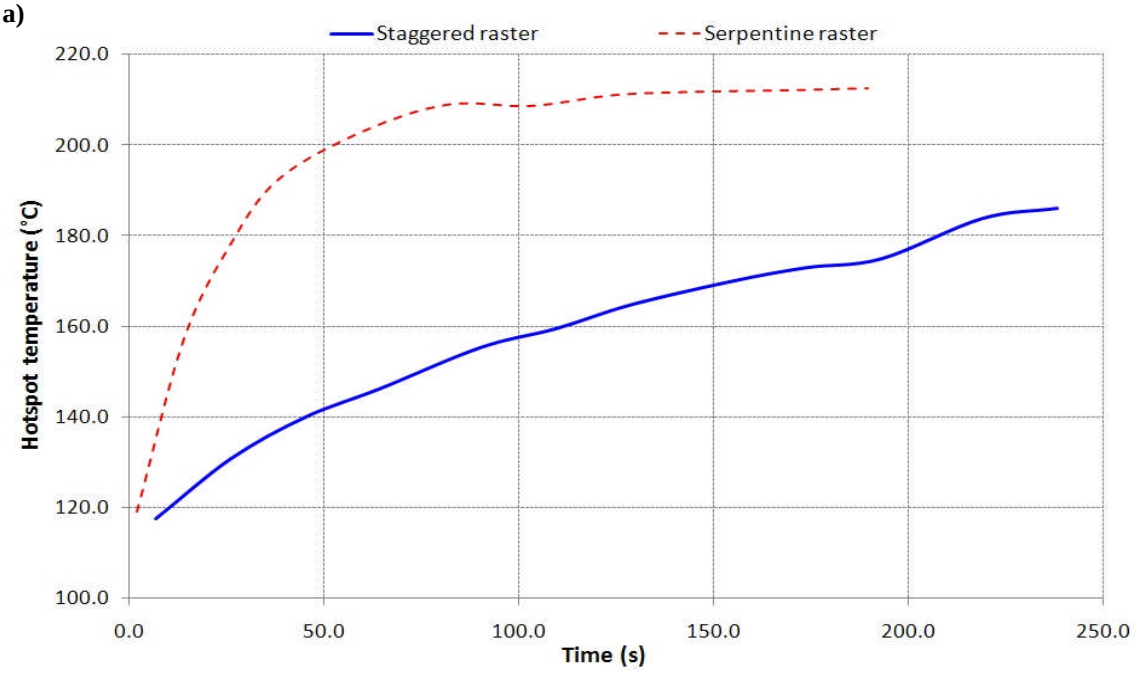

b)

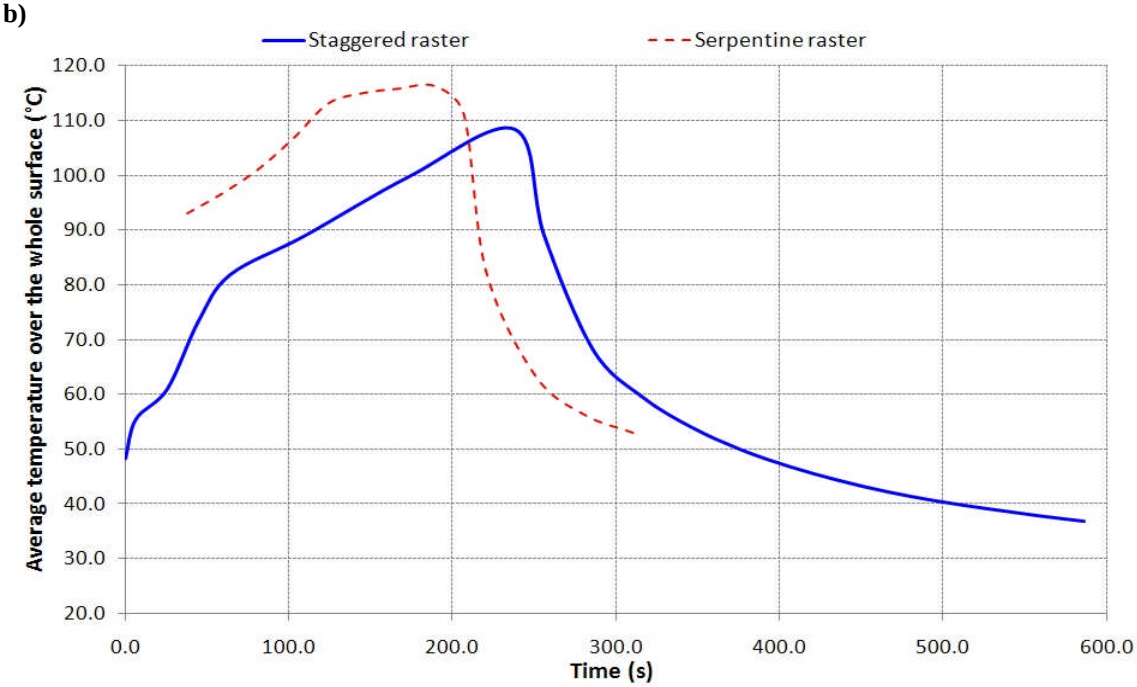

Figure 6.21 **a) Temperatures measured using the thermal imaging camera of the centre of the 'hotspot' on a ULE surface during neutral removal tests. Data for both staggered rastering and serpentine rastering programmes are plotted. In both instances, 76 passes were made across the surface equally spaced across 75 mm (i.e. a 1 mm pitch) using a constant speed of 133 mm/s.**

b) The average temperatures measured over the whole surface (excluding the 'tube reflection' region) during the same neutral removal tests. The average temperatures measured during the cooling period after etching are included. Temperatures below 52°C were not recorded when using serpentine rastering because of the particular camera settings used. The serpentine programme was completed more quickly and so the cooling period started sooner.

6.3.2 Thermal imaging measurements on silicon wafers

The emissivity of ULE had been estimated by taking a thermal image of the surface at room temperature and adjusting the emissivity value so that the temperature given by the Researcher software in the image matched that given by an RTD positioned on the surface. The same method did not work when tried upon silicon wafers. Silicon is very much more reflective than ULE to infrared radiation and when a thermal image of a silicon wafer at ambient temperature was taken (i.e. not while etching), the temperatures measured were clearly not that of the wafer, but that of the laboratory ceiling! Attempts were made to do this inside the chamber in the RAPT 300 machine with the chamber ceiling covered with aluminium foil. Unfortunately, that just added further reflections and it was not possible to cover all objects of high emissivity. Positioning the camera to examine the wafer at normal incidence also did not work as that resulted in a large cold spot appearing on the image; the camera was seeing its own cooled detector.

A test was made in which a ∅100 mm × 525 μm thick boron-doped wafer was passed through the plasma at 100 mm/s. Temperatures were recorded using both the thermal imaging camera and with an RTD placed on the underside of the wafer, such that the plasma passed directly above the RTD. Temperatures given by the thermal imaging camera depended heavily on the chosen value of the emissivity. Figure 6.22 indicates how sensitive the peak measured temperature (inferred by Researcher software) is to the chosen emissivity value.

An alternative way of selecting the most appropriate emissivity value is by consulting the literature. Unfortunately, there are many difficulties in determining the emissivity of silicon wafers, both by theory and by experiment [**145**-**147**]. Values for silicon vary enormously, between 0.2 and 0.8. It is dependent upon wavelength, temperature, impurity concentration and the presence of overlayers [**148**]. One very crucial parameter is the thickness of the surface oxide layer because the Si-O bond is a strong absorber of infrared radiation at around 9 μm, which intersects the region in which the thermal imaging camera is sensitive. Figure 6.23 shows measured values of the spectral emissivity of 2 mm-thick samples of single crystal n-type and p-type silicon.

a)

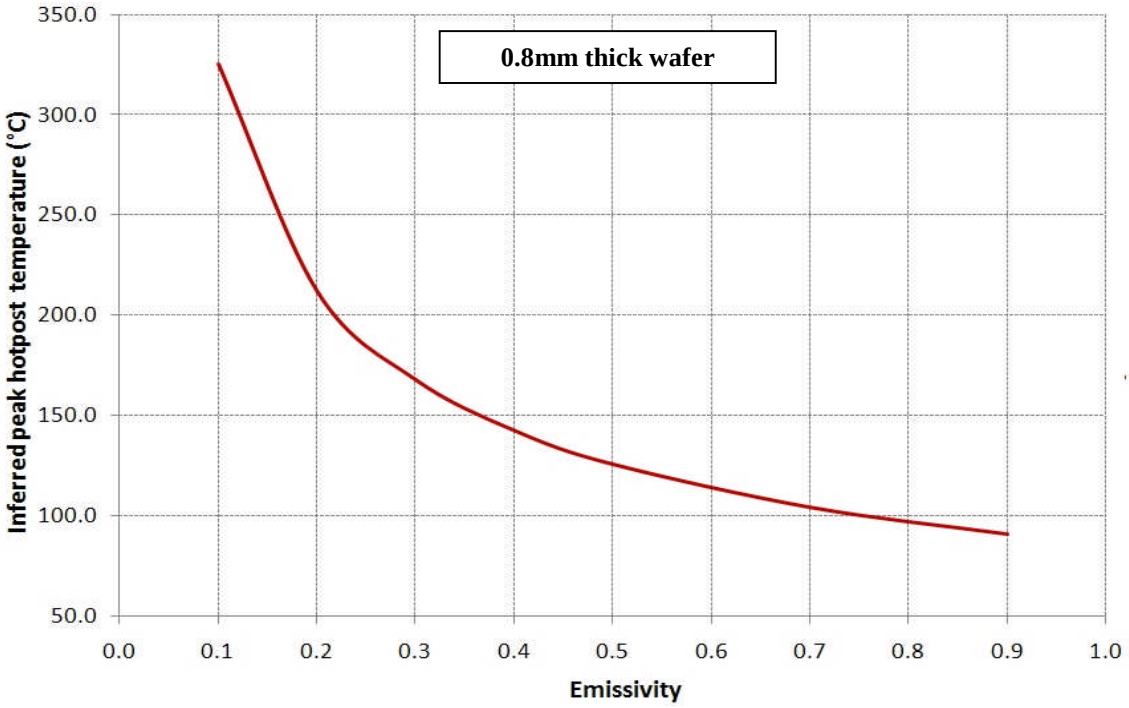

b)

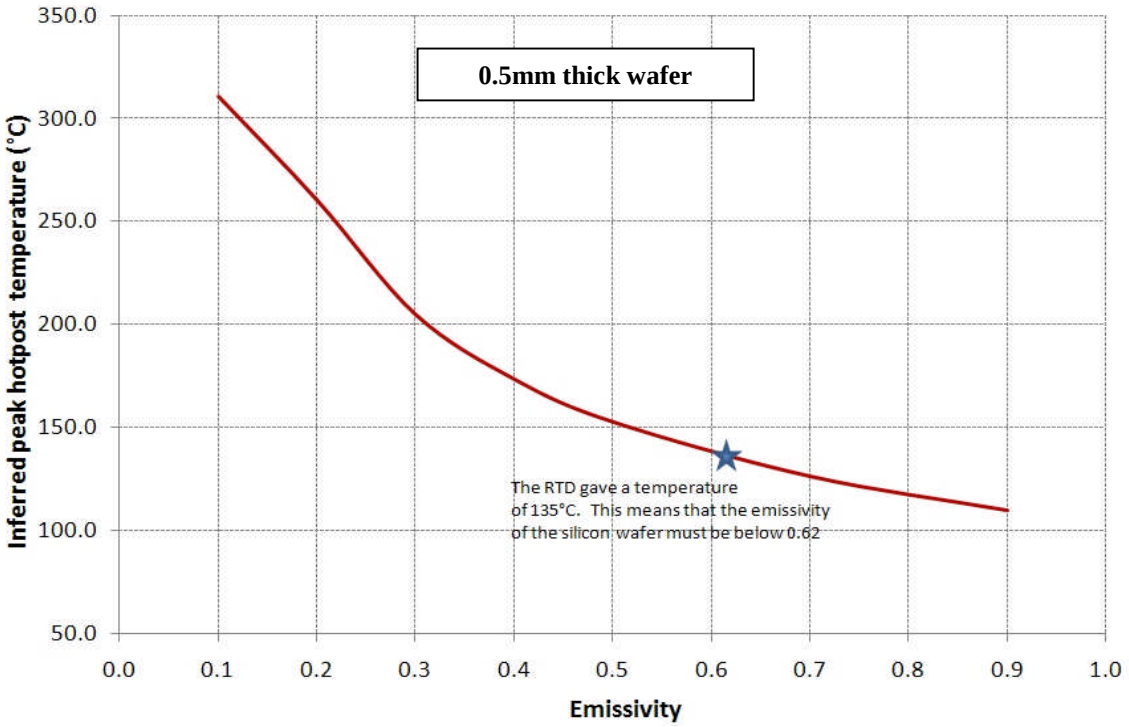

Figure 6.22 **a) The peak hotspot temperature interpreted by the Researcher software when a 0.8mm thick silicon wafer was passed through the plasma at 100 mm/s, as a function of the chosen emissivity value. The same thermal image was used for all data points. This graph illustrates the importance in choosing an appropriate emissivity value when using the thermal imaging camera.**

b) A similar graph from an identical test but when a 0.5 mm thick wafer was used.

a)

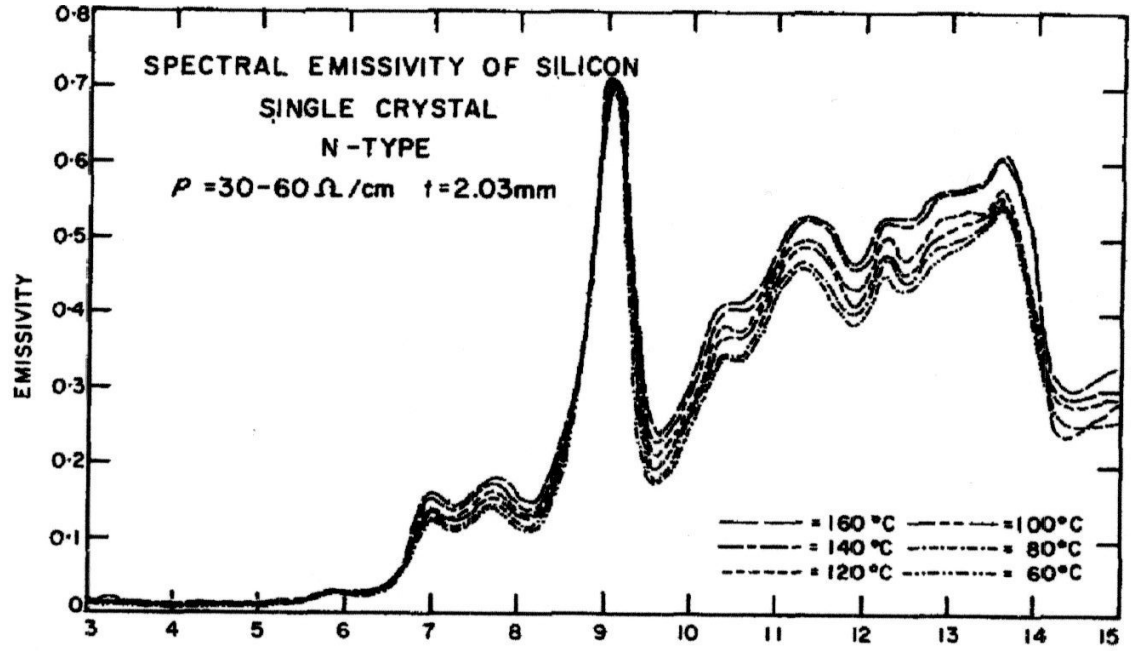

b)

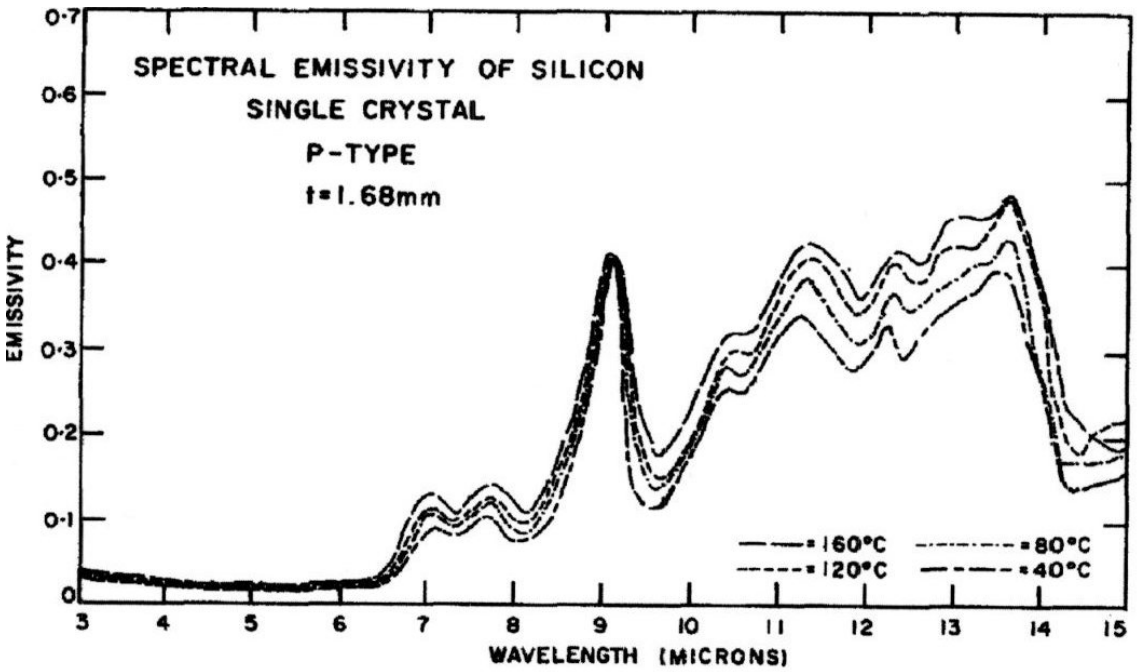

Figure 6.23 **Spectral emissivity values of 2 mm-thick samples of a) n-type and b) p-type single silicon crystal [147].**

Figure 6.24 shows a thermal image of a 0.5 mm thick silicon wafer being etched. It is evident that the wafer is not completely opaque to infrared radiation as a second reflection of the hot quartz tube is visible[30]. This reflection has come off the aluminium tray over which the wafer was supported. An image such as this provided an opportune means of setting an upper limit to the emissivity value. The first step was to select a region of the brighter reflection of the quartz tube (a region over which the detector has not been saturated) and to take the average raw intensity value within that region and to subtract from that an estimate of what the average raw intensity would be without the tube reflections. The next step was to do carry out the same process for the equivalent region of the second reflection. The ratio of the two average intensity values is an indication of the fraction of the infrared radiation incident upon the wafer that is transmitted. The aluminium sample tray was not anodised and therefore has a very high reflectivity (>95%). The value turned out to be about 34%, which implies that the emissivity cannot be higher than 0.66. If the emissivity were equal to 0.66, the maximum temperature measured on the wafer while it was passed through the plasma at 100 mm/s would be 145°C (see figure 6.22b). A lower value of the emissivity would mean that the peak temperature is higher. The temperature given by the RTD during this test was 132°C. As indicated in figure 6.22b, this value is consistent with that of the thermal imaging camera if the emissivity value were set to 0.62.

When the ∅200 mm × 0.8 mm wafers were examined, only one reflection was visible, and it was saturated throughout so it was not possible to estimate its emissivity using the method just described. If the emissivity of this wafer were also 0.62, the maximum temperature measured when the wafer was passed through the plasma at 100 mm/s would be ≈108°C (looking at figure 6.22a). However, the batch of 200 mm diameter wafers and a batch of 100 mm diameter wafers were acquired from different sources; it is likely that the two sets of wafers have different emissivites. When an RTD was placed under a ∅200 mm wafer and the wafer was passed through the plasma at 100 mm/s, measured temperatures peaked between 90°C and 98°C. This suggests that this wafer's emissivity value is probably larger than 0.62. The wafer's high opacity strengthens this claim.

However, with the information available, it has not been possible to assign accurate emissivity values to these wafers. Therefore, it is not possible to measure peak temperatures more accurately using thermal imaging than it is using RTDs. The tests and analysis or theory work required to calculate the right emissivity values are beyond the scope of this thesis.

In the material removal tests, which were discussed in chapter 4, it was observed that the material removal rates on both ULE and silicon were of the same order. Figure 2.43 suggests that for this to be the case, the temperature at which the chemical reactions are taking place when ULE is being etched might be ~200°C higher than when silicon is being etched (if the material removal rate of ULE is considered to be the same as that of silica). Results presented in this chapter do not support this hypothesis. The maximum temperatures measured on the wafers using RTDs (displayed in figure 6.4) are of similar order to those measured using the thermal imaging camera (displayed in figure 6.18). However, in all of the experiments performed using silicon wafers, the wafers were supported above a layer of air, 1cm thick, whereas all the material removal

[30] Silicon is often used in making transmissive infrared optics.

tests were performed on thick samples (at least 5mm thick) on an aluminium tray. The thermal conductivity of air at 20°C is a mere 0.026 $Wm^{-1}K^{-1}$. This means that heat was dissipated away from the underside of the silicon wafers very slowly. This means that when a section of the wafer is under the plasmas, the temperature builds up within the thickness of that section very quickly. It would be interesting to measure temperatures on the surfaces of thicker silicon samples while they were being etched for comparison.

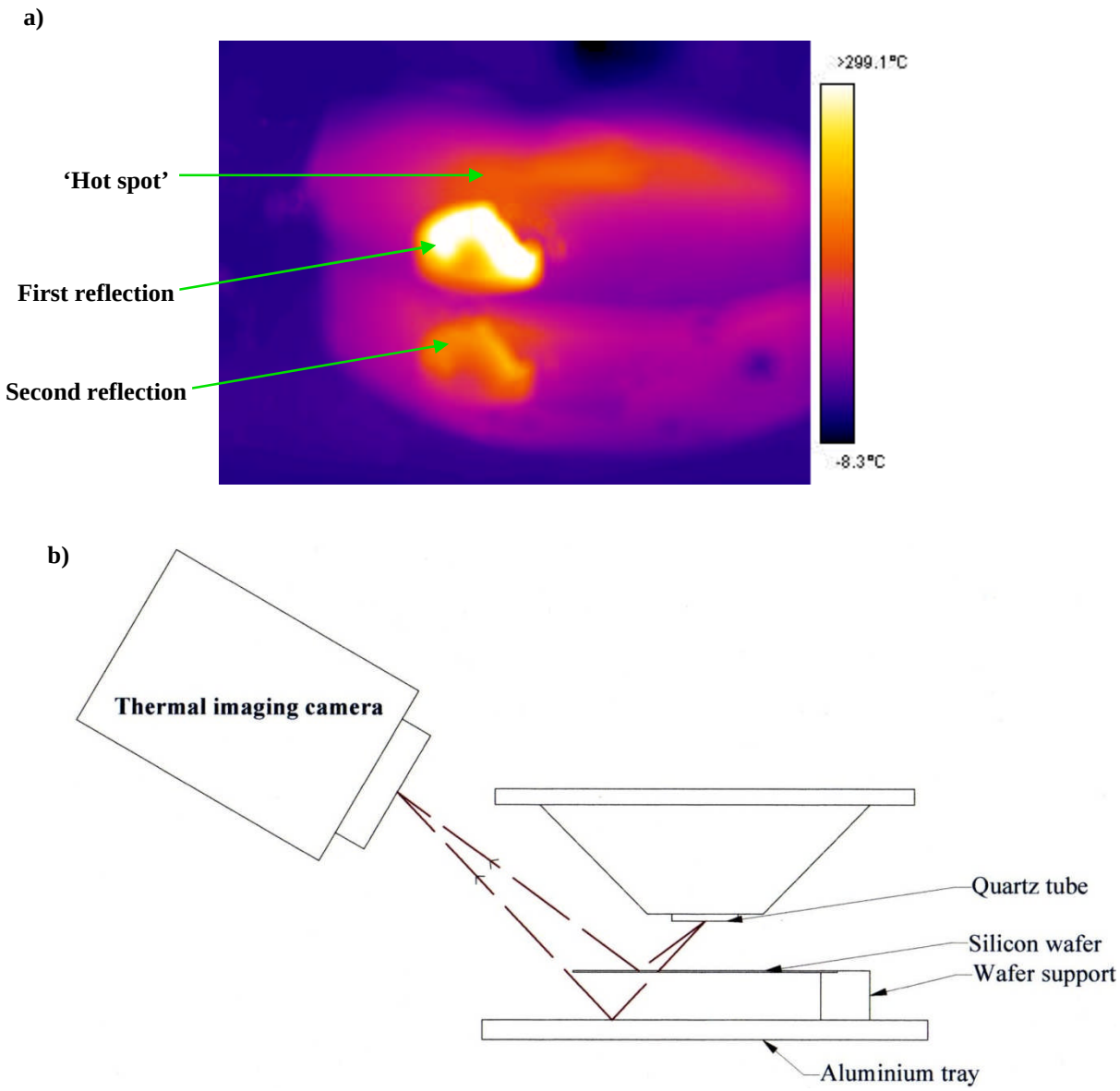

Figure 6.24 **a) A thermal image of a silicon wafer being etched by the plasma. In this image, not one but two reflections of the quartz tube can be seen. The dimmer reflection is the result of infrared radiation reflected off the aluminium tray underneath the wafer. This indicates that some infrared radiation passes through the wafer. The diagram in b) shows how some infrared light from the quartz tube is reflected directly off the wafer and some is transmitted through the wafer and reflected off the aluminium tray underneath.**

6.4 Summary of sample temperature measurements

In this chapter, experiments in which temperatures of samples being etched have been discussed. The techniques involved the use of Pt100 RTDs, pyrometry and thermal imaging. Many tests were carried out in which RTDs were affixed to the underside of silicon wafers. The results of simple one-dimensional heat conduction simulations suggested the temperature gradient through wafers less than 1 mm thick is negligible. This implies that the temperature measured on the underside is very close to that on the top surface. A series of tests was carried out in which the plasma was passed over a silicon wafer at several different speeds with an RTD underneath. The maximum temperature reached was plotted against the reciprocal of the travel speed and the result was close to being a linear fit. This meant that the temperature rise was approximately proportional to the period over which the torch was over the wafer.

Some temperature measurements were taken using the RAPT machine's installed pyrometer looking at ULE blocks being etched. Various torch travel speeds were used and temperatures up to 250°C were recorded. However, for several reasons, it was decided to perform similar experiments using a FLIR SC3000 thermal imaging camera. Passes were made across the ULE blocks using both the pure argon plasma and the reactive plasma with NF_3. The maximum temperatures measured using the thermal imaging camera, which peaked near 300°C, were slightly higher than those measured when using the pyrometer. The emissivity was set to 0.9 for these measurements. The temperatures measured here appeared to be independent of whether the pure argon or reactive plasmas were used. The peak temperatures measured on ULE using the thermal imaging camera were of similar order to those measured on the ∅200 mm silicon wafers using RTDs. However, the relationship between peak temperature and the reciprocal of the travel speed was not linear this time.

Achieving a consistent (repeatable) material removal rate when etching materials is important and, as has been stated many times, the material removal rate is temperature dependent. Temperatures on ULE surfaces at the centre of the 'hot spot' (the point on the surface immediately under the central axis of the torch) were plotted at different times while samples were passed through the plasma. When speeds of 10 mm/s and 40 mm/s were used, the hotspot temperature rose to a maximum during the period over which the first 30 mm passed through the centre of the plasma, but remained very steady thereafter, which is encouraging. Temperatures were also measured during neutral removal tests on ULE samples, 100 mm × 100 mm × 25 mm. As expected, temperatures measured at the 'hot spot' were significantly higher when a serpentine rastering sequence was used compared to when a staggered rastering sequence was used. However, there was a steady temperature rise when using staggered rastering and the average temperatures measured over the whole surface were not so much lower than those measured when serpentine rastering was used. This might result in inconsistent material removal rates when rastering. The seriousness of this problem is dependent on the nature of the application concerned.

Temperatures on silicon wafers being etched were also made using the thermal imaging camera. However, it proved to be difficult to select appropriate emissivity values and it was difficult to state whether the peak values are any more accurate than those measured using RTDs.

7 Summary

In this thesis, research into the Reactive Atom Plasma® (RAP) process which has been carried out using the prototype RAPT 300 machine at Cranfield University has been reported. The main achievements to have come from this work are as follows -

It has been shown that it is possible to measure temperatures throughout most of the plume, even with a central reactive gas flow present. Using a combination of Boltzmann plots and the absolute intensity values of the emission line at 696.5 nm, temperature maps of the plume of the pure argon plasma and in those of the plasmas with NF_3 and SF_6 have been made. To the author's knowledge, this is the first time that temperatures have been measured spectroscopically in an atmospheric pressure ICP that is used as a chemical etching tool. The temperatures measured in the plume of the argon plasma peaked at ~6000 K; those in the reactive plasma plume peaked at ~5500 K. The accuracy of the measurements is believed to be better than ±500 K. Although the highest temperatures in the reactive atom plasma plumes were lower, the warm gas was spread over a wider volume and the total amount of heat delivered into substrate materials in all cases was roughly the same. The amount of heat absorbed by the sample is believed to vary between about 200 W and 450 W depending on sample position.

A new set-up for taking spectroscopic measurements of the plume of the Reactive Atom Plasma plume has been developed. Most previous spectroscopic works on atmospheric ICPs have used optics to project an image onto the entrance of large monochromators (~1 m long). For these measurements, a very simple setup was used with an inexpensive spectrometer. Such a spectrometer cannot provide the wavelength resolution that a larger one can, but the sampling equipment worked well in the confined space and it has been possible to gather a lot of information very quickly.

Material removal rates of the process on ULE and on silicon have been established. Some material removal tests had already been performed on ULE. The work described here extended this work. Material removal rates at torch travel speeds between 10 mm/s and 100 mm/s have been studied. On ULE, volumetric removal rates up to 0.2 mm^3/s were measured. The material removal rate varies with the travel speed; increased local heating when using slower speeds leads to an increase in the material removal rate. Tests using both NF_3 and SF_6 have been performed; the removal rate was found to be proportional to the concentration of fluorine atoms passing through the ICP. Similar tests were carried out on silicon samples. The material removal rate of RAP on silicon was found to be of similar order to those on ULE, but it was much less dependent on the travel speed. It is believed that this is due to its much higher thermal diffusivity.

ULE surface roughness doubles after etching with RAP. Sa (mid-spatial frequency) roughness values of ULE surfaces generally increased from ≈1 nm to > 2 nm. This is believed to be due to redeposition of titanium compounds and the selectivity of the chemical etching process. When single trenches were etched, increases in surface roughness on the edges of the trenches were very large, due to considerable amounts of redeposition.

Temperatures up to 300°C have been measured on surfaces while they were being etched. Many measurements took place measuring temperatures upon ULE surfaces while they were being etched, using a pyrometer and a thermal imaging camera. Although the temperature rises were significant, particularly when employing slower travel speeds, they were not so much larger than those incurred using ion beam figuring (regarding the values given in [**113**]). The thermal stress or distortion incurred is not expected to be a problem on glassy materials of low thermal expansion. When a single pass is made, the temperature at the "hotspot" (the region of surface immediately under the plasma) rises to its peak value during the period within which the sample moves approximately through the first 30 mm, but the temperature remains very constant thereafter. Although the thermal plasma used by the RAP process does contain a higher heat density than any low-density ion beam plasma, it is believed that a significant proportion of the heat in the RAP plasma does not end up in the material; it either stays in the gas that bounces off the surface or is taken away by convection. In the case of ion beam figuring, heat cannot be taken away by convection because it takes place in a vacuum.

7.1 Recommendations for further work

In order to create temperature maps of plasma plume, emission coefficient distributions were determined using Nestor's method of solving the Abel inversion. This method was chosen because it is straightforward to implement. This inversion is only completely correct if axial symmetry exists. High up in the plasma plume (close to the base of the quartz tube) there are significant deviations from axial symmetry. A technique for smoothing out resulting artefacts was used. However, for improved accuracy, a better technique should be used, something similar to the techniques discussed in section 2.2.3.3. This method would involve taking a guess as to what the shape of the 2-dimensional emission coefficient distribution might be and iteratively adjusting it, using numerical methods, so that it the intensity distribution that one would measure, if the guess distribution were correct, is compatible with the real measurements taken from both the front and side of the plasma chamber. This process could be made more accurate by collecting measurements from additional angles.

If funds exist for purchasing requisite equipment, there would be value in measuring the particle densities, by Rayleigh scattering, and the gas velocities, using laser Doppler anemometry. If the RAPT 300 machine is to be upgraded, it would be wise to include the new-style 'Turbo-torch', which includes an aperture to enable the plasma to remove features of smaller spatial size. There might also be merit in fitting a pressure gauge close to the torch to regulate the ambient pressure. As was mentioned in chapter 4, it is difficult to set the pressure the same amount each time with the RAPT 300 machine due to the powerful exhaust system. The plasma parameters will depend to some extent on the pressure inside the chamber. This might be the cause of the scatter in the removal depth data that was observed when using the fastest travel speeds (see figure 4.7, for example).

All material removal tests carried out at Cranfield on ULE have been on solid blocks of the material. As the primary application of the process is the fabrication of large telescope optics, it would be more realistic to perform tests upon parts into which honeycomb-style cells have been machined into the underside. Any distortions in the surface due to the heat transfer might be more apparent in such samples. Temperatures

could be measured using RTDs or thermocouples positioned inside these pits, perhaps only a few millimetres under the top surface (as was done in [**113**]).

It would be of scientific interest to fully understand the origin of the peaks around 440 nm that were observed in the plume of the plasma of NF_3 and when etching silicon using both NF_3 and SF_6 but not in the naked plume of the SF_6 plasma. It would also be interesting to discover the origin of the broader peaks in the titanium-doped plasma.

Temperatures on silicon wafers were measured while they were being etched. It has become apparent that the highest temperature measured is dependent upon the thickness of the wafer used. It would be interesting to perform temperature measurements on the surfaces of thicker silicon samples. A hypothesis was made that the maximum temperature reached on a silicon sample should be significantly lower than that measured on a ULE sample of the thickness under the same conditions. This has yet to be proven experimentally.

There are potential benefits in adding oxygen to the discharge. In the right concentration, oxygen can significantly increase the material removal rate. It might also suppress the amount of redeposition. There is also the case for using helium as the cooling gas instead of argon as it can be more effective at cooling not only the outer tube of torch but also the plasma gas, which should lower heat impact on the substrate.

One way to remove redeposited materials from ULE surfaces might be to raster the whole surface with the pure argon plasma after etching to evaporate this material away. It would be interesting to discover whether the roughnesses of fused silica surfaces increase when etched using RAP in a similar way to that which has been observed on ULE. If this were the case, it would indicate that the observed surface roughness increase on ULE is not solely due to its titanium content.

An important step towards optimising the process to develop the "perfect" (repeatable and deterministic) material removal process would involve modelling techniques. A considerable amount of work since the early 1970s has been done in modelling atmospheric ICPs. Using computational fluid dynamics software packages, it is now possible to create three-dimensional models, such as one described by Colombo *et al.* [**67**]. The plasma physics group at The Eindhoven University of Technology have developed their own software environment of plasma modelling, called ‘Plasimo’ [**149**]. It is possible that, within a few years, a computer program might be written which would allow the user to define the dimensions and parameters of an atmospheric ICP and have it calculate solutions for the temperature, gas flow velocities and particle density distributions. The next stage in creating the definitive RAP model would be to adjust it in order to find out how these distributions change when a sample is in position. The final stage would be to find out how the motion of the plasma relative to the sample affects these physical distributions. Perhaps the quickest way to realise this would be through collaborative work with research groups at other institutions.

Research at Cranfield into the process is continuing. If RAP is to be broadly recognised as the tool of choice for the fine figure correction of precision optics, it is important to demonstrate that the process can be used to convert a moderately flat surface, which might be slightly concave or convex with a peak-valley of several hundred nanometres, into an extremely flat surface (with a peak-valley < 50 nm). In other words, reproducing the kind of surface change that is depicted in figure 2.50 (Plasma Chemical Vaporization Machining was used in that instance). This is expected

to be possible using the Helios 1200 machine. RAP's effectiveness will soon to be tried on new materials, such as Clearceram®. Modifications have been made to the RAPT 300 machine that will enable it to apply coatings to surfaces.

There is much still to do, but the future for the RAP process looks promising. Up until the end of the 20th century, Zerodur was the material of choice for the substrates of the world's largest terrestrial telescopes. However, ULE is now 'catching up' and might take the place Zerodur altogether. RAP is not effective at etching Zerodur but has proved to be very effective at etching ULE. Its effectiveness on silicon and silicon carbide is well documented. It is certainly hoped that the RAP process will bring telescopes such as the European Extremely Large Telescope into operation more quickly. It will feel as though the farthest corners of the Universe have been moved a little bit nearer!

8 Appendices

8.1 Appendix A – Symbols and constants used in equations, units and acronyms

CONSTANTS

c The speed of light, 299792458 ms^{-1}

e Electronic charge, 1.602×10^{-19} C

h Planck's constant, 6.626×10^{-34} Js

k Boltzmann's constant, 1.38×10^{-23} JK^{-1}

m_e Electronic mass, 9.1×10^{-31} kg.

R The molar gas constant, 8.31×10^{-23} $Jmol^{-1}K^{-1}$ (= Boltzmann's constant × Avogadro's number)

ε_0 Permittivity of free space, 8.854×10^{-12} Fm^{-1}

μ_0 Permeability of free space, $4\pi \times 10^{-7}$ Hm^{-1}

VARIABLES USED IN EQUATIONS (SI units)

A Einstein transition probability (s^{-1})

C Capacitance (F, farad)

f Frequency of radiation (Hz)

g Degeneracy. If two energy states are degenerate, it means that they occupy the same energy value and so the degeneracy = 2 (dimensionless)

I Intensity of light; energy received per unit area (Wm^{-2} or $Wm^{-2}nm^{-1}$)

L Inductance (H, henry)

N Atom or ion density (m^{-3})

T Atom or ion temperature (K)

N_e Electron density (m^{-3})

T_e Electron temperature (K)

v Particle velocity (ms^{-1})

Z Internal partition function, $= \sum_{i=0}^{\infty} \left(\exp\left(-\frac{E_i}{kT} \right) \right)$ (dimensionless)

δ Skin depth (m)

ε Emission coefficient of a luminous plasma ($Wm^{-3}sr^{-1}$ or $Wm^{-3}sr^{-1}nm^{-1}$) **or** the emissivity of a greybody (dimensionless)

μ_r Relative permeability (dimensionless)

σ Electrical conductivity ($(\Omega m)^{-1}$)

λ Wavelength (m)

ω Angular frequency (Hz)

UNITS

Distance

m	metre
mm	millimetre (= 10^{-3} m)
μm	micrometre (= 10^{-6} m)
nm	nanometre (= 10^{-9} m)
pm	picometre (= 10^{-12} m)
Å	ångstrom (= 10^{-10} m)

Time

s	second

Mass

kg	kilogram

Energy

J	joule
eV	Electron volt, unit of energy (= 1.602×10^{-19} J).

Power

W	watt

Pressure

Pa	pascal (= 1 N/m^2)
atm	= 1 × atmospheric pressure (= 101,325Pa).
torr	The pressure that supports a column of mercury 1 millimetre high (= 133.3 Pa).

Flow

slm	Standard litres per minute.
sccm	Standard cubic centimetres per minute.

The standard volumetric flow rate is not the actual volumetric flow rate but is the equivalent flow rate in terms of particles if it were an ideal gas at 0°C and at 1 atmosphere pressure.

Electrical units

A	ampere
V	volt

Other units

mol	mole (= 6.02×10^{23} particles, the number of atoms in 12g of carbon-12)

OTHER SYMBOLS

$\lvert x \rvert$	= Modulus. If x is a positive scalar quantity, $\lvert x \rvert = x$. If x is a negative scalar quantity, $\lvert x \rvert = -x$. If $\boldsymbol{x}$ is a vector, $\lvert \boldsymbol{x} \rvert$ = the magnitude of $\boldsymbol{x}$.
∅	Diameter symbol.

ROUGHNESS PARAMETERS

Ra The arithmetic mean deviation of the height of a one-dimensional surface cross-section. If the height of the surface, *z*, has been measured at *N* positions along the *x*-axis: x_1, x_2, x_3 up to x_N and the average height measured is $\bar{z}$, $\text{Ra} = \frac{1}{N}\sum_{i=1}^{N}|z(x_i) - \bar{z}|$.

Rq The rms (root mean square) deviation of the height of a one-dimensional surface cross-section,

$$\text{Rq} = \sqrt{\frac{1}{N}\sum_{i=1}^{N}[(z(x_i) - \bar{z})^2]}\,.$$

Sa The arithmetic mean deviation of the height of a two-dimensional surface. If the height of the surface, z, has been measured at *N* positions along the *x*-axis and *M* positions along the *y*-axis: y_1, y_2, y_3 up to y_M, and the average height measured over the whole surface is $\bar{z}$,

$$\text{Sa} = \frac{1}{NM}\sum_{j=1}^{M}\left(\sum_{i=1}^{N}\left|z\left(x_i, y_j\right) - \bar{z}\right|\right).$$

COMMONLY USED ACRONYMS

AES	Atomic emission spectroscopy.
ASCII	American Standard Code for Information Interchange.
CCD	Charge coupled device.
CCI	Coherence Correlation Interferometer.
CLTE	Complete local thermal equilibrium.
FWHM	Full width at half maximum (The separation between the points at which a Gaussian distribution, or similar, is half of that of the maximum value).
IBF	Ion beam figuring.
ICP	Inductively coupled plasma.
ISO	International Organisation for Standardisation.
LDA	Laser Doppler anemometry.
LTE	Local thermal equilibrium.
MRR	Material removal rate.
PLTE	Partial local thermal equilibrium.
RAP®	Reactive Atom Plasma.
RF	Radio frequency.
RTD	Resistance temperature detector.
rms	Root mean square.
SMA	SubMiniature version A.
ULE®	Ultra Low Expansion (a titanium silicate glass manufactured by Corning, whose coefficient of thermal expansion is 0 ± 30 nm/m.K).

8.2 Appendix B – Selected argon and titanium emission lines

Ion	Observed λ Air (nm)	Relative Intensity	Transition probability (A_{ki}) (s^{-1})	Energy levels E_i (cm^{-1})	-	E_k (cm^{-1})	Electronic configurations			Terms			Total angular momentum J_i	-	J_k	Degeneracies g_i	-	g_k
Ar I	518.775	20	1.38e+06	104 102.0990	-	123 372.9253	$3s^23p^5(^2P°_{3/2})4p$	-	$3s^23p^5(^2P°_{1/2})5d$	$^2[^1/_2]$	-	$^2[^3/_2]°$	1	-	2	3	-	5
Ar I	522.127	7	8.8e+05	105 462.7596	-	124 609.856	$3s^23p^5(^2P°_{3/2})4p$	-	$3s^23p^5(^2P°_{3/2})7d$	$^2[^5/_2]$	-	$^2[^7/_2]°$	3	-	4	7	-	9
Ar I	549.587	25	1.69e+06	105 462.7596	-	123 653.177	$3s^23p^5(^2P°_{3/2})4p$	-	$3s^23p^5(^2P°_{3/2})6d$	$^2[^5/_2]$	-	$^2[^7/_2]°$	3	-	4	7	-	9
Ar I	555.87	25	1.42e+06	104 102.0990	-	122 086.9164	$3s^23p^5(^2P°_{3/2})4p$	-	$3s^23p^5(^2P°_{3/2})5d$	$^2[^1/_2]$	-	$^2[^3/_2]°$	1	-	2	3	-	5
Ar I	591.209	50	1.05e+06	104 102.0990	-	121 011.9198	$3s^23p^5(^2P°_{3/2})4p$	-	$3s^23p^5(^2P°_{1/2})4d$	$^2[^1/_2]$	-	$^2[^3/_2]°$	1	-	1	3	-	3
Ar I	603.213	70	2.46e+06	105 462.7596	-	122 036.0704	$3s^23p^5(^2P°_{3/2})4p$	-	$3s^23p^5(^2P°_{3/2})5d$	$^2[^5/_2]$	-	$^2[^7/_2]°$	3	-	4	7	-	9
Ar I	641.631	70	1.16e+06	104 102.0990	-	119 683.0821	$3s^23p^5(^2P°_{3/2})4p$	-	$3s^23p^5(^2P°_{3/2})6s$	$^2[^1/_2]$	-	$^2[^3/_2]°$	1	-	2	3	-	5
Ar I	667.728	100	2.36e+05	93 750.5978	-	108 722.6194	$3s^23p^5(^2P°_{3/2})4s$	-	$3s^23p^5(^2P°_{1/2})4p$	$^2[^3/_2]°$	-	$^2[^1/_2]$	1	-	0	3	-	1
Ar I	675.283	150	1.93e+06	104 102.0990	-	118 906.6110	$3s^23p^5(^2P°_{3/2})4p$	-	$3s^23p^5(^2P°_{3/2})4d$	$^2[^1/_2]$	-	$^2[^3/_2]°$	1	-	2	3	-	5
Ar I	687.129	150	2.78e+06	104 102.0990	-	118 651.3950	$3s^23p^5(^2P°_{3/2})4p$	-	$3s^23p^5(^2P°_{3/2})4d$	$^2[^1/_2]$	-	$^2[^1/_2]°$	1	-	1	3	-	3
Ar I	693.766	50	3.08e+06	104 102.0990	-	118 512.197	$3s^23p^5(^2P°_{3/2})4p$	-	$3s^23p^5(^2P°_{3/2})4d$	$^2[^1/_2]$	-	$^2[^1/_2]°$	1	-	0	3	-	1
Ar I	696.543	10000	6.39e+06	93 143.7600	-	107 496.4166	$3s^23p^5(^2P°_{3/2})4s$	-	$3s^23p^5(^2P°_{1/2})4p$	$^2[^3/_2]°$	-	$^2[^1/_2]$	2	-	1	5	-	3
Ar I	706.722	10000	3.80e+06	93 143.7600	-	107 289.7001	$3s^23p^5(^2P°_{3/2})4s$	-	$3s^23p^5(^2P°_{1/2})4p$	$^2[^3/_2]°$	-	$^2[^3/_2]$	2	-	2	5	-	5
Ar I	738.398	10000	8.47e+06	93 750.5978	-	107 289.7001	$3s^23p^5(^2P°_{3/2})4s$	-	$3s^23p^5(^2P°_{1/2})4p$	$^2[^3/_2]°$	-	$^2[^3/_2]$	1	-	2	3	-	5
Ar I	763.511	25000	2.45e+07	93 143.7600	-	106 237.5518	$3s^23p^5(^2P°_{3/2})4s$	-	$3s^23p^5(^2P°_{3/2})4p$	$^2[^3/_2]°$	-	$^2[^3/_2]$	2	-	2	5	-	5
Ar I	794.818	20000	1.86E+07	94 553.6652	-	107 131.7086	$3s^23p^5(^2P°_{1/2})4s$	-	$3s^23p^5(^2P°_{1/2})4p$	$^2[^1/_2]°$	-	$^2[^3/_2]$	0	-	1	1	-	3
Ar I	826.452	10000	1.53E+07	95 399.8276	-	107 496.4166	$3s^23p^5(^2P°_{1/2})4s$	-	$3s^23p^5(^2P°_{1/2})4p$	$^2[^1/_2]°$	-	$^2[^1/_2]$	1	-	1	3	-	3

Ion	Observed λ Air (nm)	Relative Intensity	Transition probability (A_{ki}) (s^{-1})	Energy levels E_i (cm^{-1})	-	E_k (cm^{-1})	Electronic configurations			Terms			Total angular momentum J_i	-	J_k	Degeneracies g_i	-	g_k
Ti I	465.647	720	1.99E+06	0	-	21 469.494	$3d^2 4s^2$	-	$3d^2(^3F)4s4p(^3P°)$	a ^3F	-	z $^3G°$	2	-	3	5	-	7
Ti I	466.759	840	2.18E+06	170.132	-	21 588.496	$3d^2 4s^2$	-	$3d^2(^3F)4s4p(^3P°)$	a ^3F	-	z $^3G°$	3	-	4	7	-	9
Ti I	468.192	950	2.35E+06	386.874	-	21 739.713	$3d^2 4s^2$	-	$3d^2(^3F)4s4p(^3P°)$	a ^3F	-	z $^3G°$	4	-	5	9	-	11
Ti I	506.466	1400	3.79e+06	386.874	-	20 126.055	$3d^2 4s^2$	-	$3d^2(^3F)4s4p(^3P°)$	a ^3F	-	z $^3G°$	4	-	3	9	-	7
Ti I	517.375	1100	3.80e+06	0	-	19 322.988	$3d^2 4s^2$	-	$3d^2(^3F)4s4p(^3P°)$	a ^3F	-	z $^3G°$	2	-	2	5	-	5
Ti I	519.298	1300	3.49e+06	170.132	-	19 421.576	$3d^2 4s^2$	-	$3d^2(^3F)4s4p(^3P°)$	a ^3F	-	z $^3G°$	3	-	3	7	-	7
Ti I	521.039	1400	3.57e+06	386.874	-	19 573.968	$3d^2 4s^2$	-	$3d^2(^3F)4s4p(^3P°)$	a ^3F	-	z $^3G°$	4	-	4	9	-	9

Details of emission lines taken from [**141**].

8.3 Appendix C - Acquisition of CCI data

The Talysurf 6000 Coherence Correlation Interferometer, a white light interferometer described in section 3.2.2, has been used in making all of the roughness measurements described in this thesis. The interferometer is controlled using control software on the supplied computer. The software 'Talymap Gold', provided by Taylor Hobson, was used for data analysis.

The control software displays a preview image similar to that in figure C.1. The appearance of fringes indicates that the pathlengths are close to matching. The interferometer has vertical scanning range which is set using the slider to the right of the display window. The range should be set so that it covers all heights where fringes are visible. Once that has been set, the user has only to press the start button and then the interferometer measures the degree of coherence within the height range and can reconstruct a three-dimensional image of the surface accordingly.

A raw data image is then displayed using the Talymap Gold software. An example of such an image is shown in figure C.2a. There is clearly a gradient, which results from the fact that neither the stage nor the measured surface are completely perpendicular to the light beam. The Talymap software includes a levelling algorithm which converts it into something that looks like figure C.2b. The next step is to apply thresholds to exclude the very highest and lowest points. The highest points might simply be due to dust on the surface (surfaces were frequently sprayed using a nitrogen-based aerosol to remove dust). The software allows the user to apply thresholds by eliminating a chosen percentile at the top end and the bottom end of the Abbott-Firestone curve. The red curve in Figure C.2c is the Abbott-Firestone curve, a cumulative height distribution of all the sampled data points. Figure C.2d is the result of the thresholding. In all cases the top and bottom 0.0001 percentiles were excluded. Only after thresholding is it sensible to process the data. The software produced a data window like the one in figure C.2e. The user can request that separate roughness and waviness calculations be carried out by choosing a cut-off wavelength. In all instances the cut-off wavelength was 80 μm and a Gaussian filter was applied. The Gaussian filtering attenuates the value by 50% at the cut-off wavelength. The 80 μm cut-off was software's default option and was based upon the ISO standard number 4287. Maps of filtered data are shown in figure C.3 with parameter lists.

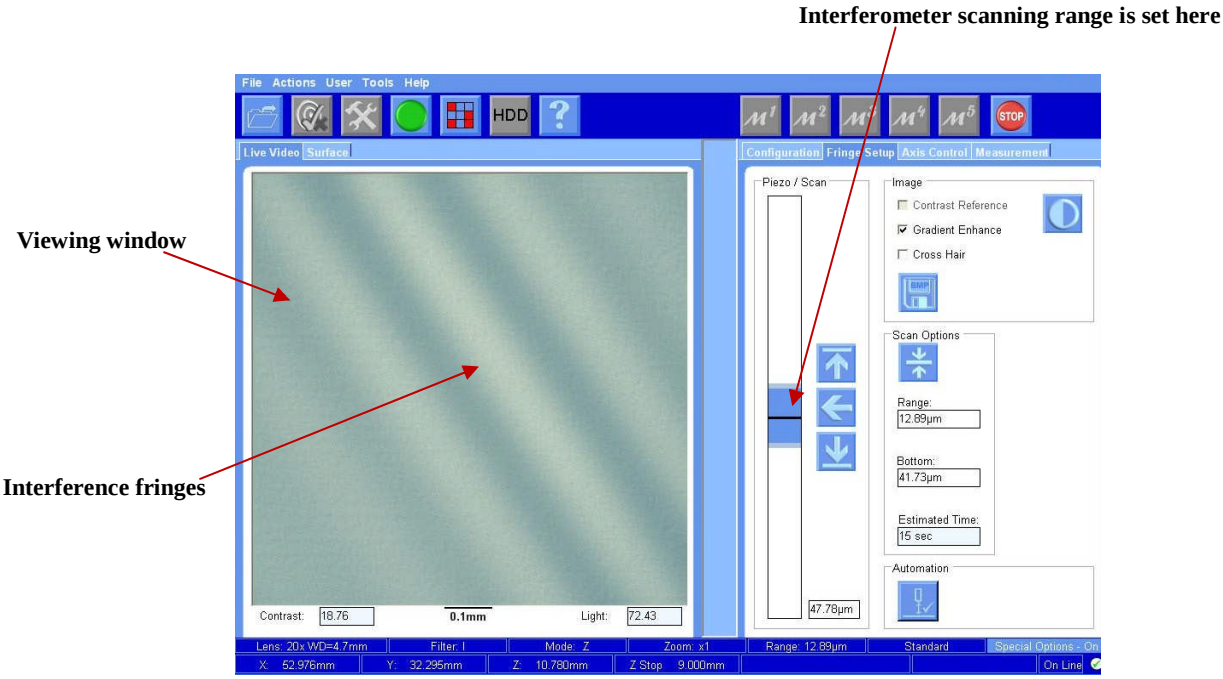

Figure C.1 **If the vertical separation between the surface and the objective is correct, fringes are visible in the 'viewing window'. The user sets the scanning range so that several fringes are included.**

a)

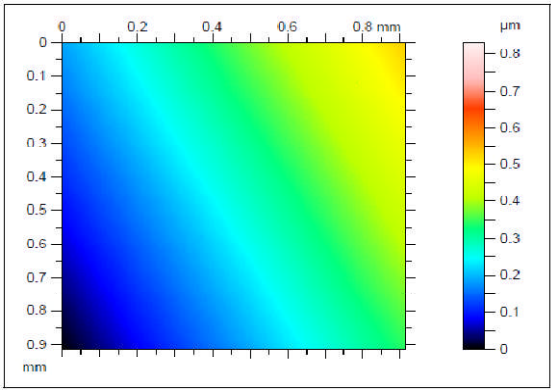

b)

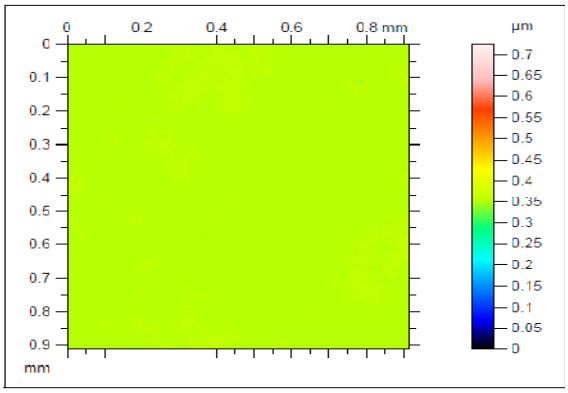

c)

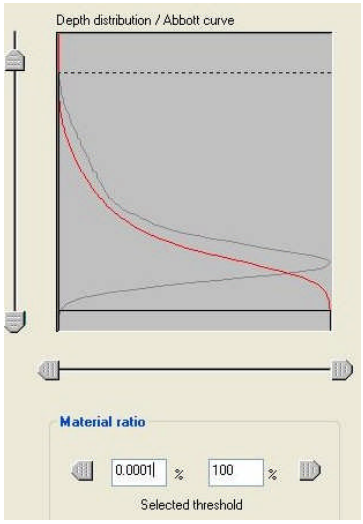

d)

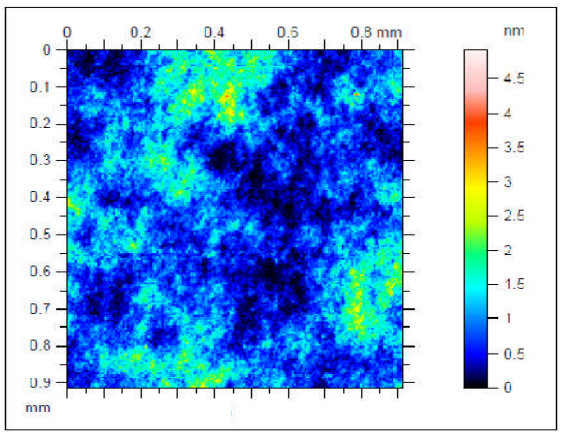

e)

Parameters calculated on the surface ules31unetched00038 > ... > Thresholded 0.0001 - 100 %

```
Sz, Sds and Ssc parameters are defined according to EUR15178N
report.

Amplitude Parameters

   Sa     = 0.774 nm
   Sq     = 0.936 nm
   Sp     = 4.03 nm
   Sv     = 0.894 nm
   St     = 4.92 nm
   Ssk    = 0.993
   Sku    = 3.42
   Sz     = 4.86 nm
```

Figure C.2 **a) Raw data image. b) Levelled data. c) Setting threshold levels using the Abbott-Firestone curve. d) Image after thresholding. e) Data for image d.**

a)

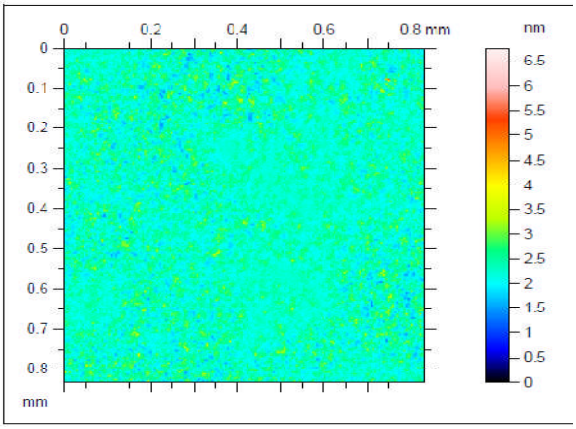

b)

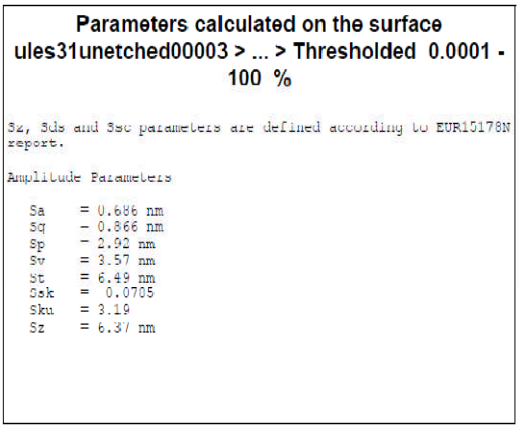

c)

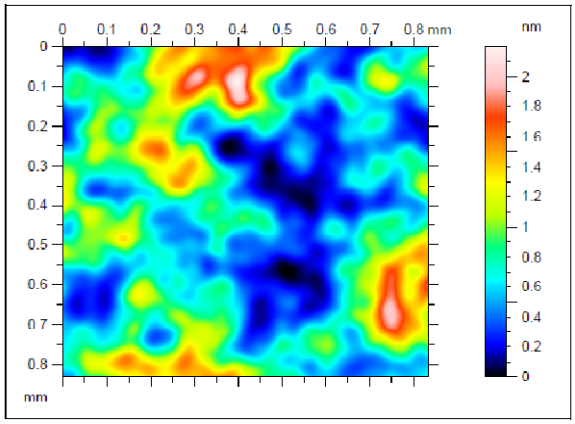

d)

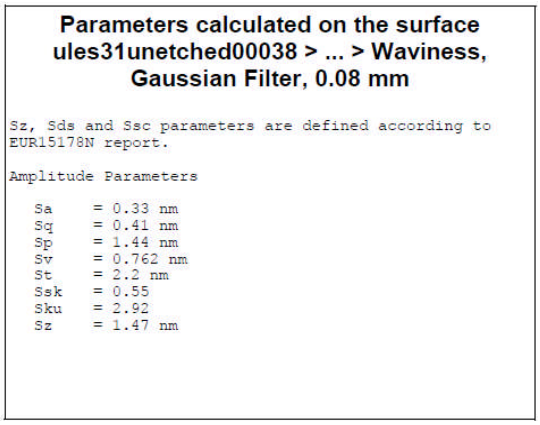

Figure C.3 **Data maps after filtering a) short wavelength (<80 μm) data map. b) Roughness data for map a. c) Long wavelength (>80 μm) data map. d) Waviness data for map b.**

9 References

[1] The Keck Observatory website, http://www.keckobservatory.org.

[2] The European Southern Observatory website, http://www.eso.org.

[3] Gilmozzi, R. (2004), *"Science and Technology Drivers for Future Giant Telescopes"*, Proceedings of SPIE - The International Society for Optical Engineering, vol. 5489, pp. 1-10.

[4] Shore, P. and Parr-Burman, P. (2003), *"Large Optics Manufacturing Study (LOMS) Final Report"*.

[5] National ignition facility & Photon Science website, https://lasers.llnl.gov.

[6] HiPER web site, http://www.hiper-laser.org.

[7] RAPT Industries web site, http://www.raptindustries.com.

[8] Lawn, B. R. and Wilshaw, T. R. (1975), *"Fracture of Brittle Solids"*, 1st ed, Cambridge University Press, Cambridge, UK.

[9] Verma, Y., Chang, A. K., Berrett, J. W., Futtere, K., Gardopee, G. J., Kelley, J., Kyler, T., Lee, J., Lyford, N., Proscia, D. and Sommer, P. R. (2006), "*Rapid damage-free shaping of silicon carbide using Reactive Atom Plasma (RAP) processing*", Proceedings of SPIE - The International Society for Optical Engineering, Volume 6273 I, Article number 62730B.

[10] Drüding, T. W., Bifano, T. G. and Fawcett, S. C. (1995), *"Contouring algorithm for Ion Figuring"*, Precision Engineering, vol. 17, no. 1, pp. 10-21.

[11] Eckert, H. U. (1974), *"The Induction Arc: A State-of-the-Art Review"*, High Temperature Science, vol. 6, pp. 99-134.

[12] Boulos, M. I. (1985), *"The Inductively Coupled R.F. (Radio Frequency) Plasma"*, Pure & Applied Chemistry, vol. 57, no. 9, pp. 1321-1352.

[13] Manos, D. M. and Flamm, D. L. (1989), *"Plasma Etching, an Introduction"*, 1st ed, Hardcourt Brace Jovanovich, Boston.

[14] Lieberman, M. A. and Lichtenberg, A. J. (2005), *"Principles of Plasma Discharges and Material Processing"*, 2nd ed, John Wiley, New York.

[15] Griem, H. R. (1997), *"Principles of Plasma Spectroscopy"*, Cambridge University Press, Cambridge, UK.

[16] Marr, G. (1968), *"Plasma Spectroscopy"*, Elsevier Publishing Company, Barking, UK.

[17] Thornton, M. F. (1993), *"Spectroscopic Determination of Temperature Distributions for a TIG arc"*, PhD Thesis, Cranfield University, UK.

[18] Boyd, T. J. M. and Sanderson, J. J. (1969), *"Plasma Dynamics"*, Thomas Nelson, London.

[19] Devoto, R. S. (1973), *"Transport Coefficients of Ionised Argon"*, The Physics of Fluids, vol. 14, no. 5, pp. 616-623.

[20] Phillips, A. C. (1994), *"The Physics of Stars"*, 1st ed, John Wiley & Sons Ltd, Chichester, West Sussex, UK.

[21] Roth, J. R. (1995), *"Industrial Plasma Engineering - Volume 1: principles"*, 1st ed, IOP Publishing, Bristol and Philadelphia.

[22] Aguilera, J. A. and Aragón, C. (2007), *"Multi-element Saha–Boltzmann and Boltzmann Plots in Laser-Induced Plasmas"*, Spectrochimica Acta Part B: Atomic Spectroscopy, vol. 62, no. 4, pp. 378-385.

[23] Aragón, C. and Aguilera, J. A. (2008), *"Characterization of Laser Induced Plasmas by Optical Emission Spectroscopy: A Review of Experiments and Methods"*, Spectrochimica Acta Part B: Atomic Spectroscopy, vol. 63, no. 9, pp. 893-916.

[24] Tomassini, P. and Giulietti, A., (2001) *"A Generalization of Abel Inversion to Non Axisymmetric Density Distribution"*, Optical Communications, vol. 199, pp 143–148.

[25] De Giacomo, A., Shakhatov, V. A., Senesi, G. S., Orlando, S. (2001), *"Reconstruction of Laser-Induced Plasma Spectral Emissivity in Non-Axisymmetric Conditions"*, Spectrochimica Acta Part B: Atomic Spectroscopy, vol. 60, no. 7-8, pp. 888-896.

[26] De Giacomo, A., Dell'Aglio, M., Santagata, A. and Teghil, R. (2005), "*Early Stage Emission Spectroscopy Study of Metallic Titanium Plasma Induced in Air by Femtosecond and Nanosecond-Laser Pulses*", Spectrochimica Acta Part B: Atomic Spectroscopy, vol. 60, no. 7-8, pp. 935-947.

[27] Griem, H. R. (1963), *"Validity of Local Thermal Equilibrium in Plasma Spectroscopy*", Physical Review, vol. 131, no. 3, pp. 1170-1176.

[28] Murphy, A. B. (1997), *"Demixing in free-burning arcs*", Physical Review E, vol. 55, no. 6, pp. 7473-7493.

[29] Babat, G. I. (1947), *"Electrodeless Discharges and some Allied Problems"*, Journal of the Institute of Electrical Engineering, vol. 94, pp. 27-37.

[30] Reed, T. B. (1961), *"Induction-Coupled Plasma Torch"*, Journal of Applied Physics, vol. 32, no. 5, pp. 821-824.

[31] Nölte, J. (2003), *"Inductively Couple Plasma Emission Spectroscopy - A Practical Guide*", Wiley-VCH.

[32] Colombo, V., Panciatichi, C., Zazo, A., Cocito, G. and Cognolato, L. (1997), "*Modeling, Project, Numerical Simulation, and AES Temperature Diagnostics of an Inductively Coupled Plasma Torch for the Deposition of High-Purity Fused Silica for Optical Waveguide Production.*", IEEE Transactions on Plasma Science, vol. 25, no. 5, pp. 1073-1080.

[33] Mostaghimi, J. and Chandra, S. (2007), *"Heat Transfer in Plasma Spray Coating Processes"*, in Fridman, A., Cho, Y. I., Greene, G. A. and Bar-Cohen, A. (ed.) *Advances in Heat Transfer*, Elsevier, pp. 143-204.

[34] Soucy, G., Jurewicz, J. W. and Boulos, M. I. (1995), *"Parametric Study of the Plasma Synthesis of Ultrafine Silicon Nitride Powders"*, Journal of Materials Science, vol. 30, pp. 2008-2018.

[35] Leparoux, M., Loher, M., Schreuders, C. and Siegmann, S. (2008), *"Neural Network Modelling of the Inductively Coupled RF Plasma Synthesis of Silicon Nanoparticles"*, Powder Technology, vol. 185, no. 2, pp. 109-115.

[36] Cai, M., Haydar, D. A., Montaser, A. and Mostaghimi, J. (1997), *"Computer Simulation of Argon-Nitrogen and Argon-Oxygen Inductively Coupled Plasmas"*, Spectrochimica Acta Part B: Atomic Spectroscopy, vol. 52, no. 3, pp. 369-386.

[37] Meyer, G. A. and Barnes, R. M. (1985), *"Analytical Inductively Coupled Nitrogen and Air Plasmas"*, Spectrochimica Acta Part B: Atomic Spectroscopy, vol. 40, no. 7, pp. 893-905.

[38] Cai, M., Montaser, A. and Mostaghimi, J. (1993), *"Computer Simulation of Atmospheric-Pressure Helium Inductively Coupled Plasma Discharges"*, Spectrochimica Acta Part B: Atomic Spectroscopy, vol. 48, no. 6-7, pp. 789-807.

[39] Tanaka, Y. and Sakuta, T. (2002), "*Chemically Non-Equilibrium Modelling of N_2 Thermal ICP at Atmospheric Pressure using Reaction Kinetics*", Journal of Physics D: Applied Physics, vol. 35, pp. 468-476.

[40] Freeman, M. P. and Chase, J. D. (1966), *"Energy-Transfer Mechanism and Typical Operating Characteristics for the RF Plasma Generator"*, Journal of Applied Physics, vol. 39, no. 1, pp. 180-190.

[41] Mensing, A. E. and Bödeker, L. R. (1969), *"Theoretical Investigations of R.F. Induction Heated Plasmas"*, CR-1312, NASA.

[42] Henderson, D. B. (1967), *"Aerodynamic Study of Argon Plasma"*, The Physics of Fluids, vol. 10, no. 9, pp. 1962-1967.

[43] Leonard, S. L. (1972), *"Evidence for Departures from Equilibrium in an RF Induction Plasma in Atmospheric-Pressure Argon"*, Journal of Quantitative Spectroscopy and Radiative Transfer, vol. 12, no. 4, pp. 619-626.

[44] Eckert, H. U. (1971), *"Measurement of the RF Magnetic Field Distribution in a Thermal Induction Plasma"*, Journal of Applied Physics, vol. 42, no. 8, pp. 3108-3113.

[45] Pei-Qi, L., Pei-Zhong, G., Tie-Zheng, L. and Houk, R. S. (1988), *"Langmuir Probe Measurements of Electron Temperature in an Inductively Coupled Plasma"*, Spectrochimica Acta Part B: Atomic Spectroscopy, vol. 43, no. 3, pp. 273-285.

[46] Lim, H. B. and Houk, R. S. (1990), *"Langmuir Probe Measurement of Electron Temperature in a Supersonic Jet Extracted from an Inductively Coupled Plasma"*, Spectrochimica Acta Part B: Atomic Spectroscopy, vol. 45, no. 4-5, pp. 453-461.

[47] Chambers, D. M., Poehlman, J., Yang, P. and Hieftje, G. M. (1991), *"Fundamental Studies of the Sampling Process in an Inductively Coupled Plasma Mass Spectrometer-I: Langmuir Probe Measurements"*, Spectrochimica Acta Part B: Atomic Spectroscopy, vol. 46, no. 6-7, pp. 741-760.

[48] Farmer, A. J. D. and Haddad, G. N. (1988), *"Rayleigh Scattering Measurements in a Free-Burning Argon Arc"*, Journal of Physics D: Applied Physics, vol. 21, no. 3, pp. 426-431.

[49] Huang, M., Hanselman, D. S., Yang, P. and Hieftje, G. M. (1992), "*Isocontour Maps of Electron Temperature, Electron Number Density and Gas Kinetic Temperature in the Ar Inductively Coupled Plasma Obtained by Laser-Light Thomson and Rayleigh Scattering*", Spectrochimica Acta Part B: Atomic Spectroscopy, vol. 47, no. 6, pp. 765-785.

[50] Chase, J. D. (1971), "*Theoretical and Experimental Investigation of Pressure and Flow in Induction Plasmas*", Journal of Applied Physics, vol. 42, no. 12, pp. 4870-4879.

[51] Waldie, B. and Hancock, R. (1978), *"Effect of a Cool Central Gas Feed on Temperatures and Velocities in an Induction Plasma Torch"*, Transactions of the Institute of Chemical Engineers, vol. 56, pp. 178-186.

[52] Lesinski, J., Gagné, R. and Boulos, M. I. (1981), *"Gas and Particle Velocity Measurements"*, 5th International Symposium on Plasma Chemistry, August 10-14, Edinburgh, pp. 527-533.

[53] Eckert, H. U. (1969), *"Analysis of Thermal Induction Plasmas Dominated by Radial Conduction Losses"*, Journal of Applied Physics, vol. 41, no. 4, pp. 1520-1528.

[54] Eckert, H. U. (1969), "*Analytical Treatment of Radiation and Conduction Losses in Thermal Induction Plasmas*", Journal of Applied Physics, vol. 41, no. 4, pp. 1529-1537.

[55] Miller, R. C. and Ayen, R. J. (1969), *"Temperature Profiles and Energy Balances for an Inductively Coupled Plasma Torch"*, Journal of Applied Physics, vol. 40, no. 13, pp. 5260-5270.

[56] Barnes, R. M. and Schleicher, R. G. (1975), "*Computer Simulation of RF Induction-Heated Argon Plasma Discharges at Atmospheric Pressure for Spectrochemical Analysis - I. Preliminary Investigations*", Spectrochimica Acta Part B: Atomic Spectroscopy, vol. 30, no. 4, pp. 109-134.

[57] Barnes, R. M. and Schleicher, R. G. (1981), *"Temperature and Velocity Distributions in an Inductively Coupled Plasma"*, Spectrochimica Acta Part B: Atomic Spectroscopy, vol. 36, no. 2, pp. 81-101.

[58] Barnes, R. M. and Genna, J. L. (1981), *"Gas Flow Dynamics of an Inductively Coupled Plasma Discharge"*, Spectrochimica Acta Part B: Atomic Spectroscopy, vol. 36, no. 4, pp. 299-323.

[59] Mostaghimi, J., Proulx, P., Boulos, M. I. and Barnes, R. M. (1985), *"Computer Modeling of the Emission Patterns for a Spectrochemical ICP"*, Spectrochimica Acta Part B: Atomic Spectroscopy, vol. 40, no. 1-2, pp. 153-166.

[60] Boulos, M. I. (1976), *"Flow and Temperature Fields in the Fire-Ball of an Inductively Coupled Plasma"*, IEEE Transactions on Plasma Science, vol. PS-4, no. 1, pp. 28-39.

[61] Yang, P., Barnes, R. M., Mostaghimi, J. and Boulos, M. I. (1989), *"Application of a Two-Dimensional Model in the Simulation of an Analytical Inductively Coupled Plasma Discharge"*, Spectrochimica Acta Part B: Atomic Spectroscopy, vol. 44, no. 7, pp. 657-666.

[62] Proulx, P., Mostaghimi, J. and Boulos, M. I. (1991), *"Radiative Energy Transfer in Induction Plasma Modelling"*, International Journal of Heat and Mass Transfer, vol. 34, no. 10, pp. 2571-2579.

[63] Mostaghimi, J., Proulx, P. and Boulos, M. I. (1987), *"A Two-Temperature Model of the Inductively Coupled RF Plasma"*, Journal of Applied Physics, vol. 61, no. 5, pp. 1753-1760.

[64] Mostaghimi, J. and Boulos, M. I. (2000), *"Relationship between the Induction Frequency and LTE in Inductively Coupled Plasmas"*, IEEE International Conference on Plasma Science, p 201.

[65] Xue, S., Proulx, P. and Boulos, M. I. (2003), *"Effect of the Coil Angle in an Inductively Coupled Plasma Torch: A Novel Two-Dimensional Model"*, Plasma Chemistry and Plasma Processing, vol. 23, no. 2, pp. 245-263.

[66] Bernardi, D., Colombo, V., Ghedini, E. and Mentrelli, A. (2005), *"Three-Dimensional Modeling of Inductively Coupled Plasma Torches"*, Pure and Applied Chemistry, vol. 77, no. 2, pp. 359-372.

[67] Colombo, V., Ghedini, E. and Mostaghimi, J. (2008), *"Three-Dimensional Modeling of an Inductively Coupled Plasma Torch for Spectroscopic Analysis"*, IEEE Transactions on Plasma Science, vol. 36, no. 4, pp. 1040-1041.

[68] Garcia Solé, J., Bausà, L. E. and Jaque, D. (2005), *"An Introduction to the Optical Spectroscopy of Inorganic Solids"*, John Wiley, Chichester, UK.

[69] Gao, G., Mostaghimi, J. and Pershin, L. (2003) "*Spectroscopic Diagnostics of Atmospheric Argon Radio Frequency Inductively Coupled Plasma*," ISPC16 2003, Taormina, Italy.

[70] Ghosh Roy, D. N. (1983), "*Radon Inversion of Plasma Emission."* Physics Letters, vol. 96A, no, 9, pp 463-466.

[71] Ghosh Roy, D. N. (1983), "*Radon Inversion of Spectral Intensities Emitted by an Asymmetric and Absorbing Plasma*", Journal of Quantitative Spectroscopy and Radiative Transfer, vol. 35, no. 1, pp. 15-21.

[72] Nestor, O. H. and Olsen, H. N. (1960), *"Numerical Methods for Reducing Line and Surface Probe Data"*, SIAM Review, vol. 2, no. 3, pp. 200-207.

[73] Aguilera, J. A., Aragon, C., Bengoechea, J. (2003), "*Spatial characterization of laser-induced plasmas by deconvolution of spatially resolved spectra*," Applied Optics, vol. 42 pp. 5938–5946.

[74] Maldonado, C. D. and Olsen, H. N. (1966), "*New Method for Obtaining Emission Coefficients from Emitted Spectral Intensities, Part II - Asymmetric Sources*", Journal of the Optical Society of America, vol. 56, pp 1305-1313.

[75] Boas, M. L. (1983), *Mathematical Methods in the Physical Sciences*, 2nd edition, John Wiley & Sons.

[76] Yasutomo, Y., Miyata, K., Himeno, S. Enoto, Y. (1981), "*A New Numerical Method for Asymmetrical Abel Inversion*", IEEE Transactions on Plasma Science, vol. PS-9, pp. 18–21.

[77] Cristoforetti, G., Legnaioli, S., Palleschi, V., Salvetti, A., Tognoni, E. and Tomassini, P. (2005), *"Reconstruction of Laser-Induced Plasma Spectral Emissivity in Non-Axisymmetric Conditions"*, Spectrochimica Acta Part B: Atomic Spectroscopy, vol. 60, no. 7-8, pp. 888-896.

[78] Elder, P., Jerrick, T. and Birkeland, J. W. (1965), "*Determination of the Radial Profile of Absorption and Emission Coefficients and Temperature in Cylindrically Symmetric Sources with Self-Absorption*", Applied Optics, vol. 4, no. 5, pp. 589-592.

[79] Franceries, X., Freton, P., Gonzalez, J., Lago, F. and Masquere, M. (2005), *"Tomographic Reconstruction of 3D Thermal Plasma Systems: a Feasibility Study."* Journal of Physics D: Applied Physics, vol. 38, pp. 3870-3884.

[80] Turgeon, E. C. and Shepherd, G. G. (1962), *"Upper Atmospheric Temperatures from Doppler line widths—II: Measurements on the OI 5577 and OI 6300 Å lines in Aurora*", Planetary and Space Science, vol. 9, no. 6, pp. 295-304.

[81] Kleinmann, I. and Cajko, J. (1970), *"Spectrophysical Properties of the Plasma of a High Frequency Low Power Discharge in Argon at Atmospherical Pressure"*, Spectrochimica Acta Part B: Atomic Spectroscopy, vol. 25, no. 12, pp. 657-668.

[82] Zemansky, M. W. and Dittman, R. (1981), *"Heat and Thermodynamics"*, 6th ed, McGraw-Hill, Singapore.

[83] Olsen, H. N. (1959), *"Thermal and Electrical Properties of an Argon Plasma"*, The Physics of Fluids, vol. 2, no. 6, pp. 614-623.

[84] Chowdhury, S. S. (1969), *"The Composition of an Argon Plasma in Saha Equilibrium"*, Journal of Quantitative Spectroscopy and Radiative Transfer, vol. 9, no. 1, pp. 129-135.

[85] Kaga, Y., Tsuge, S., Kitagawa, K. and Arai, N. (1999), "*Temporally Resolved Boltzmann Plots and Excitation Temperatures of Iron Atoms in a Helium Radiofrequency Atomization/Excitation Source for Atomic Emission Spectrometry*", Microchemical Journal, vol. 63, pp. 34-42.

[86] Ohno, N., Razzak, N. A., Ukai, H., Takamura, S. and Uesugi, Y. (2006), "*Validity of Electron Temperature Measurement by using Boltzmann Plot Method in Radio Frequency Inductive Discharge in the Atmospheric Pressure Range*", Plasma and Fusion Research, vol. 1, no. 28, pp. 1-8.

[87] De Regt, J. M., van Dijk, J., van der Mullen, J. A. M. and Schram, D. C. (1995), *"Components of Continuum Radiation in an Inductively Coupled Plasma."*, Journal of Physics D: Applied Physics, vol. 28, pp. 40-46.

[88] Wilbers, A. T. M., Kroesen, G. M. W., Timmermans, C. J. and Schram, D. C. (1991), *"The Continuum Emission of an Arc Plasma"*, Journal of Quantitative Spectroscopy and Radiative Transfer, vol. 45, no. 1, pp. 1-10.

[89] Bastiaans, G. J. and Mangold, R. A. (1985), *"The Calculation of Electron Density and Temperature in Ar Spectroscopic Plasmas from Continuum and Line Spectra"*, Spectrochimica Acta Part B: Atomic Spectroscopy, vol. 40, no. 7, pp. 885-892.

[90] Rouffet, M. E., Cressault, Y., Gleizes, A. and Hlina, J. (2008), *"Thermal Plasma Diagnostic Methods Based on the Analysis of Large Spectral Regions of Plasma Radiation"*, Journal of Physics D: Applied Physics, vol. 41, 125204 (8pp).

[91] Griem, H. R. (1974), *"Spectral Line Broadening by Plasmas"*, Academic Press, New York and London.

[92] De Regt, J. M., Tas, R. D. and van der Mullen, J. A. M. (1996), *"A Diode Laser Absorption Study on a 100 MHz Argon ICP"*, Journal of Physics D: Applied Physics, vol. 29, pp. 2404-2412.

[93] Schinköth, D., Kock, M. and Schulz-Gulde, E. (1999), *"Experimental Stark Broadening Parameters for Near-infrared ArI and KrI Lines"*, Journal of Quantitative Spectroscopy and Radiative Transfer, vol. 64, no. 6, pp. 635-643.

[94] Degout, D. and Catherinot, A. (1986), "*Spectroscopic Analysis of the Plasma Created by a Double-Flux Tungsten Inert Gas (TIG) Arc Plasma Torch*," Journal of Physics D: Applied Physics, vol. 19, pp. 811-823.

[95] Johnston, P. D., (1968), "*Determination of Temperature in a Radio-Frequency Discharge Using a Reversal Technique*." Journal of physics D: Applied Physics, vol. 1, pp. 479-484.

[96] Mahan, J. R., (2002) "*Radiation Heat Transfer - A Statistical Approach*", John Wiley & Sons, New York.

[97] Schott Optik web site, http://www.schott.com.

[98] Präzisions Glas & Optik web site http://www.pgo-online.com.

[99] Corning web site, http://www.corning.com.

[100] VanBrocklin, R. R., Hobbs, T. W. and Edwards, M. J. (2004), *"Corning's Approach to Segment Blank Manufacturing for an Extremely Large Telescope"*, Proceedings of SPIE - The International Society for Optical Engineering, vol. 5494, pp. 1-8.

[101] Gemini Observatory website, http://www.gemini.edu.

[102] Boostec web site, http://boostec.com.

[103] Bougoin, M. and Deny, P. (2004), *"The SiC Technology is Ready for the Next Generation of Extremely Large Telescopes"*, Proceedings of SPIE - The International Society for Optical Engineering, vol. 5494, pp. 9-18.

[104] Johnson, J. S., Grobsky, K. and Bray, D. J. (2002), "*Rapid Fabrication of Lightweight Silicon Carbide Mirrors*", Proceedings of SPIE - The International Society for Optical Engineering, vol. 4771, pp. 243-253.

[105] European Space Agency Herschel Telescope page, http://www.esa.int/esaMI/Herschel/SEMBM00YUFF_0.html.

[106] Parsonage, T. (2004), *"JWST Beryllium Telescope: Material and Substrate Fabrication"*, Proceedings of SPIE - The International Society for Optical Engineering, vol. 5494, pp. 39-48.

[107] Hibbard, D. L. (1997), "*Electroless nickel for optical applications*", SPIE critical reviews, C 67, 167-196.

[108] Cesic® web site, http://www.cesic.de.

[109] Krödel, M. and Lichtscheindl, J. (2004) "*Cesic® - Manufacturing study for Next Generation Telescopes*," Proceedings of SPIE - The International Society for Optical Engineering, vol. 5494, pp. 19-26.

[110] Flamm, D. L. (1990), *"Mechanisms of Silicon Etching in Fluorine- and Chlorine-Containing Plasmas"*, Pure & Applied Chemistry, vol. 62, no. 9, pp. 1709-1720.

[111] Suzuki, K. and Itabashi, N. (1996), *"Future Prospects for Dry Etching"*, Pure & Applied Chemistry, vol. 68, no. 5, pp. 1011-1015.

[112] Wilson, S. R. and McNeil, J. R. (1987), *"Neutral Ion Beam Figuring on Large Optical Surfaces"*, Proceedings of SPIE - The International Society for Optical Engineering, vol. 818, pp. 320-324.

[113] Allen, L. N. and Romig, H. W. (1990), *"Demonstration of an Ion Beam Process"*, Proceedings of SPIE - The International Society for Optical Engineering, vol. 1333, pp. 22-33.

[114] Allen, L. N., Keim, R. E. and Lewis, T. S. (1991), *"Surface Error Correction of a Keck 10 m Telescope Primary Mirror Segments by Ion Figuring"*, Proceedings of SPIE - The International Society for Optical Engineering, vol. 1531, pp. 195-204.

[115] Allen, L. N., Hannon, J. J. and Wambach, R. W. (1991), *"Final Surface Error Correction of an Off-Axis Aspheric Petal by Ion Figuring"*, Proceedings of SPIE- The International Society for Optical Engineering, vol. 1543, pp. 190-199.

[116] Egert, C. M. (1992), *"Roughness Evolution of Optical Materials Induced by Ion Beam Milling"*, Proceedings of SPIE - The International Society for Optical Engineering, vol. 1752, pp. 63-72.

[117] Kurashima, Y., Miyachi, S., Miyamoto, I., Ando, M. and Numata, A. (2008), *"Evaluation of Surface Roughness of ULE® Substrates Machined by Ar+ Ion Beam"*, Microelectronic Engineering, vol. 85, no. 5, pp. 1193-1196.

[118] Kurashima, Y., Uozumi, R., Miyamoto, I., Ando, M. and Numata, A. (2007), *"Evaluation of Surface Roughness of Zerodur® Substrates Machined by Ar+ Ion Beam with Energy of 3-10 keV"*, Journal of Vacuum Science and Technology B, vol. 25, no. 6, pp. 2104-2109.

[119] Gailly, P., Collette, J., Renson, L. and Tock, J. (1999), *"Ion Beam Figuring of Small BK7 and Zerodur Optics: Thermal Effects"*, Proceedings of SPIE - The International Society for Optical Engineering, vol. 3739, pp. 124.

[120] Frost, F., Fechner, R., Ziberi, B., Flamm, D. and Schindler, A. (2004), *"Large Area Smoothing of Optical Surfaces by Low-Energy Ion Beams"*, Thin Solid Films, vol. 459, no. 1-2, pp. 100-105.

[121] Leibniz-Institute for Surface Modification biennial report 2004/2005, available online at http://www.iom-leipzig.de/html/eng/berichte.cfm.

[122] Frost, F., Schindler, A. and Bigl, F. (1998), *"Reactive Ion Beam Etching of InSb and InAs with Ultrasmooth Surfaces"***,** Semiconductor Science & Technology, vol. 13, pp. 523-527.

[123] Golini, D., Kordonski, W. I., Dumas, P. and Hogan, S. (1999), "*Magnetorheological Finishing (MRF) in Commercial Precision Optics Manufacturing*", Proceedings of SPIE - The International Society for Optical Engineering, vol. 3782, pp. 80-91.

[124] Shorey, A. Kordonski, W. L., Tricard, M. (2004), "*Magnetorheological Finishing and Sub-Aperture Stitching Interferometry of a Large and Lightweight Optics*", Proceedings of SPIE - The International Society for Optical Engineering, vol. 5494, pp. 81-89.

[125] Arnold, T., Böhm, G., Fechner, R., Meister, J., Nickel, A., Frost, F., Hänsel, T. and Schindler, A. (2010), *"Ultra-Precision Surface Finishing by Ion Beam and Plasma Jet Techniques—Status and Outlook"*, Nuclear Instruments and Methods in Physics Research Section A: Accelerators, Spectrometers, Detectors and Associated Equipment, vol. 616, pp. 147-156.

[126] Nikon web site, http://www.nikon.com/about/technology/core/precision/plasma_cvm_e/index.htm.

[127] Yamamura, K., Shimada, S. and Mori, Y. (2008), *"Damage-Free Improvement of Thickness Uniformity of Quartz Crystal Wafer by Plasma Chemical Vaporization Machining"*, CIRP Annals - Manufacturing Technology, vol. 57, no. 1, pp. 567-570.

[128] Yamamura K., Sano, K., Shibahara, M., Yamauchi, K., Mimura, H., Endo, K. and Mori, Y. (2006), "*Ultra Precision Machining Utilizing Numerically Controlled Scanning of Localized Atmospheric Pressure Plasma*," Japanese Journal of Applied Physics, vol. 45, pp. 8270–8276.

[129] Zhang, J., Wang, B. and Dong, S. (2007), "*Application of Atmospheric Pressure Plasma Polishing Method in Machining of Silicon Ultra-Smooth Surfaces"*, Frontiers of Electrical or and Electronic Engineering in China, vol. 3(4), pp. 480-487.

[130] McFadden, K. O. and Tschuikow-Roux, E. (1973), "*Spectrophotometric determination of the rate of dissociation of nitrogen trifluoride behind shock waves*," Journal of Physical Chemistry, vol. 77, pp. 1475-1478.

[131] Henderson, P. B. and Woytek, A. J. (1994) "*Fluorine Compounds, Inorganic, Nitrogen*" in *Kirk-Othmer Encyclopedia of Chemical Technology*, John Wiley & Sons, New York.

[132] Lemmon, E. W., McLinden, M. O. and Friend, D. G., *"Thermophysical Properties of Fluid Systems"* in NIST Chemistry WebBook, NIST Standard Reference Database Number 69, Eds. Linstrom, P. J. and Mallard, W. G., National Institute of Standards and Technology, Gaithersburg MD, 20899, http://webbook.nist.gov.

[133] Armstrong, G. T., Marantz, S. and Coyle, C. F. (1959), *"Heat of Formation of Nitrogen Trifluoride and the N-F Bond Energy"*, Journal of the American Chemical Society, vol. 81, no. 14, pp. 3798-3798.

[134] Lambropoulos, J. C., Xu, S., Fang, T. and Golini, D. (1996) "*Twyman effect mechanics in grinding and microgrinding*", Applied Optics, vol. 35, no. 28, pp 5704-5712.

[135] Fanara, C., Shore, P., Nicholls, J. R., Lyford, N., Kelley, J., Carr, J. and Sommer, P. (2006), *"A new reactive atom plasma technology (RAPT) for precision machining: The etching of ULE® surfaces"*, Advanced Engineering Materials, vol. 8, no. 10, pp. 933-939.

[136] RAPT Industries, private communication.

[137] Subrahmanyan, P. K. and Gardopee, G. J. (2008), *"Reactive Atom Plasma (RAP) Processing of Mirrors for Astronomy"*, Proceedings of SPIE - The International Society for Optical Engineering, vol. 7018, pp. 9-13.

[138] Mainsah, E., Greenwood, J. A. and Chetwynd, D. G. (2001), "*Metrology and Properties of Engineering Surfaces*", 2nd ed, Kluwer Academic Publishers, Boston, USA.

[139] Gåsvik, J. G., (1995), "*Optical Metrology*", John Wiley & Sons, Trondheim, Norway.

[140] Wyant, J. C. "*White Light Interferometry*", Optics Science Center, University of Arizona. Available online at http://www.optics.arizona.edu/jcwyant/pdf/Meeting_papers/WhiteLightInterferometry.pdf.

[141] Ralchenko, Y., Kramida, A. E., Reader, J. and NIST ASD Team (2008). *NIST Atomic Spectra Database* (version 3.1.5). Available on-line: http://physics.nist.gov/asd3, National Institute of Standards and Technology, Gaithersburg, MD.

[142] Steiger, W. and Rüdenauer, F. G. (1974), *"Internal Partition Functions for Neutral Atoms of the Iron Group Elements in the Temperature Range 0–15000 K"*, International Journal on Mass Spectrometry and Ion Physics, vol. 13, no. 4, pp. 411-414.

[143] Patankar, S. V. (1980), "*Numerical Heat Transfer and Fluid Flow*", Hemisphere, Washington, New York and London.

[144] Shaw, M. C. (1996), "*Principles of Abrasive Processing*", Clarendon, Oxford.

[145] Iuchi, T. and Gogami, A. (2010), "*Simultaneous measurement of emissivity and temperature of silicon wafers using a polarization technique*", Measurement, vol. 43, no. 5, pp. 645-651.

[146] Redgrove, J. S. (1990), *"Measurement of the spectral emissivity of solid materials"*, Measurement, vol. 8, no. 2, pp. 90-95.

[147] Stierwalt, D. L. and Potter, R. F. (1962), *"Lattice absorption bands observed in silicon by means of spectral emissivity measurements"*, Journal of Physics and Chemistry of Solids, vol. 23, no. 1-2, pp. 99-102.

[148] Ravindra, N. M., Ravindra, K., Mahendra, S., Sopori, B. and Fiory, A.T. (2003), "*Modeling and Simulation of Emissivity of Silicon-Related Materials and Structures*" Journal of Electronic Materials, vol. 32, no. 10, pp. 1052-1058.

[149] Benoy, D. A. (1993), "*Modelling of Thermal Argon Plasmas*", PhD thesis. Available online http://plasimo.phys.tue.nl.